1-1-2003

Surface and interfacial structures induced by electrohydrodynamic instabilities.

Zhiqun Lin
University of Massachusetts Amherst

SURFACE AND INTERFACIAL STRUCTURES INDUCED BY ELECTROHYDRODYNAMIC INSTABILITIES

A Dissertation Presented

by

ZHIQUN LIN

Submitted to the Graduate School of the
University of Massachusetts in partial fulfillment of the
degree requirements for the degree of

DOCTOR OF PHILOSOPHY

February 2003

Polymer Science and Engineering

SURFACE AND INTERFACIAL STRUCTURES INDUCED BY ELECTROHYDRODYNAMIC INSTABILITIES

A Dissertation Presented

by

ZHIQUN LIN

Approved as to style and content by:

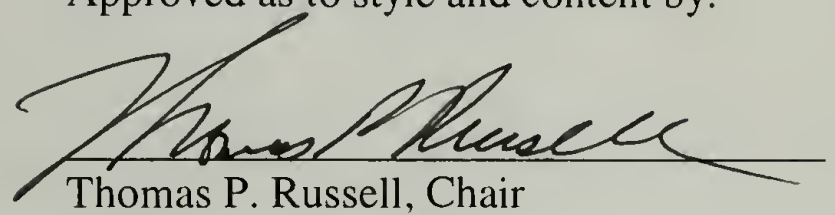

Thomas P. Russell, Chair

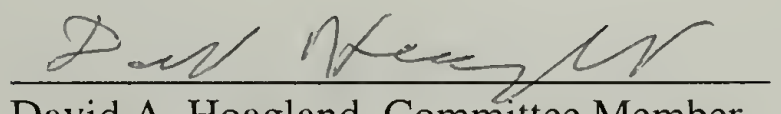

David A. Hoagland, Committee Member

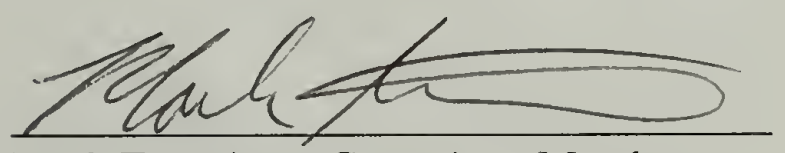

Mark Tuominen, Committee Member

Thomas J. McCarthy, Department Head
Polymer Science and Engineering

To My Family

ACKNOWLEDGEMENTS

Not only just a pleasure of an achievement, but also a heavy-heated feeling surge to my mind at this particular moment of completing my thesis. Last four years have been passed very quickly. Although it is not that long in comparison to one's life, I learn and gain tremendously through these years, which would direct me to the future I had ever dreamed.

First and foremost, I am most thankful to my great advisor, Prof. Tom Russell for his wise guidance, infinite patience, continuous support and encouragement over the years. He guided me into the surface and interface, this deserves elaborative cultivated rich field. I am always amazed by his broad knowledge of polymer physics, together with his unbelievable sharp insight to identify the relevant physics in a particular problem. I am very grateful for having had the honor of working with him. His creativity, enthusiasm and sincere interest in the field of polymer physics, his popularity and loving-kindness as a senior have been and will be my unlimited fortune, which I can benefit from through my life.

I am also extremely grateful to my committee members, Prof. David Hoagland, Prof. Mark Tuominen for their time, many valuable comments and discussions. David provided me his expertise in fluid dynamics. Mark provided me his expertise in the electric field lines calculations. Another, less official, committee member is Prof. Ullrich Steiner. He provided me many insightful comments and suggestion for my research work through the years.

Advisorship didn't stop here. I have also learned a great deal from our group visiting scientists Jinkon Kim, Shenda Baker, Thomas-Thurn Albrecht, Injoo Chin, as well as Postdoc fellows Tobias Kerle, Hocheol Kim, Dongha Kim, Keisuke

Kuriyama, Mashahiro Kimura and Xiaodong Wu. I would like to especially thank Tobias Kerle for giving me numerous advice for my project. We worked together as a team. I owe a great debt to Hocheol Kim, a super nice person, for initiating me into the ways of the group.

I also always appreciate the helps and stimulating discussions from the past in our group Elbert Huang, Lee Rockford, Michael Pollard, Jason DeRouchey, Chris Stafford, Scott Kennedy as well as current students James Goldbach, Amada Leach, Irene Tsai, Ting Xu, Yao Lin, Matt Misner and Kris Lavery. They have been fun to work with and made the lab hours a memorable experience. I learned how to use evaporator from Lee, how to operate SAXS from Michael. Jason gave me many excellent suggestions to improve my presentation skill.

I wish to express my gratefulness to Prof. Shaw Ling Hsu, Prof. Tom McCarthy, Prof. Sam Gido, Prof. Murugappan Muthukumar and Prof. Frank Karasz for their many helps and encouragement. Prof. Hsu interviewed me in China and gave me a chance to come to UMass to pursue my Ph.D. in the number one polymer research center all over the world. He took greatest care of me for the first couple months of my life at UMass.

In addition, I would like to thank all other assistances outside of my research group. Xinqiao Jia helped me run couples of XPS measurements. Huiqing Zhang provided me a TGA measurement. Terry showed me how to use dielectric spectroscopy in detail. Vivek Prabuh assisted me SAXS measurement. Alan Waddon taught me to use WAXD. Mustafa Bal transferred his electric beam lithography technique to me over a period of several days.

I also would like to thank Linda Strzewgowski, Eileen Besse, Sophia Hsu, Ann Brainerd for helping me in many ways with research and bureaucracy.

Finally, I want to thank my parents, my sister, my wife and my daughter for everything they have done for me in my life. Especially my wife Haiqing, her love, consistent support, consistent understanding and sacrifice have made four years at UMass one of the best time in my life. She pushed me to know that setback can help you accumulate experience, and experience can, in turn, enrich your mind. Their endless support and love have been the basis of my achievement.

ABSTRACT

SURFACE AND INTERFACIAL STRUCTURES INDUCED BY

ELECTROHYDRODYNAMIC INSTABILITIES

FEBRUARY 2003

ZHIQUN LIN, B.S., XIAMEN UNIVERSITY, FUJIAN, CHINA

M.S., FUDAN UNIVERSITY, SHANGHAI, CHINA

M.S., UNIVERSITY OF MASSACHUSETTS AMHESRT

Ph.D., UNIVERSITY OF MASSACHUSETTS AMHESRT

Directed by: Professor Thomas P. Russell

Subjecting a liquid/liquid interface to an electrohydrodynamic pressure enhances fluctuations of a characteristic wavelength, leading to an instability and eventually the formation of well-defined columnar structures. Extending the linear stability analysis of a single fluid interface to a liquid/liquid bilayer produced generalized results applicable to any interface. Countering the electrohydrodynamic pressure is the Laplace pressure, which is dictated by the surface energy or the interfacial energy. Consequently, the characteristic length scale for the bilayer instability is reduced. Results presented for different polymer bilayers under a wide range of experimental conditions show quantitative agreement with the generalized theory with no adjustable parameters. Data over four orders of magnitude in reduced wavelength and field strength can be described by the theory.

External electric fields are also used to amplify interfacial fluctuations in a air/polymer/polymer system where one polymer dewets the other. Two different hydrodynamic regimes are found as a function of electric field strength. For weak fields, heterogeneous nucleation can lead to the formation of holes before the

electrostatically driven instability sets in and the dewetting kinetics are not influenced by the electric field. Stronger electric fields lead to a spinodal instability that causes the formation of polymer columns on top of the second polymer. In addition, the analysis of the polymer-polymer interface during the early stage of the instability indicates a slip boundary condition for the upper layer on the lower fluid substrate.

Columnar structures with a characteristic hexagonal order increase in diameter at a rate dictated by a balance of the forces exerted on the surface of the columns and on the underlying reservoir. If the reservoir is exhausted, or if dewetting occurs, the columns are isolated and growth is arrested, kinetically trapping the size of the columns.

An alternative way to control structure formation at the surface of a thin liquid film is presented by creating topographical patterns comprised of stripes with well defined widths. It is seen that undulations beneath a stripe pattern lead to the formation of columns. The width of the stripes is seen to markedly alter the wavelength of lateral growth of the fluctuations.

TABLE OF CONTENTS

LIST OF TABLES

LIST OF FIGURES

CHAPTER 1

SINGLE LAYER FILM IN AN ELECTRIC FIELD

Introduction

Controlling structure formation at interfaces on length scales micrometers or less has been studied extensively. One route to achieve such control relies on instabilities at the interfaces. The dynamic instability of thin dielectric films is of interest not only academically, but also technologically, for example in microlithography, coatings and adhesion. There are three different categories of instabilities that are of current interest.

Instabilities Driven by Dispersive Forces

Instabilities induced by van der Waals interactions, i.e. spinodal dewetting,[1] for example, have been the subject of many studies theoretically[2-10] and experimentally.[11-18] Spinodal dewetting is triggered by thermally excited capillary waves and amplified by the disjoining pressure. It is characterized by the development of correlated fluctuations at the surface of a liquid film, ultimately leading to the disruption of the film and dewetting, where the height fluctuations of thin liquid film are analogous to composition fluctuations in polymer mixture system[19,20]. Brochard theoretically studied the mechanism of dewetting of liquid A / liquid B bilayers.[4] The microscopic films are unstable and spinodally decomposed by amplifying the fluctuation of capillary waves. The deformation in upper liquid A gives rise a pressure gradient in lower liquid B and induces a Poiseuille flow in

liquid B.[21] Sharma et al. simulated the pattern formation in the unstable thin liquid films based on a 3D nonlinear equation of motion.[6,22] Lambooy et al. qualitatively compared their experimental results with Brochard's theory.[23] They found by varying the degree of the coupling between two flows, the buried interface between PS (MW=95K) and PMMA is less deformed with the increased molecular weight (MW) of PMMA. Figure 1.1 shows the section analysis of the AFM images. The molecular weight (MW) of upper PS layer is 95K, while MWs of PMMA are varied. The dash and solid lines are the profiles of the PS surface and the "buried" PS/PMMA interface. The equilibrium of contact angle Θ_E is proportional to the viscosity ratio of PS to PMMA. The contact angle at the PS/PMMA interface is decreased with the increased MW of PMMA. Qu et al. investigated Brochard's theory and established a quantitative comparison of their experiments with theory.[24] The scaling behavior of dewetting velocity with PS molecular weight was determined and three regimes, as predicted by Brochard, were observed. Sferrazza et al. studied deuterated PMMA (d-PMMA) dewets from PS substrate by specular and off specular neutron reflectivity to characterize the typical distance and time scale for this buried polymer interface.[25]

Wetting and dewetting are well known phenomena. Another mechanism to initiate the dewetting is by nucleation and growth via particulate impurities, air bubbles or defects inside the system. Herminghaus and coworkers[8] showed the presence of air bubbles and other defects, such as indentations in the polymer surface, can lead to hole formation by heterogeneous nucleation. Stange and Evans[26] pointed out the spinodal dewetting dominates over the nucleation process under

clean room conditions. Particle nucleation increases in higher aerosol concentration environments. This indicates the airbone particles might fall onto the film surface to act as nucleation sites. Stange and Evans also found a third type of nucleation occurs upon the thermal cycling of the films by scan probe microscopy, due to a delamination-induced buckling of polystyrene film which film thickness is about 22nm.

de Gennes, Brochard and Joanny had investigated the dewetting dynamics in great detail theoretically.[4,21,26,27] Brochard pointed out dewetting evolves by balancing the capillary force F_d, which promotes dewetting, with the viscous force F_v, which retards dewetting.[4]

$$F_d = \frac{1}{2}\gamma(\theta_E^2 - \theta^2)$$

and $$F_v = k\eta\frac{V_A}{\theta} \qquad (1)$$

where θ and Θ_E are the dynamical and equilibrium contact angle, respectively. The dewetting behavior can be described by the spreading coefficient S.

$$S = \gamma_B - (\gamma_A + \gamma_{AB}) . \qquad (2)$$

If S is smaller than zero, liquid A will dewet liquid B.

Electrohydrodynamic (EHD) Instabilities Driven by External Electric Field

All the above studies were based on instabilities of the system driven by dispersive forces in the absence of an applied external field. The application of electric field has been shown to orient the morphologies of dielectric fluids[12,13,28-45],

as seen in the alignment of diblock copolymers.[28-36] Electrical fields have been used to overcome the interfacial interactions to produce well ordered arrays of nanoscopic morphologies.

The influence of an electrical field on the surface of a polymer or viscous fluid was first investigated by Swan in 1897.[39] In conjunction with the development of xerography, Glenn described a process called "thermoplastic recording", for recording electrical signals that involved focusing an electron beam on low melting thermoplastics films.[40] Cressman subsequently developed a one-dimensional model to describe instabilities on the surface of a thin, thermoplastic film between two electorodes after placing a uniform charge on the surface.[41] Killat extended these studies to thicker films under the influence of a surface charge that led to a deformation of the thermoplastic.[42] Using low viscosity fluids, Reynolds investigated the interface between two fluids under an alternating field where the influence of surface charge is minimized.[43] These studies indicated that the interface would be unstable when the applied field exceeded a critical value. Melcher subsequently examined the electrodynamic charge relaxation at interfaces in a field applied normal to the interface.[44] Experiments using AC and DC fields indicated that conductance from charge convection at the interface played a role in destabilizing the interface. Saville has extensively investigated the electrohydrodynamic deformation of colloidal dispersions in weakly conducting liquids under static and oscillatory fields.[46-51] Onuki theoretically treated instabilities at the interface between two immiscible, nonionic fluids.[45] Herminghaus theoretically predicted a dynamical instability of dielectric coating between electrically conductive media. He showed

Figure 1.1. The section analysis of AFM images. The molecular weight (MW) of upper PS layer is 95K, while MWs of PMMA are varied. The dash and solid lines are the profiles of PS surface and the "buried" PS/PMMA interface, respectively.[23]

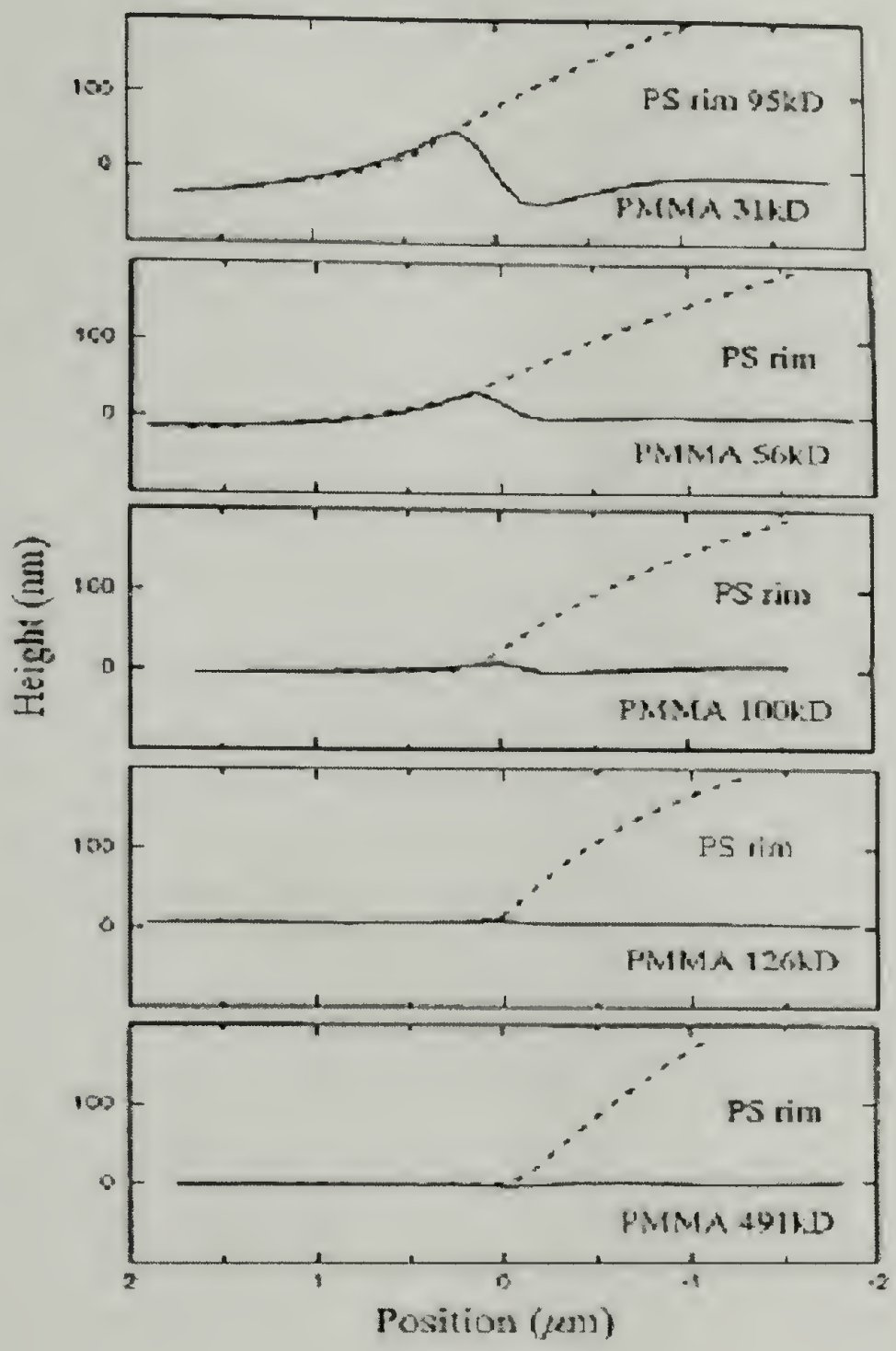

that electric forces are effective in overcoming dispersive forces and, thereby, amplify surface fluctuations.[37] The fastest growth mode is given by

$$q_{\max} = U\sqrt{\varepsilon\varepsilon_0/2\sigma}\, h_0^{-\frac{3}{2}} \tag{3}$$

where U is the applied voltage, ε is the dielectric constant of dielectric liquid, σ is interfacial tension between the film and the upper medium and h_0 is the film thickness. Pelrine et al. have recently used dielectric elastomers (for instance, silicones), sandwiched in between conductive materials, to make electrical actuators.[38] The potential applications in artificial muscles, loudspeakers, robotics etc. by using these highly electrically responsive elastomer actuators were proposed. More recently, Nagel and coworkers investigated the time evolution of instabilities at liquid interfaces driven by an electric field applied normal to the interface using high speed film movie camera.[52] Figure 1.2 shows the time sequences of an electrohydrodynamic spout at the oil/water interface with an instantaneous electric field applied. The upper and lower fluids are silicon oil and distilled water, respectively. The low concentration sodium chloride is added into distilled water in order to control the conductance. The initially flat interface grows into a hump whose curvature increases with time. The curvature of the tip diverges between the frame 6 and the frame 7, thereafter the instability continues to develop, emitting a jet as can be seen in the frame 9. In the frame 10 a spray reaches the upper electrode and eventually the lightning occur. Both curvature and height of the fluctuations exhibit scaling law with respect to a critical time corresponding to a critical point in the dynamics underlying the instabilities.

Schäffer et al. recently reported that electrostatic forces across the surface of a polymer above its glass transition temperature will amplify surface waves resulting in a laterally-ordered array of columns of the polymer spanning the gap between the electrodes.[12,13] Their calculations indicated that a well defined lateral wavelength follows a power-law dependence as a function of the applied electric field.[12,13] Experiments on films between parallel capacitor plates leaving an air gap under both DC and AC fields, showed good agreement with theory. The characteristic wavelength is given by

$$\lambda_{\max} = 2\pi\sqrt{\frac{\gamma U}{\varepsilon_0 \varepsilon_P (\varepsilon_P - 1)^2}} E_P^{-\frac{3}{2}} \tag{4}$$

where U is the applied voltage, γ is the surface tension of polymer, ε is the dielectric constant of polymer, ε_0 is the permittivity in vacuum, and E is the electric field strength in the polymer.

Observations similar to those of Schäffer et al were made by Chou and coworkers,[14,15] who were able to create a periodic arrays of polymer cylinders in the absence of an applied external field. They proposed an electrostatic attraction between two surfaces that overcome surface tension and the gravitational force on the films.

Thermomechanical Instabilities Driven by Temperature Gradient

Thin polymer film can also be unstable in the presence of temperature gradient.[53] The thermomechanical pressure caused by the temperature gradient at the

interface between two different media is strong enough to overcome the surface tension γ and the viscous drag to induce the instabilities.

It is well known that temperature gradient induces the density and surface tension variation when crossing a liquid. The pattern formation is caused as a result of convective instabilities for a macroscopic film.[54] In the case of thin film, the density variation induced Rayleigh-Bernard convection and surface tension driven Bernard-Marangoni effect can be neglected in comparison to the heat diffusion which causes a thermomechanical force to destabilize the film. The general temperature gradient in the range of 10-50°C/μm is applied in between the bottom and top plates.[53] In addition to the typical columnar morphology, the stripes and spiral patterns are also observed in a same sample. Figure 1.3 shows the optical micrographs of polystyrene films heated in the presence of different temperature gradients. The most unstable wavelength under various experimental conditions can be scaled with a characteristic parameter -- heat flux across the film and is found to be proportional to the square root of the temperature gradient.

Creating controlled structures from micron to nanometer scale is very important technologically. Besides temperature gradient[53,55] and directional eutectic solidification,[56] an external electric field has been shown to generate the controlled structures at the polymer/air interface.[12,13]

To better understand the physics at the polymer/air interface first discussed by Schäffer et al.[12,13], this work sets forth a series of systematic studies on thin film to generate structures under well defined conditions.

Figure 1.2. Time development of an electrohydrodynamic spout at the oil-water interface in electric field.[52] The width of the upper electrode is 6.4 mm. The first six snapshots (counting from the upper left corner) show how the initially flat interface grows into a hump whose apex curvature increases with time. Between the sixth and seventh snapshots the curvature of the tip diverges. Thereafter, the instability continues to develop, emitting a jet as can be seen in snapshots 7, 8, and 9. In snapshot 10 the spray has reached the upper electrode and "lightning strike," line is seen in the photograph. In frames 11 and 12 the charged spray is repelled from the upper electrode towards the body of the spout.

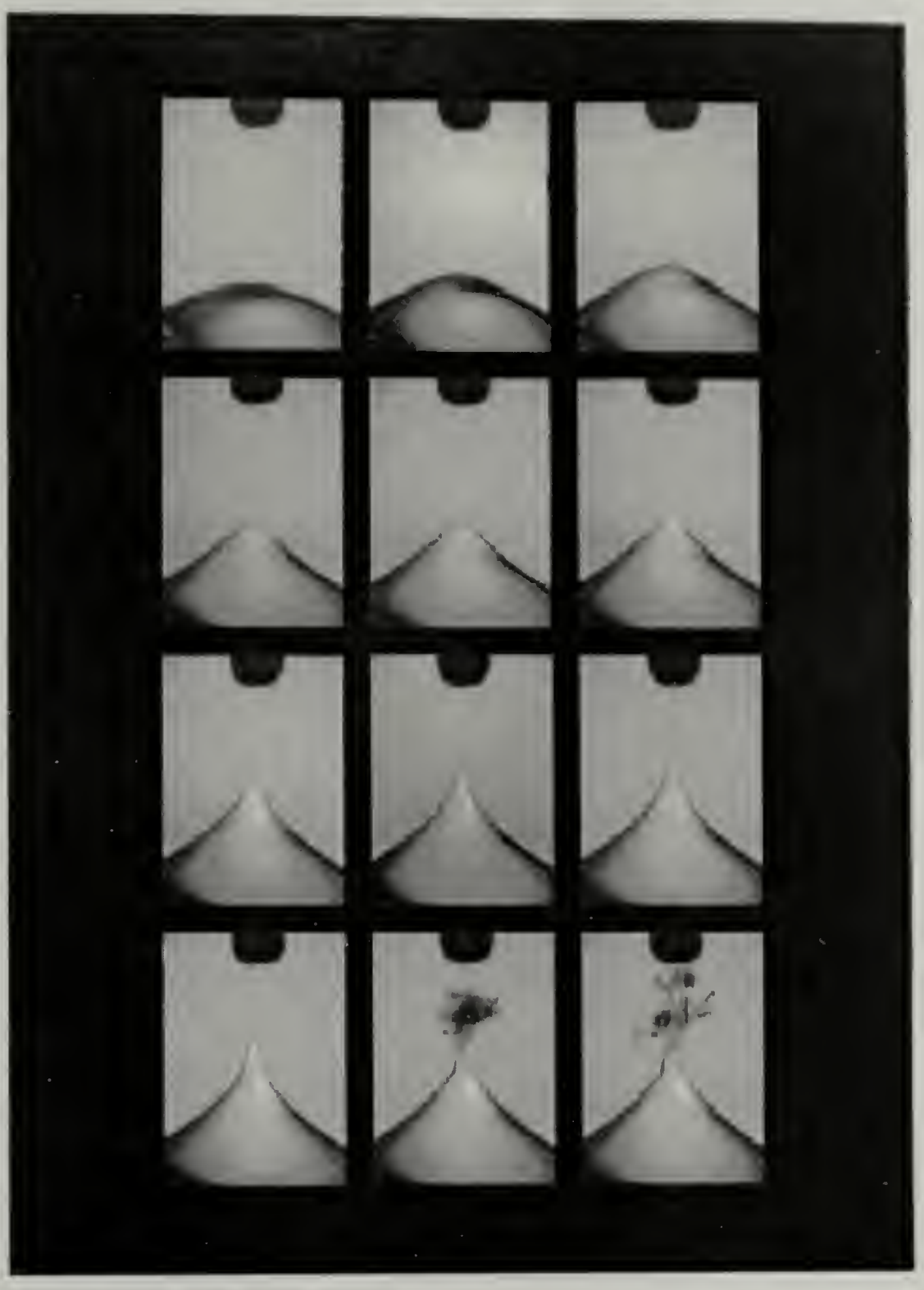

Experimental

Materials

Poly(4-bromo styrene) (PSBr) (MW=6.5x10^4) and poly(dimethylsiloxane) (PDMS) (200®Fluid, with a viscosity η=10,000Cst.) were purchased from Aldrich Chemical Co. Deuterated polystyrene (dPS) with a molecular weight of 99.9K (PDI=1.017) was synthesized in our laboratory by anionic polymerization. Indium-tin-oxide coated (ITO) microscope slides, a transparent electrode used in this study, were purchased from Delta Technologies (25x50x1.1mm^3, Rs$\leq$ 100ohms).

Sample Preparation

The general sample configuration used in the study is shown in Figure 1.4. The transparent ITO glass serves as the upper electrode. The separation distance between Si substrate and ITO glass can be controlled by evaporating thin rails of SiOx on the top of ITO glass or Si substrate as an insulating spacer. In the case of single layer and bilayer studies, medium 1 and medium 2 are air/liquid, and liquid 1/liquid 2, respectively.

In the single layer study, 530 nm thick deuterated polystyrene (d-PS) (MW=99.9K) thin films are spun from toluene solution on a clean Si substrate. The thickness of the air gaps above the d-PS films was varied. Samples were then exposed to 30 V. In a second set of studies, a 730 nm thick PSBr (MW=65K) film was spin-coated from toluene onto a clean Si wafer. Both the applied voltages and thickness of the gap height was varied. All single layer samples were annealed at 170°C above the glass transition temperatures of d-PS and PSBr ($T_{g,PS}$=100°C and $T_{g,PSBr}$=119°C), under N_2 for a day with an applied electric field and quenched to room temperature before removing the applied field.

Figure 1.3. Optical micrographs of polystyrene films heated in the presence of a temperature gradient.[53] The formation of (a) columnar patterns (h = 100 nm, d = 285 nm and ΔT = 46°C); (b) striped pattern (h = 110 nm, d = 170 nm, ΔT = 54°C).

(a)

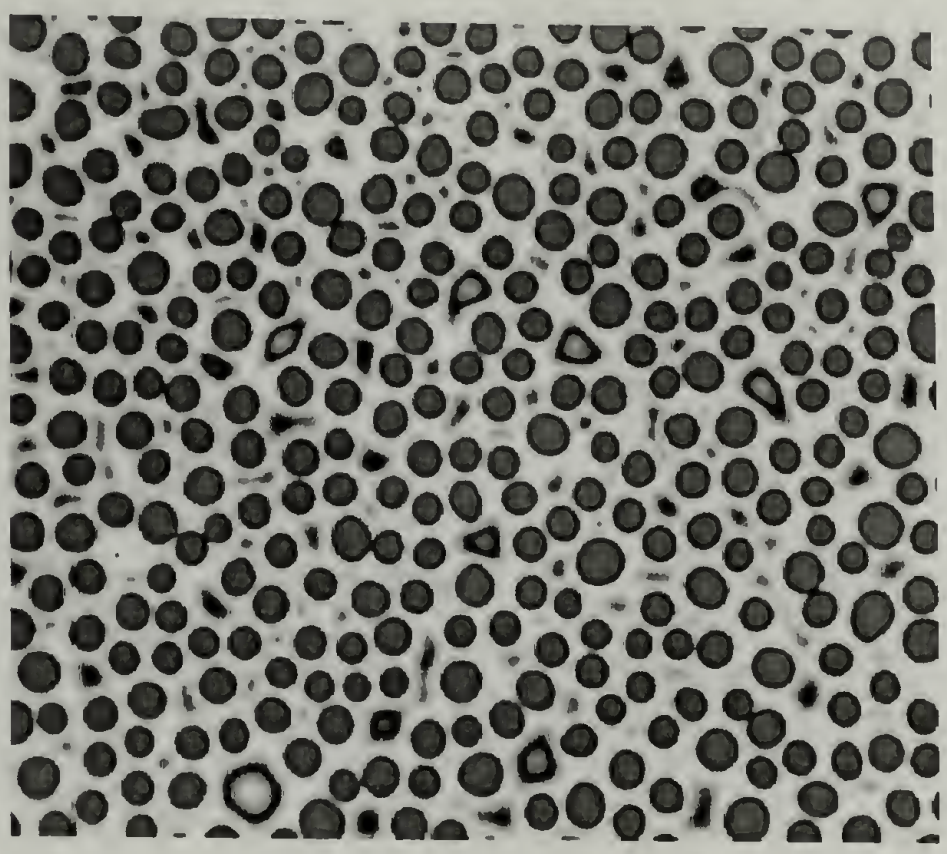

(b)

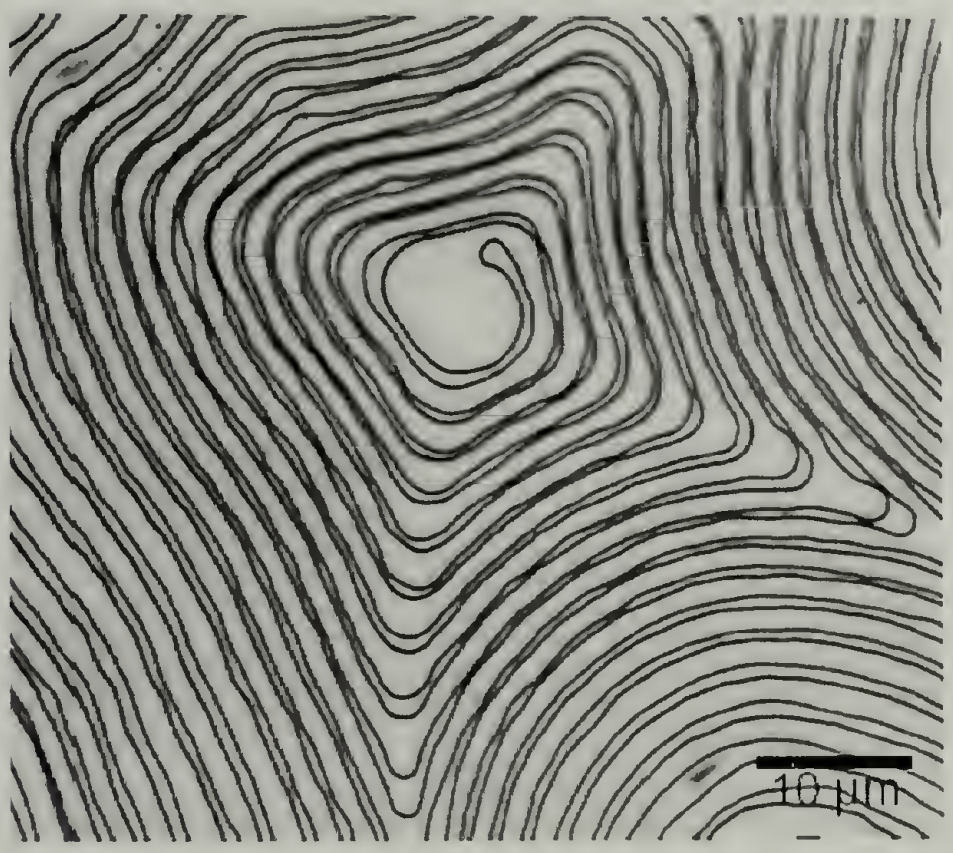

All film thicknesses were measured with a Rudolph Research AutoEL®-II ellipsometer using a helium-neon laser (λ=632.8 nm) at a 70° incidence angle. The dielectric constants of the solid polymers used in our studies (PSBr, PS and PMMA) were measured on melt-pressed 1.9 cm diameter, 1 mm thick disks, using a Novocontro dielectric spectrometer. The solid polymers were confined between two electrodes in a closed chamber under N_2. The dielectric constants of PDMS and PI were measured using the BDS 1200 liquid sample cell. Dielectric measurements were performed at 5Hz from 0 to 180°C. The dielectric constants of all the polymers at 170°C used in this study are given in Table 1. An Olympus 8x60 optical microscope in the reflection mode was used to investigate the structure development at the interface between the two polymers. Atomic force microscopy (AFM) studies were performed with a Digital Instrument D3100 scanning force microscope in the tapping mode. Silicon nitride tips on cantilevers (Nanoprobe™) with spring constants from 29.3 to 63.9 N/m were used.

Results and Discussion

Dielectric Constants Measurements

The dielectric constant difference $\Delta\varepsilon$ between polymer and air will cause a gradient field at the liquid/air interface, which translates into an electrostatic pressure at the interface and dictates the magnitude of the gradient and therefore pressure.[12,13] The dielectric constants of the polymers used in our study as a function of the temperatures and the frequencies are shown in the Figure 1.5. Instead of applying the general ε value from the literatures or other sources, where ε is usually given at

Figure 1.4. Sketch of the sample geometry used in the experiments. A bilayer of two liquids with film thickness of h_0 and d-h_0, respectively, is confined between two solid electrodes: a highly polished silicon wafer (lower electrode) and an ITO coated microscope slide (upper electrode). The distance between the two electrodes is controlled by the height of spacer structures (SiO) evaporated at the edges of the slides on top of the ITO. The temporal evolution of the confined samples under an applied electric field is studied by optical microscopy in the reflectance mode.

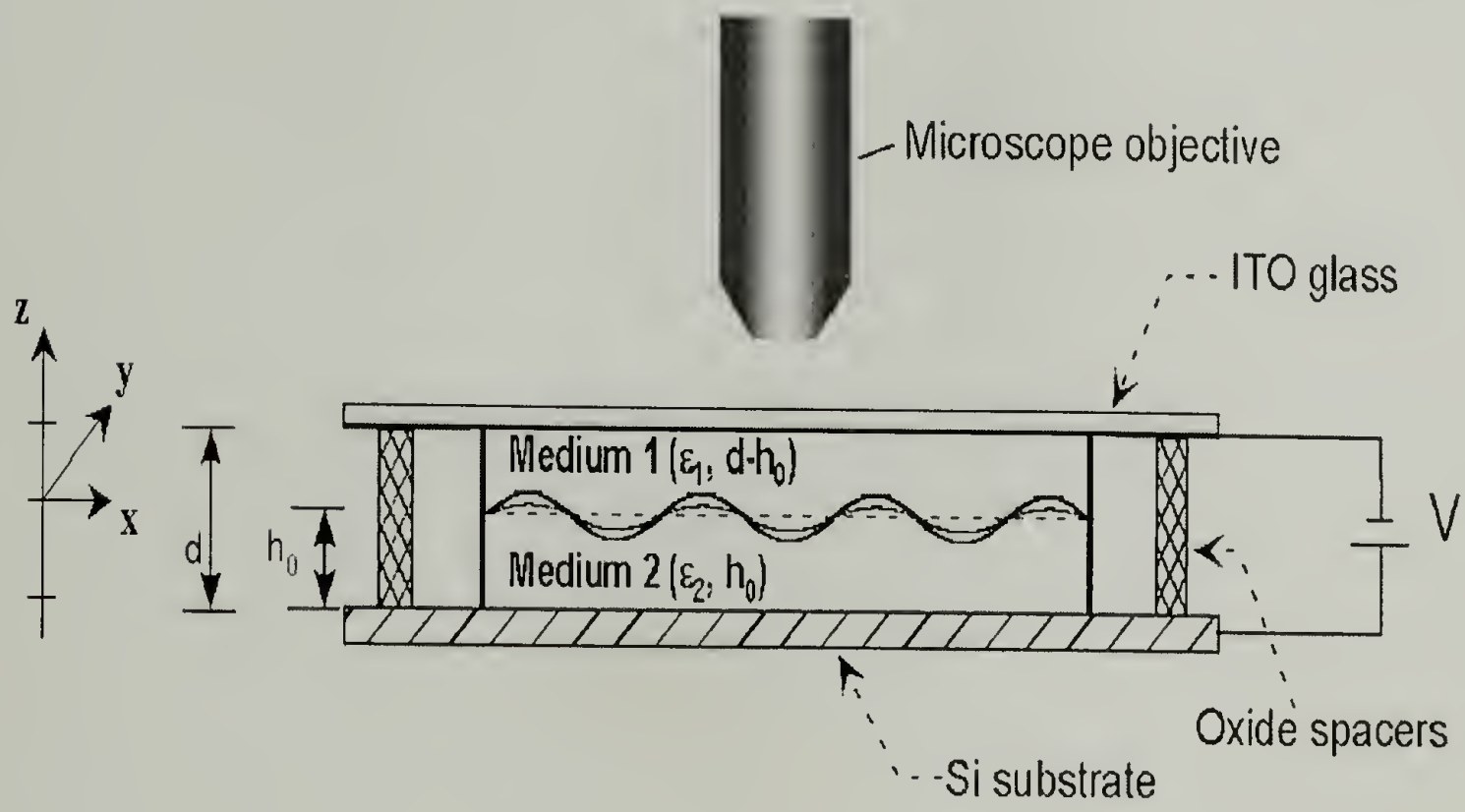

25°C, the precise value of Δε between two media under a particular experimental temperature can be readily obtained based on Figure 1.5.

Theory

It is well known that there are thermal excited capillary waves at the liquid/air interface. When an external electric field is applied, as discussed by Schaffer et al, the pressure at the surface of a thin liquid film under an applied field is given by[12,13]

$$P = P_0 + P_{el}(h) + P_{Lap}(h) + P_{dis}(h) \tag{5}$$

where P and P_0 are the pressures in the liquid film and the air, respectively. P_{el} is the electrostatic pressure, arises from the difference in the dielectric constants Δε between two media.[13]

$$P_{el}(h) = -\varepsilon_0 \varepsilon_P (\varepsilon_P - 1) E_P^2 \tag{6}$$

where ε_0 and ε_P are the permittivity in vacuum and the liquid dielectric constant, *Ep* is the electric field strength in the liquid layer,

$$E_P = \frac{U}{\varepsilon_P d - (\varepsilon_P - 1)h} \tag{7}$$

P_{Lap} is the Laplace pressure that can be written as

$$P_{Lap} = -\gamma\left(\frac{\partial^2 h}{\partial x^2} + \frac{\partial^2 h}{\partial y^2}\right) \tag{8}$$

The disjoining pressure, P_{dis}, arises from the dispersive van der Waal interaction, is given as $P_{dis} = -\frac{A}{6\pi h^3}$ (9)

where A is Hamaker constant.

Figure 1.5. Dielectric constants of polymers as a function of the temperatures and frequencies. (a) PS; (b) PMMA; (c) PSBr; (d) PDMS; (e) PI.

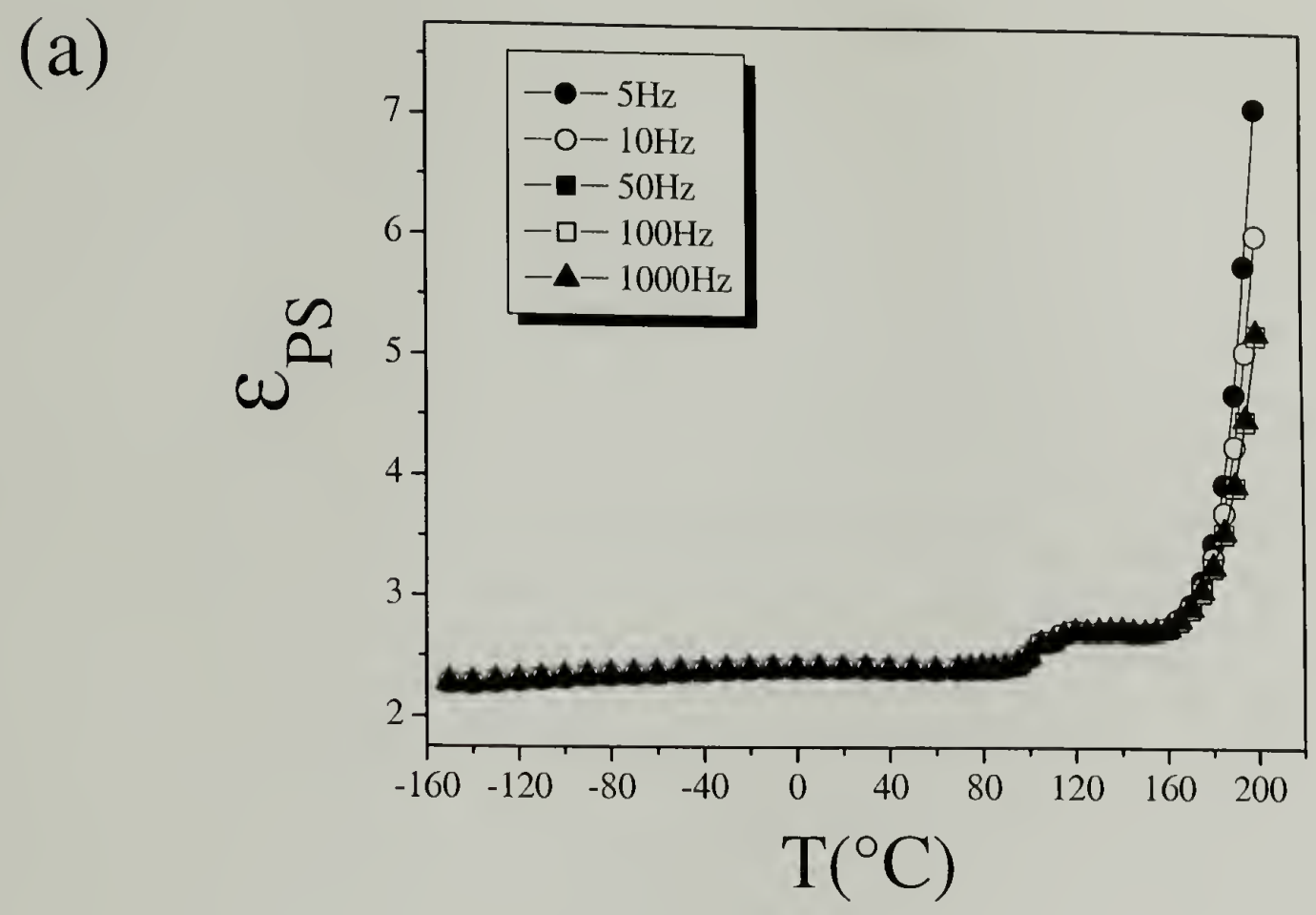

Continued on next page

(b)

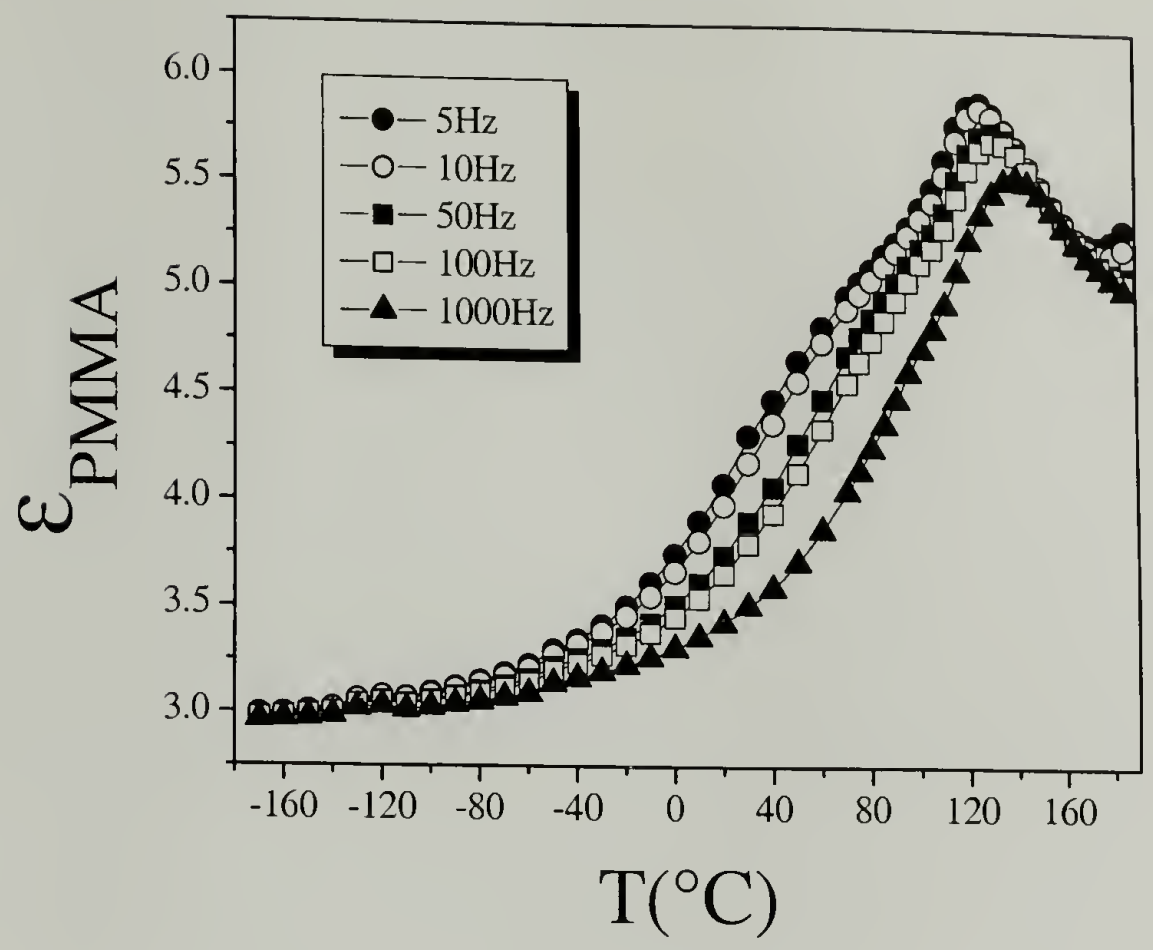

(c)

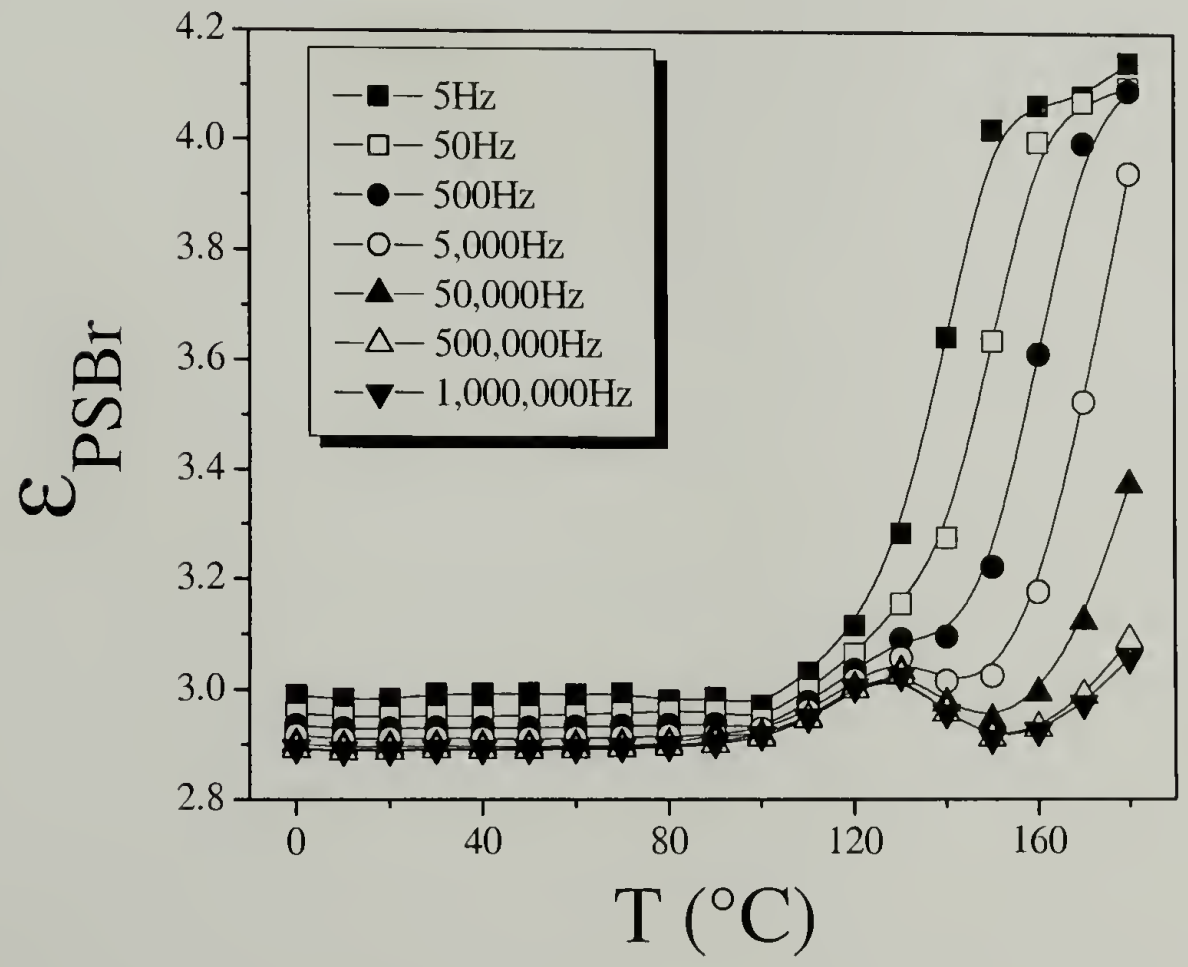

Continued on next page

(d)

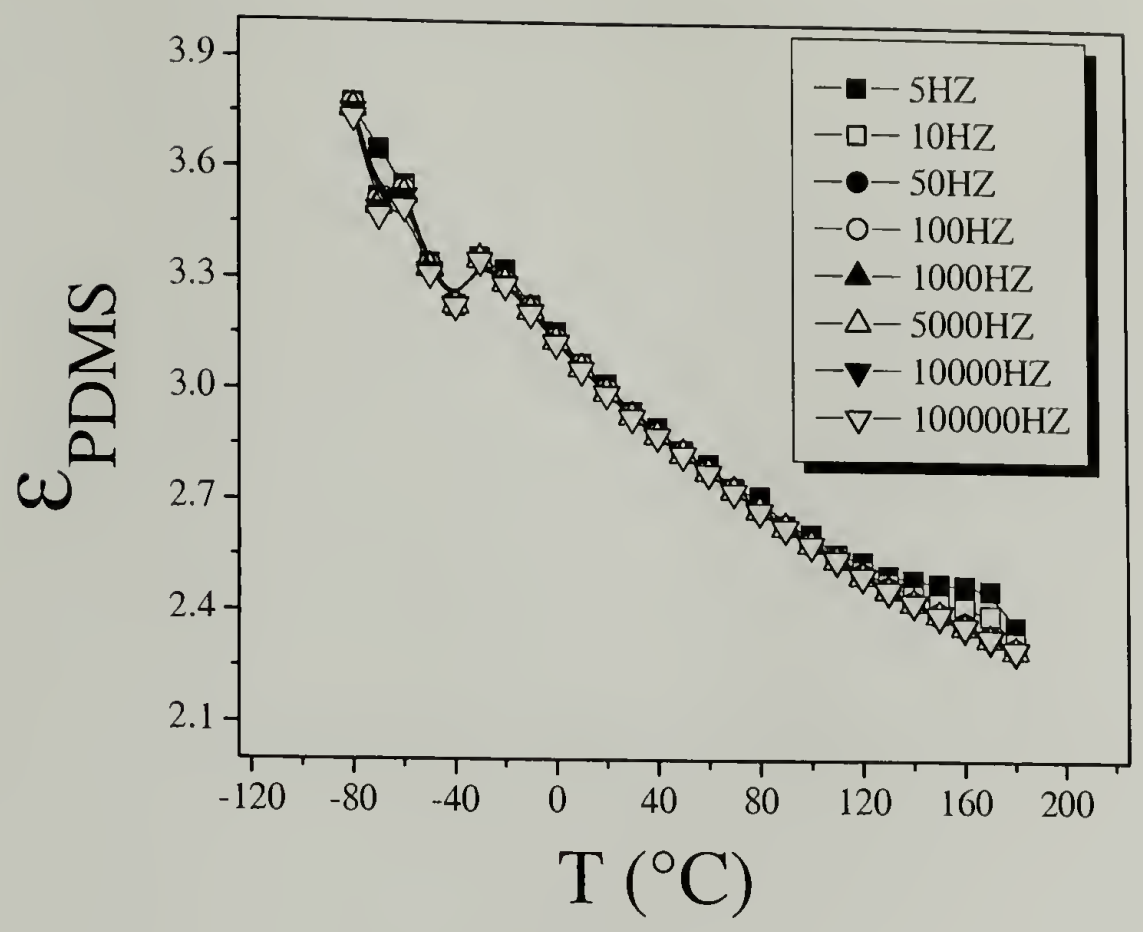
3.9
3.6
3.3
3.0
2.7
2.4
2.1
ε_{PDMS}
-120
-80
-40
0
40
80
120
160
200
T (°C)
5HZ
10HZ
50HZ
100HZ
1000HZ
5000HZ
10000HZ
100000HZ

(e)

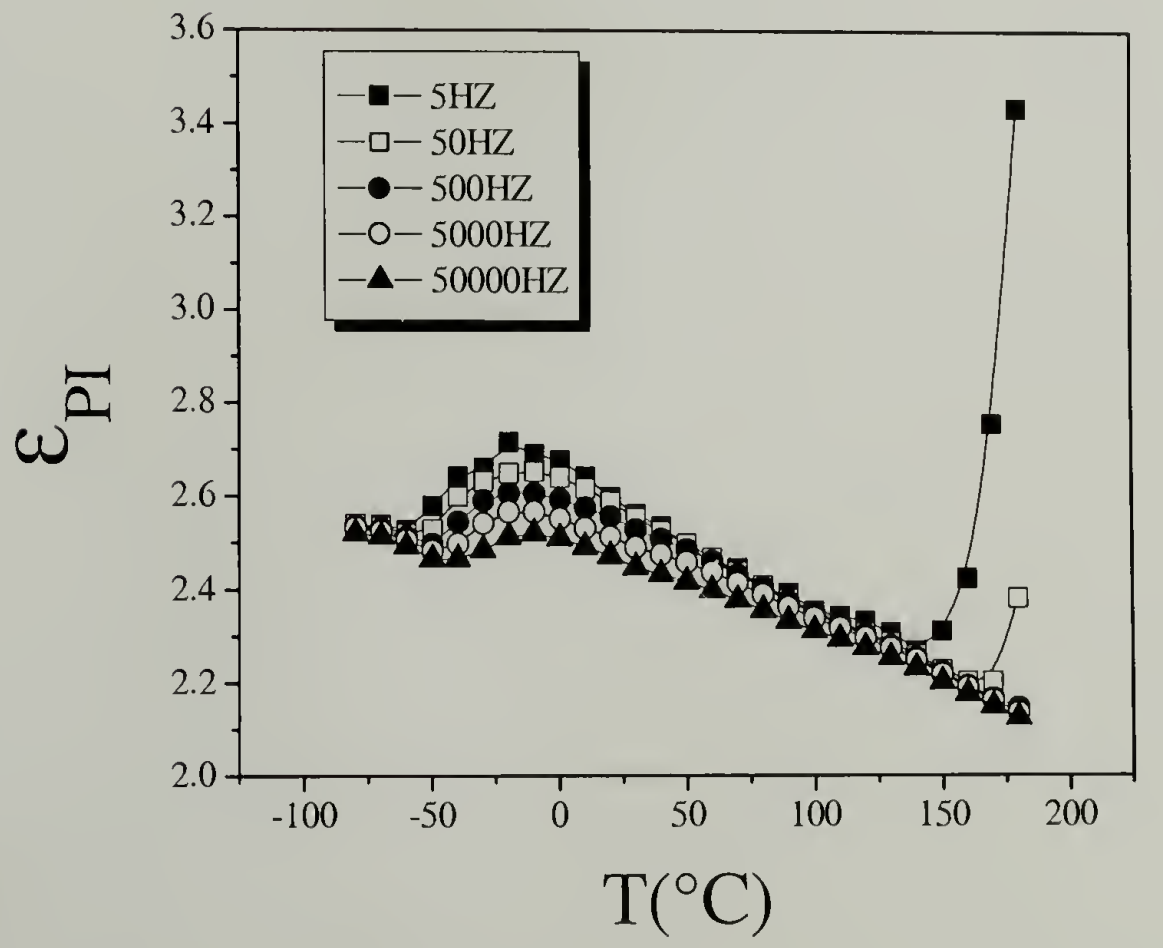
3.6
3.4
3.2
3.0
2.8
2.6
2.4
2.2
2.0
ε_{PI}
-100
-50
0
50
100
150
200
T(°C)
5HZ
50HZ
500HZ
5000HZ
50000HZ

Figure 1.6 shows the orders of the magnitudes of the disjoining and electrostatic pressures in a thin film. According to this figure, A is larger or less than zero for a wetting or nonwetting substrate, respectively. When the films are thicker than 100 nm, the contribution of the disjoining pressure (~10N/m^2), in comparison with the electrostatic pressure (~10^{6}N/m^2), is negligible. Typical film thicknesses in our study are ~100 nm, so P_{dis} will be ignored. The Navier-Stokes equation yields:

$$\frac{\partial P}{\partial x} = \eta \frac{\partial^2 Vx}{\partial z^2}; \qquad \frac{\partial P}{\partial y} = \eta \frac{\partial^2 Vy}{\partial z^2} \quad \text{and} \quad \frac{\partial P}{\partial z} = 0 \tag{10}$$

The mass conservation requires

$$\frac{\partial \rho}{\partial t} + \nabla \cdot (\rho V) = 0 \tag{11}$$

Kinematics equation is given as[22]

$$V_z = \frac{\partial h}{\partial t} + V_x \frac{\partial h}{\partial x} + V_y \frac{\partial h}{\partial y} \tag{12}$$

Assume small pertubation along the liquid/air interface in both x and y directions (see Figure 1.4),

$$h = h_0 + \mu e^{iq_x x + iq_y y + \frac{t}{\tau}} \tag{13}$$

Solve eq (11), the velocities profiles in x, y and z directions can be obtained.

Figure 1.6. Comparison of orders of magnitudes of the disjoin pressure (A>0: solid points; A<0: open points) and the electrostatic pressure (d=500nm, U=30V, ε=2.95).

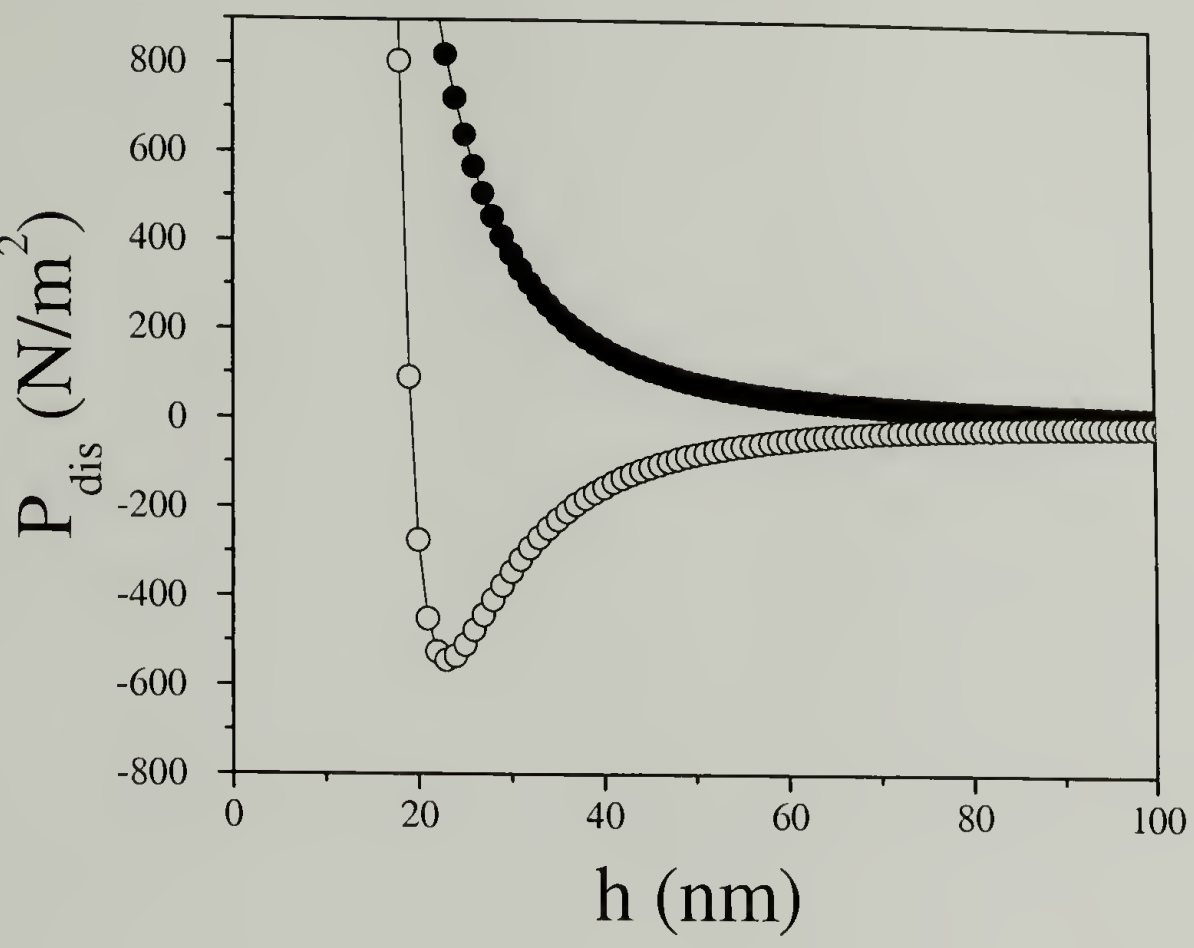

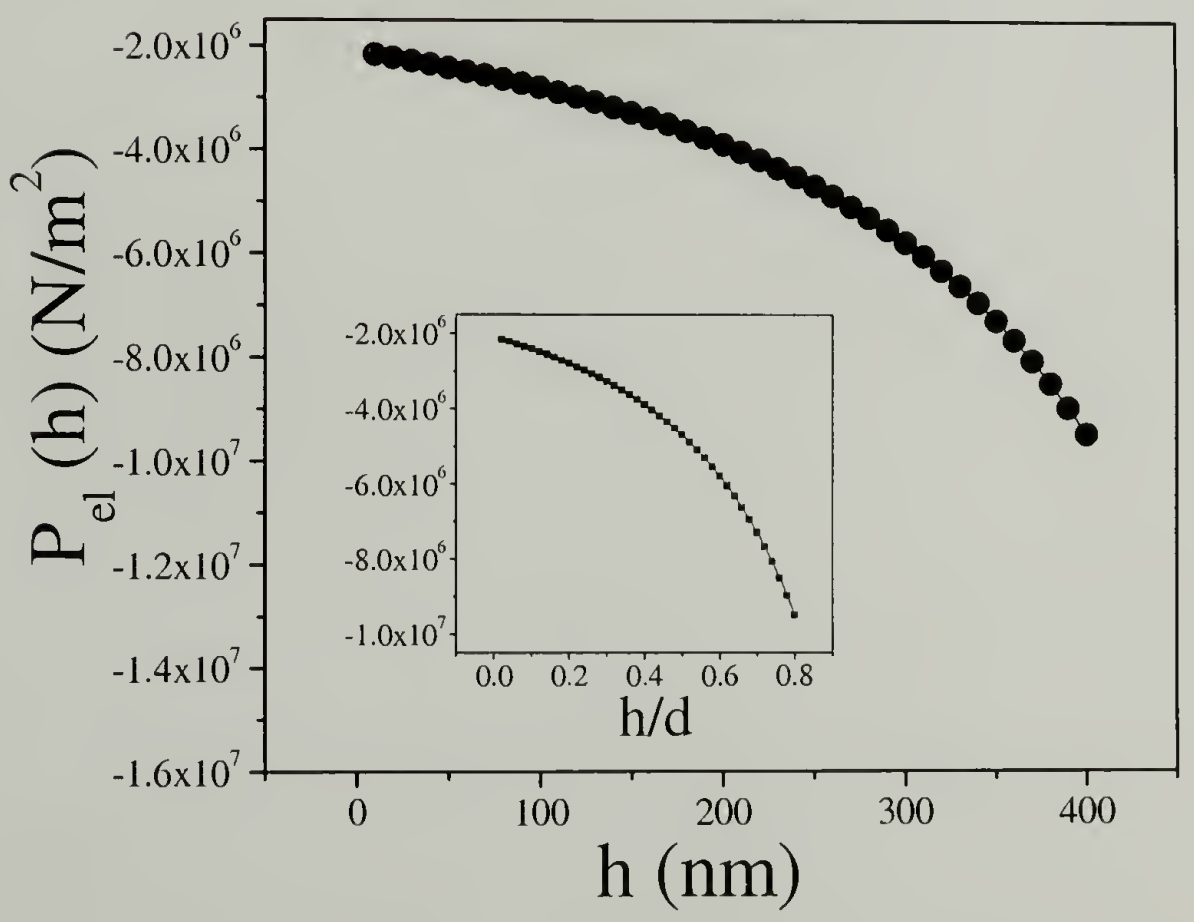

substituting them into eq (12) with the boundary conditions

$$V_x = V_y = V_z = 0 \quad @\ z = 0$$
$$\frac{\partial V_x}{\partial z} = \frac{\partial V_y}{\partial z} = 0 \quad @\ z = h \tag{14}$$

In the linear approximation (long wave and small amplitude), a dispersion relation is obtained:

$$\frac{1}{\tau} = -\{\frac{h^3}{3\eta}(q_x^2 + q_y^2)[\gamma(q_x^2 + q_y^2) + \frac{2U^2(\varepsilon-1)^2\varepsilon\varepsilon_0}{[h_0(\varepsilon-1) - d\varepsilon]^3}]\} \tag{15}$$

The fastest growth modes in both x and y corresponding to the maximum in eq (15):

$$q_{x,\max} = [-q_y^2 + \frac{U^2(\varepsilon-1)^2\varepsilon\varepsilon_0}{\gamma[d\varepsilon - h_0(\varepsilon-1)]^3}]^{1/2}$$
$$q_{y,\max} = [-q_x^2 + \frac{U^2(\varepsilon-1)^2\varepsilon\varepsilon_0}{\gamma[d\varepsilon - h_0(\varepsilon-1)]^3}]^{1/2}$$

In the orthogonal direction,

$$q_{\max} = (q_{x,\max}^2 + q_{y,\max}^2)^{1/2} = [\frac{U^2(\varepsilon-1)^2\varepsilon\varepsilon_0}{\gamma[d\varepsilon - h_0(\varepsilon-1)]^3}]^{1/2} \tag{16}$$

The characteristic wavelength is

$$\lambda_{\max} = \frac{2\pi}{q_{\max}} = \frac{2\pi}{U(\varepsilon-1)}\left\{\frac{\gamma[d\varepsilon - h_0(\varepsilon-1)]^3}{\varepsilon\varepsilon_0}\right\}^{1/2} \tag{17}$$

The eq (17) is exactly the same as derived by Schaffer et al from equation of motion approach in one dimension.[13]

Structure Formation at the Surfaces

Optical microscopy (OM) and atomic force microscopy (AFM) were used to examine the polymer surfaces after quenching the samples below the glass transition temperature of polymers to fix the structures. A typical result for a d-PS thin film exposed to 30 V is shown in Figure 1.7. Micron-sized cylindrical structures that bridge between the two electrodes are seen. A well defined lateral distance in between cylinders is clearly evident in Figure 1.7 (a) and (b). The second order structures are observed for the nucleated instabilities in Figure 1.7 (c) and (d). The locally higher value of the film thickness at the nucleation points leads to a higher electric field and increased driving force. This causes a depletion of nearest-neighbor undulations. Figure 1.8 shows the AFM scans at the surface of d-PS thin film after removing the ITO cover slide from the sample surface. Substituting the relevant experimental parameters into eqs (4) or (17), yields a characteristic distance of 24.6 μm, which agree well with 21.7 μm value determined experimentally. By varying the separation distance d between the two electrodes while keeping the applied voltage fixed at 30 V, the characteristic wavelength λ_{max} as a function of h_0/d, where h_0 is the film thickness of d-PS, is shown in the Figure 1.9. The experimental data are shown to fit with the theoretical model in terms of characteristic wavelength λ_{max} developed by Schäffer et al.[12,13]

In the second set of single layer film experiments, 740 nm thick PSBr films were exposed to a wide range of the applied voltage from 20 V to 60 V, meanwhile the separation distances d between the electrodes were varied. Figure 1.10 showed the OM images of PSBr thin films after exposure to 30 V and 40 V, respectively.

Figure 1.7. The optical micrographs of 530 nm d-PS thin film in 30 V from top view through ITO cover slide. The separation distance d is 1.42 μm. The image sizes are $109\mu m^2$ x $109\mu m^2$ in (a), (c) and (d), and is $54.5\mu m^2$ x $54.5\mu m^2$ in (b), respectively. The second order effect structures are observed for the nucleated instabilities in (c) and (d).

(a)

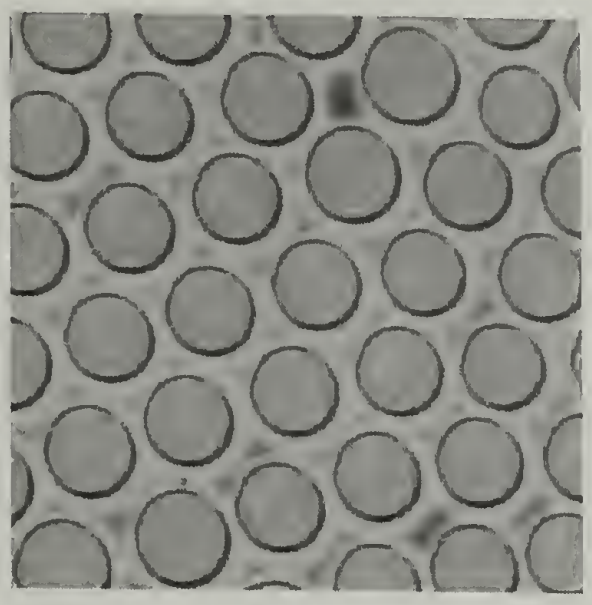

(b)

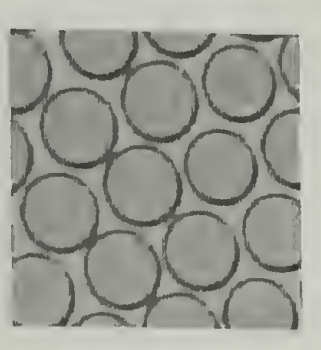

(c)

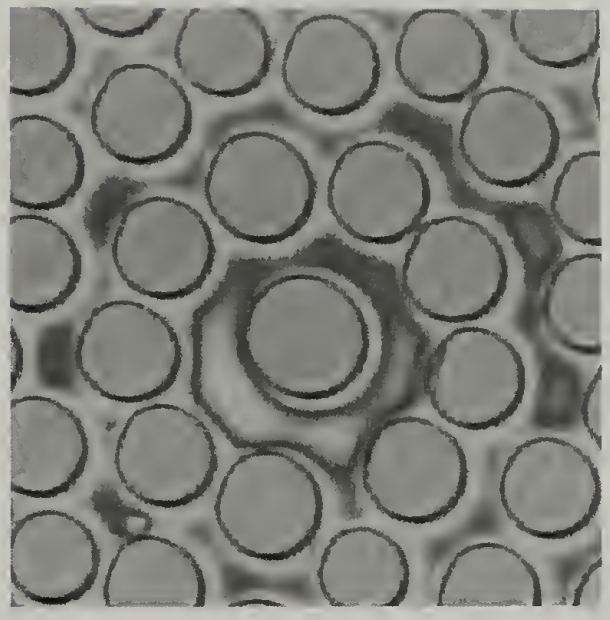

(d)

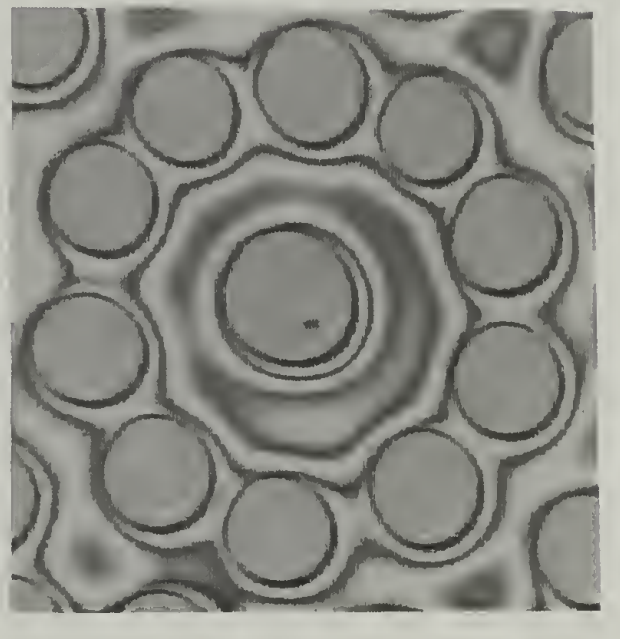

Figure 1.8. 2D AFM height images of d-PS thin film after exposed to 30 V. The separation distances d between two electrodes are 1.4 μm and 1.2 μm in (a) and (b), respectively.

(a)

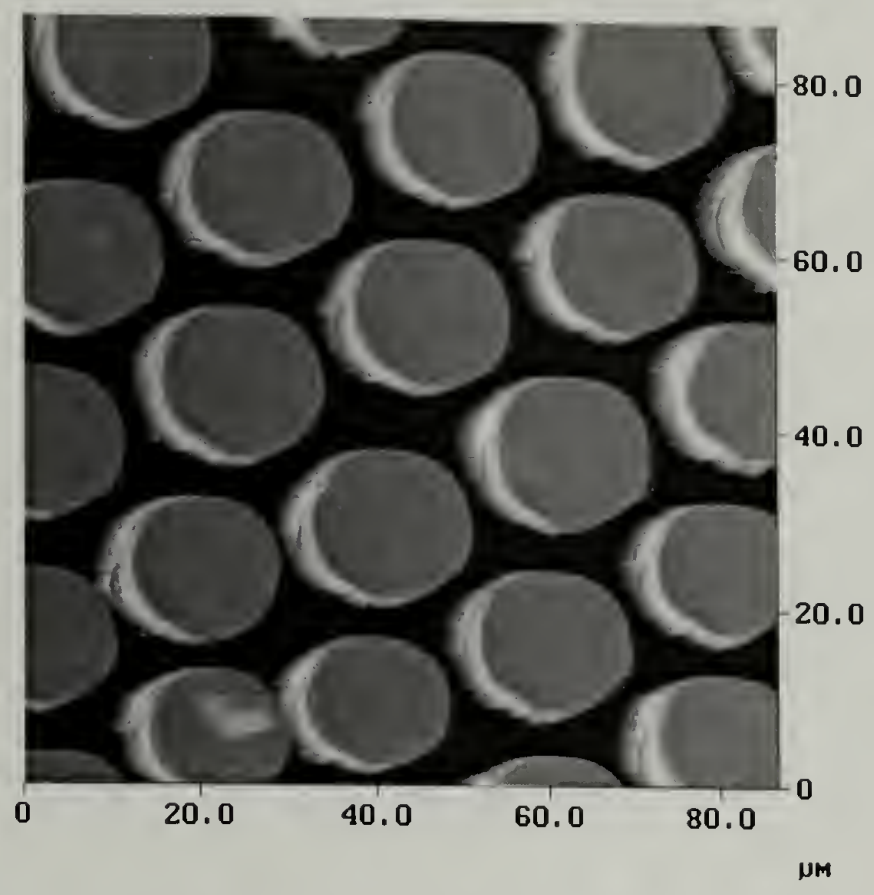

(b)

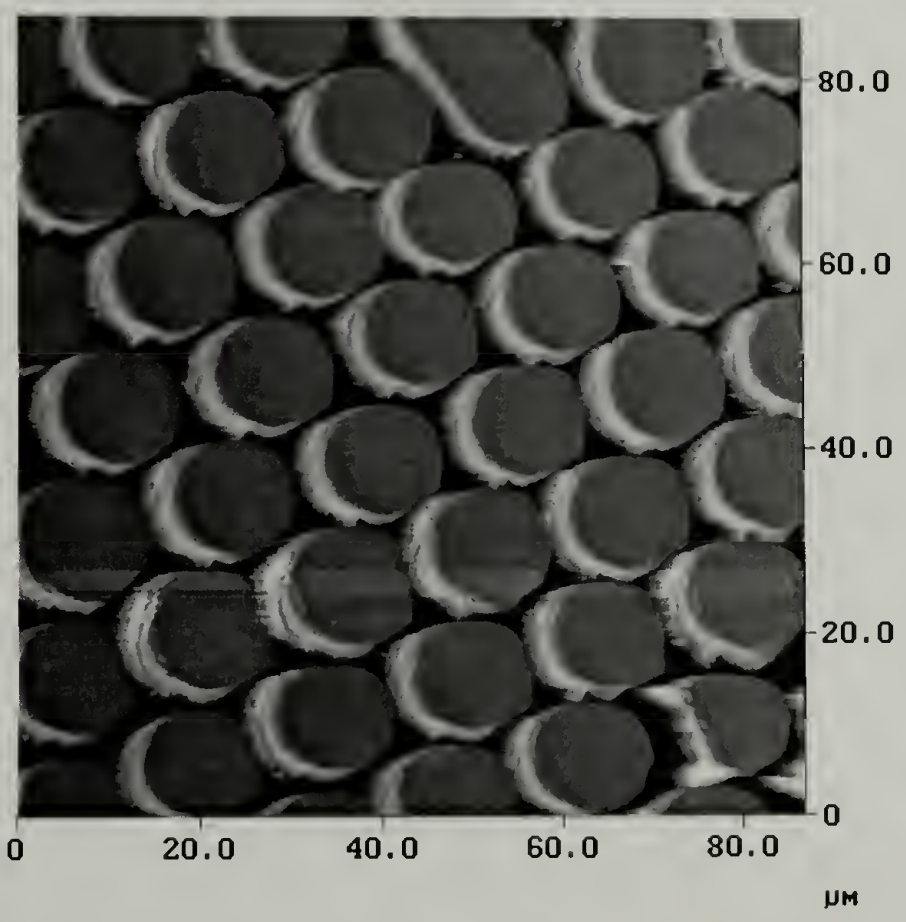

λ_{max} in between the cylindrical structures decreases with an increase of the applied voltage from 30 V to 40 V. The 2D fast Fourier Transform (FFT) and section analysis of the AFM image shown in Figure 1.11 indicate that well-ordered, columnar-like structures are obtained. The aspect ratio of the diameter to height of the PSBr column is ~ 4, which illustrate that rather than the polymer column, the "pancake" like feature is achieved. It can be further revealed in the scanning electron micrograph (SEM) or laser scan confocal microscropy (LSCM) measurements. Shown in Figure 1.12 is an example of the SEM image of 530 nm d-PS thin film in 30 V.

Diffusion Coefficient in the Electric Field

The electric field works against the interfacial tension to initialize the fluctuation at the interface, the fastest growth mode is selected from the system. The apparent maximum diffusion coefficient D_{app}, which describes the dynamic behavior of fluctuations at the interface of polymer/air in the electric field in the early stage, can be determined at that fastest growth mode from the classic diffusion equation

$$\frac{\partial h}{\partial t} = \frac{\partial}{\partial x}\left[D(h)\frac{\partial h}{\partial x} \right] \tag{18}$$

Compare eq (18) with the continuity equation[13]

$$\frac{\partial h}{\partial t} + \frac{\partial J}{\partial x} = 0 \tag{19}$$

Figure 1.9. The characteristic wavelength λ_{max} as a function of the sample geometry ratio h_0/d. The film thickness of d-PS is 530 nm, d is the separation distance between two electrodes.

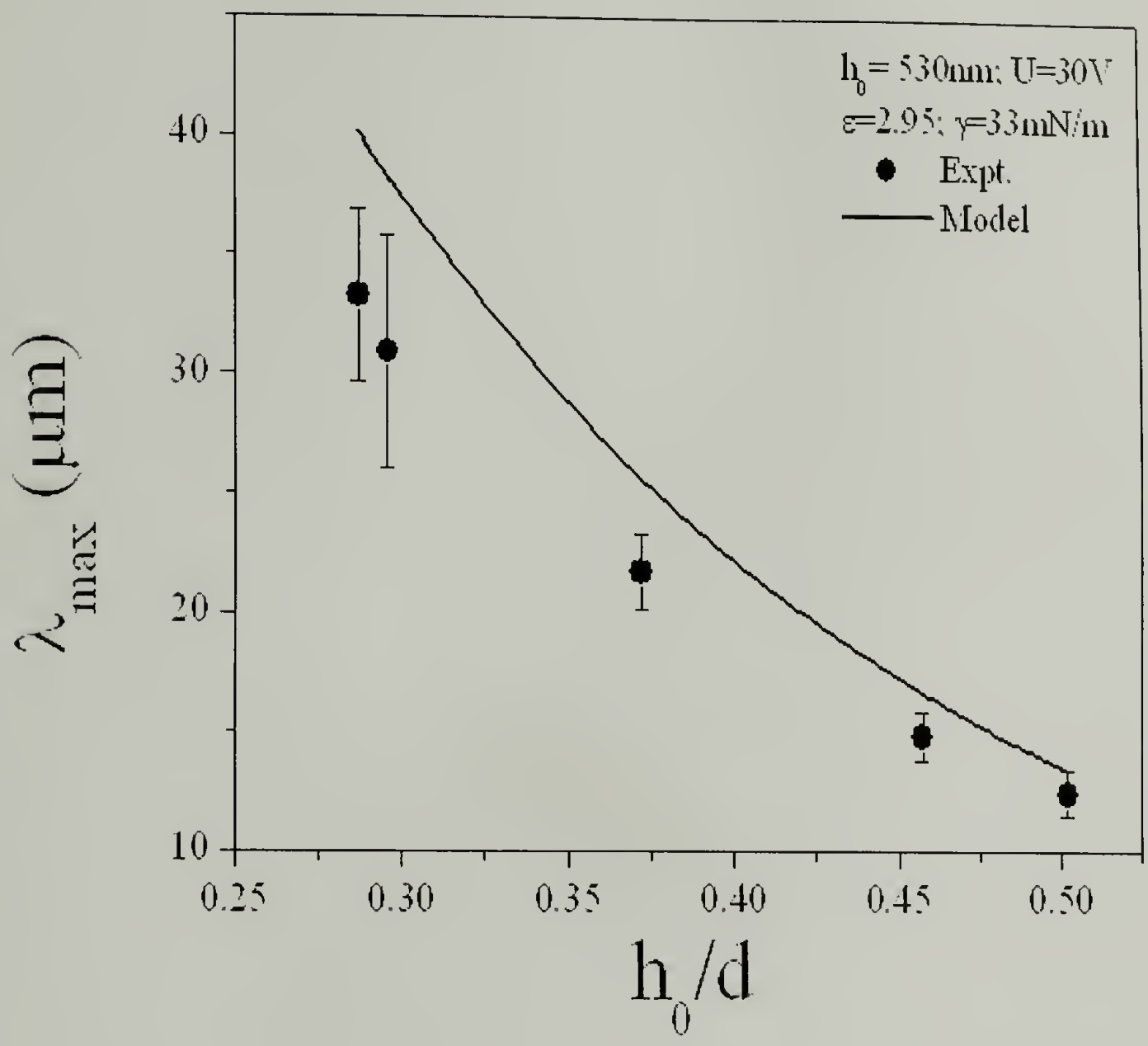

Figure 1.10. 740 nm PSBr thin films are exposed in (a) 30 V and (b) 40 V, respectively. The image sizes are 45x45μm^2. The separation distance d in (a) and (b) are 1.69 μm and 1.72 μm, respectively.

(a)

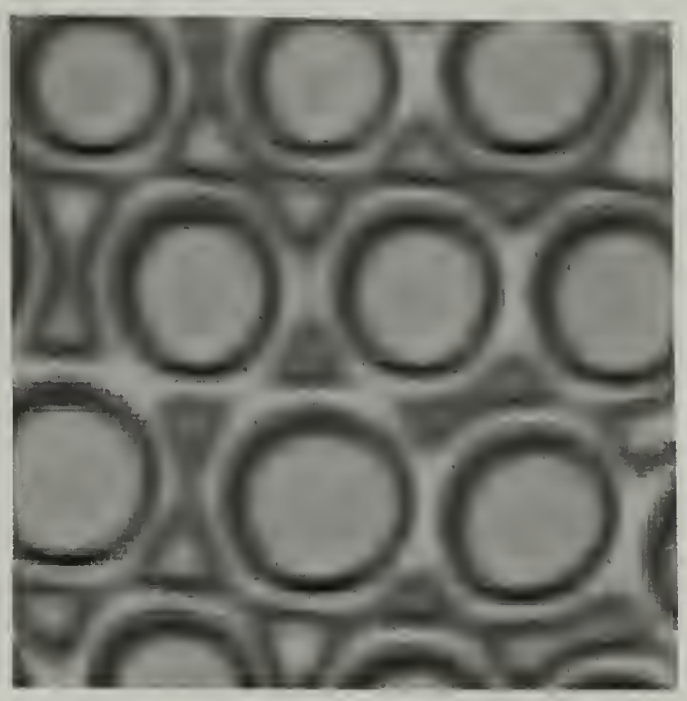

(b)

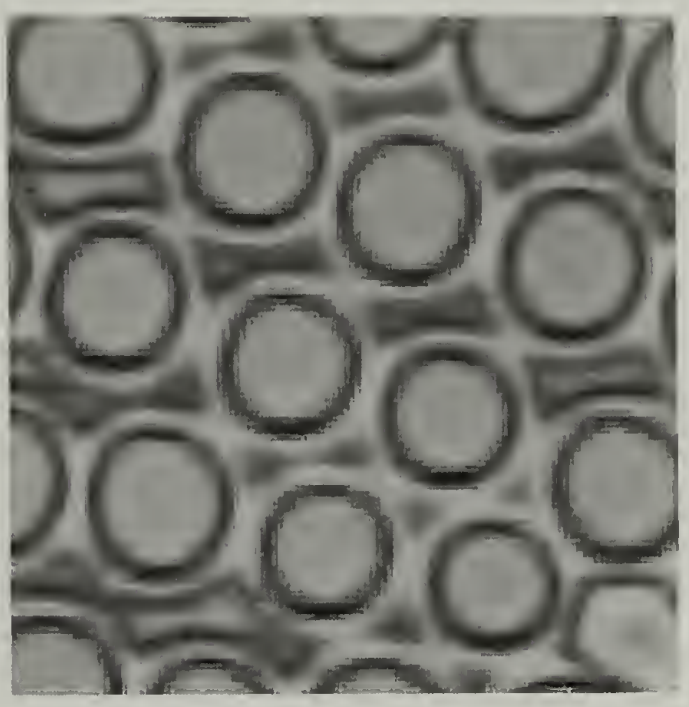

Figure 1.11. The 3D AFM height images, 2D fast Fourier transforms (FFT) and the cross sections of 740 nm PSBr thin films in (a) 30 V; (b) 40 V, respectively.

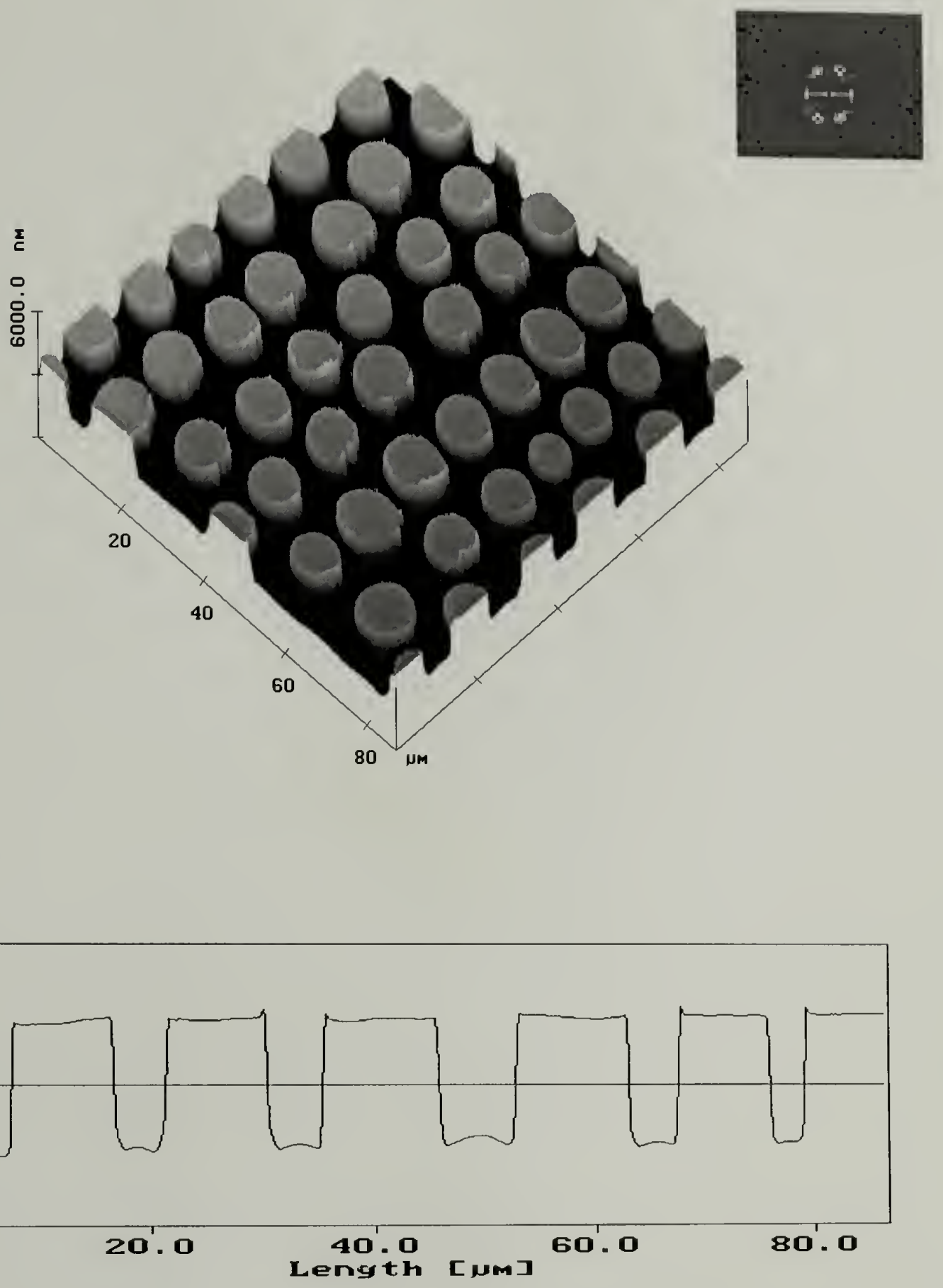

(a)

Continued on next page

Figure 1.11, continued

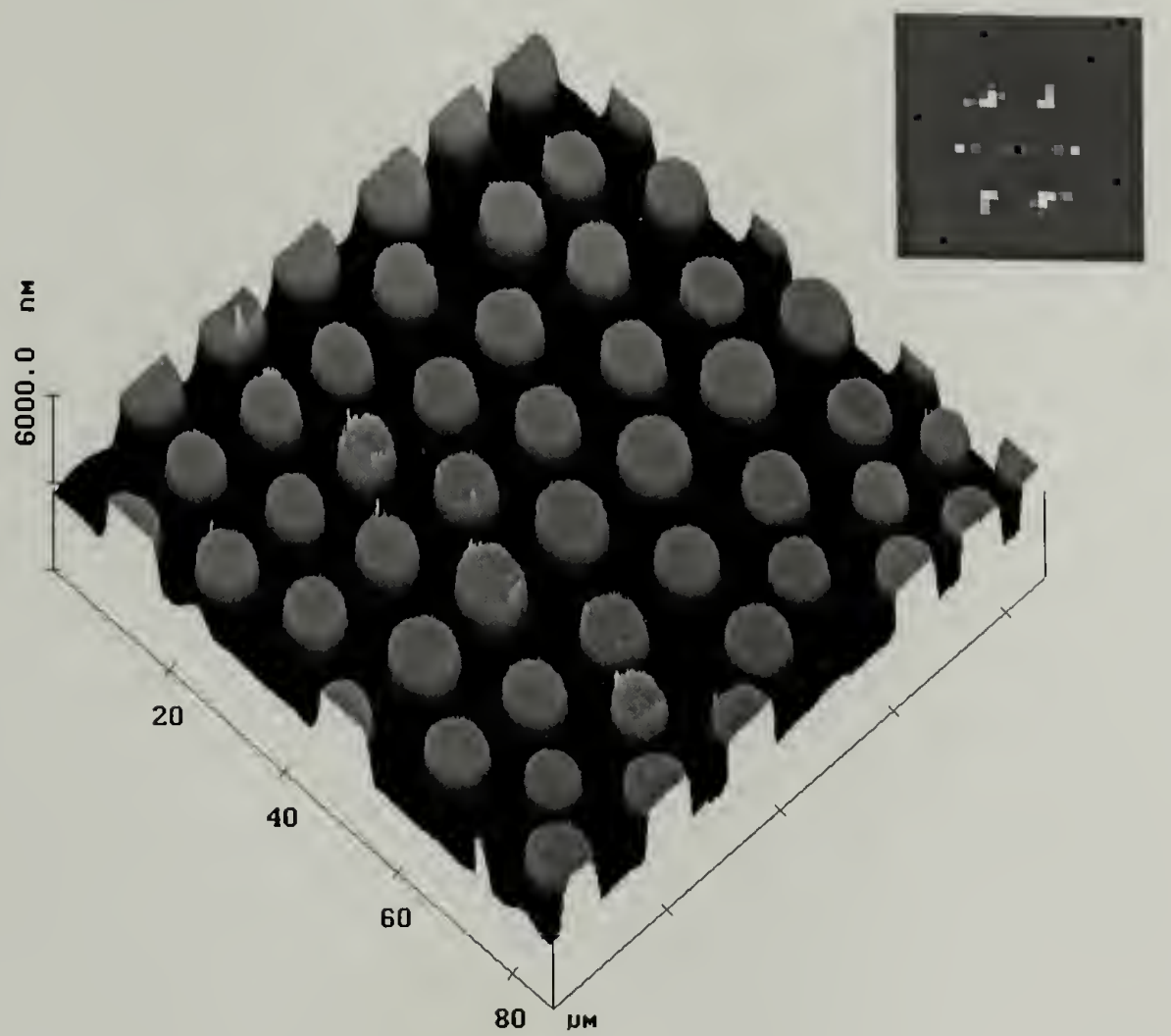

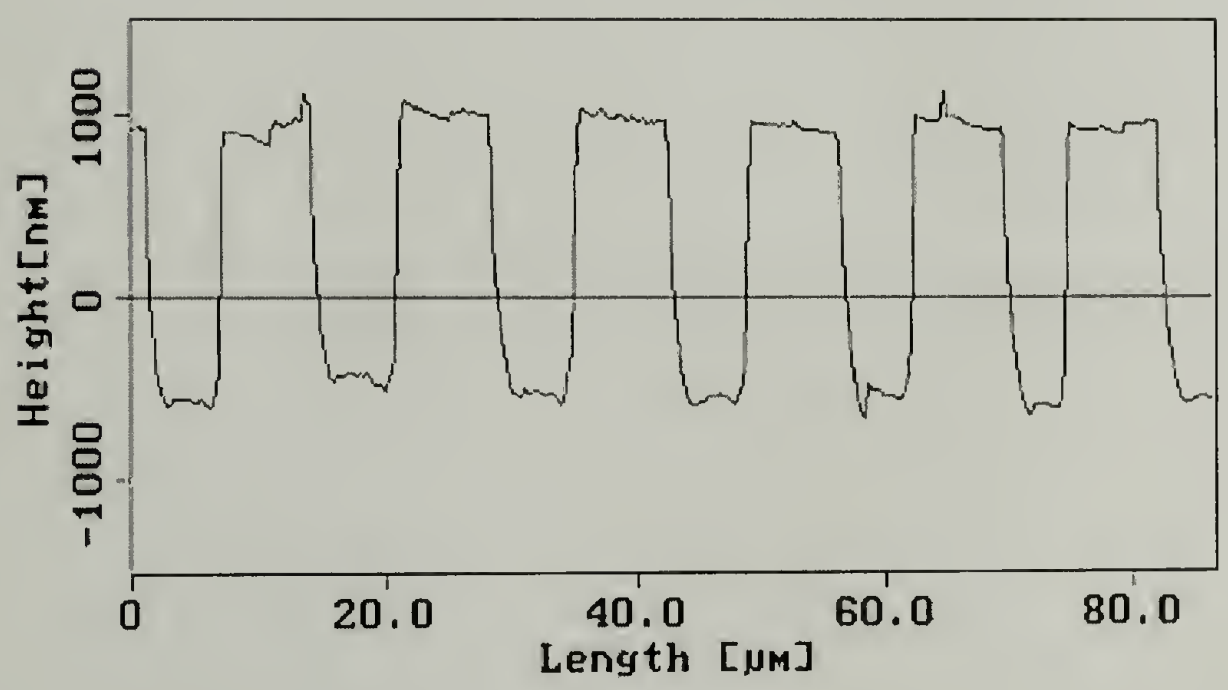

(b)

D_{app} can be obtained in the case of single layer film in electric field

$$D_{\text{app.,max}} = -\frac{h_0^3}{3\eta_P}\frac{\varepsilon_0 U^2}{(d-h_0+\frac{h_0}{\varepsilon})^3}\cdot(\frac{1}{\varepsilon}-1)^2 \tag{20}$$

where η_P is the viscosity of the liquid.

The time dependent Ginzburg-Laudau equation is used to describe the dynamics of phase separation in polymer mixtures.

$$\frac{\partial\phi}{\partial t} = D\nabla^2\frac{\delta H[\phi(r,t)]}{\delta\phi} + \eta(t) \tag{21}$$

where the $H[\phi(r,t)] = \int\left[F(\phi)+\frac{1}{2}|\nabla\phi|^2\right]dr$, and η(t) is the thermal noise. The kinetic parameter of interest in the early stage of spinodal decomposition is the collective diffusion coefficient, $D_{coll.}$.[20]

$$D_{coll.} = \lim(q\to 0)\frac{\Gamma(q)}{2q^2} \tag{22}$$

where the rate constant Γ(q) is determined by

$$\Gamma(q) = 2q^2\lambda(q)S_c^{-1}(q) \tag{23}$$

Therefore the collective diffusion coefficient, D_{coll} is

$$D_{coll.} = \lambda(0)S_c^{-1}(0) \tag{24}$$

where $S_c^{-1}(0) = \frac{K_B T}{\left(\frac{\partial^2 F}{\partial\phi^2}\right)_{\phi=\phi_C}}$ ~T-T_C < 0, and T_C is the critical temperature. The phase separation in polymer mixtures is driven by the temperature gradient ΔT, i.e., T – T_C. The collective diffusion coefficient, D_{coll}, is proportional to T - T_c. The negative

value of D_{coll} indicates the mixture is unstable and phase separated. And the apparent diffusion coefficient, D_{app}, at the liquid/air interface in the electric field is proportional to $-U^2$ (eq (20)). The driving force is the competition between the electrostatic force with the interfacial tension.

The characteristic distance, λ_{max}, in polymer blends at early time, is proportional to $\frac{1}{(T-T_C)^{\frac{1}{2}}}$. Here the characteristic distance λ_{max} in the liquid/air system in an external electric filed is proportional to $\frac{1}{U}$. With an increase of the temperature gradient ΔT, λ_{max} decreases. λ_{max} in bilayer decreases with an increase of the applied voltage. Therefore, both phase-separating polymer mixtures and polymer thin film with an applied electric field are analogous. The height fluctuations in the single layer system under electric field can be mapped to the concentration fluctuations in polymer blends.

Substituting the relevant experimental parameters into eq (20), D_{app}. in d-PS thin film study at early times can be predicted in Figure 1.13. As the separation distance d increases, the driving force decreases, therefore D_{app} of d-PS thin films in 30 V reduces (less negative). The negative D_{app} indicated the liquid/air system was unstable and fluctuated.

Figure 1.12. Scan electron microscopy image of 530 nm d-PS thin film in 30 V.

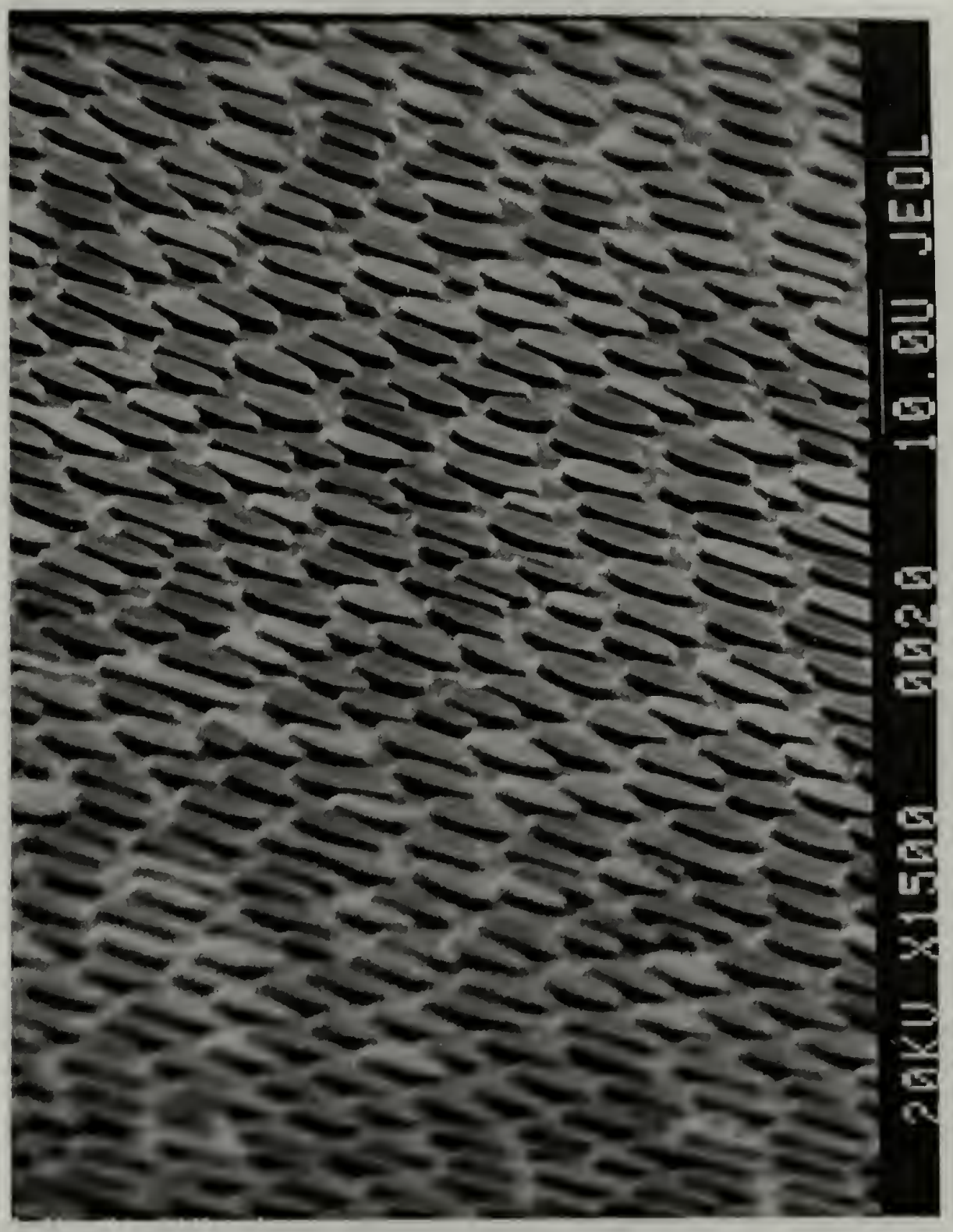

Figure 1.13. The apparent diffusion coefficients, D_{app}, of 530 nm d-PS thin films in 30 V as a function of the sample geometry. (h_0=530nm, ε_2 = 2.95, η_P≈13KpaS, MW=99,800)

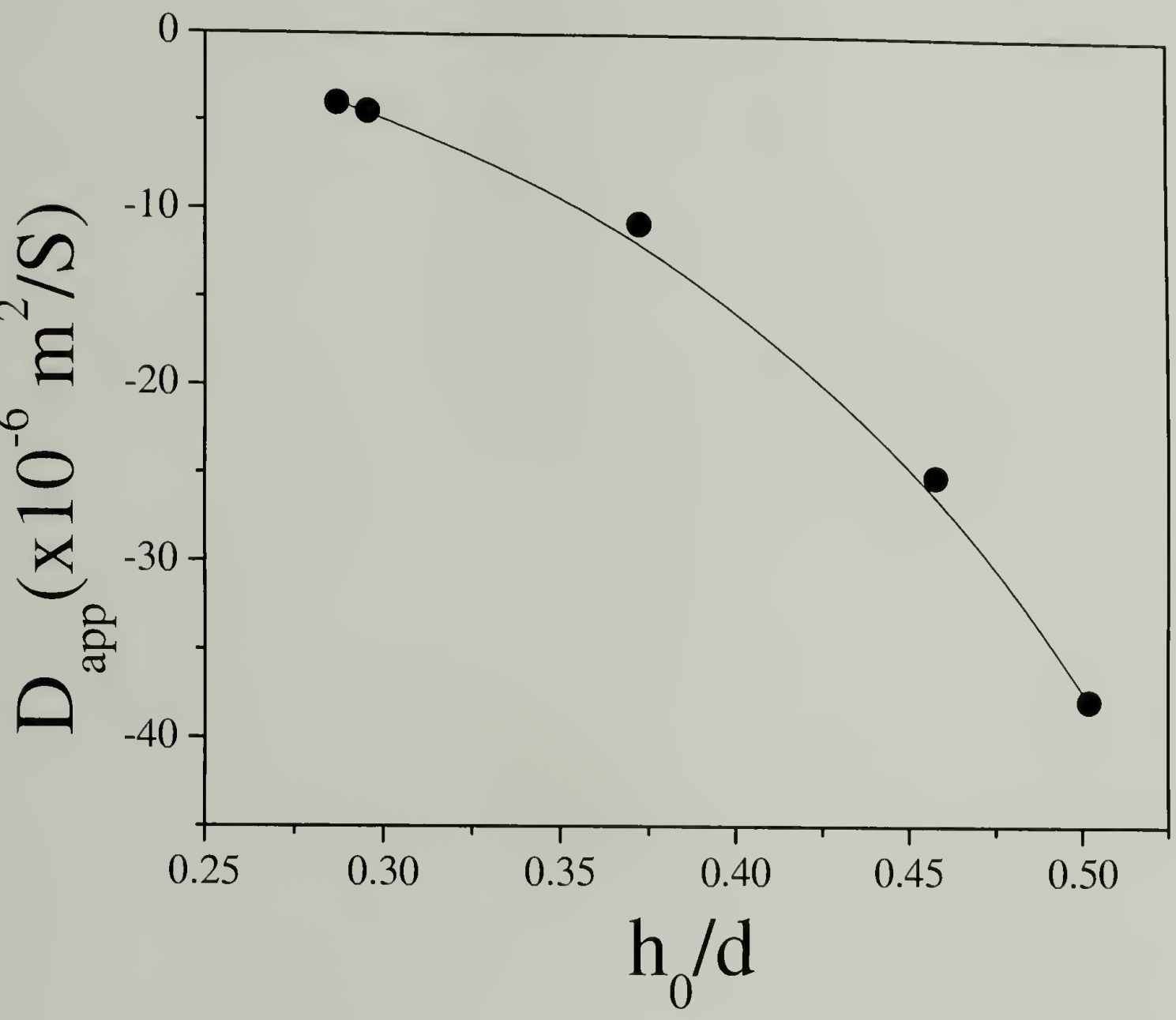

Conclusions

External electric field is used to amplify the surface wave of a liquid/air single layer to induce the electrohydrodynamic instabilities as a result of the competition of the electrostatic force with the surface tension. The electrostatic force arises from the dielectric constant difference between two media, and acts to destabilize the liquid surface, increasing the surface area. However, countering to the electrostatic force, the surface tension tends to minimize the surface energy. The long wavelength fluctuations are suppressed due to the fluid dynamics. The small wavelength fluctuations, on the other hand, are suppressed since they cost too much energy. Consequently, a most unstable wavelength is selected and leads to the structure formation at the liquid/air interface eventually bridging between two electrodes. A well ordered columnar structure at the interface is seen.

The characteristic wavelength λ_{max} of the fluctuation in two dimensions, which has been reported by Schaffer et al based on equation of motion in one dimension, can be predicted in a linear approximation from kinematics approach. Good agreement between experimental observations with the theoretical model is shown.

References

1. Weiss, P. To bead or not to bead. *Science News* **155**, 28-30 (1999).

2. Vrij, C. *Discuss Faraday Soc.* **42**, 23 (1967).

3. Brochard-Wyart, F. & Daillant, J. Drying of solids wetted by thin liquid films. *Can. J. Phys.* **68**, 1084-1088 (1990).

4. Brochard-Wyart, F., Martin, P. & Redon, C. Liquid/liquid dewetting. *Langmuir* **9**, 3682-3690 (1993).

5. Ruckenstein, E. & Jain, R. K. Spontaneous rupture of thin liquid films. *Faraday Trans. 2* **70**, 132-146 (1974).

6. Sharma, A. & Khanna, R. Pattern formation in unstable thin liquid films. *Physical Review Letters* **81**, 3463-3466 (1998).

7. Bischof, J., Scherer, D., Herminghaus, S. & Leiderer, P. Dewetting modes of thin metallic films: Nucleation of holes and spinodal dewetting. *Physical Review Letters* **77**, 1536-1539 (1996).

8. Jacobs, K., Herminghaus, S. & Mecke, K. Thin liquid polymer films rupture via defects. *Langmuir* **14**, 965-969 (1998).

9. Reiter, G. Dewetting of thin polystyrene films. *Phys. Rev. Lett.* **68**, 75-78 (1992).

10. Kerle, T., Yerushalmi-Rozen, R., Klein, J. & Fetters, L. J. van der Waals stable thin liquid films: Correlated undulations and ultimate dewetting. *Europhys. Lett.* **44**, 484-490 (1998).

11. Xie, R., Karim, A., Douglas, J. F., Han, C. C. & Weiss, R. A. Spinodal dewetting of thin polymer films. *Phys. Rev. Lett.* **81**, 1251-1254 (1998).

12. Schaffer, E., Thurn-Albrecht, T., Russell, T. P. & Steiner, U. Electrically induced structure formation and pattern transfer. *Nature* **403**, 874-877 (2000).

13. Schafer, E., Thurn-Albrecht, T., Russell, T. P. & Steiner, U. Electrohydrodynamic instabilities in polymer films. *Europhysics Letters* **53**, 518-524 (2001).

14. Chou, S. Y. & Zhuang, L. Lithographically induced self-assembly of periodic polymer micropillar arrays. *J. Vac. Sci. Technol. B* **17**, 3197-3202 (1999).

15. Chou, S. Y., Zhuang, L. & Guo, L. Lithographically induced self-construction of polymer microstructures for resistless patterning. *Appl. Phys. Lett.* **75**, 1004-1006 (1999).

16. Wu, S. *Polymer interface and adhesion* (Marcel Dekker, 1982).

17. Helfand, E. & Tagami, Y. Theory of the interface between immiscible polymers. II. *J. Chem. Phys.* **56**, 3592-3601 (1972).

18. Helfand, E. & Wasserman, Z. R. Block copolymer theory. 4. narrow interface approximation. *Macromolecules* **9**, 879 (1976).

19. Mitlin, V. S. Dewetting of solid surface: analogy with spinodal decompostion. *J Colloid and Interface Science* **156**, 491 (1993).

20. Strobl, B. *The physics of polymer* (Spinger-Verlag, Inc., 1997).

21. deGennes, P. G. Wetting: statics and dynamics. *Reviews of modern physics* **57**, 827-863 (1985).

22. Khanna, R. & Sharma, A. Pattern formation in spontaneous dewetting of thin apolar films. *J Colloid and Interface Science* **195**, 42-50 (1997).

23. Lambooy, P., Phelan, K. C., Haugg, O. & Krausch, G. Dewetting at the liquid-liquid interface. *Physical Review Letters* **76**, 1110-1113 (1996).

24. Qu, S. et al. Dewetting dynamics at a polymer-polymer interface. *1997* **30**, 3640-3645 (1997).

25. Sferrazza, M., Heppenstall-Bulter, M. & Cubitt, R. Interfacial Instability Driven by Dispersive Forces: The Early Stages of Spinodal Dewetting of a Thin Polymer Film on a Polymer Substrate. *Physical Review Letters* **81**, 5173 (1998).

26. Stange, T. G. & Evans, D. F. Nucleation and growth of defects leading to dewetting of thin polymer films. *Langmuir* **13**, 4459 (1997).

27. Joanny, J. F. Wetting of a liquid substrate. *PhysicoChemical Hydrodunamics* **9**, 183-196 (1987).

28. Morkved, T. L. et al. Local control of microdomain orientation in diblock copolymer thin films with electric fields. *Science* **273**, 931-933 (1996).

29. Mansky, P. et al. Large-area domain alignment in block copolymer thin films using electric fields. *Macromolecules* **31**, 4399-4401 (1998).

30. Amundson, K. et al. Effect of an electric-field on block copolymer microstructure. *Macromolecules* **24**, 6546-6548 (1992).

31. Amundson, K., Helfand, E., Quan, X., Hudson, S. D. & Smith, S. D. Alignment of lamellar block-copolymer microstructure in an electric-field. 2. mechanisms of alignment. *Macromolecules* **27**, 6559-6570 (1994).

32. Amundson, K., Helfand, E., Quan, X. & Smith, S. D. Alignment of lamellar block-copolymer microstructure in an electric-field. 1. alignment kinetics. *Macromolecules* **26**, 2698-2703 (1993).

33. Thurn-Albrecht, T., DeRouchey, J., Russell, T. P. & Jaeger, H. M. Overcoming interfacial interactions with electric fields. *Macromolecules* **33**, 3250-3253 (2000).

34. Thurn-Albrecht, T. et al. Ultrahigh-density nanowire arrays grown in self-assembled diblock copolymer templates. *Science* **290**, 2126-2129 (2000).

35. Thurn-Albrecht, T. et al. Nanoscopic Templates from Oriented Block Copolymer Films. *Advanced Materials* **12**, 787-791 (2000).

36. Ashok, B., Muthukumar, M. & Russell, T. P. Confined thin film diblock copolymer in the presence of an electric field. *Journal of Chemical Physics* **115**, 1559-1564 (2001).

37. Herminghaus, S. Dynamical Instability of Thin Liquid Films Between Conducting Media. *Phys. Rev. Lett.* **83**, 2359-2361 (1999).

38. Pelrine, R., Kornbluh, R., Pei, Q. & Joseph, J. High-Speed Electrically Actuated Elastomers with Strain Greater Than 100%. *Science* **287**, 836-839 (2000).

39. Swan, J. W. Stress and other effects produced in resin and in a viscid compound of resin and oil by electrification. *Proc. R. Soc. London* **62**, 38-46 (1897).

40. Glenn, W. E. Thermoplastic recording. *J. Appl. Phys.* **30**, 1870-1873 (1959).

41. Cressman, P. J. New type of thermoplastic deformation. *J. Appl. Phys.* **34**, 2327-2330 (1963).

42. Killat, U. Revised dynamical theory of thermoplastic deformation. *J. Appl. Phys.* **46**, 5169-5172 (1975).

43. Reynolds, J. M. Stability of an electrostatically supproted fluid column. *The Physics of Fluids* **8**, 161-170 (1965).

44. Melcher, J. R. & Smith, C. V. Electrohydrodynamic charge relaxation and interfacial perpendicular-field instability. *Phys. Fluids* **12**, 778-790 (1969).

45. Onuki, A. Interface instability induced by an electric field in fluids. *Physica A* **217**, 38-52 (1995).

46. Vizika, O. & Saville, D. A. The electrohydrodynamic deformation of drops suspend in liquid in steady and oscillatory electric-fields. *J. Fluid Mech.* **239**, 1-21 (1992).

47. Saville, D. A. Dielectric behavior of colloidal dispersions. *Colloid Surf.* **92**, 29-40 (1994).

48. Trau, M., Sankarn, S., Saville, D. A. & Aksay, I. A. Pattern formation in nonaqueous colloidal dispersions via electrohydrodynamic flow. *Langmuir* **11**, 4665-4672 (1995).

49. Trau, M., Sankarn, S., Saville, D. A. & Aksay, I. A. Electric-field-induced pattern formation in colloidal dispersions. *Nature* **374**, 437-439 (1995).

50. Saville, D. A. Electrohydrodynamics: the Taylor-Melcher leaky dielectric model. *Annu. Rev. Fluid Mech.* **29**, 27-64 (1997).

51. Anklam, M. R., Saville, D. A. & Prud'home, R. K. Electric-field-induced rupture of polymer-stabilized oil films. *Colloid Polym Sci* **277**, 957-964 (1999).

52. Oddershede, L. & Nagel, S. R. Singularity during the onset of an electrohydrodynamic spout. *Physical Review Letters* **85**, 1234-1237 (2000).

53. Schäffer, E., Harkema, S. & Steiner, U. Thermomechanical film instabilities induced by a temperature gradient. Submitted.

54. Cross, M. C. & Hohenberg, P. C. Pattern formation outside of equilibrium. *Rev. Mod. Phys.* **65**, 851-1112 (1993).

55. Bodycomb, Y., Funaki & Kimishima, K. Single-grain lamellar microdomain from a diblock copolymer. *Macromolecules* **32**, 2075 (1999).

56. Rosa, C. D., Park, C. & Thomas, E. L. Microdomain patterns from directional eutectic solidification and epitaxy. *Nature* **405**, 433 (2000).

CHAPTER 2

LIQUID/LIQUID BILAYER IN AN ELECTRIC FIELD

Introduction

A new method to control structure formation at liquid/air interfaces, where electrostatic forces were used to induce an instability at the liquid/air surface of a thin film, was recently discussed by Schäffer et al.[1,2] Experiments on thin polymer films between parallel capacitor plates showed that the enhancements of fluctuations on the surface of the film produced columns with a characteristic separation distance that spanned between the two plates. The columns separation distance was found to be proportional to the surface tension of liquid. If, however, the air is replaced with a second polymer forming a bilayer, the surface tension is replaced with the interfacial tension that can be about an order of magnitude smaller.

Here the theoretical model for a single layer is extended to the more general liquid/liquid bilayer and experimental data are shown that test the model. A systematic characterization of structure formation at the liquid/liquid bilayer interface in an applied electric field is reported. Regardless of the polymers used, very good agreement over many orders of magnitude in reduced wavelength and field strength is observed using no adjustable parameters. Routes towards even smaller size-scale structures are discussed.

Experimental

Materials

Polyisoprene (PI) (MW= MW=4.0x10^4), oligomeric dimethylsiloxane (ODMS) (commercial grade), Poly(4-bromo styrene) (PSBr) (MW=6.5x10^4) and poly(dimethylsiloxane) (PDMS) (200®Fluid, with a viscosity η=10,000Cst.) were purchased from Aldrich Chemical Co. Oligomeric styrene (OS) (MW=580), Polystyrene (PS) and poly(methyl methacrylate) (PMMA) were purchased from Polymer Laboratories LTD. The molecular weight of PMMA and PS were PMMA–27K, MW=2.7x10^4 (PDI=1.04), PS–30.3K, MW=3.03x10^4 (PDI=1.02) and PS–96K, MW=9.6x10^4 (PDI=1.04). Deuterated polystyrene (dPS) with a molecular weight of 99.9K (PDI=1.017) was synthesized in our laboratory by anionic polymerization. Indium-tin-oxide (ITO) microscope slides, a transparent electrode used in this study, were purchased from Delta Technologies (25x50x1.1mm^3, Rs$\leq$ 100ohms).

Sample Preparation

Figure 1.1 shows the typical sample configuration of the study. Thin liquid films of polyisoprene (PI) and oligomeric styrene (OS) were spin-coated from toluene solutions onto bare and gold-coated silicon wafers, respectively. The film thickness was 140 nm. For some experiments, a small air gap was left above the liquid to form liquid/air single layer. In the remaining experiments, the air was replaced with a layer of oligomeric dimethylsiloxane (ODMS), thus forming a liquid/liquid bilayer. No solvent was used to deposit the ODMS layer. The overall thickness of the single layer and the bilayer was nominally 1 μm. Table 1

summarizes the physical constants of the liquid oligomers and polymers. The interfacial tension of OS/ODMS, OS/PI and PI/ODMS are 6.1 mN/m, 1.68 mN/m and 3.2 mN/m, respectively[45]. The last value was estimated from the segmental interaction parameters, χ, of different polymer pairs, which follow the order $\chi_{PS/PDMS} > \chi_{PI/PDMS} > \chi_{PI/PS}$.[3,4] Thin rails of silicon oxide were evaporated on top of indium-tin-oxide (ITO)-coated microscope slides (Delta Technologies), and these slides were mounted on top of the bilayer samples with the ITO and silicon oxide side facing downwards, as shown in Figure 1.4. The separation distance between the substrate (Si wafer) and the upper boundary was thus controlled by the height of the evaporated spacers and was typically 1.08 μm. The samples were placed under an optical microscope and a small voltage (U = 20 V for PI/air single layer, PI/ODMS bilayer experiments and U = 50 V for OS/air single layer, OS/ODMS bilayer experiments) was applied between the Si substrate (electrode 1) and the ITO layer (electrode 2). We independently determined the resistivity of the ITO layer (R_{ITO} = 320 Ω) and the resistivity of the highly doped Si wafers (R_{Si} = 0.01~0.03 Ω/cm). The typical currents measured during the experiment $I \approx 5$ μA indicate that the applied potential indeed dropped over the sample-capacitor. As the ITO-coated substrates do not significantly absorb light in the visible range, this geometry permitted a direct observation of the temporal evolution of the thin liquid films in the electric field. Since the glass transition temperature of the polymers used in these single layer and bilayer are less than zero, the experiments are preformed at room temperature with no heat applied.

In the first systematic study of structure formation at the interface of liquid/liquid bilayers in the electric field, a film of PS (MW=30.3K), 550 nm in thickness, was spin coated onto a freshly cleaned Si substrate. A layer of PDMS was then spin coated directly on top of the PS film from a heptane solution to form a bilayer. Heptane is a nonsolvent for PS. Two bilayers with overall thicknesses 1.12 and 1.25 μm were prepared. In a second bilayer experiment, a 730 nm thick PS (MW=96K) film was spin-coated from toluene solution on a cleaned Si wafer. A 290 nm thick film of PMMA (MW=27K) was spin coated on top of the PS film from an acetic acid solution where acetic acid is a nonsolvent for PS. Experiments were also performed on PMMA/PDMS bilayers. A thin layer of PMMA (MW=27K) film was spin coated from a toluene solution onto a Si wafer. A PDMS film was spin coated from a heptane solution onto the PMMA layer, where heptane is a nonsolvent for PMMA, to form the PMMA/PDMS bilayer. The thickness of the PMMA and PDMS ranged from 180-290 nm and 690-1030 nm, respectively. Rails of silicon oxide were evaporated on the top of ITO-coated microscope slides. These were then placed on the top of the bilayers. The bilayers were annealed at 170°C under N_2 for a day under an applied electric field and quenched to room temperature before removing the applied field. To examine the polymer/polymer interface, the upper layer was removed with either heptane, in the case of PDMS, or acetic acid, in the case of PMMA. Residual heptane was removed by placing the sample under vacuum. Residual acetic acid was removed by thorough rinsing with de-ionized water and drying under vacuum at room temperature.

All film thicknesses were measured with a Rudolph Research AutoEL®-II ellipsometer using a helium-neon laser (λ=632.8 nm) at a 70° incidence angle. The dielectric constants of all the polymers at 170°C used in this systematic study of structure formation at the interface of liquid/liquid bilayers in the electric field are given in Table 2. An Olympus Bx60 optical microscope in the reflection mode was used to investigate the formation of structures at the interface between the two polymers. Atomic force microscopy (AFM) studies were performed with a Digital Instrument D3100 scanning force microscope in the tapping mode. Silicon nitride tips on cantilevers (Nanoprobe™) with spring constants from 29.3 to 63.9 N/m were used.

Results and Discussion

Reduction of Characteristic Wavelength

In the first set of experiments, a layer of PI was placed between the electrodes, leaving an air gap of 940 nm. Similar to the experiments reported recently by Schäffer and et al.,[1,2] an amplification of fluctuations at the PI/air interface, occurred, ultimately leading to the creation of an array of vertically standing PI columns. A typical image of this morphology can be seen in Figure 2.1 (a). The average distance between the center of two neighboring columns is $\langle d_{cyl\text{-}cyl} \rangle = 47.4 \pm 4.4\ \mu m$.

The influence of changes in ε and γ of the upper layer on the time and size scales of the evolving structures was investigated in the second set of experiments. Figure 2.1 (b) shows the final state of a PI/ODMS bilayer annealed at ambient

conditions. A visual comparison of Figures 2.1 (a) and (b) shows a clear reduction in length scale, associated with the replacement of air by ODMS. The cylinder structures now exhibit a typical spacing of $\langle d_{cyl\text{-}cyl} \rangle = 20.6 \pm 1.3\ \mu m$. This spacing is about one-half that observed in the single film experiments. The characteristic times for the growth of the cylinders were determined for both the single and bilayers cases by optical microscopic observations. The time required to produce the first observable features was taken as the characteristic

time. It is important to note that the time required to produce the cylindrical structures at the PI/ODMS interface was about one hour, nearly 50 times faster than the time needed to produce the columns in the single film case. Additional experiments on OS/air and OS/ODMS bilayers showed essentially the same behavior, with $\langle d_{cyl\text{-}cyl} \rangle = 12.7 \pm 2.8\ \mu m$ for OS/air and $\langle d_{cyl\text{-}cyl} \rangle = 7.6 \pm 2.9\ \mu m$ of OS/ODMS.

Theoretical Model

The central finding of the experiments presented is a reduction of the length scale of dynamical instabilities induced by an electric field and the pronounced reduction in the time to generate the features when the liquid/air interface is replaced by a liquid/liquid interface. A reasonable starting point for the discussion of the dynamical instability is the pressure distribution along the interface itself. Similarly to the case of a thin liquid film mounted between parallel capacitor plates leaving an air gap,[1,2] following previous work the overall pressure at the interface can be written as:[1,2,5]

$$p_2 = p_1 - \gamma_{12}\frac{\partial^2 \Delta h}{\partial x^2} + p_{el}(\Delta h) + p_{dis}(\Delta h) \qquad (1)$$

where p_i is the pressure in medium i having thickness h_i; the second term is the Laplace pressure, arising from changes in interfacial energy contribution due to changes in the interfacial area, Δh is the local displacement of interface position, p_{el} is the electrostatic pressure and p_{dis} is the disjoining pressure.

To evaluate eq (1) let the origin of the coordinate system be located at the interface between the liquid layers, such that at $t=0$ the interface is located $z=0$. The system is bounded at $z=h_1$ and $z=h_2$ $(h_2 < 0)$, where h= $-h_2$ and d-h= h_1. Local changes in the thickness of the layers are given by $\Delta h_1 = h_1 - \Delta h$ and $\Delta h_2 = \Delta h - h_2$.

The disjoining pressure p_{dis} is given as

$$p_{dis} = \frac{-A_1}{6\pi h_1^3} + \frac{A_2}{6\pi(-h_2)^3} \qquad (2)$$

Table 2.1. The physical constants of liquid oligomers and polymer

	OS	PI	ODMS
γ (mN/m)	39	32	20
ε	2.5	2.37	2.93
Mn	580	40,000	commercial grade
η (Poise)	15	400	0.1

Table 2.2. The characteristics of the polymers

Polymers	PDMS	PS	PMMA	PSBr	dPS
MW[a] (g/mol)	η=10,000CS t	30,300 /96,000	27,000	65,000	99,900
(mN/m)	$\gamma_{PDMS/PS}$=6.1			39	33
		$\gamma_{PS/PMMA}$=1.2			
	$\gamma_{PDMS/PMMA}$=3.8		$\gamma_{PDMS/PMMA}$=3.8		
ε [c]	2.46	2.95	5.24	4.09	2.95
N [d]	1.406	1.591	1.490	1.784	1.591
Tg [e] (°C)	-127	100	105	120	100

(a) Molecular weight.
(b) Interfacial tension γ_{12} or surface tension γ at 170°C.[6]
(c) Dielectric constants at 170°C. The dielectric constant of PMMA at 170°C was found to be 5.3 in the measurement by Mazur,[7] which is consistent with our measurement.
(d) Refractive index.
(e) Glass transition temperature

where each of the two terms describes the dispersive vdW interaction between an electrode and one of the liquids through a thin layer of the other liquid. The Hamaker constant A_1 and A_2 can be readily calculated on the basis of the Lifshitz theory of vdW forces. Since h_1 and $-h_2$ are large in these studies, p_{dis} is negligible in comparison to p_{el} and the Laplace pressure and, therefore, will be neglected.[8,9] The electric field in the capacitor system is given by

$$\mathrm{E}_i = \frac{\varepsilon_j U}{\varepsilon_1 \Delta h_2 + \varepsilon_2 \Delta h_1} \quad (i, j = 1,2; i \neq j) \tag{3}$$

Where U is the applied voltage and ε_i is the dielectric constant of medium i. For the initial stage of the instability, when the wavelength of the instability λ is much larger than Δh, the electrostatic pressure is,

$$p_{el} = -\varepsilon_0 (\varepsilon_2 - \varepsilon_1) \mathrm{E}_1 \mathrm{E}_2 \tag{4}$$

where ε_0 is the permittivity in a vacuum. It should be noted that this scalar approximation of the electrostatic pressure holds only for the early stages of fluctuation growth, as treated within the framework of the linear instability analysis. Similar to the model calculations of Vrij,[10] Brochard et al.[11,12] and Schäffer et al.[1,2], a linear stability analysis, which assumes small height fluctuations at the liquid/liquid interface of the form $\Delta h(x,t) = Be^{iqx} e^{t/\tau}$, will yield the fastest growing mode of waves in the system. Here, q is the wavenumber, τ^{-1} is the growth rate, and B is the amplitude. The modulation of the interface gives rise to a pressure gradient, which induces a lateral flow J of material. The detailed flow behavior of the coupled system strongly depends on the ratio of the viscosities of the two liquids, η_1 and η_2.[13,14] The flux J can be readily obtained from $J_1 = \int_{\Delta h}^{h_1} v_{x,1} dz$ and $J_2 = \int_{h_2}^{\Delta h} v_{x,2} dz$ using the boundary conditions $v_{x,2}(z = h_2) = 0$, $v_{x,1}(z = h_1) = 0$, $v_{x,1}(z = 0) = v_{x,2}(z = 0)$ and

$\eta_1 \left.\frac{dv_{x,1}}{dz}\right|_{z=\Delta h} = \eta_2 \left.\frac{dv_{x,2}}{dz}\right|_{z=\Delta h}$ where $v_{x,i}$ is the lateral fluid velocity in medium i. This

Figure 2.1. a) Optical microscopy image of a thin liquid film of polyisoprene, b) Optical microscopy image of a bilayer of polyisoprene and oligomeric dimethylsiloxane annealed for 2 days in an electric field (d-h = 940 nm, h = 140 nm, V = 20 V). In both figures the original color images were converted to greyscale. The dimensions of the images are 528 μm by 692 μm.

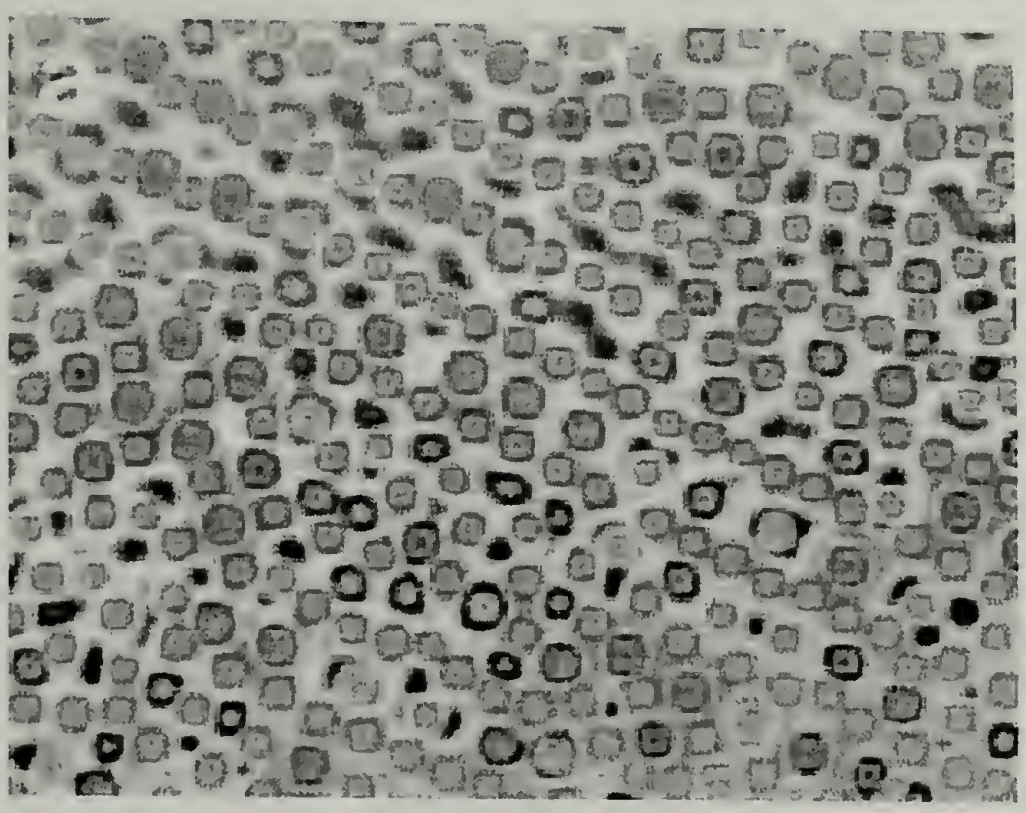

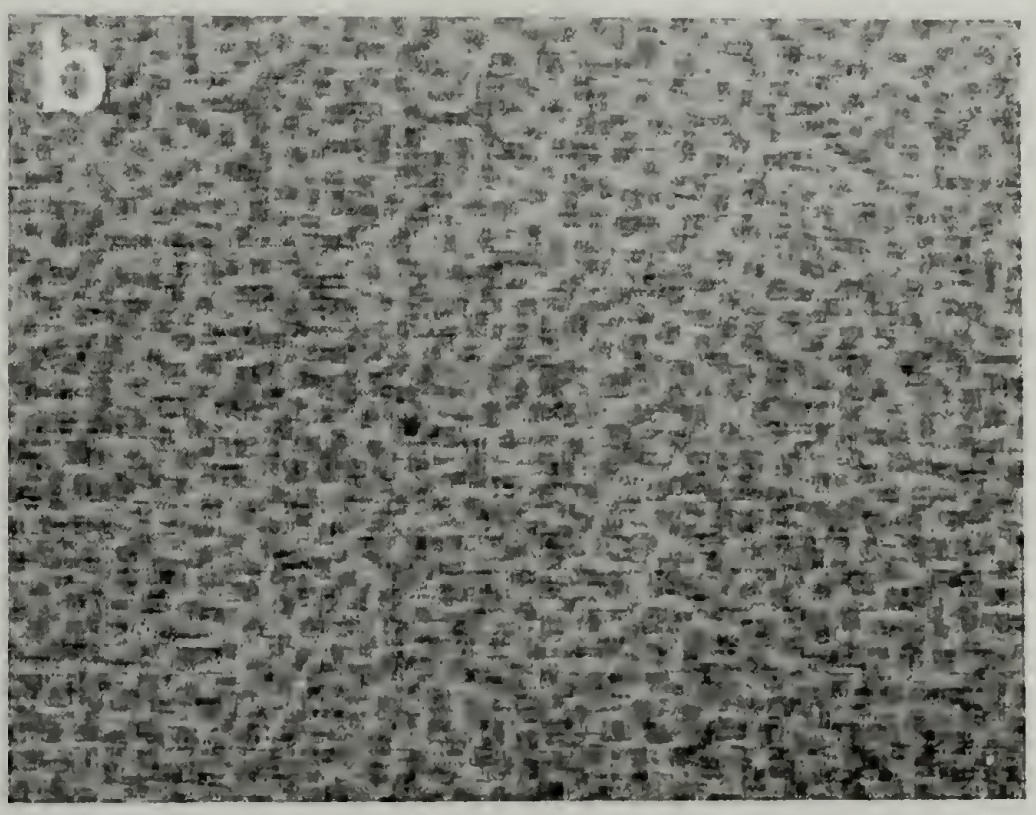

yields

$$J_i = \frac{h_i^2}{12\eta_i(\eta_1\Delta h_2 + \eta_2\Delta h_1)}\left[\eta_j\Delta h_i^2\left(-\frac{\partial p_1}{\partial x}\right) + 4\eta_i\Delta h_i\Delta h_j\left(-\frac{\partial p_1}{\partial x}\right) + 3\eta_i\Delta h_j^2\left(-\frac{\partial p_2}{\partial x}\right)\right. \quad (5)$$

$$(i, j = 1,2; i \neq j)$$

Assuming two incompressible liquids coupled by the continuity equations

$$\frac{\partial J_1}{\partial x} + \frac{\partial J_2}{\partial x} = 0 \quad (6a)$$

$$\frac{\partial \Delta h}{\partial t} + \frac{\partial (J_1 - J_2)}{2\partial x} = 0 \quad (6b)$$

which show the relationship of flow within the two layers, a differential equation describing the dynamic response of the interface is obtained. In the linear approximation, the dispersion relation

$$\frac{1}{\tau} = -\frac{(-h_1h_2)^{3/2}}{3C(\eta)}\left(\gamma_{12}q^4 + \frac{\partial p_{el}}{\partial \Delta h}q^2\right) \quad (7)$$

is found where $C(\eta)$ contains all terms involving viscosity, and is given by

$$C(\eta) = \frac{\eta_1^2h_2^4 - \eta_1\eta_2h_1h_2(4h_1^2 - 6h_1h_2 + 4h_2^2) + \eta_2^2h_1^4}{(-h_1h_2)^{3/2}(\eta_2h_1 - \eta_1h_2)} \quad (8)$$

The fastest growing wave number, corresponding to the maximum in eq (7),

is given by

$$q_{max}^2 = \frac{\varepsilon_0(\varepsilon_2 - \varepsilon_1)^2}{\gamma_{12}U(\varepsilon_1\varepsilon_2)^{1/2}}(E_1E_2)^{3/2} \quad (9a)$$

The fastest growing wavelength is found from

$$\lambda_{max} = 2\pi/q_{max} = 2\pi\sqrt{\frac{\gamma_{12}U(\varepsilon_1\varepsilon_2)^{1/2}}{\varepsilon_0(\varepsilon_2 - \varepsilon_1)^2}}(E_1E_2)^{-3/4} \quad (9b)$$

The characteristic response time τ_{max} is then given by

$$\tau_{\max} = \frac{3C(\eta)\gamma_{12}U^2\varepsilon_1\varepsilon_2}{\left(-h_1h_2\right)^{\frac{3}{2}}\varepsilon_0^2\left(\varepsilon_2-\varepsilon_1\right)^4\left(E_1E_2\right)^3} \tag{10}$$

Consequently τ_{max} is proportional to γ_{12} as would be expected.[15] If we wish to compare the liquid-liquid case to the liquid-air case presented previously[1,2] eq (10) can be rewritten in terms of the fastest growing wave number defined in eq (9a). By substitution we get

$$\tau_{\max} = \frac{3C(\eta)}{\gamma_{12}\left(-h_1h_2\right)^{\frac{3}{2}}} q_{\max}^{-4} \tag{11}$$

In the limit of $\eta_1 << \eta_2$, , the instability is dominated by the medium with the higher viscosity. In the case where $\eta_1=0$, $\varepsilon_1=1$ and $\gamma_{12}=\gamma$ (the surface tension of component 2), the equations reduce to the polymer/air case previously described by Schäffer et al.[1,2] The model calculations presented describe only one specific case (comparable to the experimental conditions) but it should be noted that other, more general, theoretical developments have been published by others[16-18] that include cylindrical bilayer configurations, gravity contributions, convection effects, and interfacial charge effects.

A comparison of experimental results to theoretical values calculated from eq (9b) shows qualitatively good agreement. The model calculations yield $\lambda_{max} = 32.47\ \mu$m for the PI/air interface and 17.27 μm for the PI/ODMS interface, which can be compared to the experimental values of 47.4 μm and 20.6 μm, respectively. While experimental values are slightly higher than those predicted, both theory and experiment show a reduction of the length scale by roughly a factor of two. Also, for the OS/air and OS/ODMS experiments, the model calculations and

experimental values agree reasonably well, giving values of λ_{max} = 13.75 μm and 12.94 μm, and 12.7 μm and 7.6 μm, respectively.

The dependence of λ_{max} on the dielectric constant difference between the liquids, i.e. $\Delta\varepsilon = \varepsilon_1 - \varepsilon_2$, while keeping other variables constant, is shown in Figure 2.2 (dashed line, left and top axis). λ_{max} diverges at the point where the dielectric constants of the two media are equal, i.e. $\Delta\varepsilon = 0$. This is understandable since the polarizabilities of the liquids are equal and the electric field does not exert any pressure on the liquid/liquid interface. By increasing the difference between two dielectric constants, a slow decay of the preferred wavelength is observed. However, decreasing λ_{max} significantly is not possible by simply modifying the dielectric constant or increasing the applied voltage – keeping in mind that the static dielectric constants of typical materials range between 1 and 80, and that dielectric breakdown defines an upper limit for the applied voltage. The solid line (left and bottom axis) of Figure 2.2 illustrates a simple route to achieve smaller sized structures. These results show the scaling of λ_{max} as a function of the interface or surface tension. Figure 2.3 shows the model calculation of λ_{max} as a function of the geometry ratio h_0/d, where λ_{max} is seen to be substantially reduced in liquid/liquid bilayer in comparison to liquid/air single layer. It is seen that $\lambda_{max} \propto \sqrt{\gamma_{12}}$. A well-known strategy to reduce γ_{12} is addition of a small amount of a diblock-copolymer that segregates to the liquid/liquid interface[19-21]. Similarly, one can achieve an effective reduction of the surface tension of a single layer by placing a surfactant at the liquid/air interface. Studies are underway in the group to determine the minimum achievable λ_{max} by this route.

One consequence of the reduction in λ_{max} for the bilayer is the dramatic decrease in time required to amplify fluctuations. Intuitively, one would expect that the presence of the second viscous medium would slow the growth of fluctuations substantially. On the contrary, the opposite is found. Eq (11) relates the characteristic relaxation time τ_{max} to $C(\eta)$, a term containing the viscosities, $\lambda_{max,}$ the characteristic wavelength, and $\gamma_{12,}$ the interfacial tension. Consider, now, $C(\eta)$ in terms of a viscosity ratio $r = \eta_1 / \eta_2$. If $h=h_1=-h_2$, i.e. the layer thicknesses are equal, and $\eta_2=\eta$, then

$$C(\eta) = \eta \frac{1 + 14r + r^2}{1 + r} \tag{12}$$

If $r=0$, i.e. $\eta_1=0$ (thin film case) or $\eta_1 << \eta_2$, then $C(\eta)=\eta$ and λ_{max} reduces to the result shown by Schäffer et al. for a thin film with air.[1,2] In the opposite extreme, $r=1$, i.e. $\eta_1=\eta_2=\eta$, then $C(\eta)=8\eta$, representing an effective eight-fold increase in the viscosity. Consequently, λ_{max} would decrease by a small amount and τ_{max} should increase by a factor of 8. The observation of the 50 folds reduction in the characteristic time is in disagreement with this, as seen just by looking at eq (10). If we compare instabilities with the same q vector, in going from the single layer to the bilayer case, C(η) increases and γ_{12} decreases. From eq (11) it is seen that this should lead to an increase of τ_{max}. For the case of (PI/PDMS), C(η) is increased by a factor of 1.01 and γ_{12} decreases by a factor of 10, yielding a combined increase in τ of 14. Now, q increases by a factor of 1.9 or q^4 increases by a factor of 13.0. Together, these factors should cancel each other, meaning that the growth rate of the instabilities in the PI single layer and in the PI/PDMS double layers is approximately

Figure 2.2. Variation of the instability wavelength λ_{max} with the dielectric constant difference $\Delta\varepsilon = \varepsilon_1 - \varepsilon_2$, while keeping all other parameters constant ($h_1 = 940$ nm, $-h_2 = 140$ nm, $V = 20$ V, $\varepsilon_1 = 1$, $\gamma = 32$ mN/m), as predicted by the model calculations. (dashed line, left and top axis). Variation of the instability wavelength λ_{max} with γ_{12} the interfacial tension at the interface between media 1 and 2, while keeping all other parameters constant ($h_1 = 940$ nm, $h_2 = 140$ nm, $V = 20$ V, $\varepsilon_1 = 2.93$, $\varepsilon_2 = 2.37$), as predicted by the model calculations (solid line, left and bottom axis). The open and solid diamonds show the measured value of $\langle d_{cyl\text{-}cyl} \rangle$ and the predicted value of λ_{max}, corresponding to Figure 2.1 (a) (PI single layer). The open and solid circles are $\langle d_{cyl\text{-}cyl} \rangle$ and λ_{max} corresponding to Figure 2.1 (b) (PI/ODMS bilayer).

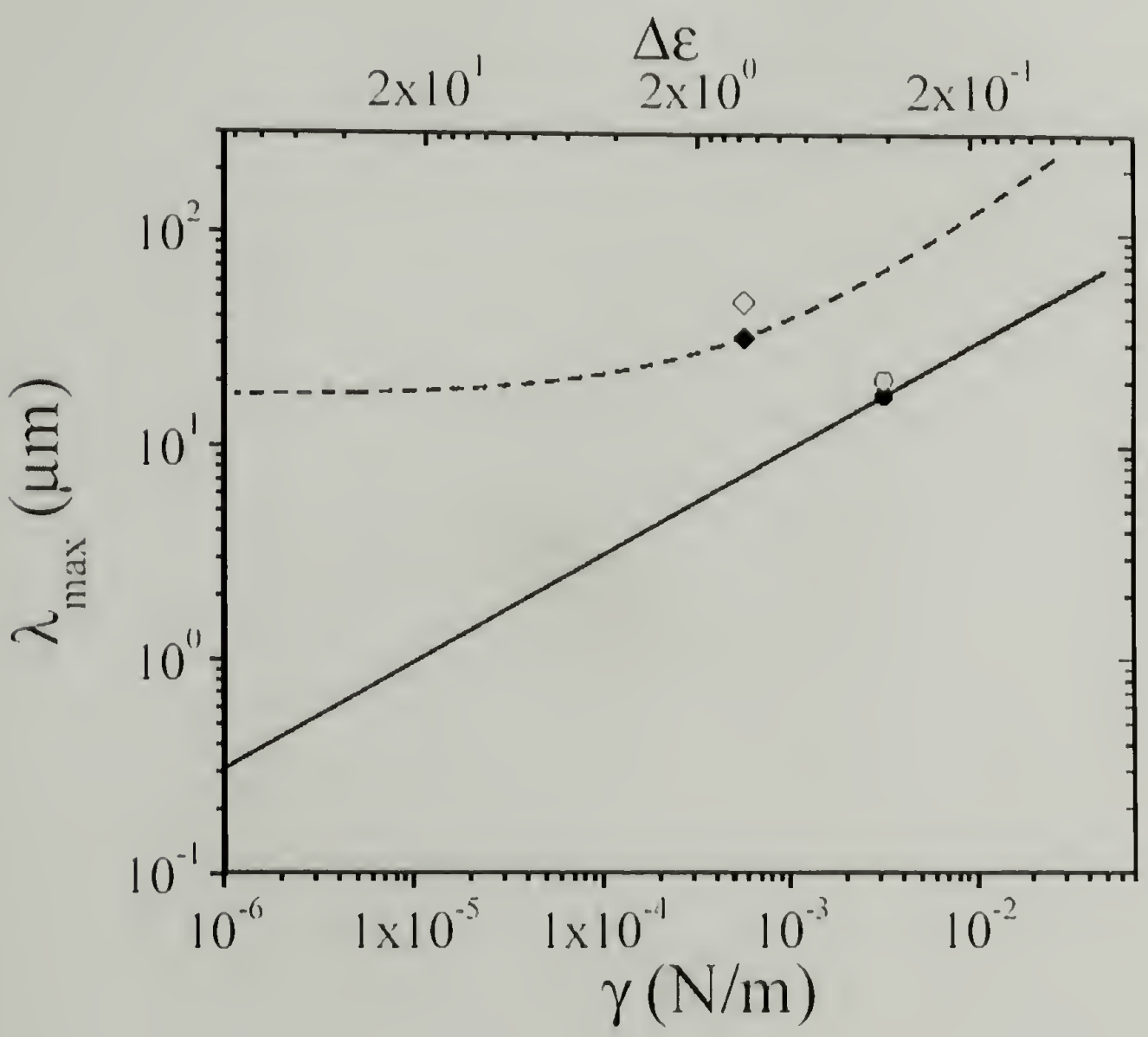

the same (τ_{max} = 0.27 h for the PI/air case and τ_{max} = 0.22 h for the PI/ODMS case). However, the time at which features are observed in the bilayers case is nearly 50 times shorter than that seen in the single layer case. The exact origin of this discrepancy is not known at present. However, the arguments presented here are valid only for the early stages of growth. Late stage which govern the formation of columns (the experimental observable), require a much more detailed analysis.

Structure Formation at Liquid/Liquid Interface

An optical micrograph of the 550 nm PS/ 570 nm PDMS bilayer after one day under a 50 V is shown in Figure 2.4 (a). In the case of polymer/air system, where the refractive index difference between polymer and air is rather large, the formed structures have good optical contrast through ITO cover slide ($I \sim \Delta n^2$). However, since the refractive indices of PS and PDMS are 1.591 and 1.406, respectively, the optical resolution is rather weak. The autolevel, auto contrast and the conversion to gray scale are done to improve the optical contrast (Adobe Photoshop 5.0). On the other hand, this indicates the system is "pure" PMDS/PS bilayer with no air gap above it. In contrast, the images with good optical contrasts can be observed in air/liquid 1/liquid 2 trilayer system, which will be discussed in detail in chapter 3. Columns of PS through the upper PDMS layer are evident in the micrograph in 550 nm PS/ 700 nm PDMS bilayer after one day under a 50 V in Figure 2.5. The formation of the cylindrical structures at the interface is clearly seen. A 2D Fast Fourier Transform (FFT) of the optical micrograph is shown in the inset. The appearance of a ring in the transform indicates that there is a well-defined

Figure2.3. Model calculation of the instability wavelength λ_{max} as a function of the geometry ratio h_0/d in 30 V. (a) $\varepsilon_1 = 1$, $\varepsilon_2 = 2.95$, $\gamma = 33$ mN/m; (b) $\varepsilon_1 = 5.24$, $\varepsilon_2 = 2.95$, $\gamma = 1.2$ mN/m.

(a)

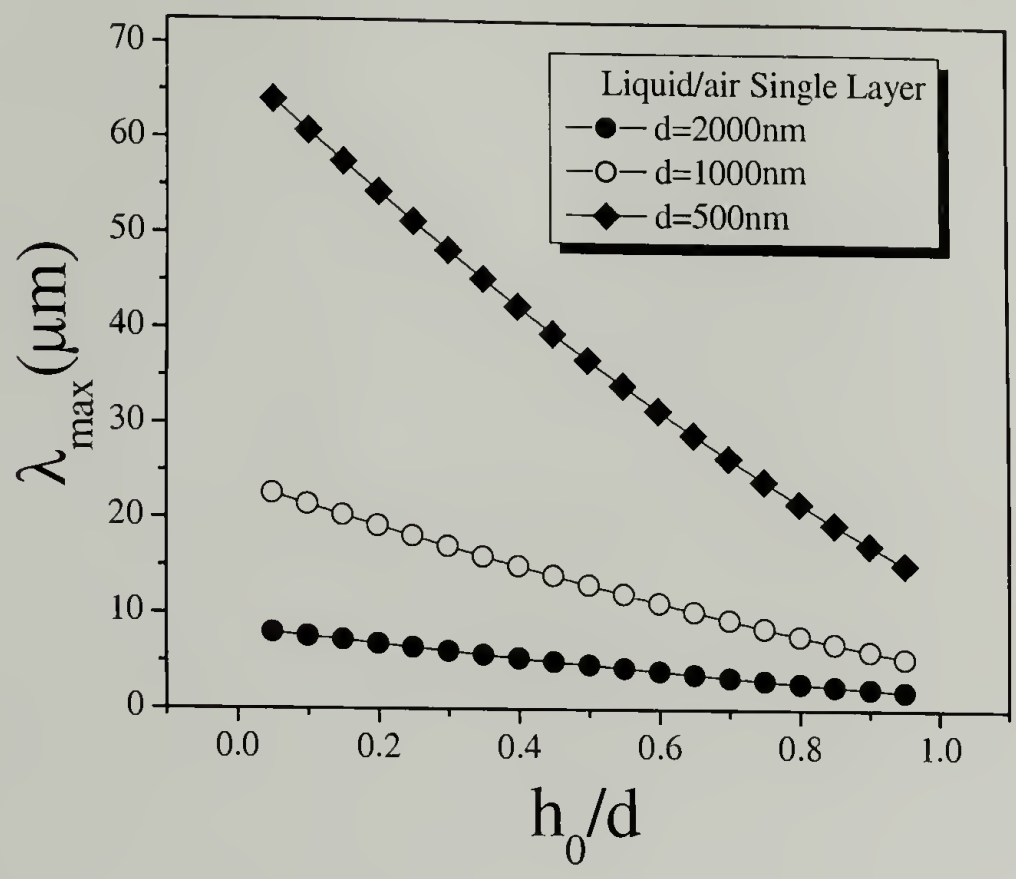

(b)

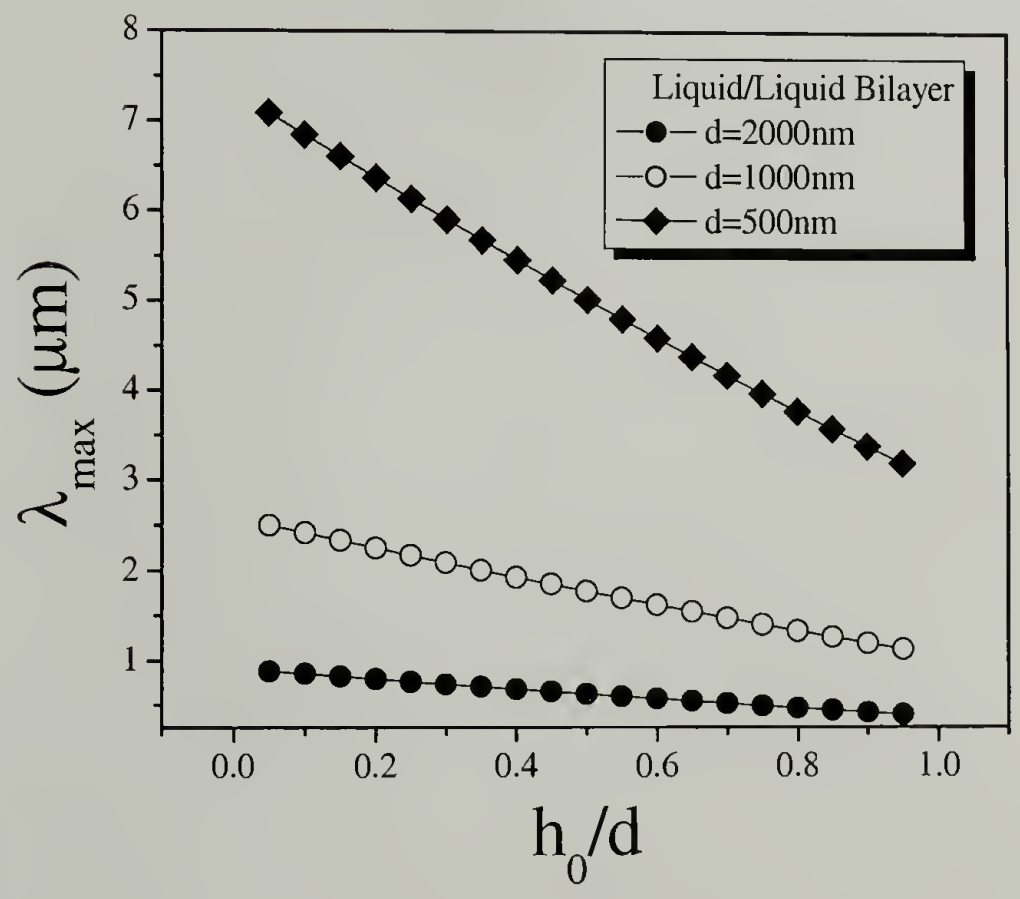

center-to-center distance between adjacent PS columns of PS of 13.0 μm. From the micrograph the distribution of the center-to-center distances of adjacent columns was determined and is shown in Figure 2.5 (b). As seen, the average separation distance is 12.9 μm, with a full width at half maximum (FWHM) of 1.86 μm. The average diameter of the PS columns determined from the optical micrograph is 8.6 ± 0.5 μm.

After removing the upper PDMS layer with heptane, AFM was used to examine the surface of the underlying PS layer, i.e. the interface between the PDMS and PS layers. Shown in Figure 2.5 (c) is the AFM image of the PS surface obtained in the height mode. As seen, columns of PS have been produced by the electrostatic pressure acting on the original PDMS/PS interface. The average size of the columns is 8.5± 0.3 μm with an average center-to-center distance between adjacent PS columns of 13.0 ± 1.0 μm. Shown in the inset is a 2D FFT of the AFM image. The six spots evident in these data indicate that, locally, there is a hexagonal symmetry in the lateral arrangement of the columns.

In a foresaid discussion, the electrohydrodynamic instability at the interface between two polymers under an applied voltage U across two electrodes separated by a distance d causes an amplification of fluctuations of a characteristic wavelength λ_{max} . The λ_{max} in eq (9b) can be rewritten as[22]

$$\lambda = \frac{2\pi}{U\left|\frac{1}{\varepsilon_2} - \frac{1}{\varepsilon_1}\right|}\left(\frac{\gamma_{12}}{\varepsilon_0}\right)^{1/2}\left(\frac{d-h_0}{\varepsilon_1} + \frac{h_0}{\varepsilon_2}\right)^{3/2} \tag{13}$$

where d-h and h are the film thicknesses of polymer 1 and polymer 2 with dielectric constants ε_1 and ε_2 , respectively. γ_{12} is the interfacial tension between polymer 1

Figure 2.4. Optical micrograph of a PS (h_{PS} =550 nm) / PDMS (h_{PDMS} =570 nm) bilayer exposed to 50 V at 170°C for one day. The image size is 531x398 μm^2. (a) The original color images; (b) black/white image obtained by auto leveled and contrasted, and then converted to a grayscale to enhance the weak contrast.

(a)

(b)

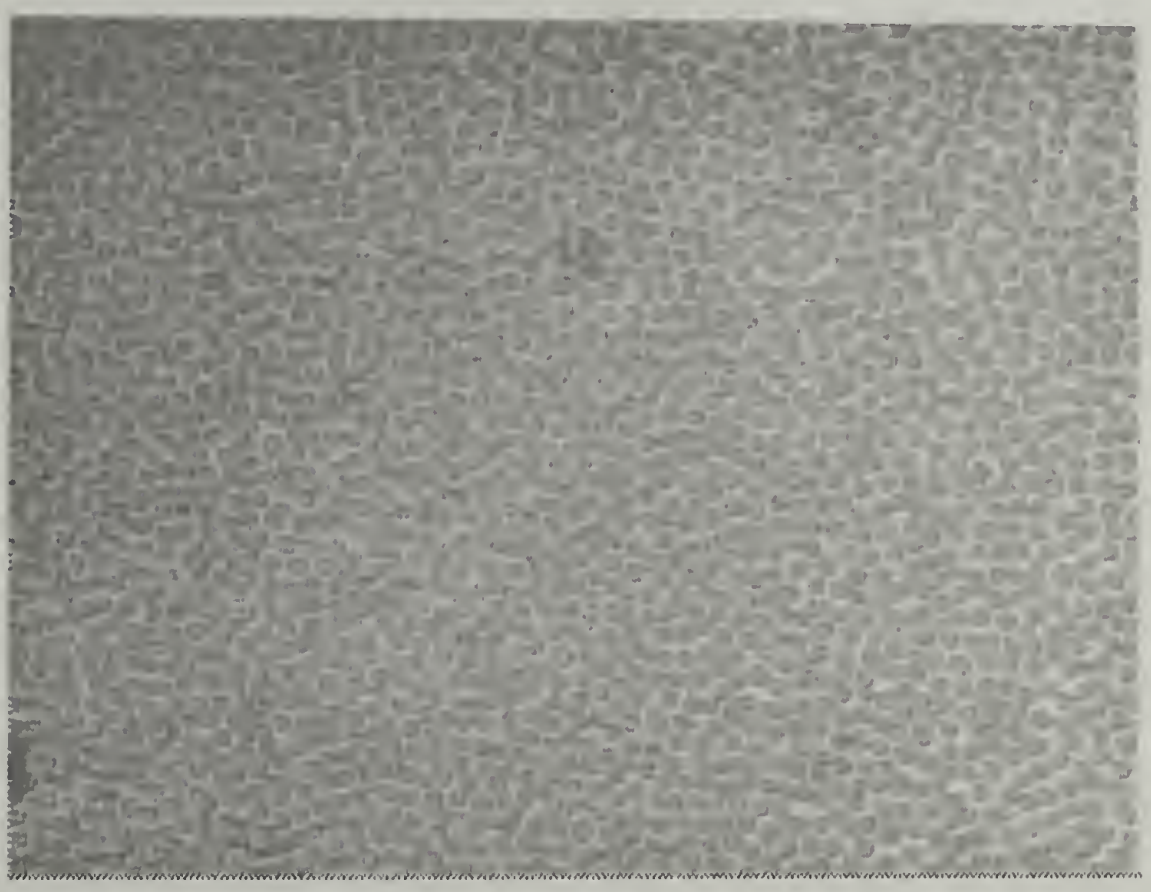

and 2, and ε_0 is the dielectric permittivity in vacuum. Substituting the relevant parameters for the PDMS/PS bilayer case into eq (1) yields a characteristic distance of 15.8 μm, which agrees well with the 12.9 μm value measured experimentally.

In a second set of experiments, the upper PDMS layer was replaced by a PMMA layer to form PS/PMMA bilayer. Since the interfacial tension between PS and PMMA ($\gamma_{PS/PMMA}$=1.2mN/m at 170°C) is smaller than that for a PS/PDMS bilayer, ($\gamma_{PS/PDMS}$ = 6.1mN/m) at any given temperature,[6] then, from eq (13), it would be expected that the characteristic wavelength λ would decrease. Shown in Figure 2.6 (a) is the optical micrograph of the PS/PMMA bilayer after one day at 170 °C with 30 V applied after selectively removing the upper PMMA layer. Direct images of the bilayer without removal of the upper layer were not easily seen, since the refractive indices of PS and PMMA, 1.591 and 1.49, respectively, are very similar. The 2D FFT shown in the inset exhibits a ring, indicative of a well-defined separation distance between the features at the interfaces. Analysis of the optical micrograph yields an average diameter of the columns of 1.7 ± 0.3 μm. The distribution of the center-to-center distance between the columns, shown in Figure 2.6 (b), exhibits a maximum at 4.0 μm with a FWHM of 0.7 μm. Shown in Figure 2.6 (c) is an AFM height image after removal of the PMMA layer by rinsing with acetic acid. Rather than columns, however, the AFM image shows that the features are holes penetrating through the PS film. This results, primarily, from the thickness of the individual layers. Here, the underlying PS layer was much thicker than the PMMA overlayer. Consequently, in this case, PMMA columns form within the PS

Figure 2.5. (a) Optical micrograph of a PS (h_{PS} =550 nm) / PDMS (h_{PDMS} =700 nm) bilayer exposed to 50 V at 170°C for one day. The image size is 438x398 μm^2. The original color images were auto leveled and contrasted, and then converted to a grayscale to enhance the weak contrast due to the small refractive index difference between PS and PDMS. The inset shows the 2D fast Fourier transform (FFT) pattern of the corresponding optical micrographs. (b) The distribution function of the center-to-center distance between adjacent columns. (c) The 3D AFM height image of the PS/PDMS bialyer after removal of the upper PDMS layer with heptane. The 2D FFT of the AFM image is shown in the inset.

(a)

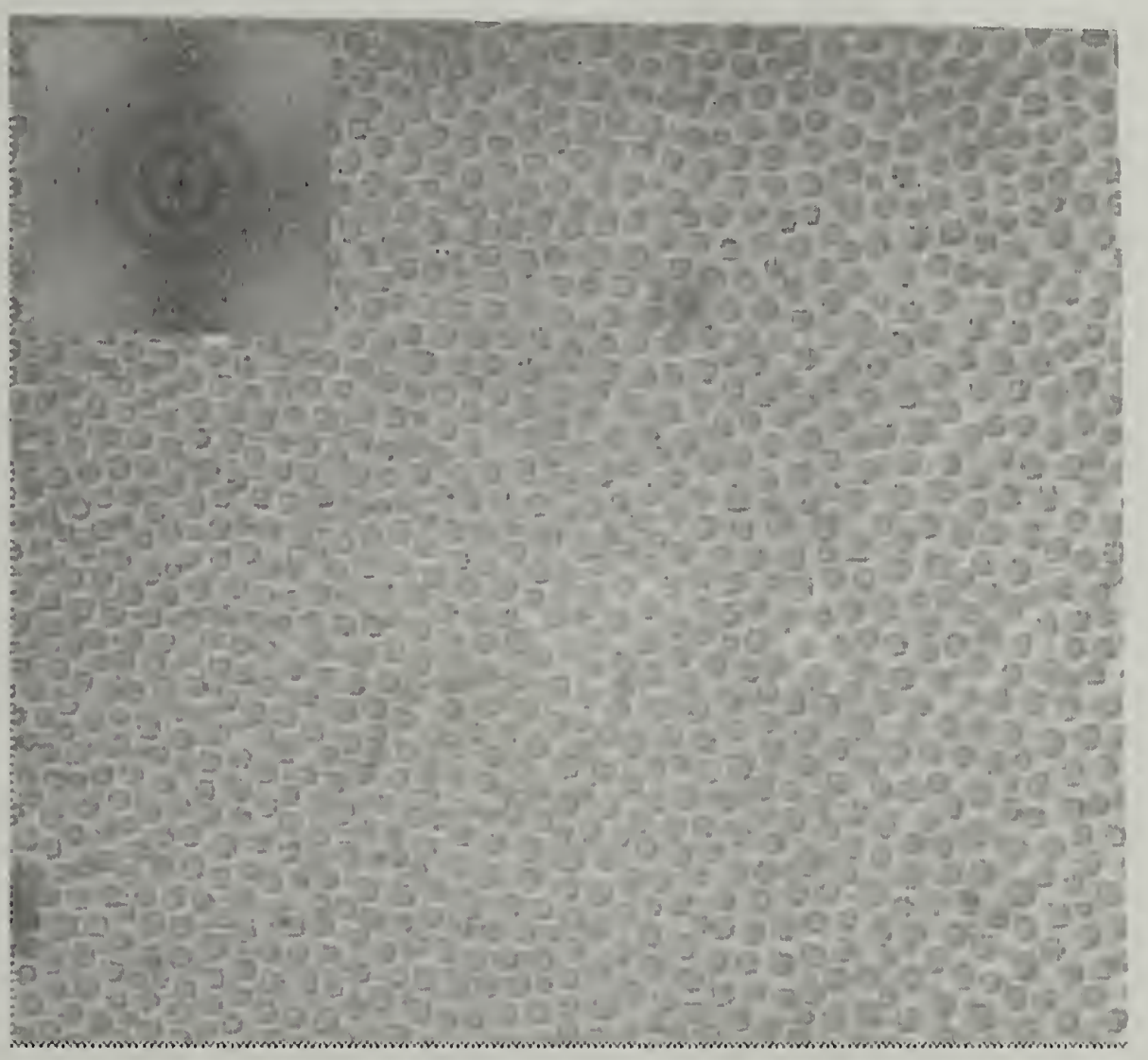

Continued on next page

(b)

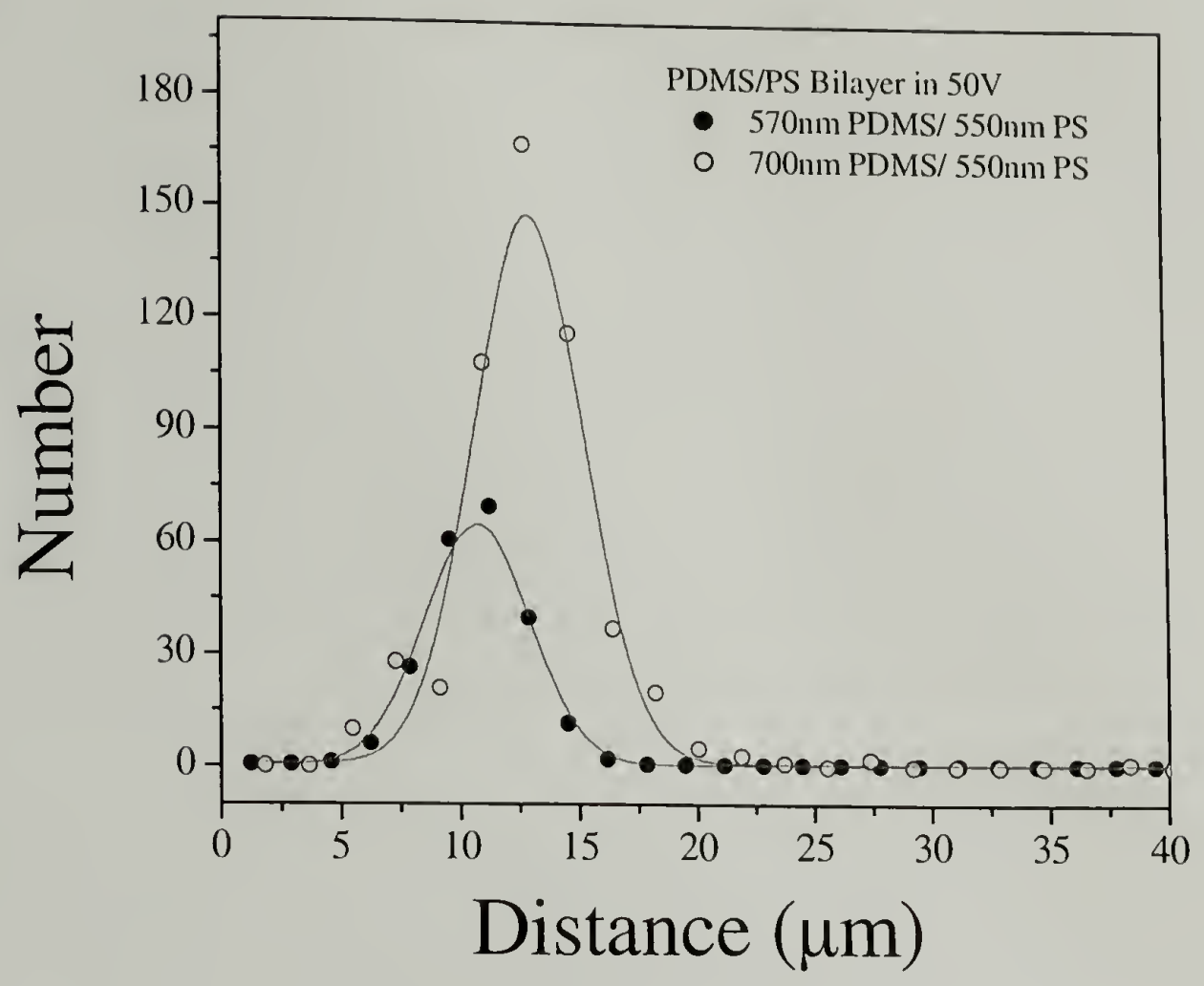
PDMS/PS Bilayer in 50V
570nm PDMS/ 550nm PS
700nm PDMS/ 550nm PS
Number
Distance (μm)
0
30
60
90
120
150
180
0
5
10
15
20
25
30
35
40

(c)

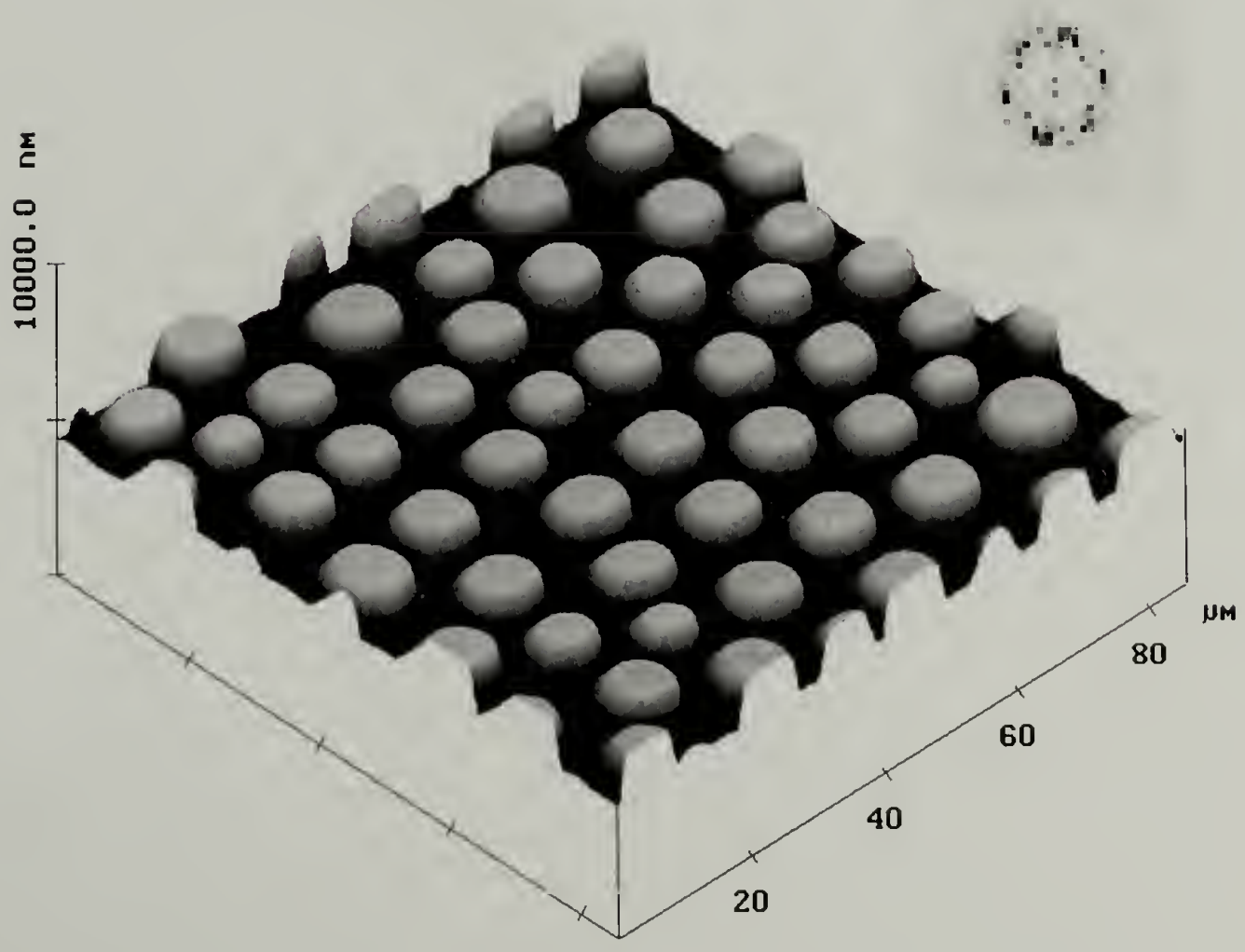
10000.0 nm
μm
20
40
60
80

layer. From eq (13) λ=2.8 μm which is in good agreement with the value determined experimentally.

Experiments on PMMA/PDMS bilayers showed essentially the same behavior as that of the PS/PDMS bilayers. The film thickness of underlying PMMA layer was much thinner than that of the upper PDMS layer, therefore the PMMA columns were obtained. It should be pointed out that since the refractive index difference between PMMA and PDMS is quite small, ~0.08, the cylindrical structures at the PMMA/PDMS interface were barely visible with an the optical microscope. After removing the PDMS layer with heptane, both optical microscopy and AFM were used to characterize the surface of the underlying PMMA. While numerous experiments were done on this bilayer, results from one experiment will be cited. This bilayer, under 19 V for one day, an average column diameter of 3.0 μm was found with and average center-to-center distance of 10.5 μm. When the film thickness of two layers are equal, the interconnected structures might be obtained. Figure 2.7 shows an example of an observation in the PMMA/PDMS bilayer experiment.

The characteristic wavelength, λ, of fluctuations at the interface that are amplified by the applied electric field depends upon the sample geometry, the applied field, and the dielectric constants of the materials. These parameters are explicitly shown in eq (13). We can define a reference wavelength and electric field as follows:

$$\lambda_0 = \frac{\varepsilon_0 U^2 (\varepsilon_1 - \varepsilon_2)^2}{\gamma_{12} (\varepsilon_1 - \varepsilon_2)^{1/2}} \tag{14}$$

Figure 2.6. (a) An optical microscope image of PS/PMMA bilayer after removing the upper PMMA layer with acetic acid. The bilayer system held under 30 V at 170°C for one day. The image size is 266x199 μm^2. The initial film thickness of PS and PMMA were 730 and 290 nm, respectively. The inset shows the 2D fast Fourier transform (FFT) pattern of the corresponding optical micrographs. (b) The distribution function of the center-to-center distance between adjacent columns. (c) An AFM height image together with a cross section of the bilayer after removal of the upper PMMA layer. The 2D FFT of the AFM image is shown in the inset.

(a)

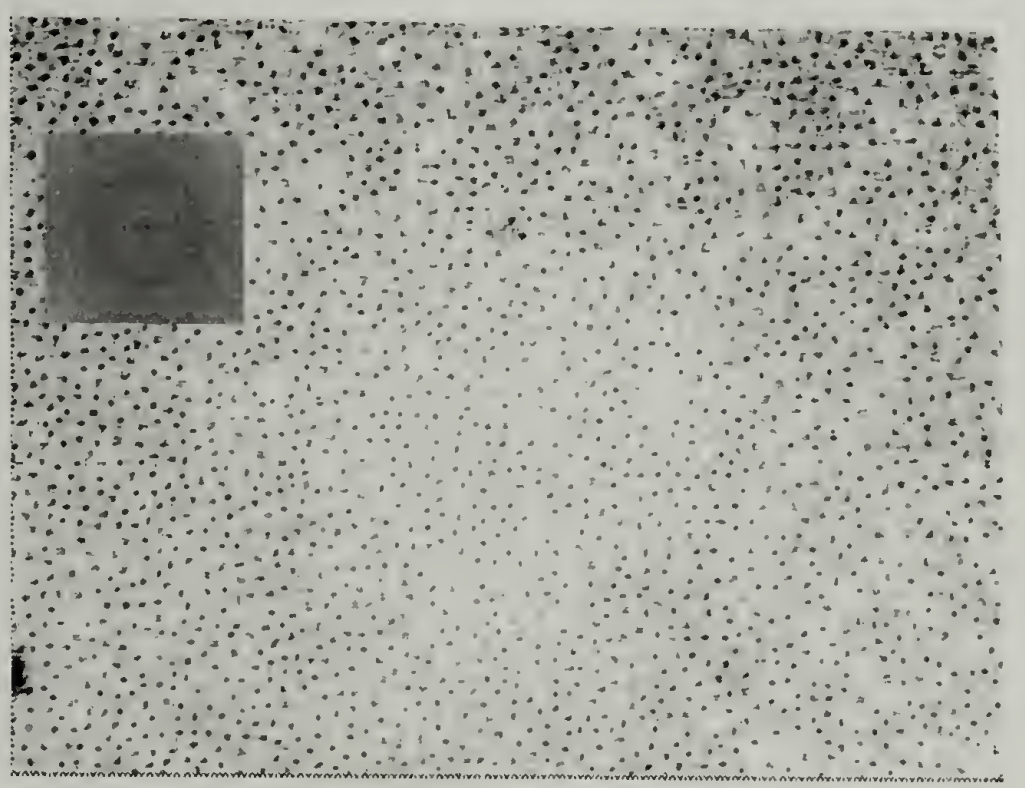

(b)

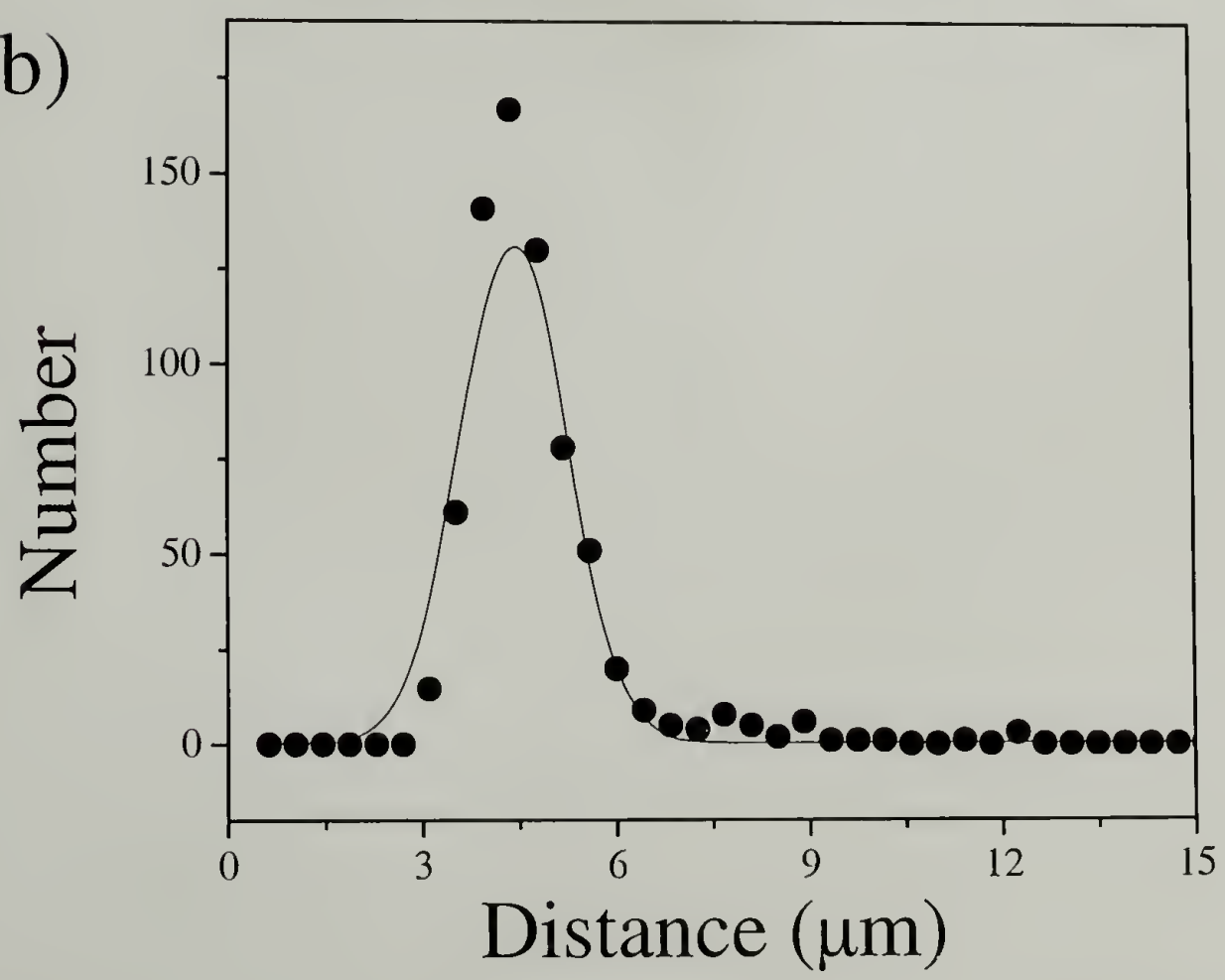

Continued on next page

Figure 2.6, continued

(c)

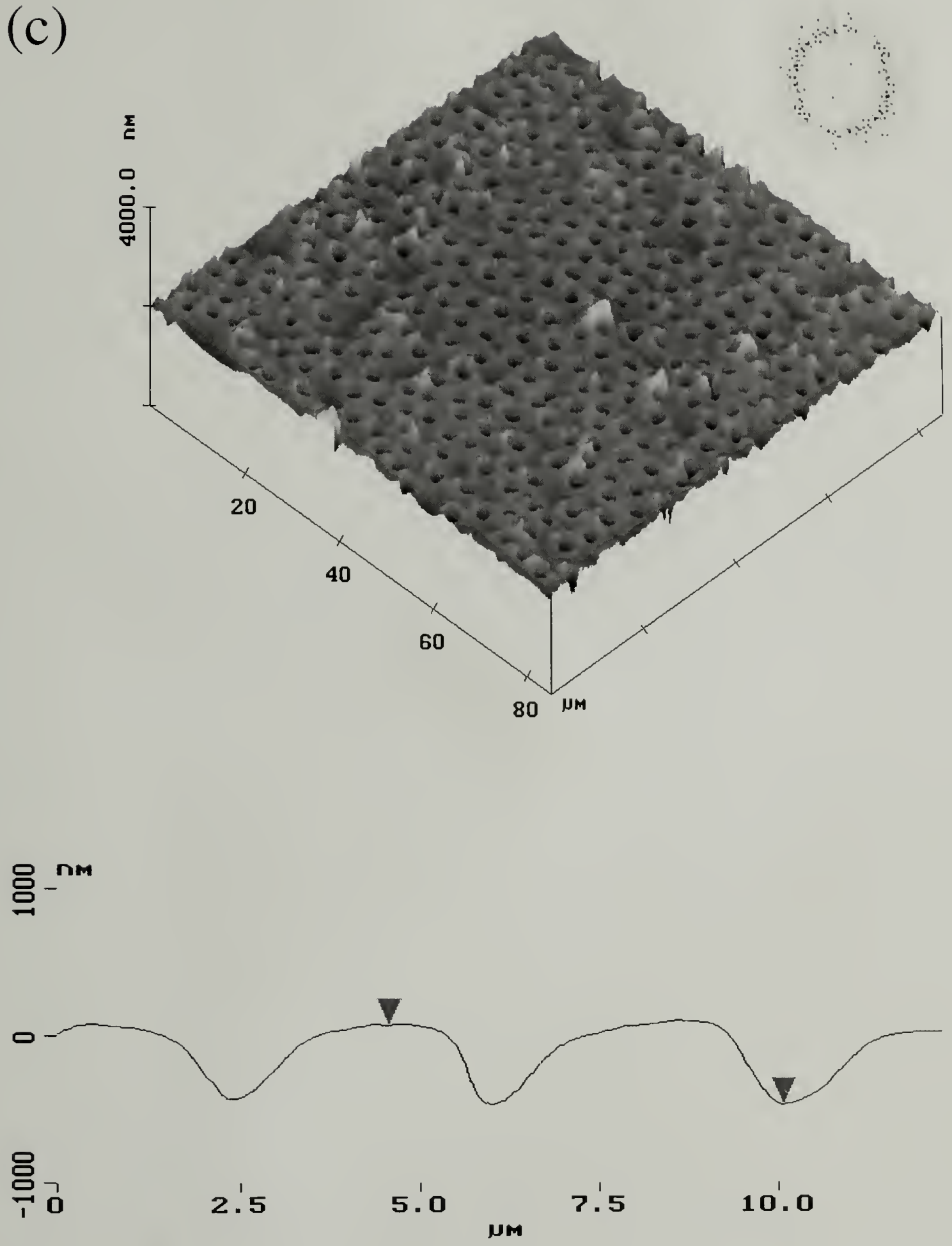

and $$E_0 = \frac{U}{\lambda_0} \tag{15}$$

Using these we can define a reduced wavelength and field by dividing λ and E by λ_0 and E_0, respectively. For the reduced wavelength we have:

$$\frac{\lambda}{\lambda_0} = 2\pi\left(\frac{E_1 E_2}{{E_0}^2}\right)^{-3/4} \tag{16}$$

where E_1 and E_2 are the electric field strengths in layer 1 and 2, respectively. By replacing ε_1 with 1.0, E_2 with E_P, the dimensionless variables, can be reduced to the polymer thin film case investigated by Schäffer et al.[1,2]

A master curve where the reduced wavelength λ/λ_0 is plotted as a function of the reduced field strength $\frac{E_1 E_2}{{E_0}^2}$ is shown in Figure 2.8. Shown are experimental data obtained from different experiments where the geometry of the system, the field strengths, and the polymers have been varied. In addition, data from previous experiments on single polymer layers are included. The solid line in the figure is the theoretical reduced wavelength as a function of the reduced field strength using no adjustable parameters. As can be seen, there is excellent agreement between experiment and theory over four orders of magnitude in the reduced wavelength and reduced field strength.

The derivation of eq (13) uses a linear approximation in treating the amplitude of fluctuations at the interface. Consequently, eq (13) should only be valid at the early stages of fluctuation growth and not, necessarily, at the latter stages of the process which includes the results shown here. Shown in Figure 2.9 are a series

Figure 2.7. An observation of the interconnected structures at PDMS/PMMA interface after exposed to 25 V at 170°C for a day after selectively removal of upper PDMS layer. (a) Optical micrograph (b) & (c) 2D and 3D AFM height images.

(a)

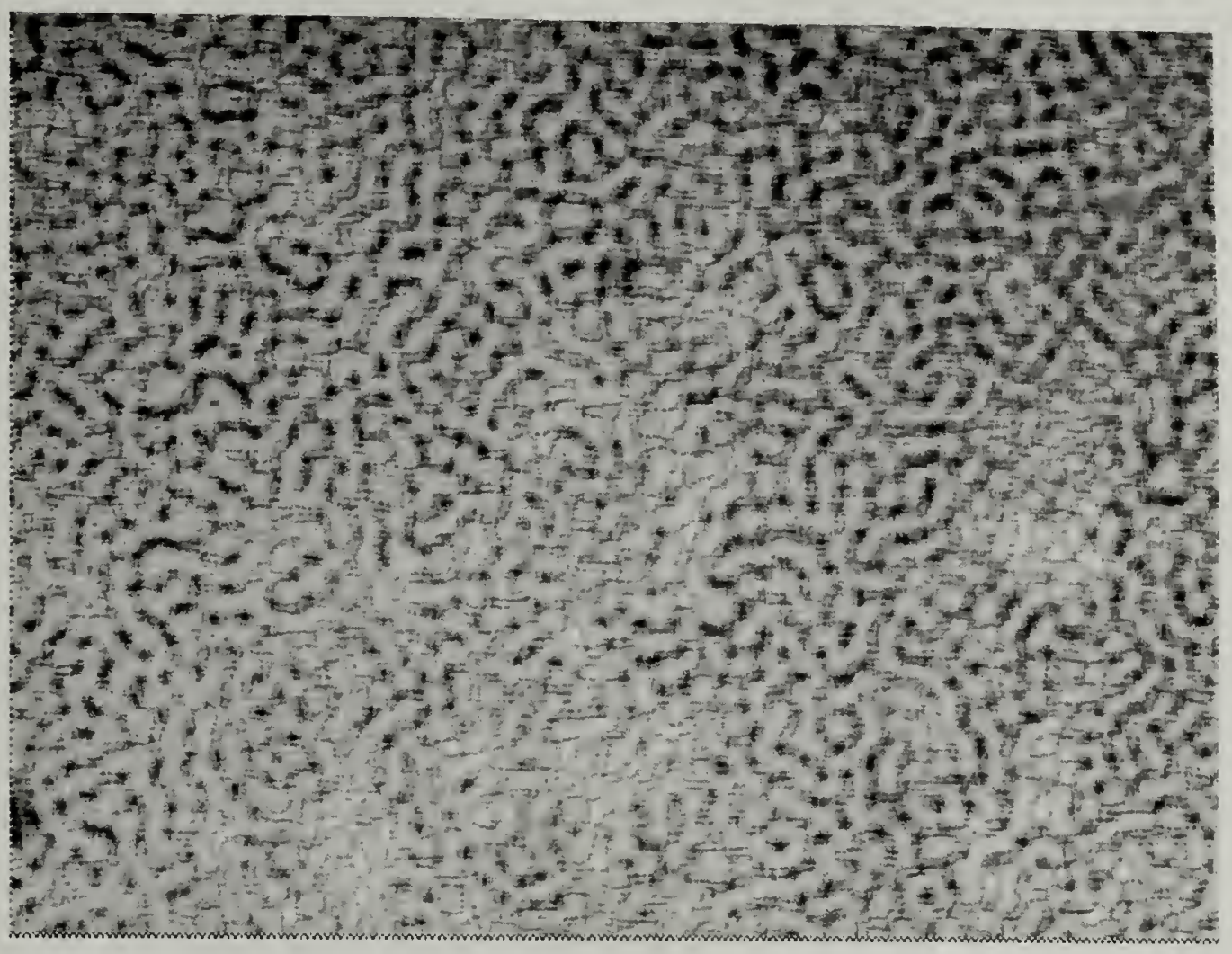

Continued on next page

(b)

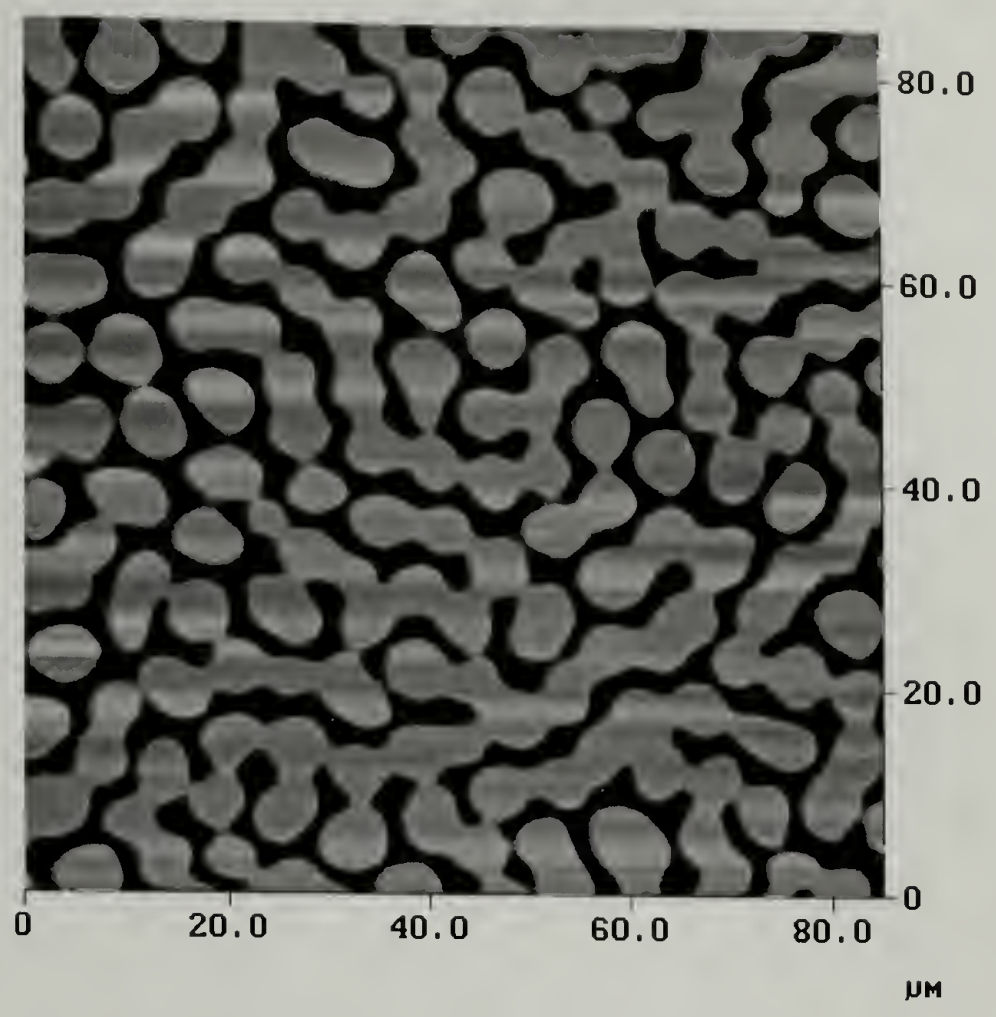

(c)

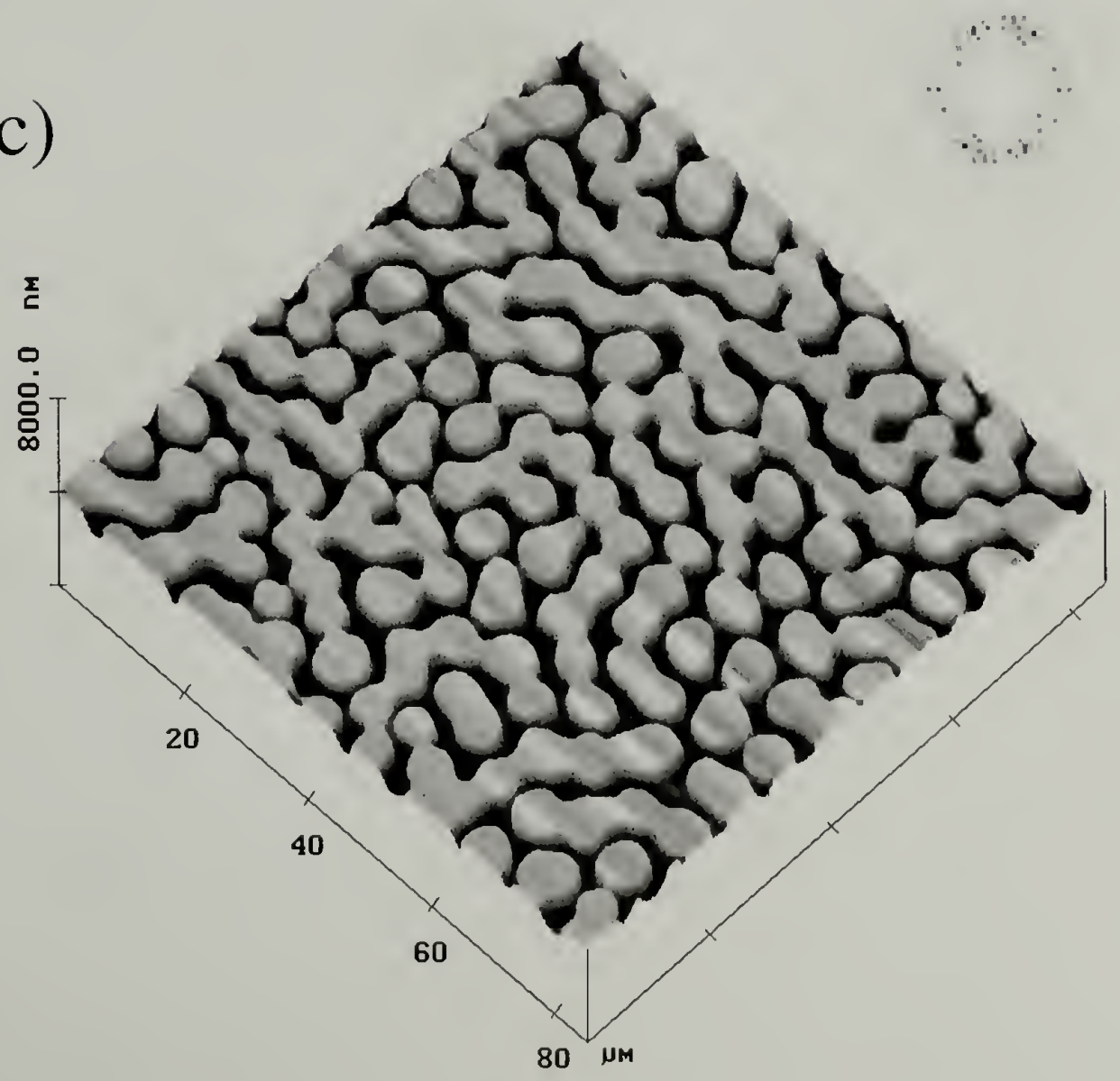

of AFM height images characterizing the development of structure at the interface of a PMMA/PDMS bilayer with 19 V applied at 170°C at different times. Each of the images was obtained on different bilayer samples where the upper PDMS layer was removed with heptane. Figure 2.9 (a) shows that the initial interface was featureless. With time, fluctuations having a well-defined lateral wavelength are seen to emerge (Figure 2.9 (b)). The 2D FFT of this image, shown in the inset, exhibits a maximum characteristic of a wavelength or average center-to-center distance of 10.5 μm. As time progresses, the amplitude of the fluctuations increases, the fluctuations become sharper and well-defined and begin to show a lateral order, and instabilities that give rise to the formation of columns appear (Figure 2.9 (c)). The 2D FFT of this AFM image, shown in the inset, exhibits a maximum corresponding to an average center-to-center distance of 10.5 μm, the same spacing seen at earlier times. The surface of the PMMA after the formation of PMMA columns that extend to the upper electrode is shown in Figure 2.9. Contact with the upper electrode is evidenced by the flattened top of the columns and a well-defined lateral ordering is evident. The 2D FFT shown in the inset exhibits a maximum corresponding to a cent-to-center distance between adjacent columns of 10.5 μm, the same as that seen at earlier times. The preservation of the characteristic distance throughout the growth of the columns justifies the comparison of the results obtained at later times to the linearized theoretical predictions. However, this does not hold true for the characteristic times describing the kinetic growth of these structures. As discussed earlier, discrepancies between the predicted times and those observed, based on the late stages of growth,

Figure 2.8. The master curve of the typical distance λ in varieties of thin film and bilayer experiments as a function of the electric field strength in the layer 1 and layer 2. The different symbols corresponded to ten data sets: ◆ PS/PMMA bilayer with h_{PS} = 730 nm, $(d-h_{PS})_{PMMA}$ =290 nm, U=30 V; ▼ PMMA/PDMS bilayer with h_{PMMA} = 180-290 nm, $(d-h_{PMMA})_{PDMS}$ =690-1030 nm, U=19-50 V; ★ PS/PDMS bilayer with h_{PS} = 305 nm, $(d-h_{PS})_{PDMS}$ =400 nm and 720 nm respectively, U=50 V; ▲ PS/PDMS bilayer with h_{PS} = 550 nm, $(d- h_{PS})_{PDMS}$ =570 nm and 700 nm respectively, U=50 V; O PSBr/air single layer with h_{PSBr} = 740 nm, d =1.66-1.98 μm, U=20-60 V; ● dPS/air single layer with h_{dPS} = 530 nm, d =1.06-1.85 μm, U=30 V, ▼, ∇ , ■ and □ were the measurements from reference 20, which corresponded to PI/air thin film, PI/ODMS bilayer, OS/air thin film and OS/ODMS bilayer systems respectively. The straight line was calculated based on the eq (16) with a slope of –3/4.

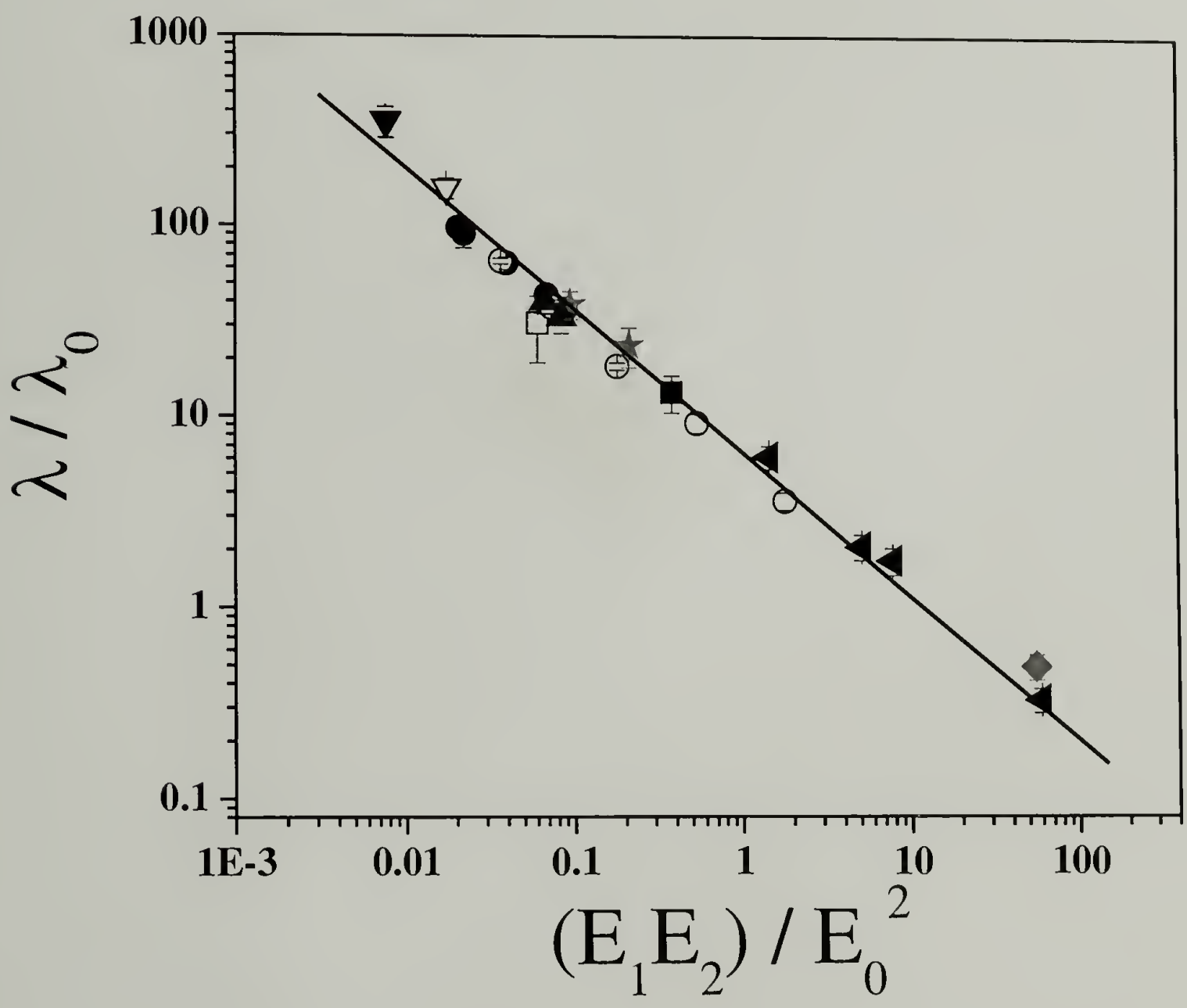

are seen due to our inability to characterize the kinetics of the growth quantitatively.[22] These studies are currently in progress using fluorescent confocal microscopy and will be discussed later.

The quantitative agreement between experiment and theoretical predictions in the master curve of Figure 2.8 shows that by controlling the sample geometry, the applied field or the interfacial energy, the size scale of the fluctuations can be controlled or manipulated. For a given geometry, polymer pair and field strength, reducing the interfacial tension provides a route to decrease the size scale of the fluctuations. Smaller size scale fluctuations that produce a larger interfacial area, can be amplified if the interfacial tension is reduced. It is well known that the addition of block copolymers that segregate to the to polymer/polymer interfaces reduces the interfacial tension and, hence, provides an easy route towards structures that are hundreds to tens of nanometers in size. In the case of thin polymer films, a surface active agent should cause a similar effect. With fixed interfacial energies, increasing the electric field provides the easiest route to control the lateral length scales of the fluctuations. By combining both these effects the characteristic lateral length scale of the fluctuations can easily be placed in the nanscopic level. By changing the relative thickness of the two layers, either columns or holes can be produced that have lateral length scales defined by the linearized theoretical arguments. Finally, it should be pointed out that polymers offer a unique advantage over low molar fluids, since the structures produced by the applied field can be frozen-in by quenching below the glass transition temperature.

Figure 2.9. A series of AFM height images as a function of time of a PMMA/PDMS bilayer after removal of the PDMS layer (h_{PMMA} = 220 nm, h_{PDMS} = 890 nm) with 19 V applied with heptane. The insets show a FFT of the images. The time sequence of the images correspond to the (a) initial interface, (b) initial stages of fluctuation growth, (c) amplification of fluctuations, and (d) the impingement of PMMA columns on the upper electrode.

(a)

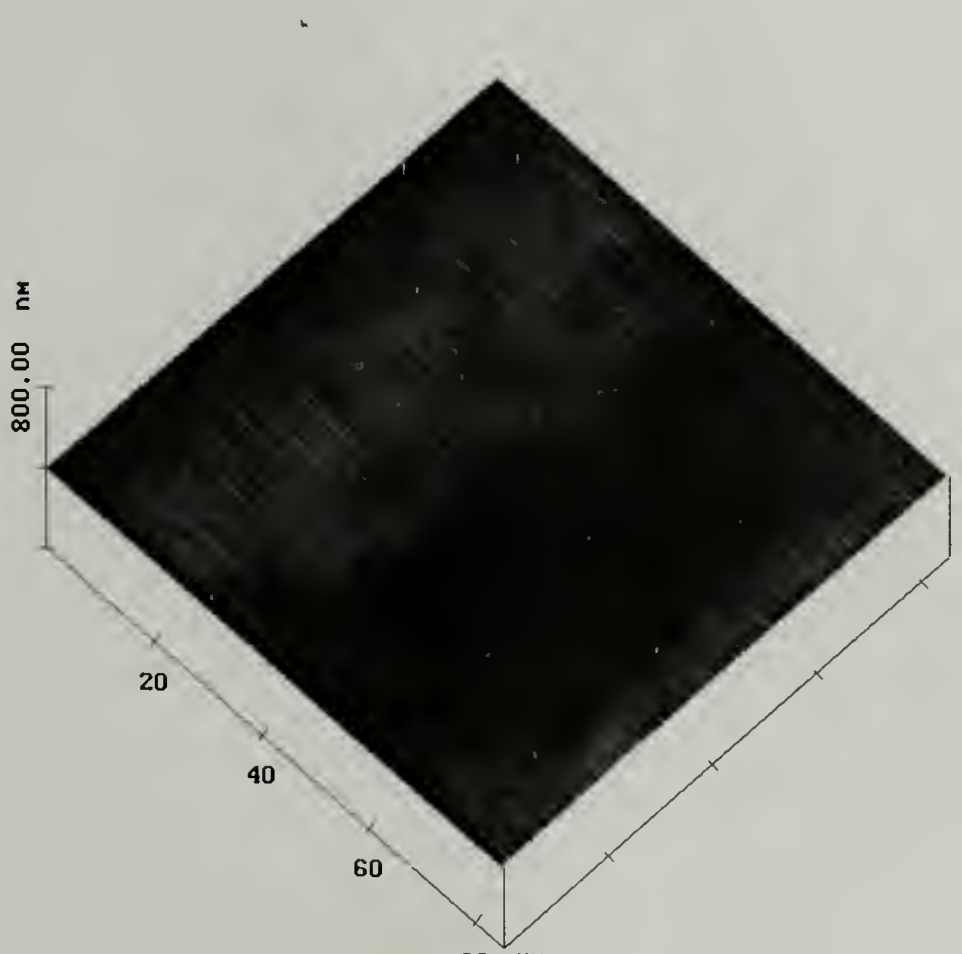

(b)

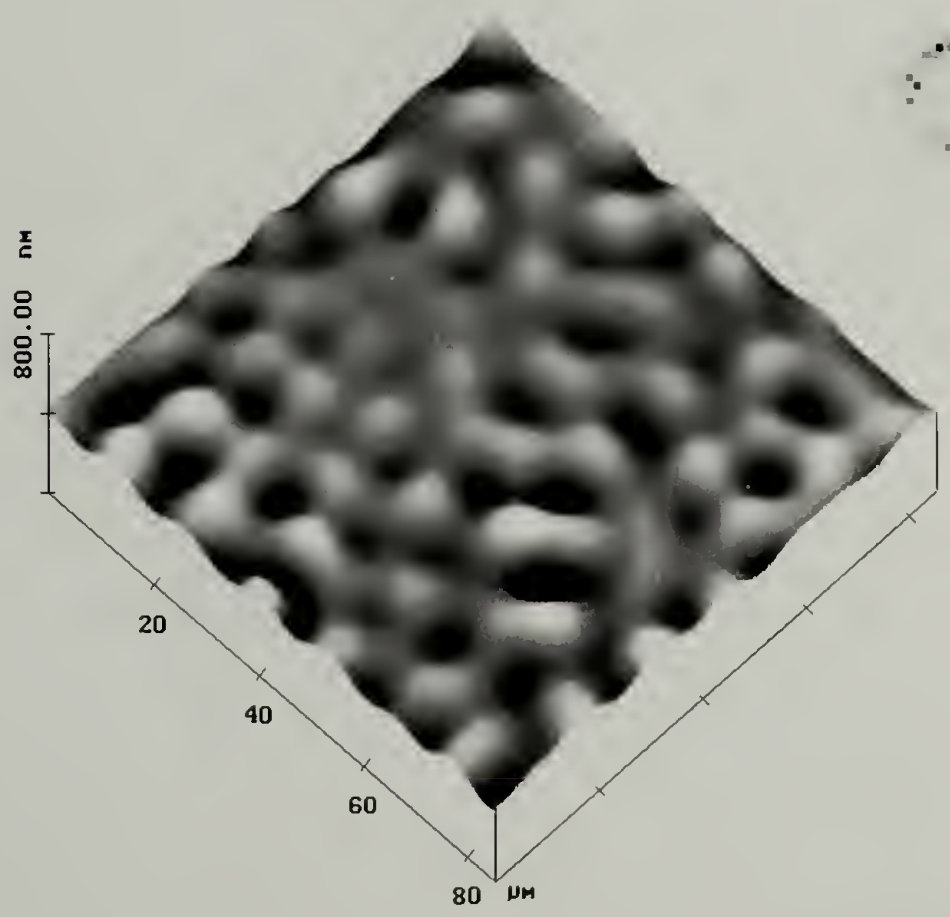

Continued on next page

(c)

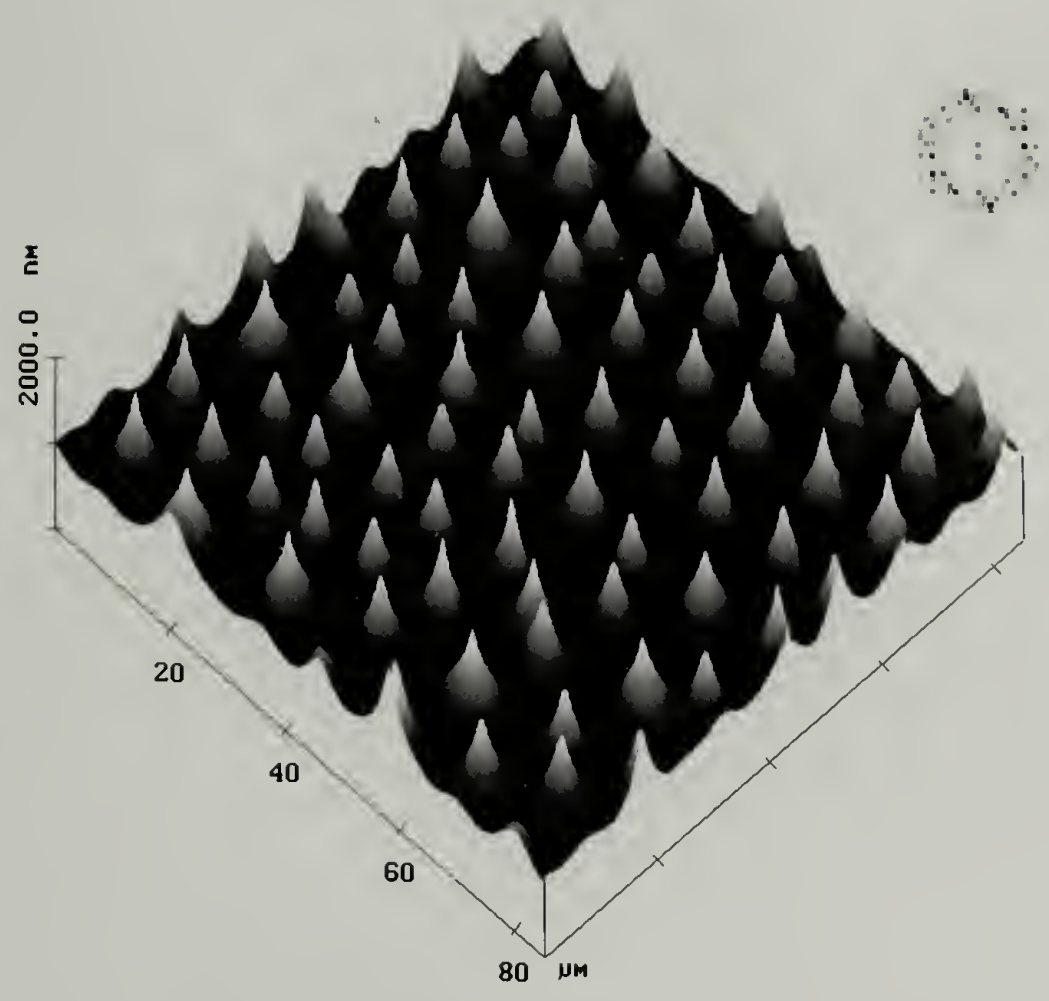

(d)

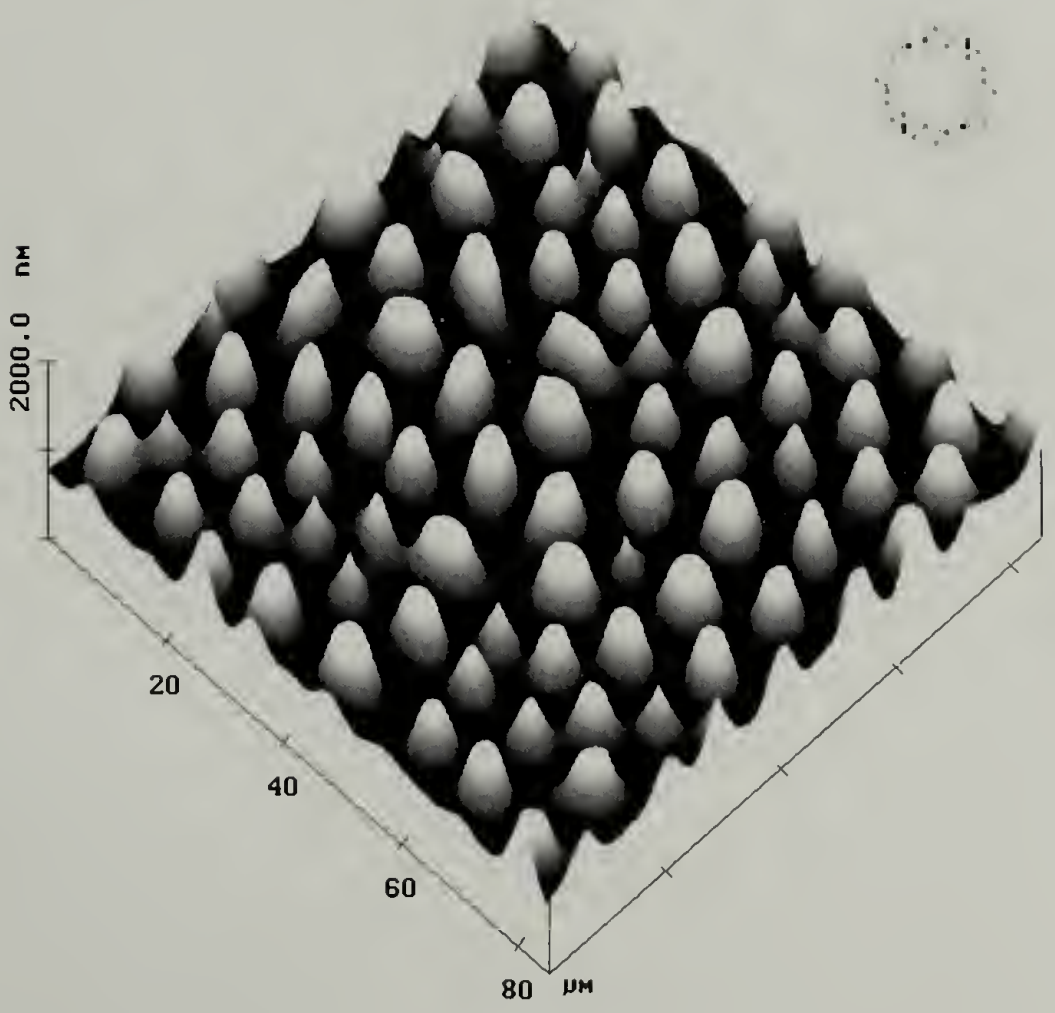

Conclusions

We have extended earlier studies of field-induced structure formation in single layer liquid films to include the more general case of a bilayer. An electric field applied normal to polymer interface was shown to enhance fluctuations which, eventually, led to the growth of columnar structures. Initial experiments show, consistent with an extended model, a reduction of the characteristic length scale of fluctuations at the liquid/liquid interface. However, a marked decrease in the time constant was found in the contrast to the simple model.

A master curve, using no adjustable parameters, was shown to describe the results from a wide range of systems over many orders of magnitude in reduced field strength and distance. The applicability of the linearized theory to describe the lateral length scales of the fluctuations from the early stages of amplification to the formation of columnar structures was shown. Clear routes have been shown by which the size scale of the structures can be manipulated over many lengths scales ranging from the microscopic to the nanoscopic. Calculations also indicate that a further decrease in the size scale is possible by a reduction of interfacial tension between the two media by placing surfactant at the liquid/air interface or adding small amount of copolymer as a "buffer" layer at the liquid/liquid interface.

Our process is quite simple and cheap. If one liquid is conductive polymer, the other one is insulated or semi-conductive polymer, circuits can be produced in a one-step process. We anticipate many applications.

References

1. Schaffer, E., Thurn-Albrecht, T., Russell, T. P. & Steiner, U. Electrically induced structure formation and pattern transfer. *Nature* **403**, 874-877 (2000).

2. Schafer, E., Thurn-Albrecht, T., Russell, T. P. & Steiner, U. Electrohydrodynamic instabilities in polymer films. *Europhysics Letters* **53**, 518-524 (2001).

3. Helfand, E. & Tagami, Y. Theory of the interface between immiscible polymers. II. *J. Chem. Phys.* **56**, 3592-3601 (1972).

4. Helfand, E. & Wasserman, Z. R. Block copolymer theory. 4. narrow interface approximation. *Macromolecules* **9**, 879 (1976).

5. Herminghaus, S. Dynamical Instability of Thin Liquid Films Between Conducting Media. *Phys. Rev. Lett.* **83**, 2359-2361 (1999).

6. Wu, S. *Polymer interface and adhesion* (Marcel Dekker, 1982).

7. Mazur, K. More data about dielectric and electret properties of poly(methyl methacrylate). *J. Phys. D: Appl. Phys.* **30**, 1383-1398 (1997).

8. Derjaguin, B. V., Churaev, N. V. & Muller, V. M. *Surface forces* (Consultants Bureau, New York, 1987).

9. Israelachvili. *Intermolecular and surface forces* (Academic, London, 1992).

10. Vrij, C. *Discuss Faraday Soc.* **42**, 23 (1967).

11. Brochard-Wyart, F. & Daillant, J. Drying of solids wetted by thin liquid films. *Can. J. Phys.* **68**, 1084-1088 (1990).

12. Brochard-Wyart, F., Martin, P. & Redon, C. Liquid/liquid dewetting. *Langmuir* **9**, 3682-3690 (1993).

13. Batchelor, G. K. *An introduction to fluid dynamics* (Cambridge University Press, Cambridge, 1967).

14. Macosko, C. W. *Rheology principles, measurements and applications* (Wiley, New York, 1994).

15. Reiter, G., Khanna, R. & Sharma, A. Enhanced Instability in thin liquid films by improved compatibility. *Physical Review Letters* **85**, 1432 (2000).

16. Onuki, A. Interface instability induced by an electric field in fluids. *Physica A* **217**, 38-52 (1995).

17. Reynolds, J. M. Stability of an electrostatically supproted fluid column. *The Physics of Fluids* **8**, 161-170 (1965).

18. Melcher, J. R. & Smith, C. V. Electrohydrodynamic charge relaxation and interfacial perpendicular-field instàbility. *Phys. Fluids* **12**, 778-790 (1969).

19. Kohler, J., Riess, G. & Banderet, A. *Eur. Polym. J.* **4**, 187 (1968).

20. Anastasiadis, S. H., Gancarz, I. & Koberstein, J. T. Compatabilizing effect of block copolymers added to the polymer/polymer interface. *Macromolecules* **22**, 1449-1453 (1989).

21. Budkowski, A., Klein, J., Steiner, U. & Fetters, L. J. Diblock copolymers attached to homopolymer surfaces and interfaces. *Macromolecules* **26**, 2470-2478 (1993).

22. Lin, Z. Q. et al. Electric field induced instabilities at liquid/liquid interfaces. *Journal of Chemical Physics* **114**, 2377-2381 (2001).

CHAPTER 3

ELECTRIC FIELD INDUCED DEWETTING AT LIQUID / LIQUID INTERFACES

Introduction

The stability and homogeneity of thin films and multilayer structures is of interest both academically and technologically.[1-14] If liquid A dewets a solid substrate B, such as a Si wafer, Young's construction shows that the shape of the dewetting droplet depends on the surface energies of the polymer and substrate and the interfacial energy. If the lower substrate is liquid, such as an amorphous polymer above its glass transition temperature, the interface between liquid A and liquid B will be deformed to minimize the interfacial energy between A and B in accordance with the Neuman construction. If a liquid is spread on a surface it does not wet and the resulting film is metastable, then, with time, dewetting will occur. de Gennes, Brochard and Joanny theoretically investigated the dewetting dynamics at the liquid/liquid interface in great detail.[2,3,5]

Lambooy et al.[10] investigated thin PS films on PMMA as a function of the molecular weight of PMMA at 170°C, and qualitatively compared their experimental results to the Brochard theory.[5] By varying the degree of coupling of the flows in the two layers, deformation at the PMMA/PS was found to decrease with the increasing PMMA molecular weight or viscosity. Qu et al.[11] examined the dewetting of PS on PMMA at 162°C and quantitatively compared their experiments with theory. The dewetting velocity scaled inversely with the PS molecular weight and three growth regimes, as predicted by Brochard et al.,[5] were observed. The earlier theoretical[3,5]

and experimental studies[10,11] indicated that the flow of the dewetting liquid A couples into the substrate layer B due to a non-slip boundary condition at the A/B interface, as schematically shown in Figure 3.1. For a low enough viscosity of the lower liquid layer, the high viscous stresses at the contact line lead to a wave front at the liquid/liquid interface that precedes the dewetting front.

All of these studies focused on systems driven dominantly by differences in the interfacial energies. Electric fields,[15-28] on the other hand, have been shown to be an effective means of overcoming interfacial interactions to produce highly oriented arrays of nanoscopic structures.[20-22] Electric fields also have been used to induce instabilities at the liquid/air surface of a thin film, producing ordered lateral structures.[25-28] The calculations of Schäffer et al.[25,26] indicate that the instability exhibits a well-defined lateral wavelength that follows a power-law dependence on the applied electric field. Experiments on films between parallel capacitor plates with a well-defined air gap showed good agreement with theory.[25,26] Herminghaus theoretically predicted a dynamical instability of a dielectric layer between conductive media[29] and showed that electrostatic pressure can overcome dispersive forces and amplify surface fluctuations. The more general case of a liquid/liquid bilayer confined between two solid electrodes has been discussed by Lin et al.[27,28] In general, the model calculations show a means by which the amplification of fluctuations at an interface can be used to tune the size scale of self-assembled structures from the micron to sub-micron level.

Here, a systematic study on the influence of an applied electric field on two interfaces in a polymer bilayer is discussed. One interface is between the two

polymer layers whereas the second interface is at the air surface. As in the thin film case, the electrostatic pressure generates columns of polymer comprising the upper layer that extend to the upper electrode surface. However, the flow in the upper layer required to generate the columns, coupled with the flow in the underlying liquid, produces a deformation at the polymer/polymer interface. With time, this deformation is expected to increase, drawn upward along the outside of the primary polymer cylinder by the electrostatic pressure. The extent of this deformation was measured as a function of the ratio of the molecular weights of the two polymers and the electric field.

Experimental

Materials

Poly(methyl methacrylate) (PMMA) and polystyrene (PS) were purchased from Polymer Laboratories LTD. The relevant material parameters of the three polymers are given in Table 3.1. Conductive indium-tin-oxide (ITO) microscope slides were purchased from Delta Technologies ($25x50x1.1mm^3$, $R_s \leq 100\Omega$).

Sample preparation

Figure 3.2 shows the sample configuration used in this study. A thin film of PMMA was spin coated onto a freshly cleaned Si substrate. The film thickness was 228 nm for PMMA-95k and 182 nm for PMMA-27k. A thin film of PS-96k was spin coated onto a clean glass slide having a film thickness of 284 nm. The PS film was floated onto a pool of deionized water and transferred onto the PMMA layer to form the PMMA/PS bilayer. This bilayer was then heated to 60°C under vacuum for 2

days to remove residual water and entrapped air. All film thickness were measured with a Rudolph Research AutoEL®-II ellipsometer using a helium-neon laser (λ=632.8 nm) at a 70° incidence angle.

A small air gap, controlled by evaporating silicon oxide rails of a specified thickness onto the ITO microscope slides (the upper electrode), was then used to separate the PMMA/PS bilayer from the ITO glass.[27] Typically, the spacing between the electrodes was not constant, but the samples exhibited a wedge geometry (i.e. the height varied by several μm over a lateral distance of 1cm). After annealing at 170°C under N_2 for one day at various applied voltages, the samples were quenched to room temperature before removal of the applied field. The experimental parameters of the samples used in the experiments are given in Table 3.2.

To examine the polymer/polymer interface, the upper PS layer was removed by washing with cyclohexane for 5h, followed by ultrasonic cleaning in cyclohexane for 30min. Subsequently, the sample was placed in another cyclohexane bath for 5h. Finally, the sample was rinsed with de-ionized water and dried in a vacuum oven at the room temperature.

An experiment was also performed to examine the influence of an applied field on the dewetting velocity and the dynamic contact angle. Here, in situ optical microscopy studies of the PMMA-95k/PS-96k/air system in the absence of an applied field were performed at 170°C. The dewetting of PS-96k on PMMA-95k was allowed to proceed for 24h whereupon 60V was applied for another 24h.

Optical microscopy (OM) studies were performed in reflection mode using an Olympus BX60 microscope. Atomic force microscopy (AFM) studies were done

Table 3.1. Material parameters of the polymer used

Polymer	Molecular weight *Mw* (kDa)	Poly-dispersity (*Mw* / *Mn*)	Dielectric constant[28] ε	Viscosity[a] η (KPa S)	Surface tension γ (mN/m)	Interfacial tension $\gamma_{PMMA-PS}$ (mN/m)
PMMA	27	1.11	5.24	0.3 13	28.9	
PMMA	95	1.04				1.1
PS	96	1.04	2.95	13	27.8	

[a]at 170°C, extrapolated from ref. [30]

with a Digital Instruments D3100 scanning force microscope in the tapping mode. Silicon nitride tips on cantilevers (Nanoprobe^{TM}) with spring constants from 29.3 to 63.9N/m were used.

Results and Discussion

The sample setup of the air /liquid 1 /liquid 2 trilayer is shown in Figure 3.2. Since the two capacitor plates were not parallel, but varied by several μm over a lateral distance of ~1cm, several different instabilities of the liquid 1 layer can be observed on the same sample:

1.For very large electrode spacings, the double film was predominately stable, except for isolated dewetting holes.

Table 3.2. Sample list

Sample number	Polymers	Mw (kDa)	Layer thickness (nm)	Average electrode spacing (μm)	Applied voltage (V)	Shown in Figure
1	PMMA/PS	95/96	228/284 228/284	1.7 1.7	0	4, 5
2	PMMA/PS	95/96			30	3, 5, 6, 7,8
3	PMMA/PS	95/96	228/284	1.7	60	5, 8
4	PMMA/PS	95/96	228/284	1.9	30	8
5	PMMA/PS	95/96	570/284	2.1	60	8 inset
6	PMMA/PS	95/96	570/284	2.5	60	8 inset
7	PMMA/PS	95/96	570/284	2.8	60	8 inset
8	PMMA/PS	27/96	182/284	2.1	0	5
9	PMMA/PS	27/96	182/284	2.1	60	5, 8

2.For intermediate electrode spacings, an undulatory instability of the liquid 1 surface with a characteristic wavelength is observed (see Figure 3.3 (a), bottom left).

3.At small enough electrode spacings, an electrohydrodynamic instability caused the formation of liquid columns. This instability is accompanied by the dewetting

Figure 3.1. Dewetting at the liquid-liquid interface. A flow of the dewetting liquid A couples viscously to the substrate layer B at the A/B interface.

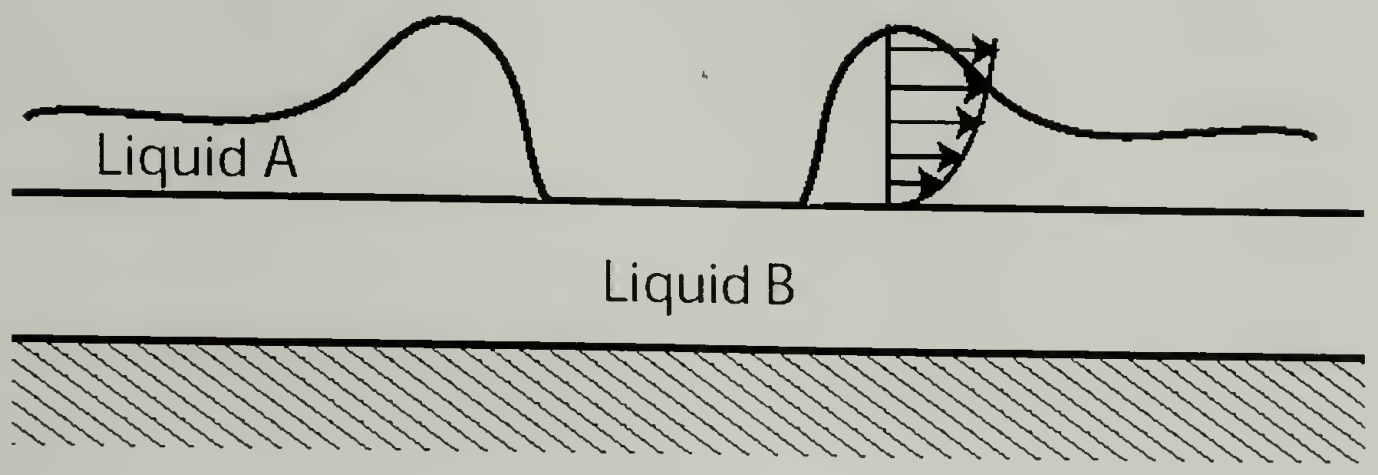

Figure 3.2. Typical sample configuration in this study. The air / Polystyrene(PS) / Poly(methyl methacrylate) (PMMA) system was sandwiched between a highly polished and doped silicon wafer (lower electrode) and an ITO microscope slide (upper electrode). The distance between the two electrodes was controlled by evaporating SiO_x as a spacer (at the edges of the slides on top of the ITO). Typically, the electrode spacing varied by a few micrometers over a lateral distance of approx. 1 cm. The structure formations of the system under an applied electric field (0V, 30 V and 60 V) was studied by optical microscopy in the reflectance mode. After removal of the top electrode, the sample was imaged by atomic force microscopy.

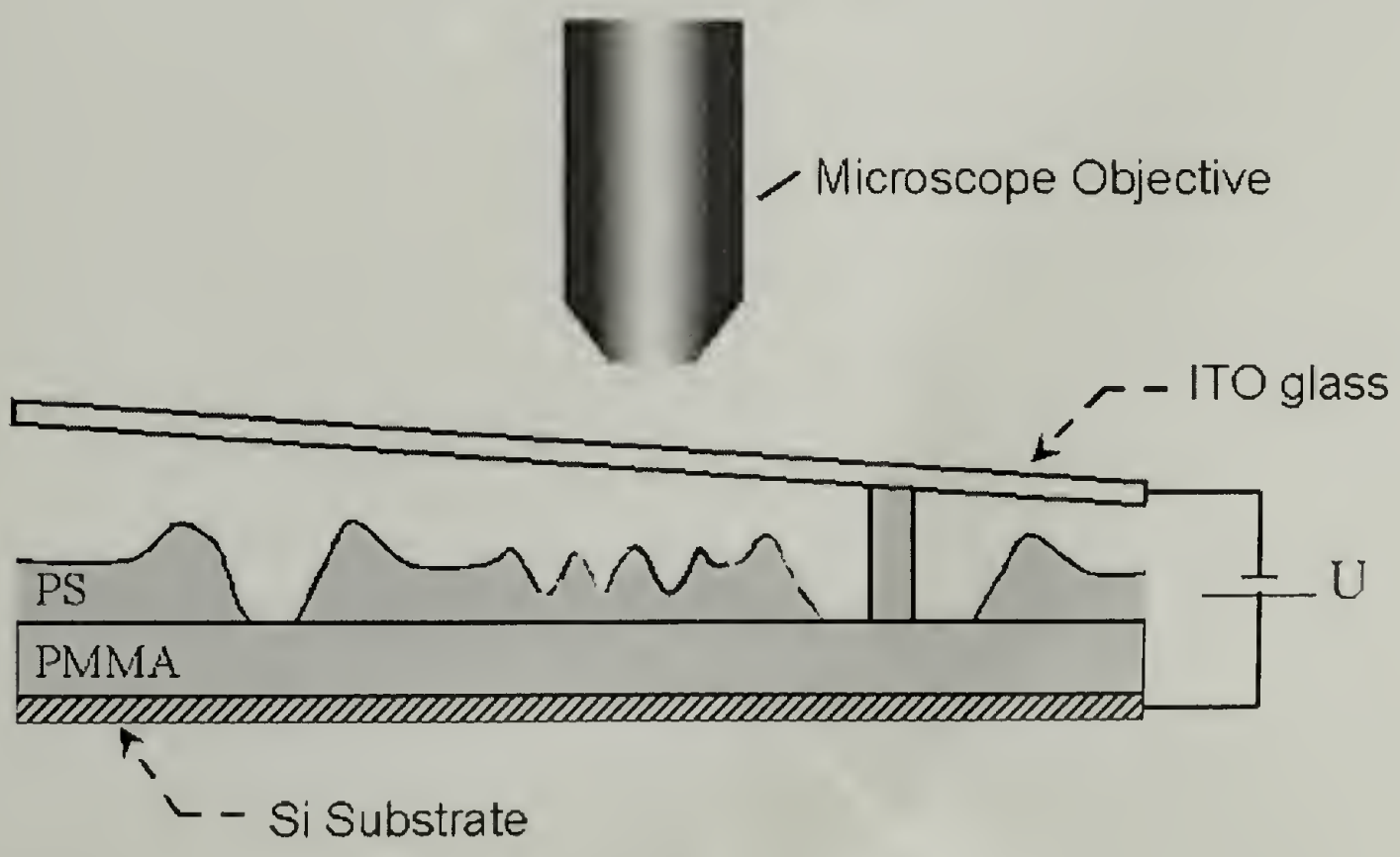

of the liquid 1 on top of liquid 2. Both, the nucleated and spinodal instabilities are observed (see Figure 3.3 (a) center and top right, respectively).

A summary of the experiments performed in this study is given in Table 3.2. We start with large capacitor spacings and sequentially discuss the experimentally found morphologies as the electric field is increased. Rather than carrying out a time series with a constant applied field (which limits us to an optical investigation of the sample only), the use of a wedge geometry is an alternative way to observe (in a quasi static manner) the way how the instability forms with time, since the onset of the instability scales with the sixth power of the electric field in the polymer film.[26]

Dewetting at the Liquid/Liquid Interface at Low Electric Field

For large plate spacings (Figure 3.2 left), the influence of external electric fields on the characteristics of the dewetting was investigated. A constant potential was applied between the Si wafer and the ITO glass slide, as schematically shown in Figure 3.2. Subsequently, the samples were annealed as dewetting and growth of the holes occurred. Two different PMMA/PS bilayers were used and two different voltages were applied, corresponding to samples 2, 3, and 9 in Table 3.2. As a reference, identical samples were annealed in the absence of an applied potential (samples 1 and 8).

The optical micrograph in Figure 3.4 (a) shows two dewetting holes in a thin liquid layer of PS-96k on top of PMMA-95k (sample 1) that are impinging onto one another. With time, the diameters of the isolated holes increase, driven by the imbalance of the interfacial and surface energies. The influence of flow in the upper

Figure 3.3. (a) An optical microscopic image of sample 2 (30 V) in the configuration shown in Figure 2. The image size was 212x212μm^2. (b) The corresponding 3D AFM image shows the columns of PS-96k on top of a PMMA-95k layer.

(a)

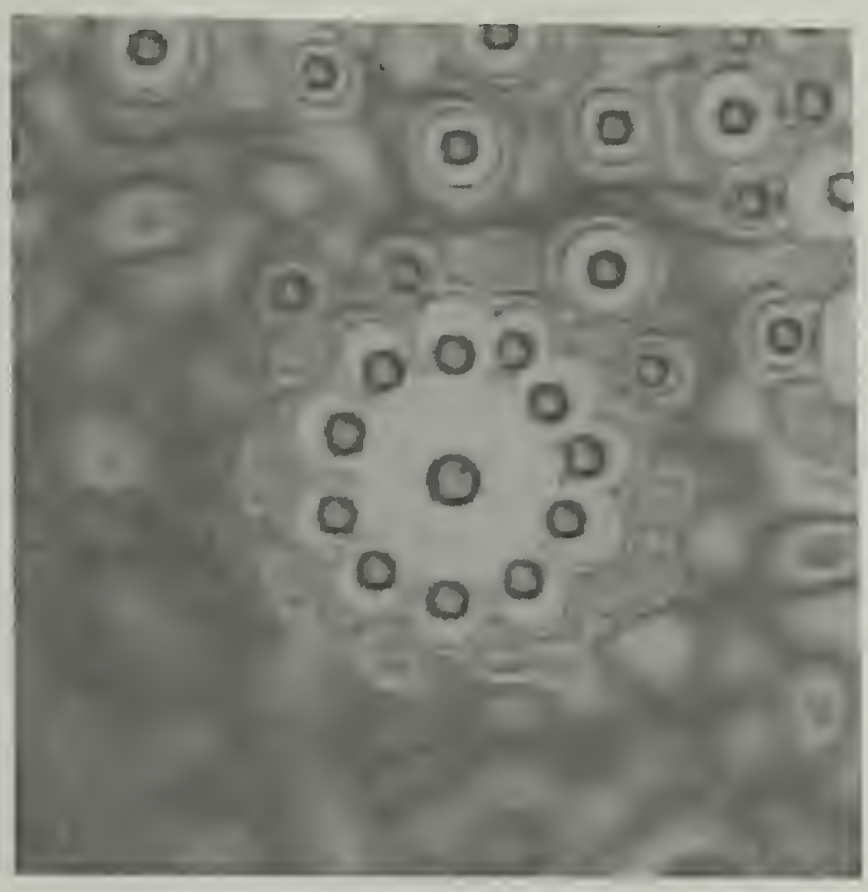

(b)

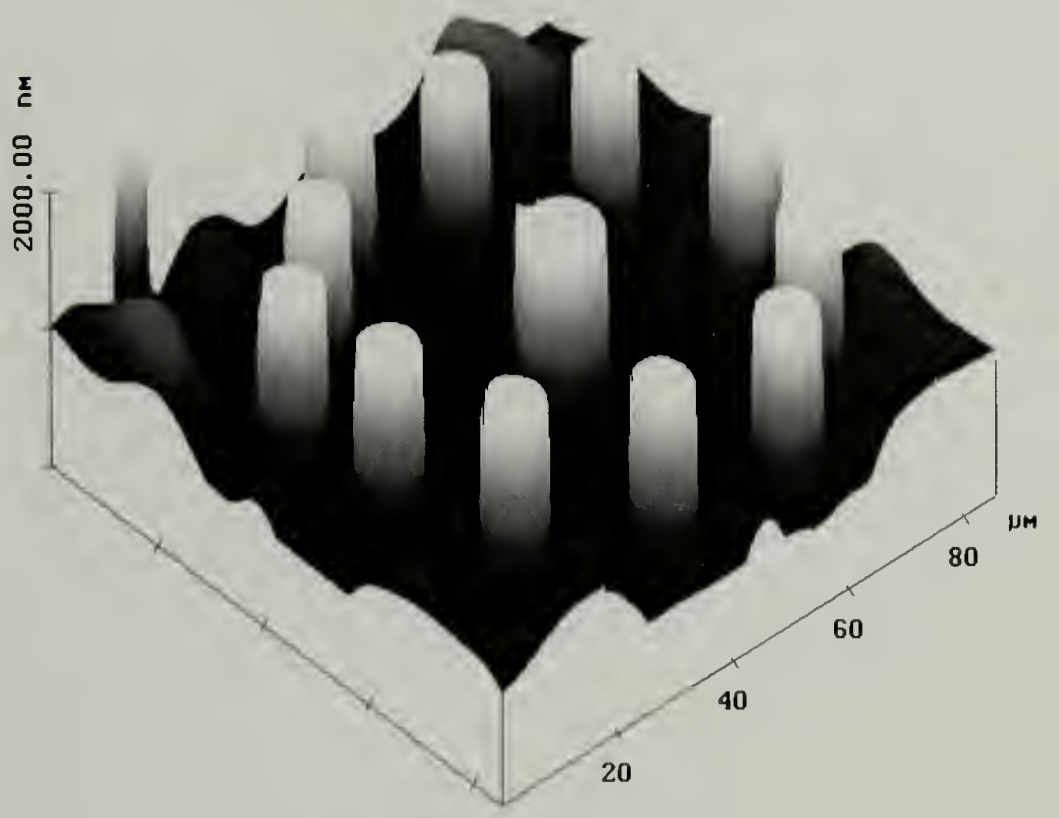

PS layer during dewetting on the lower PMMA layer can be examined by removing the PS layer with cyclohexane, a selective solvent for PS. The inset to the left in Figure 3.4 (b) shows a tapping mode atomic force microscopy (AFM) image of the sample before removal of PS, whereas the inset on the right shows the same area after removal of the PS with cyclohexane. Superposed line scans of these images are shown in Figure 3.4 (b). Deformation of the PMMA/PS interface is evident in the vicinity of the 3-phase contact line.

Following the procedure by Lambooy et al.,[10] the extent of the deformation can be characterized by the height h, i.e. peak to baseline distance, and full width at half maximum (FWHM). Figure 3.5 shows the variation of h and FWHM as a function of the ratio of the molecular weights of the two polymers. Both h and FWHM increase with an increase in the ratio of the molecular weights. Thus, the coupling of the flows in the two layers increases with a greater mismatch in the molecular weight of PMMA and PS. A comparison of the data in Figure 3.5 to that obtained by Lambooy et al.,[10] who studied the characteristics of dewetting for the same system, shows reasonable agreement for the functional dependency of the height. However, differences are seen in the full width at half maximum (FWHM). While the general trend is the same, the data obtained by Lambooy et al.[10] are consistently lower than the data obtained in this study. This difference arises mainly from the greater thickness of the PMMA layers used in this study (182 nm, 228 nm) as compared to 95nm used by Lambooy et al.[10,31]

A comparison in Figure 3.5 of data obtained in the presence or absence of an electric field show no systematic deviations. For this early stage of dewetting (i.e. for

rim heights that are much smaller than the electrode spacing), no time dependence of either the dewetting velocity or the contact angle was observed by in situ optical microscopy. This was confirmed by a control experiment, where the sample was first annealed for 24h at 160°C in the absence of an electric field, with subsequent annealing for 24h with 60 V applied. This is in contrast to electrowetting experiments,[32,33] where drop spreading is strongly modified by the electric field. The difference is due to the different electrostatic boundary conditions (a parallel plate capacitor geometry as opposed to a charged conducting liquid on a planar substrate), combined with a small value of the contact angle of the dewetting rim (~2.5°).

More quantitatively, we can estimate the relative strength of the electrostatic force acting at the dewetting rim. The electrostatic pressure at the interface, which operates against the Laplace pressure and viscous forces can be obtained by taking the derivative of free energy stored in this capacitor system.[25-29] It is given as

$$p_{el,PS/air} = -\frac{U^2}{A}\frac{dC}{dh_{PS}} = \frac{U^2 \varepsilon_{air}\varepsilon_{PS}\varepsilon_{PMMA}\varepsilon_0}{K^2}\varepsilon_{PMMA}(-\varepsilon_{PS}+\varepsilon_{air}) \quad (1)$$

where $K = \varepsilon_{PS}\varepsilon_{PMMA}(d - h_{PS} - h_{PMMA}) + \varepsilon_{air}\varepsilon_{PMMA}h_{PS} + \varepsilon_{air}\varepsilon_{PS}h_{PMMA})$, and U, ε_0, ε_{air}, ε_{PS}, ε_{PMMA} are the applied voltage, the permitivity in vacuum, the dielectric constants of air, PS, and PMMA respectively. d, h_{PS} and h_{PMMA} are the separation distance between the two electrodes, the film thickness of PS and PMMA respectively.

This has to be compared with the capillary force per unit length that favors dewetting

$$F_{cap} = \frac{1}{2}\gamma_{PS}(\theta_e^2 - \theta^2) \quad (2)$$

Figure 3.4. (a) A typical optical micrograph of an intermediate stage of the dewetting process of a thin liquid layer of PS-96k on top of a liquid PMMA-95k substrate (sample 1). (b). A section analysis of AFM images of the dewetting process without an applied electric field. The dotted and the solid curves corresponded to AFM scans before and after removing the PS by rinsing the sample with the selective solvent cyclohexane. Insets are AFM height images before and after removal of the PS layer (left and right).

(a)

(b)

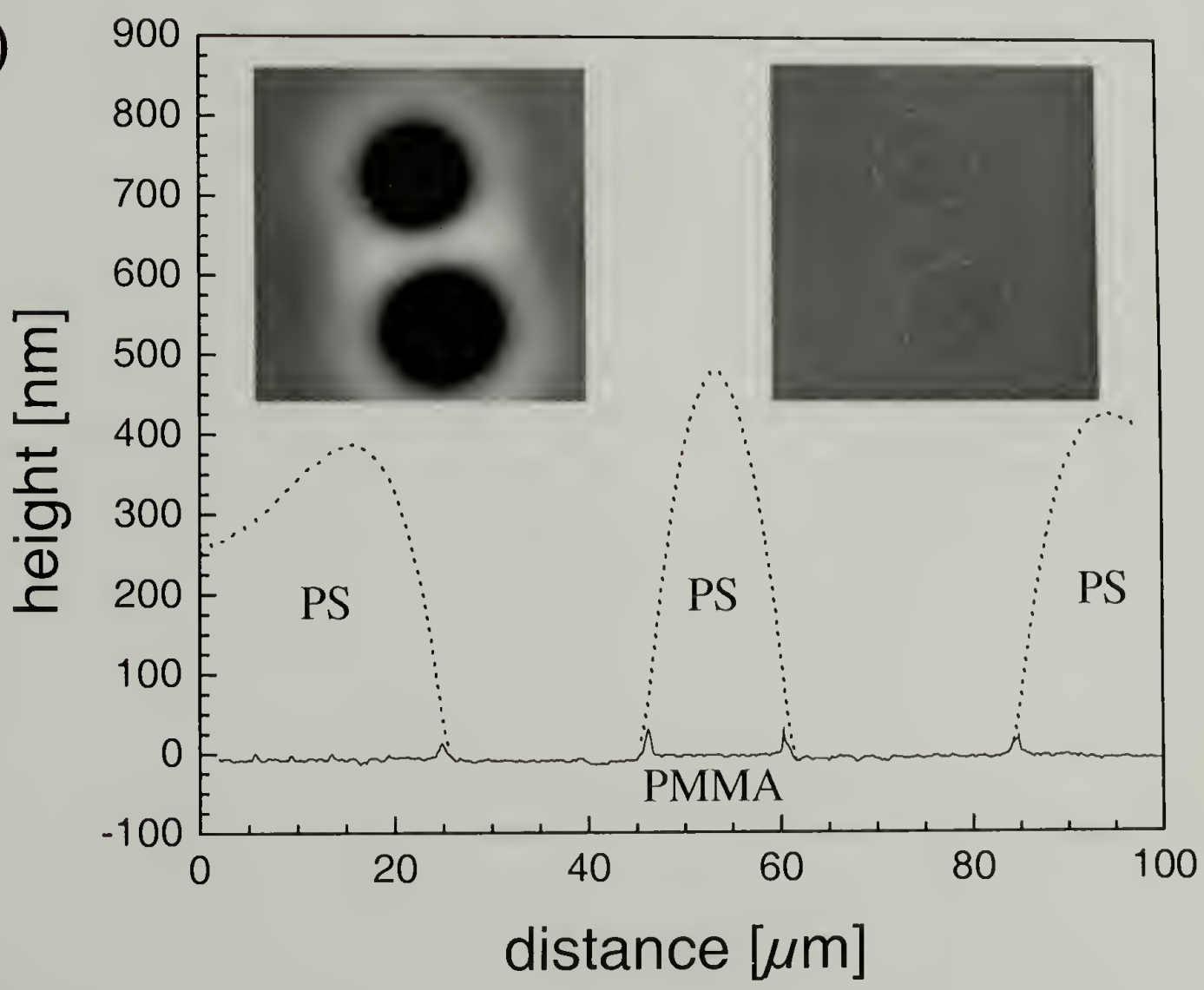

Figure 3.5. Height (peak to baseline distance) and full width at half maximum (FWHM) (inset) of the PMMA layer deformation at the PMMA/PS contact line, as a function of the ratio of the molecular weights of the two polymeric liquids. The black squares are the data obtained by analyzing the published measurements of Lambooy et al.[10] The triangle corresponds to sample 2 with 30 V applied. The inverted triangles were obtained with an applied voltage of 60 V (samples 3 and 9). The circles stem from samples with no applied field (samples 1 and 8).

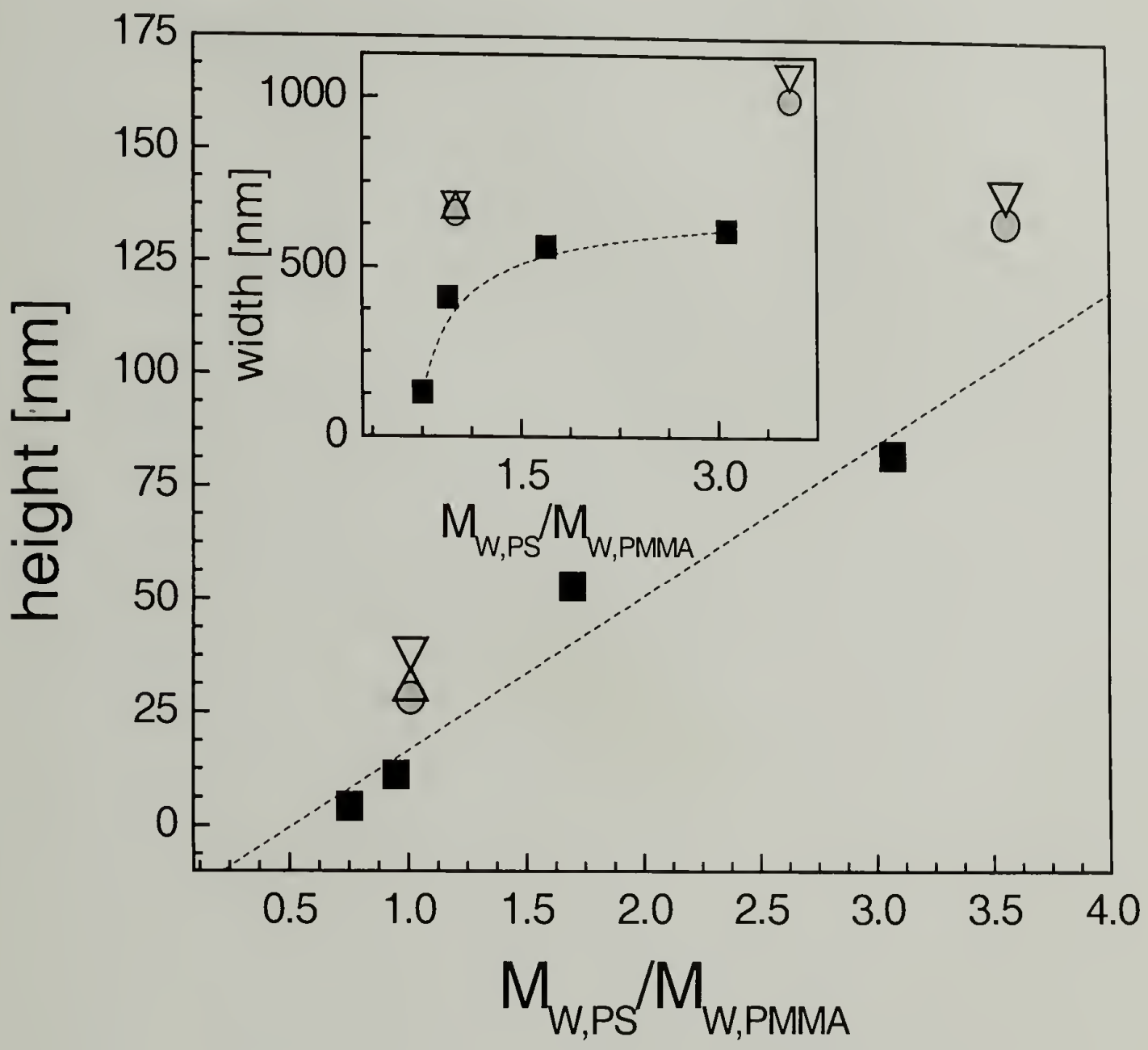

θ is the dynamic contact angle and θ_e is the equilibrium contact angle as obtained from Young's equation $\gamma_{PS}\cos(\theta_e) + \gamma_{PS/PMMA} = \gamma_{PMMA}$ with γ_{PS}, γ_{PMMA} the PS and PMMA surface tensions, and $\gamma_{PS/PMMA}$ the PMMA/PS interfacial tension. The viscous force that retards dewetting is given by

$$F_{visc} \sim \eta_{PS}\frac{v_d}{\theta} = \gamma_{PS}\theta^2 \qquad (3)$$

where we have used the relation for the dewetting velocity v_d given by Tanner's law:[1] $v_d \sim \gamma_{PS}\theta^3/\eta_{PS}$, with η_{PS} the viscosity of PS.

With a dynamic contact angle of $\theta \approx 2.5°$ determined from Figure 3.4 and $\theta_e \approx 5°$, we find from eq 2 $F_{cap} \approx 2.4\cdot10^{-1}$ N/m. The retarding viscous force is (eq 3) $F_{visc} \sim 1\cdot10^{-1}$N/m. The electrostatic force per unit length is obtained by integrating eq 1 over the cross-section of the PS rim. $F_{el,PS/air} \approx \int P_{el,PS/air}\, dh_{PS} \sim 1\cdot10^{-1}$ N/m. All three forces are comparable and determine the spreading kinetics in the parameter regime of Figure 3.3. As opposed to the other two terms, $F_{el,PS/air}$ exhibits a strong variation with d (~ 1/d) and falls off rapidly for $h_{PS} + h_{PMMA} << d$. This explains the morphology of the PS layer in Figure 3.3, which shows the cross-over, where $F_{el,PS/air}$ becomes dominant. Due to the strongly non-linear d dependence, $F_{el,PS/air}$ plays only a negligible role in the dewetting of PS on PMMA and modifies neither the contact angle nor the dewetting kinetics, if d is larger than a critical value. If, on the other hand, d is smaller than this critical value, it dominates the force balance and columns are formed by the rapid acceleration of PS towards the top electrode. Figure 3.3 shows a stage in the PS dewetting, where the PS rim height has grown to 400 nm. At this specific stage, the cross-over value of d lies at ~1.7 μm.

Electrohydrodynamic Interfacial Instabilities

For a decreased plate spacing, corresponding to an increased field in the three layers, the electrostatic pressure at the liquid-air surface is strong enough to destabilize the film surface for the experimental conditions (temperature, annealing time) used here. Similar to the polymer-air bilayer system,[25,26] an undulation with a characteristic wavelength is observed.

The influence of the growth of surface fluctuations and column formation in the upper PS layer on the underlying PMMA layer can be seen by selective removal of the PS layer with cyclohexane. Shown in Figure 3.6 (a) is an AFM image of the PS surface at an early stage of the growth of fluctuations. A line scan of the surface is shown in Figure 3.6 (b) where substantial growth in the surface fluctuations is evident with a characteristic period of ~35 μm and an amplitude of ~0.1 μm. However, after removing the PS layer with cyclohexane, a line scan of the PMMA surface, corresponding to the interface between the PS and PMMA, is featureless. Consequently, the PS/air interface deforms much more readily than the PMMA/PS interface.

Qualitatively, the PS/air surface is expected to deform much more readily than the PMMA/PS interface, since the dielectric contrast between PS and air is much larger compared to the PMMA/PS interface and the viscous damping for the deformation of a free surface is much lower than of a polymer-polymer interface. On the other hand, the PS/PMMA interfacial tension is lower, facilitating interfacial deformation.[27] In the presence of an electric field, both interfaces are expected to become unstable. To obtain more quantitative information on the instabilities of the

two interfaces, it is instructive to compare the characteristic times at which the instabilities occur. For the PS/air interface, we have the dispersion relation for the mode spectrum[26] q

$$\frac{1}{\tau_{PS/air}} = -\frac{h_{PS}^3}{3\eta_{PS}}(\gamma_{PS/air}q^4 + \frac{\partial p_{el,PS/air}}{\partial h_{PS}}q^2) \qquad (4)$$

For the PMMA/PS interface, the equivalent relation is[27]

$$\frac{1}{\tau_{PS/PMMA}} = -\frac{(h_{PS}h_{PMMA})^{3/2}}{3C(\eta)}(\gamma_{PMMA/PS}q^4 + \frac{\partial P_{el,PS/PMMA}}{\partial h_{PMMA}}q^2) \qquad (5)$$

$C(\eta)$ is a function of the viscosities and film thicknesses of the PS and PMMA layers.[27] In the limit $\eta_{PMMA} \approx \eta_{PS}$ and $h_{PS} \approx h_{PMMA}$, $C(\eta) \approx 8\eta_{PS}$. The electrostatic pressure acting at the PS surface is given by eq 1. Similarly, the pressure at the PMMA/PS interface can be given as

$$P_{el,PS/PMMA} = -\frac{U^2}{A}\frac{dC}{dh_{PMMA}} = \frac{U^2\varepsilon_{air}\varepsilon_{PS}\varepsilon_{PMMA}\varepsilon_0}{K^2}\varepsilon_{air}(-\varepsilon_{PMMA} + \varepsilon_{PS}) \qquad (6)$$

where K is the same as in eq 1.

Maximizing $1/\tau$ in eqs 4 and 5 with respect to q yields the most unstable mode and the maximal growth rates.[26,27] Using the experimental parameters from Tables 1 and 2, we have $\tau_{PS/air} \approx 6$ h, as found in Figure 3.6 and $\tau_{PS/PMMA} \approx 16$ days. Note that eq 5 assumes a non-slip boundary condition at the PMMA/PS interface. Perfect slip at the PMMA/PS boundary reduces $\tau_{PMMA/PS}$ by almost a factor of 8 ($C(\eta) \approx \eta_{PS}$). For both boundary conditions, however, $\tau_{PS/air}$ is considerably smaller than $\tau_{PMMA/PS}$. The instability of the polymer-air interface is therefore expected to

Figure 3.6. (a) A typical AFM image of the early stages of the instability, corresponding to Figure 3.3 bottom left (sample 2, 30 V). The section analysis of the image before and after removal of the upper PS layer by cyclohexane are given in (b) and (c), respectively.

(a)

(b)

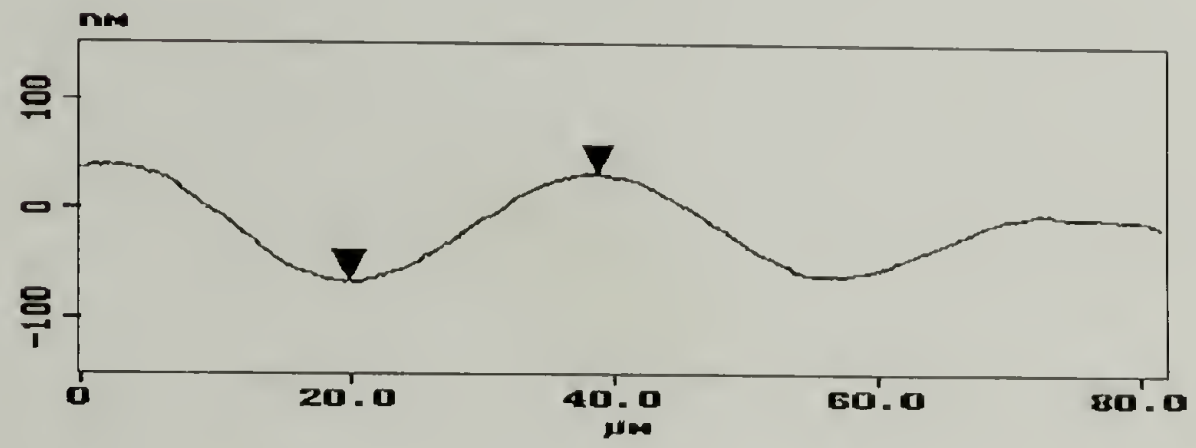

(c)

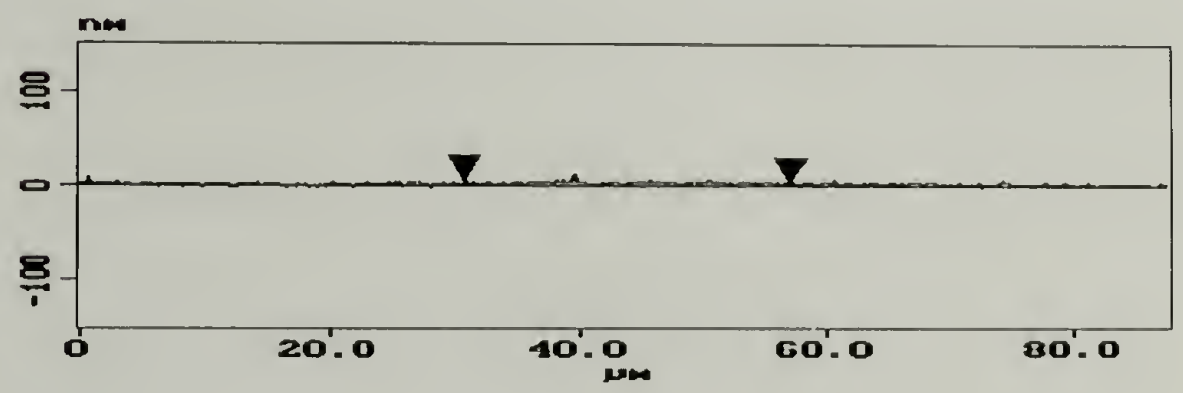

preempt the instability at the polymer-polymer interface, in agreement with our experimental observations.

We now turn our attention to the lack of hydrodynamic deformation of the PMMA/PS interface. In an earlier paper,[27] we investigated the electrohydrodynamic instability of liquid polymer/polymer interfaces. There, we assumed the hydrodynamic flow profiles in the two polymers were viscously coupled. Here, in the case of polymers with comparable viscosities, this implies a Poiseulle-type flow profile extending from the solid substrate to the air interface, which is nearly continuous at the polymer-polymer interface. In such a model, the polymer-polymer interface is expected to mirror the undulations of the PS/air surface. In contrast, the results in Figure 6 show an undeformed PMMA layer. Since PMMA is liquid and cannot sustain a shear stress, our experimental observations are direct evidence for interfacial slip at the polymer-polymer interface.

Interfacial slip between two polymers is not unusual. Due to their incompatibility, the interfacial interpenetration of PS and PMMA is ~5 nm.[34] In particular, PS and PMMA chains are not expected to be entangled at the interface. In addition, liquid surfaces are more homogeneous compared to solid substrates, both in terms of their chemical composition and surface roughness. Slip at a polymer interface was previously reported by Reiter and Khanna.[35] In a very recent study, Wang et al.[31] found evidence for slippage when studying the dewetting of PS on PMMA. Slippage could also explain the accelerated electrohydrodynamic instability of polymer-polymer interfaces in our earlier study.[27]

Electric Field Induced Structure Formation

For even smaller values of the electrode spacing (Figure 3.2 right) the amplification of surface waves discussed in the previous paragraph led to the formation of PS columns that spanned from the surface of the PMMA film to the top electrode. Evidence for both nucleated and spinodal instabilities were found. In the upper right hand section of Figure 3a, columns of PS are evident that are surrounded by a dewetting zone that propagates away from the columns. The structure in the center of the micrograph consists of an initial column (primary cylinder) that was heterogeneously nucleated early in the experiment. As the dewetting rim grew in size and height, fluctuations with a characteristic spacing were amplified and grew into regularly spaced columns (secondary cylinders). Each secondary column was then surrounded by its own dewetting zone. As discussed above there is no influence of the electric field on the interfacial structure at the dewetting front. However, as PS dewets the PMMA, PS accumulates in the dewetting rim, changing the position of the PS/air interface locally. This creates an instability along the rim which, in turn leads to the formation of secondary cylinders. An AFM image of the structure in the center of the optical micrograph is shown in Figure 3.3 (b). This image more clearly shows the columnar shape of these features that are ~1.5 μm in height with a diameter of ~10 μm. It should be noted that the central column is much larger than the column formed on the dewetting rim. Similar to the nucleated instability, the columns formed by a spinodal process (Figure 3.3 top right) are each surrounded by a dewetting zone.

These findings are reminiscent of the electric field induced structures formed with a single polymer film on a solid substrate,[25] with two main differences. First, the dewetting around the PS columns on the PMMA film is much more pronounced compared to the structure formation of PS on a silicon substrate.[25] Second, the PMMA surface, which plays the role of the substrate here, is significantly deformed at the PS-PMMA-air contact line. The greater amount of dewetting is presumably due to the higher negative spreading coefficient for PS on PMMA, compared to a silicon wafer, PS wets clean silicon wafers (with a native oxide layer) but only partially wets PMMA.

The dewetting of a liquid on a liquid substrate results in the deformation of the contact line, since the liquid substrate cannot sustain the high shear stresses that build-up at the contact line. In addition, the electrostatic forces cause a secondary instability at the PMMA-air surface that is revealed once the PS columns have formed. To analyze the deformation of the liquid/liquid interface caused by the flow into the primary cylinders, the line scans of PS/air and PMMA/PS interfaces, after removal of the upper PS layer, were overlaid. Shown in the inset of Figure 3.7 is an AFM image of the PS surface. Here, the initial column formed is in the center, surrounded by a ring of columns formed on the dewetting rim. The dashed line in the data shows a line scan across the primary cylinder. The height of the column is ~1.5 μm with a diameter of ~10μm. After removal of the PS layer by rinsing with cyclohexane, the line scan shown by the solid line was obtained. The two scans were overlaid by normalizing the height at the exposed PMMA layer surrounding the

column. Salient features of these data are the three phase contact line located ~10 μm around the column, the dewetting rim and the deformation of PMMA/PS interface induced by the formation of the column. Surrounding the column is a depression of the PMMA underlayer due to the coupling of flow between the two layers. At the edges of the columns, the underlying PMMA layer is substantially deformed. The extent of this deformation is a direct consequence of the flow of the PS into columns that couples into the underlying PMMA through the interface. In the case shown, this underlying rim at the PS and PMMA interface is ~400 nm in height. The magnitude of the deformation at this buried interface was found to depend on the ratio of the molecular weight of the PS and PMMA.

Shown in Figure 3.8 is the height of the deformation of the primary cylinder at the PMMA/PS interface under the PS columns as a function of the ratio of PS and PMMA molecular weights. Shown also in this plot are the data of Lambooy et al.[10] obtained by dewetting PS on PMMA in the absence of an applied field. As seen, as this ratio increase or as the mobility of PMMA increases in comparison to that of PS, the extent of deformation at the PMMA/PS interface increases. In addition, for a given ratio of molecular weights, as the applied field strength increases by increasing the applied voltage while keeping the separation distance, d, between two electrode fixed, or by decreasing d while keeping the applied voltage fixed (inset in Figure 3.8), the magnitude of the deformation increases.

Since the time constants for either the PMMA/PS interface or the exposed PMMA surface to become unstable are much larger compared to the initial

Figure 3.7. Deformation of the PMMA-95k/PS-96k interface (sample 2 with 30 V applied) caused by the flow of PS into the primary cylinder. The main graph shows superposed line scans of the PS/air (dotted line) and PMMA/PS (full line) interfaces. The inset is the corresponding AFM height image.

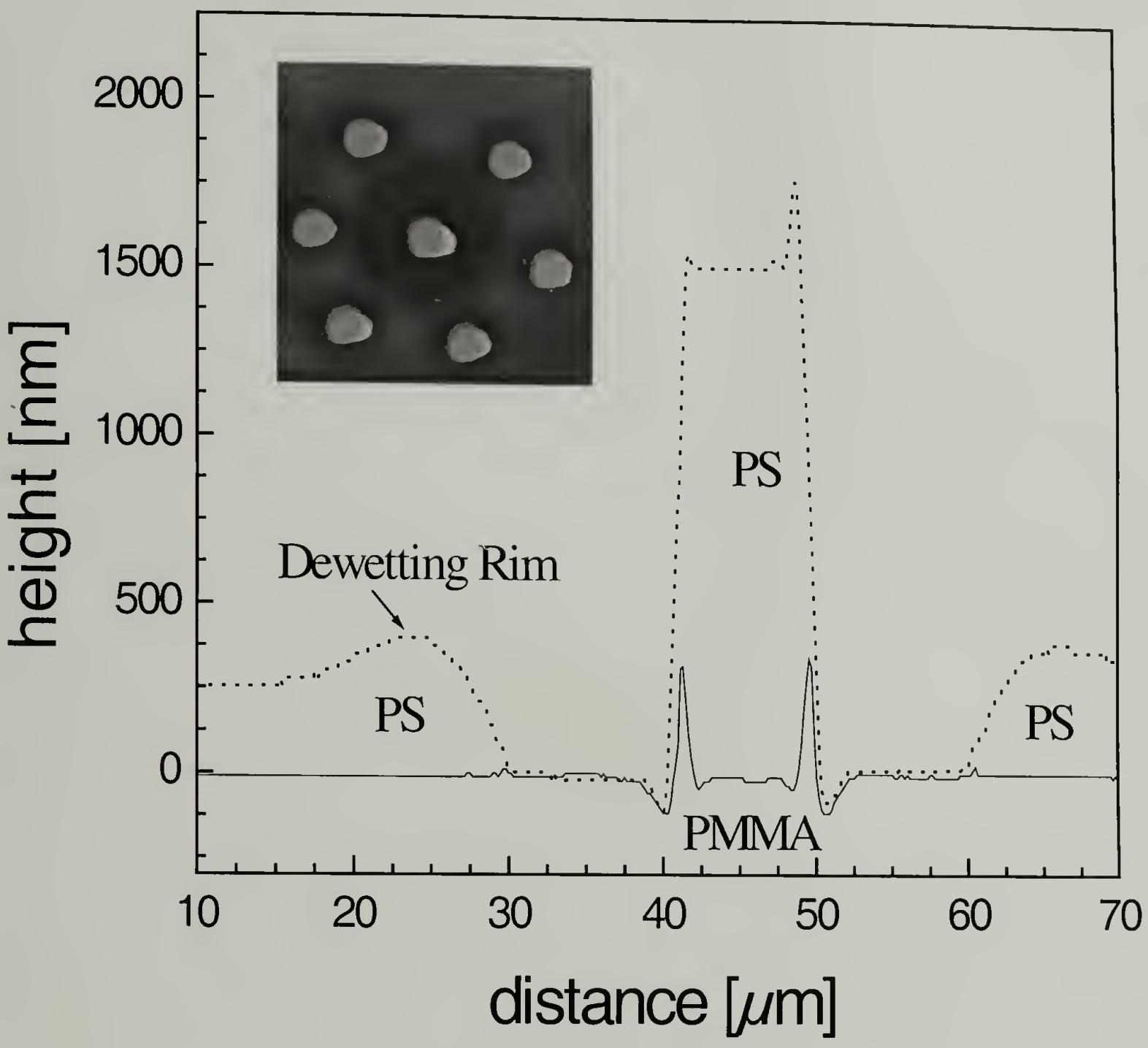

instability of the PS surface, the contact line deformation of the PMMA under the cylinders is a secondary process that builds up once the PS columns have formed. It is due to two effects. Initially, it is caused by the hydrodynamic deformation of the PMMA/PS/air contact line, similar to the generic dewetting process of Figure 3.5. While regular dewetting proceeds at a constant and slow speed (or as a weak power-law, in the case of a slip boundary condition[35]), the electrohydrodynamic instability proceeds much more rapidly. The initial undulations seen in Figure 3.3 (bottom-left) are exponentially amplified, leading to a very rapid formation of the columns.[27] This leads to a fast motion of the contact line and, therefore, to a much higher viscous stress concentration there. As a consequence, the liquid PMMA substrate is deformed to a much greater extent than in standard dewetting, as is observed here. This can be seen in the cross-sectional scan in Figure 3.7, where clearly more PS has been displaced into the electrohydrodynamically formed PS column than into the dewetted PS rims. Once the primary PS columns have formed, (and along with it the PMMA contact line deformation), a secondary electrohydrodynamic instability sets in. The electrostatic forces that act on the PMMA-air surface are much larger than those on the PMMA/PS interface. They are maximal at the location of the PMMA/PS contact line, where the local PMMA film height is largest. With time, the PMMA can be drawn up on the outside of the PS columns forming annuli around the existing PS columns with a suitable field strength and combination of viscosities of PS and PMMA.

Other Observations

While the formation of polymer columns in the trilayer can induce the dewetting rim and change the film thickness locally, the nucleation effect can induce a hole formation of the upper liquid 1 on the underlying liquid 2 surface through the dewetting process. As time progresses, the undulations around the dewetting rim are amplified and break up into the columns. A typical example is shown in Figure 3.9, where the central column, which is seen in Figures 3.3 and 3.7, is missing.

If the dwetting continues, a successive bands of columns would be formed under strong influence of electrostatic force until the fronts from two different nucleation sites impinged to form a ring as can be identified from the wiggly shapes of the rings. Figure 3.10 shows the formation of concentrated rings at the PMMA surface in the air/PMMA/PS trilayer with 50 V applied.

If the two electrodes are not parallel, distortions in the generations of the columns will occur. This can give rise to unusual patterns as evidence by the map of Cape Cod, shown in Figure 3.11, observed in one experiment.

Figure 3.8. Deformation of height under the dewetting rim as a function of the ratio of the molecular weights of the PS and PMMA from Lambooy et al.[11] (black squares) and our experiments (gray area). The triangles are the deformations observed for the PMMA-95k/PS-96k system with 30 V applied (▲: sample 2, Δ: sample 4) and the inverted triangles were obtained with 60 V applied for PMMA-95k/PS-96k (sample 3) and PMMA-27k/PS-96k (sample 9). The inset shows the deformation of height as a function of separation distance of the electrodes, *d*, for the PMMA-95k/PS-96k bilayer at 60 V applied field (samples 5, 6, 7).

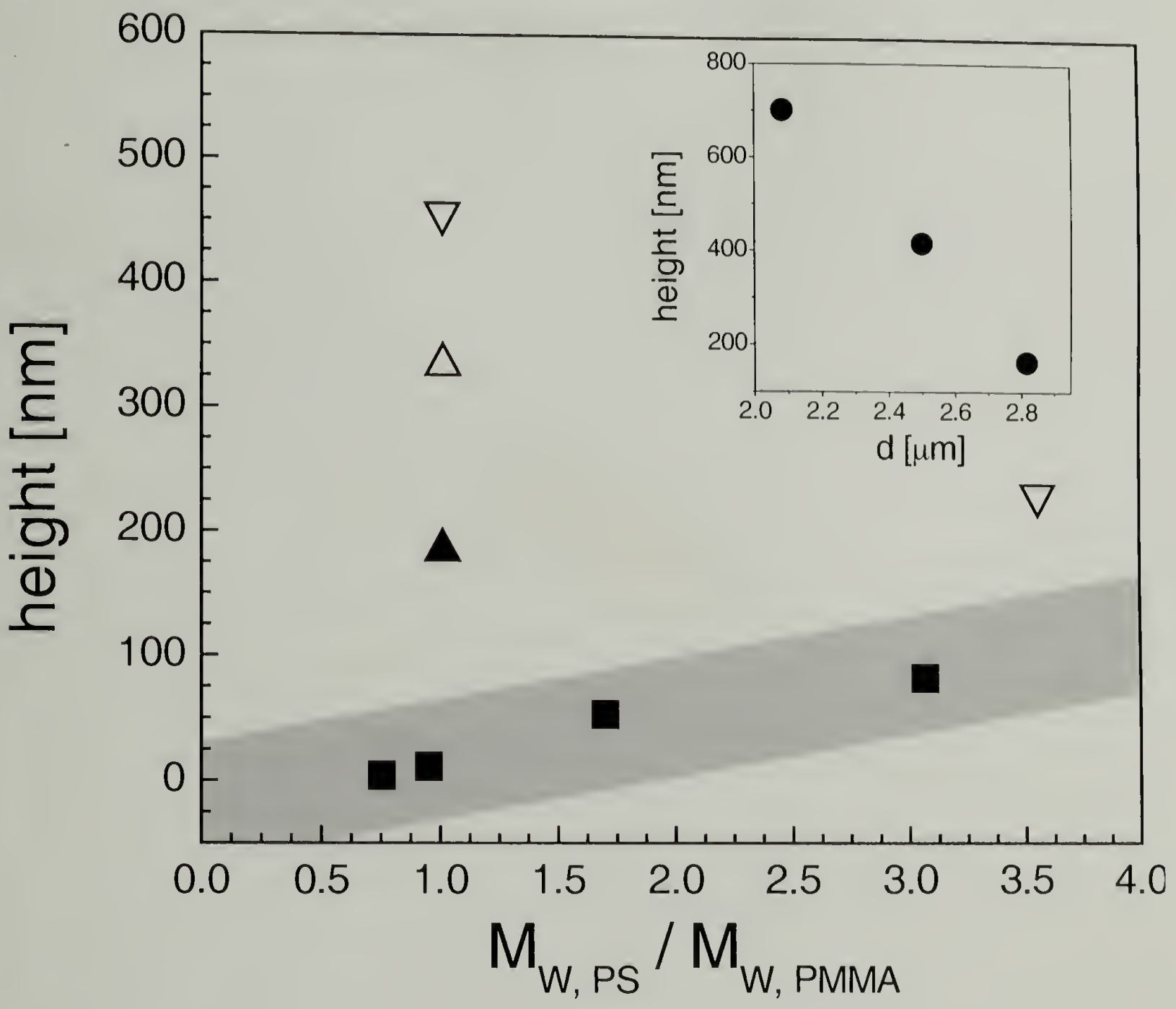

Figure 3.9. Columnar structure formation with a central column missing in air/PMMA-95K/PS-96K trilayer (sample 2 with 30 V applied).

(a)

(b)

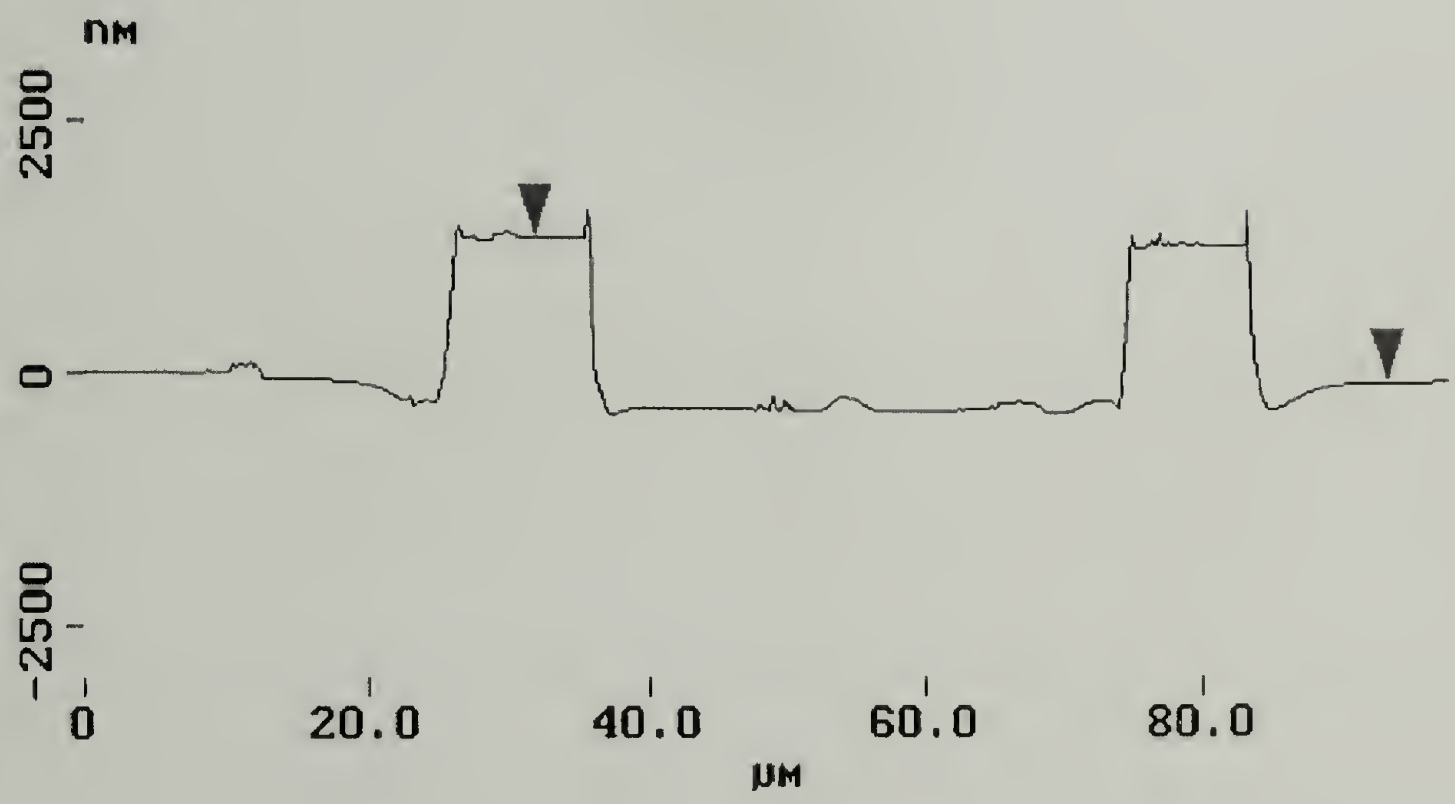

Continued on next page

Figure 3.9, continued

(c)

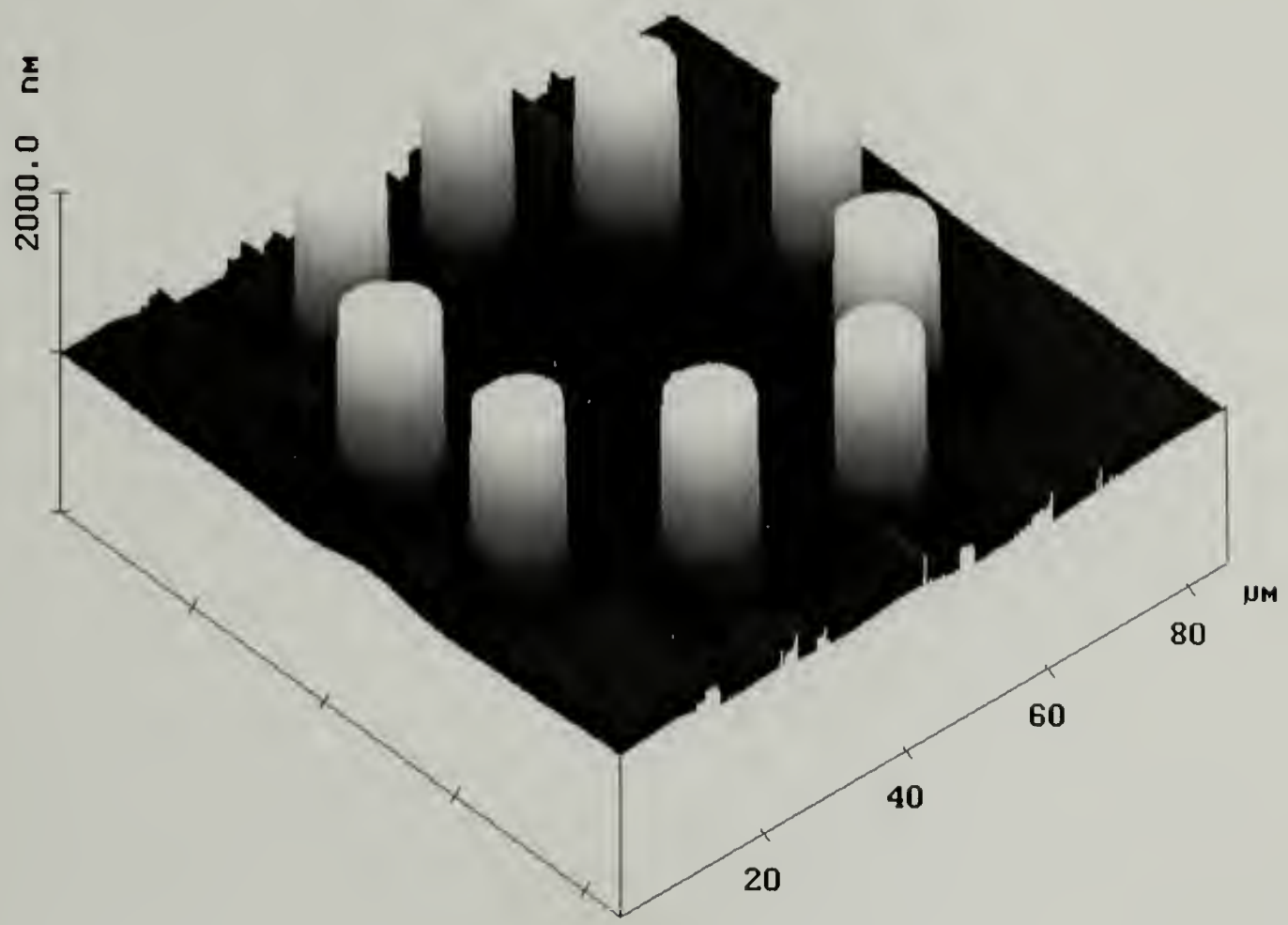

(c)

(d)

Figure 3.11. The air/PS-96K/PMMA-27K trilayer is exposed to 60 V. The formation of a map of "Cape Cod" in Massachusetts is seen.

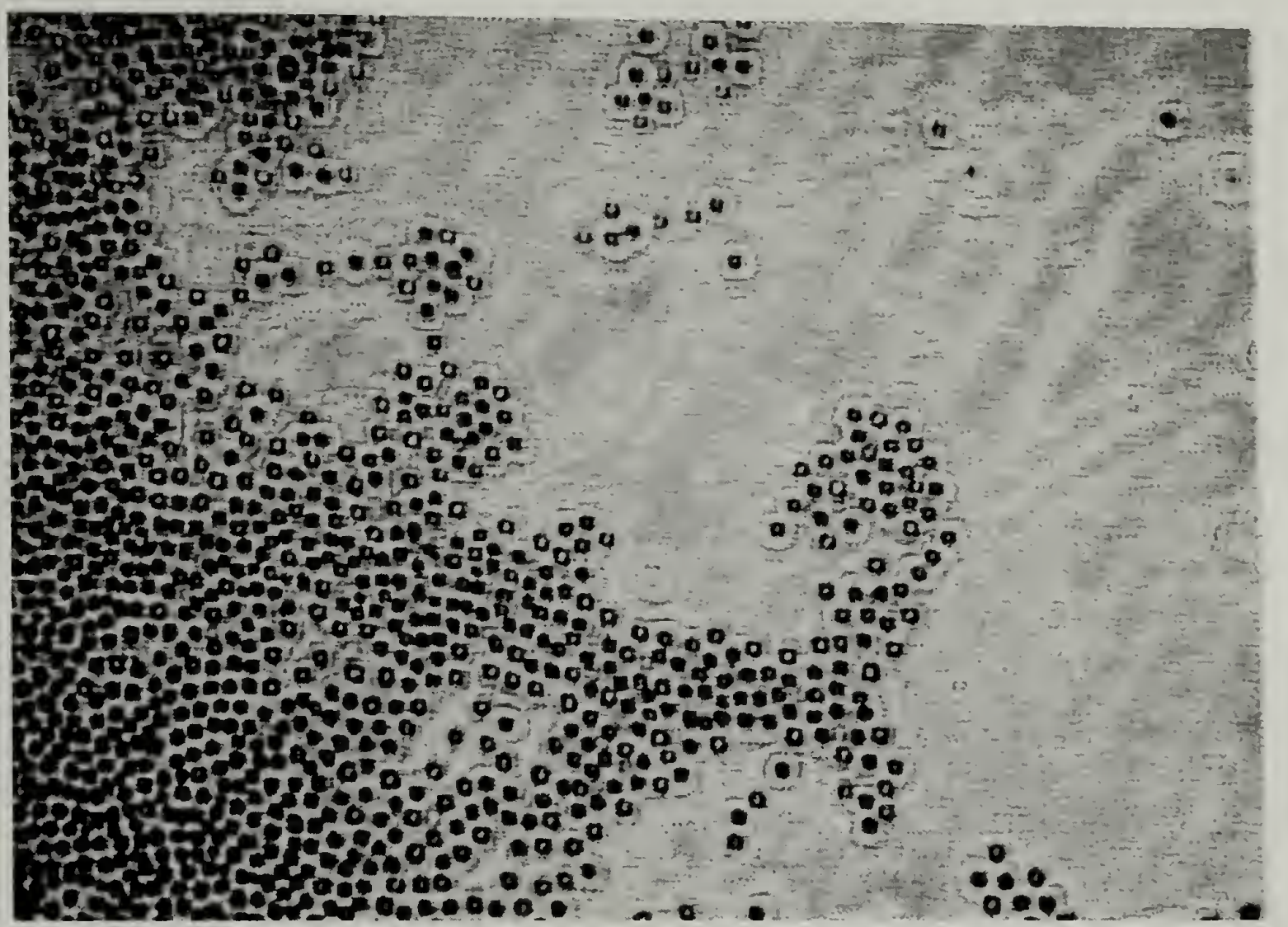

Conclusions

We have studied the electrohydrodynamically driven amplification of surface capillary waves in bilayers comprising of two incompatible polymers. Surprisingly, a minor variation of one of the experimental parameters, the electric field in the three layers (which was varied by changing the electrode spacing by a few percent), results in two distinct hydrodynamic regimes. For low enough electric fields, holes are heterogeneously nucleated in the top polymer layer (PS) which then dewets the liquid substrate, PMMA. This dewetting process is only marginally modified by the electric field. If the electric field is increased (by slightly decreasing the electrode spacing), the build-up of electrostatically amplified surface waves preempts heterogeneous nucleation, resulting in the formation of columns that span from the PMMA to the upper electrode. In this case, the dominant driving force is caused by the electric field. Apart from the different force balances that characterize the two regimes, they are very different in terms of their hydrodynamics. While the slow motion of the contact line during dewetting causes only a small deformation of the PMMA underlayer, the much faster collective motion of the electrohydrodynamic instability leads to high shear stresses and, therefore, to a substantial deformation of the PMMA/PS contact line. With time, PMMA is drawn further upward on the outside of the PS columns by the electric field. Studies of the deformation of the PMMA/PS interface during the early stage of the electrically driven spinodal instability of the PS surface allow us to deduce the hydrodynamic coupling of the two layers. The fact that the PMMA layer does not participate in the instability indicates the presence of slip at this interface.

Both results indicate that the present experiments may be useful in obtaining quantitative information on liquid-liquid spreading and dewetting. As opposed to dewetting in the absence of an electric field, an applied voltage may be useful as an additional, freely-variable external parameter that alters both the force balance as well as the hydrodynamics. With a suitable (presently unavailable) model, such experiments may yield valuable (and technologically important) insight in the contact line dynamics at the liquid-liquid boundary. In addition, the study of the liquid-liquid interface in the presence of a spinodal electrohydrodynamic instability (rather than rheological studies) may reveal more direct information about slip boundary conditions between incompatible liquids.

References

1. Tanner, L. H. The spreading of silicone oil drops on horizontal surfaces. *J. Phys. D: Appl. Phys.* **12**, 1473-1484 (1979).

2. deGennes, P. G. Wetting: statics and dynamics. *Reviews of modern physics* **57**, 827-863 (1985).

3. Joanny, J. F. Wetting of a liquid substrate. *PhysicoChemical Hydrodunamics* **9**, 183-196 (1987).

4. Brochard-Wyart, F. & Daillant, J. Drying of solids wetted by thin liquid films. *Can. J. Phys.* **68**, 1084-1088 (1990).

5. Brochard-Wyart, F., Martin, P. & Redon, C. Liquid/liquid dewetting. *Langmuir* **9**, 3682-3690 (1993).

6. Buguin, A., Vovelle, L. & Brochard-Wyart, F. Shocks in Inertial Dewetting. *Phys. Rev. Lett.* **83**, 1183-1186 (1999).

7. Xie, R., Karim, A., Douglas, J. F., Han, C. C. & Weiss, R. A. Spinodal dewetting of thin polymer films. *Phys. Rev. Lett.* **81**, 1251-1254 (1998).

8. Reiter, G. Dewetting of thin polystyrene films. *Phys. Rev. Lett.* **68**, 75-78 (1992).

9. Reiter, G. et al. Destabilising effect of long-range forces in thin liquid films on wettable substrates. *Europhys. Lett.* **46**, 512-518 (1999).

10. Lambooy, P., Phelan, K. C., Haugg, O. & Krausch, G. Dewetting at the liquid-liquid interface. *Physical Review Letters* **76**, 1110-1113 (1996).

11. Qu, S. et al. Dewetting dynamics at a polymer-polymer interface. *1997* **30**, 3640-3645 (1997).

12. Kerle, T., Yerushalmi-Rozen, R., Klein, J. & Fetters, L. J. van der Waals stable thin liquid films: Correlated undulations and ultimate dewetting. *Europhys. Lett.* **44**, 484-490 (1998).

13. Wu, S. *Polymer interface and adhesion* (Marcel Dekker, 1982).

14. Brochard-Wyart, F., Debregeas, G. & deGennes, P. G. Spreading of viscous droplets on a non viscous liquid. *Colloid Polym Sci* **274**, 70-72 (1996).

15. Morkved, T. L. et al. Local control of microdomain orientation in diblock copolymer thin films with electric fields. *Science* **273**, 931-933 (1996).

16. Mansky, P. et al. Large-area domain alignment in block copolymer thin films using electric fields. *Macromolecules* **31**, 4399-4401 (1998).

17. Amundson, K. et al. Effect of an electric-field on block copolymer microstructure. *Macromolecules* **24**, 6546-6548 (1992).

18. Amundson, K., Helfand, E., Quan, X. & Smith, S. D. Alignment of lamellar block-copolymer microstructure in an electric-field. 1. alignment kinetics. *Macromolecules* **26**, 2698-2703 (1993).

19. Amundson, K., Helfand, E., Quan, X., Hudson, S. D. & Smith, S. D. Alignment of lamellar block-copolymer microstructure in an electric-field. 2. mechanisms of alignment. *Macromolecules* **27**, 6559-6570 (1994).

20. Thurn-Albrecht, T., DeRouchey, J., Russell, T. P. & Jaeger, H. M. Overcoming interfacial interactions with electric fields. *Macromolecules* **33**, 3250-3253 (2000).

21. Thurn-Albrecht, T. et al. Nanoscopic Templates from Oriented Block Copolymer Films. *Advanced Materials* **12**, 787-791 (2000).

22. Thurn-Albrecht, T. et al. Ultrahigh-density nanowire arrays grown in self-assembled diblock copolymer templates. *Science* **290**, 2126-2129 (2000).

23. Pelrine, R., Kornbluh, R., Pei, Q. & Joseph, J. High-Speed Electrically Actuated Elastomers with Strain Greater Than 100%. *Science* **287**, 836-839 (2000).

24. Onuki, A. Interface instability induced by an electric field in fluids. *Physica A* **217**, 38-52 (1995).

25. Schaffer, E., Thurn-Albrecht, T., Russell, T. P. & Steiner, U. Electrically induced structure formation and pattern transfer. *Nature* **403**, 874-877 (2000).

26. Schafer, E., Thurn-Albrecht, T., Russell, T. P. & Steiner, U. Electrohydrodynamic instabilities in polymer films. *Europhysics Letters* **53**, 518-524 (2001).

27. Lin, Z. Q. et al. Electric field induced instabilities at liquid/liquid interfaces. *Journal of Chemical Physics* **114**, 2377-2381 (2001).

28. Lin, Z. Q., Kerle, T., Russell, T. P., Schafer, E. & Steiner, U. Structure formation at the interface of liquid/liquid bilayer in electric field. *Macromolecules* **35**, 3971-3976 (2002).

29. Herminghaus, S. Dynamical Instability of Thin Liquid Films Between Conducting Media. *Phys. Rev. Lett.* **83**, 2359-2361 (1999).

30. Fox, T. G. & Flory, P. J. The glass temperature and related properties of polystyrene. Influence of molecular weight. *J. Polym Sci* **14**, 315-319 (1954).

31. Wang, C., Krausch, G. & Geoghegan, M. Dewetting at a polymer-polymer interface: Film thickness dependence. *Langmuir* **17**, 6269-6274 (2001).

32. Blake, T. D., Clarke, A. & Stattersfield, E. H. An investigation of electrostatic assist in dynamic wetting. *Langmuir* **16**, 2928-2935 (2000).

33. Oddershede, L. & Nagel, S. R. Singularity during the onset of an electrohydrodynamic spout. *Physical Review Letters* **85**, 1234-1237 (2000).

34. Anastasiadis, S. H., Russell, T. P., Satija, S. K. & Majkrzak, C. F. Neutron reflectivity studies of the surface-induced ordering of diblock copolymer films. *Physical Review Letters* **62**, 1852-1855 (1989).

35. Reiter, G. & Khanna, R. Real-time determination of the slippage length in autophobic polymer dewetting. *Physical Review Letters* **85**, 2753-2756 (2000).

CHAPTER 4

LATE STAGE GROWTH OF STRUCTURES PRODUCED IN THIN FILMS VIA ELECTROHYDRODYNAMIC INSTABILITIES

Introduction

When an external electric field is applied normal to a liquid/liquid or liquid/air interface, height fluctuations, on the surface are amplified by an electrostatic pressure. The Laplace pressure operates against this, acting to minimize surface area and, hence, acts to suppress fluctuations. The competition of these pressures results in the amplification of fluctuations with a characteristic wavelength. These fluctuations grow, become unstable and produce an array of columns with a characteristic period. The general response of interfaces to applied fields has been studied by numerous researchers.[1-22] Oddershede and Nagel studied the development of instabilities at a liquid/water interface under the influence of an electric field.[14] Herminghaus theoretically predicted dynamical instabilities in dielectric coatings between electrically conductive media.[15] Onuki treated instabilities at the interface between two immiscible, nonionic fluids.[16] More recently, Schäffer et al investigated the electrohydrodynamic instabilities in thin polymer films that led to the formation of a laterally-ordered array of columns bridging between two electrodes in the parallel-plate capacitor geometry.[17,18] A simple linear instability analysis, valid in the early stage of development, successfully predicted a characteristic distance λ, that agreed well with experimental observations.[18] The more general cases of the liquid/liquid bilayer and air/liquid/liquid trilayer confined between two solid electrodes were subsequently discussed by Lin et al.[19-21] Using reduced variables,

experimental results were described with no adjustable parameters over many orders of magnitude in reduced field strength and characteristic distance.[20] Pease and Russel have also treated this problem in a more sophisticated theoretical approach and arrived at a similar agreement.[22]

While the early stages of growth of electrohydrodynamic instabilities in polymers is essential to test the theoretical arguments,[23] it is also important to understand the coarsening of structures after they are formed. This, for example, is key in optimizing the fidelity in replication of topographies in electrodes. Here, changes in diameters of the columns at the late stages of growth are investigated. The columns are shown to grow by diffusion of polymer from the underlying reservoir into the columns. Growth of the columns ceases when the reservoir is exhausted or when dewetting occurs.

Experimental

Materials

Poly(dimethyl siloxane) (PDMS) was made from Sylgard 184 (Dow Corning Corp.). A 10:1 ratio (w:w) of the liquid prepolymer and curing agent were mixed for 2hrs at the room temperature before being spin-coated onto the substrate. Oligomeric Polystyrene (OS) (MW=580) was purchased from Polymer Laboratories LTD. Poly(4-bromo styrene) (PSBr) (MW=6.5×10^4) was purchased from Aldrich Chemical Co. Deuterated Polystyrene (dPS) was synthesized anionically and had a molecular weight of 99.9K (PDI=1.017). The conductive media, indium-tin-oxide (ITO) microscope slides, were purchased from Delta Technologies ($25 \times 50 \times 1.1 mm^3$, $R \leq 100 ohms$).

Sample preparation

The general sample configuration is shown in Figure 4.1. Thin films of PDMS and OS (MW=580) were spin coated from the bulk and toluene solution onto freshly cleaned Si substrates with thicknesses of 6.5 μm and 196 nm, respectively. Kapton thin films (Polyimide, Dupont) and silicon oxide rails evaporated onto a clean ITO microscope slide were placed on the top of the PDMS and OS film, respectively, so as to create an air gap between the polymer film and ITO glass electrode. *In-situ* optical microscopy studies were performed at room temperature to avoid thermal gradients. In the first *in-situ* optical microscopy study, a 6.5 μm PDMS film was exposed to 100 V with the electrode spacing of 50 μm separated by Kapton film. In a second study, 30 V was applied to a 196 nm film of OS (MW=580) with a 1.2 μm separation distance between the two electrodes. Studies were also performed on a 740 nm thick film of PSBr (MW=65,000) and 530 nm thick film of dPS (MW=99,900) with several different separation distances between the electrodes. Experiments were preformed at 170°C which is above the glass transition temperature of the polymers, under N_2 for 3 days. The samples were then quenched to room temperature before removal of the applied voltage and the upper electrode.

The film thickness of OS, dPS and PSBr were measured with a Rudolph Research AutoEL®-II ellipsometer using a helium-neon laser (λ=632.8 nm) at a 70° incidence angle. For the thick PDMS film, Filmetrics F20 (working range: 10 nm ~ 50 μm) was used to measure the film thickness. The structures formed in the PSBr and dPS thin film systems were investigated by optical microscopy and atomic force

Figure 4.1. Sketch of the sample configuration in the study. The liquid/air system is confined between a highly polished and doped silicon wafer (lower electrode) and an ITO microscope slide (upper electrode). The distance between the two electrodes is controlled by evaporating SiOx as the spacer (in OS thin film study) at the edges of the slides on top of the ITO or applying thin Kapton (in PDMS thin film study) between two electrodes. The structure formations at the interface of the liquid/air under an applied electric field were studied by optical microscopy in the reflectance mode.

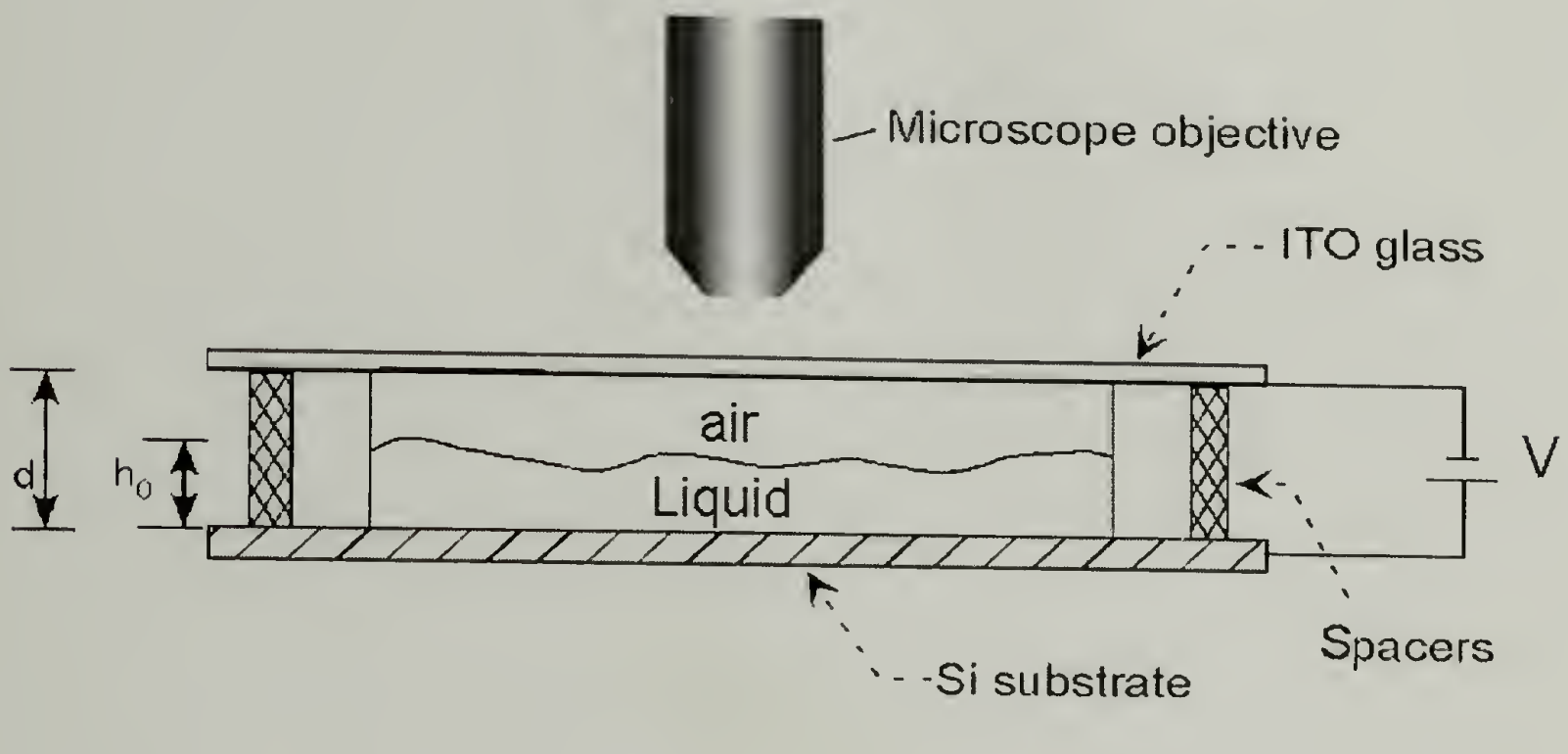

microscopy. Optical microscopy (OM) studies were performed in the reflection mode using an Olympus BX60 microscope. Atomic force microscopy (AFM) studies were done with a Digital Instrument D3100 scanning force microscope in the tapping mode. Silicon nitride tips on cantilevers (Nanoprobe™) with spring constants from 29.3 to 63.9 N/m were used. Table 4.1 summarizes the physical constants of the oligomeric polymer and other polymers used in the studies.

Table 4.1. The characteristics of the polymers used in the studies.

Polymers	OS	PSBr	dPS	PDMS
MW[(a)] (g/mol)	580	65,000	99,900	—
γ [(b)] (mN/m)	33	39	33	—
ε [(c)]	2.5	4.09	2.95	—
Tg [(d)] (°C)	—	120	100	< 0

(a) Molecular weight.
(b) Surface tension γ.
(c) Dielectric constants. ε_{dPS} and ε_{PSBr} are the dielectric constants measured at 170°C[20], ε_{OS} is the dielectric constant at the room temperature.
(d) Glass transition temperature.

Results and Discussion

Shown in Figure 4.2a are top-view optical micrographs of PDMS columns as a function of time after exposure to 100 V with an electrode spacing of 50 μm.

PDMS columns with hexagonal order are seen to span between the two electrodes. The average diameter of the columns increases with increasing time, indicating the presence of a thin layer of PDMS at the base of columns on the lower electrode. As shown in Figure 4.2b, the individual PDMS column diameters increase rapidly with time initially (before 400 minutes) and saturate at later times (after 1000 minutes in the example shown). The final diameters are 147 μm for PDMS columns 2, 3 and 4, and 138μm for column 1. The growth of each individual column diameter before saturation can be scaled as

$$D(t) \sim t^n \tag{1}$$

where n is the growth exponent. By taking column 1 as the reference, the time axis of columns 2, 3 and 4 are shifted to overlap all the data points together as shown in Figure 4.2c. A further normalization of column diameters as a function of shifted time is shown in Figure 4.2d. The small growth exponent, n= ~ 0.05, is readily obtained from the slope, which reflects a slow flow of polymer from the reservoir at the base of the columns into the columns. In addition, the driving force giving rise to the flow must be weak. Based on the increment of column diameter from the initial state to the first saturation and the corresponding elapse time, the diffusion coefficient of PDMS, D_{diff}, can be estimated as $D_{diff} \sim \frac{\Delta(D(t)/2)^2}{\Delta t} \sim \frac{(D_{\inf} - D_{ini})^2}{t_{\inf} - t_{ini}} \sim 10^{-10}\, cm^2/s$, which supports the slow growth of the column diameters (n ~ 0.05), where D_{ini} and D_{inf} are the initial and saturated column diameters, respectively.

A typical AFM scan of a 740 nm thick PSBr thin film after 3 days under 30V, with an electrode separation distance d of 1.69 μm, is shown in Figure 4.3a. The 3D AFM height image shows the PSBr columns with an average radius 6 μm±0.63 μm and λ=17.4 μm±0.8 μm. The 2D Fast Fourier Transform (2DFFT) of the AFM image is shown in the inset. Six spots are seen indicating a well-ordered hexagonal packing of the columns, with a lattice constant of 15 μm. A line scan across the sample is shown in Figure 4.3b. The columnar shape of the features is clearly evident in this profile. However, between the columns there is clear evidence of an underlying film. At the base of the columns there are depressions that are reminiscent of depletion zones. This would be expected if the flow of the polymer into the columns was faster than the relaxation of the polymer to produce a smooth surface. Based simply on the minimization of the surface area under the restraint of maintaining the columnar structures, the lowest free energy is achieved when all polymers are in the columns. However, by scratching the film with a razor blade, the film at the midpoint between two cylinders is found to be h_{min}, ~210 nm.

As shown previously,[17,18] the average center-to-center distance between adjacent columns, λ, is given by

$$\lambda = 2\pi \sqrt{\frac{\gamma U}{\varepsilon_0 (\varepsilon - 1)^2 \varepsilon}} \, E^{-\frac{3}{2}} \tag{2}$$

where U is the applied voltage, γ is the surface tension of the polymer, ε is the dielectric constant of the polymer, ε_0 is the dielectric permittivity in vacuum and E is the electric field strength in the polymer.

For a hexagonal array of columns, schematically shown in Figure 4.4, the total volume of polymer V in the initial thin film within the triangular unit cell is

Figure 4.2. (a) Time sequences of 6.5μm PDMS thin film in 100 V with an electrode spacing of 50 μm from top view in optical microscopy measurement. (b) The plot of the diameters, D(t), of each marked individual column as a function of time. (c) The ln D(t) ~ ln t plot, from which the growth exponent, n, is found to be 0.05. (d) The ln $D(t) / D_{inf}$ ~ ln t plot, where D_{inf} is the saturated column diameter. The time scales of columns 2, 3, and 4 are shifted in order to overlap all the data point into a master curve shown in (c) and (d), where the amount shifting is shown in the insets. The scale bar is 80 μm.

(a)

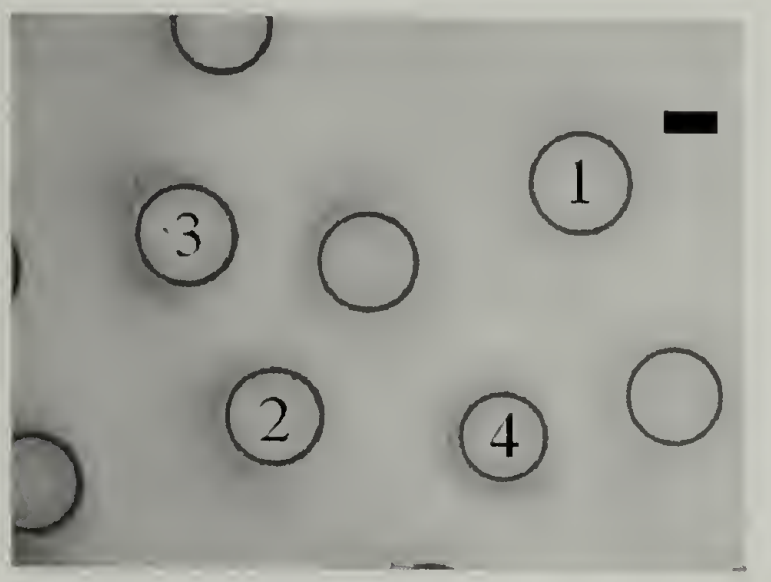

20 mins

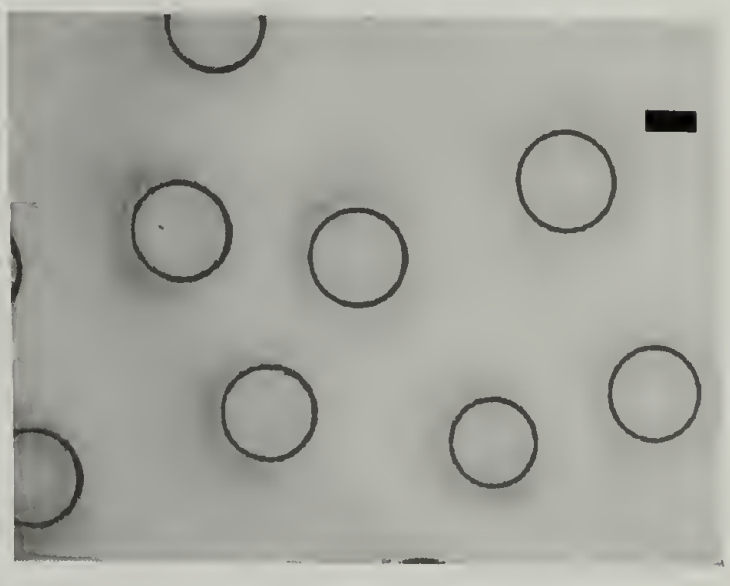

21.5 mins

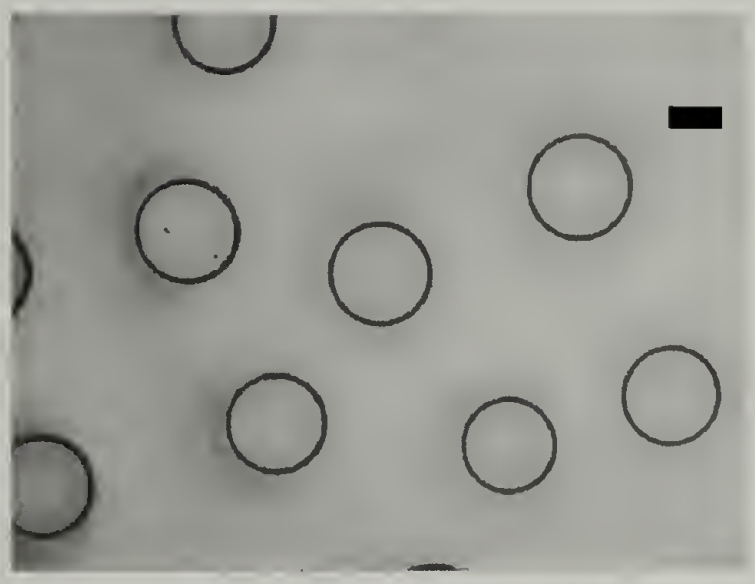

31.5 mins

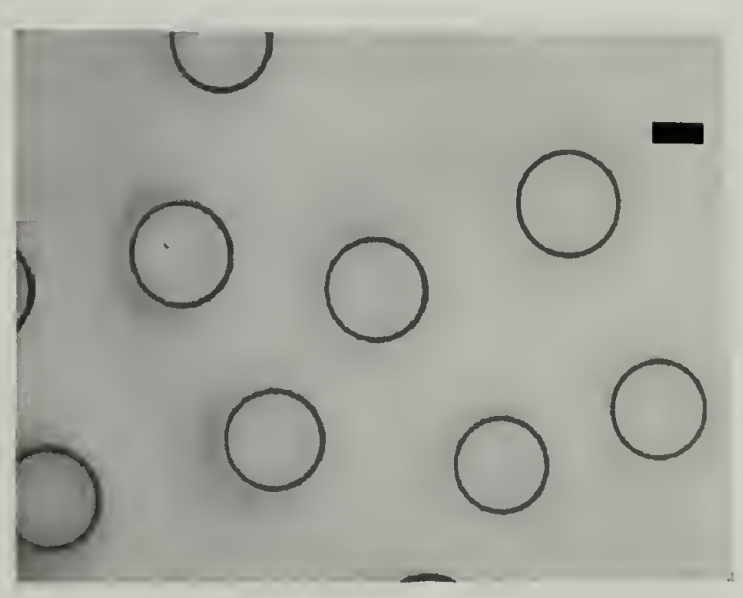

44 mins

Continued on next page

Figure 4.2, continued

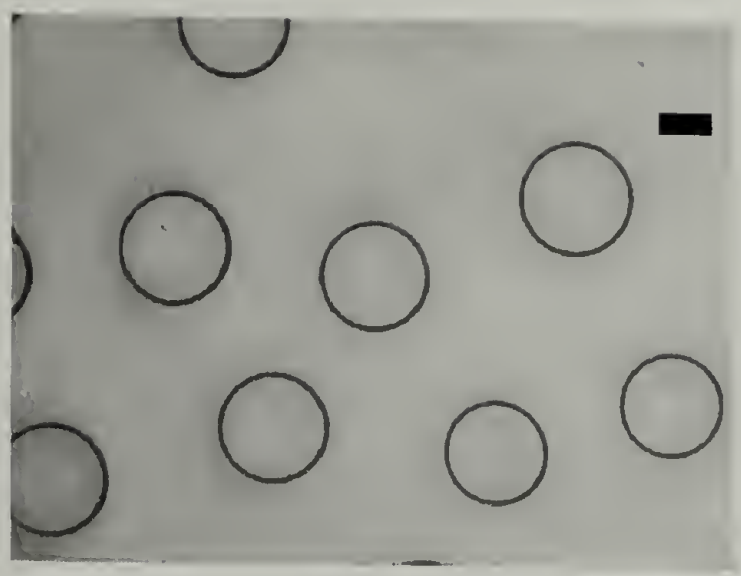

472 mins

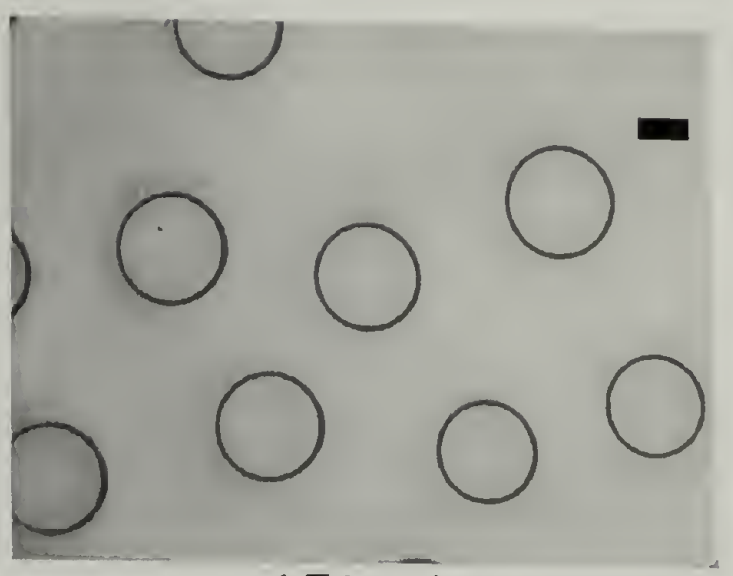

972 mins

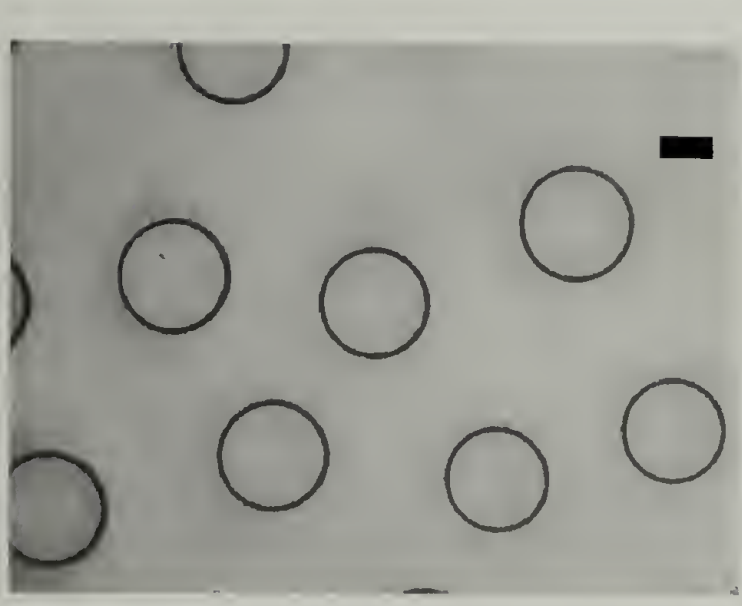

2712 mins

Continued on next page

Figure 4.2, continued

(b)

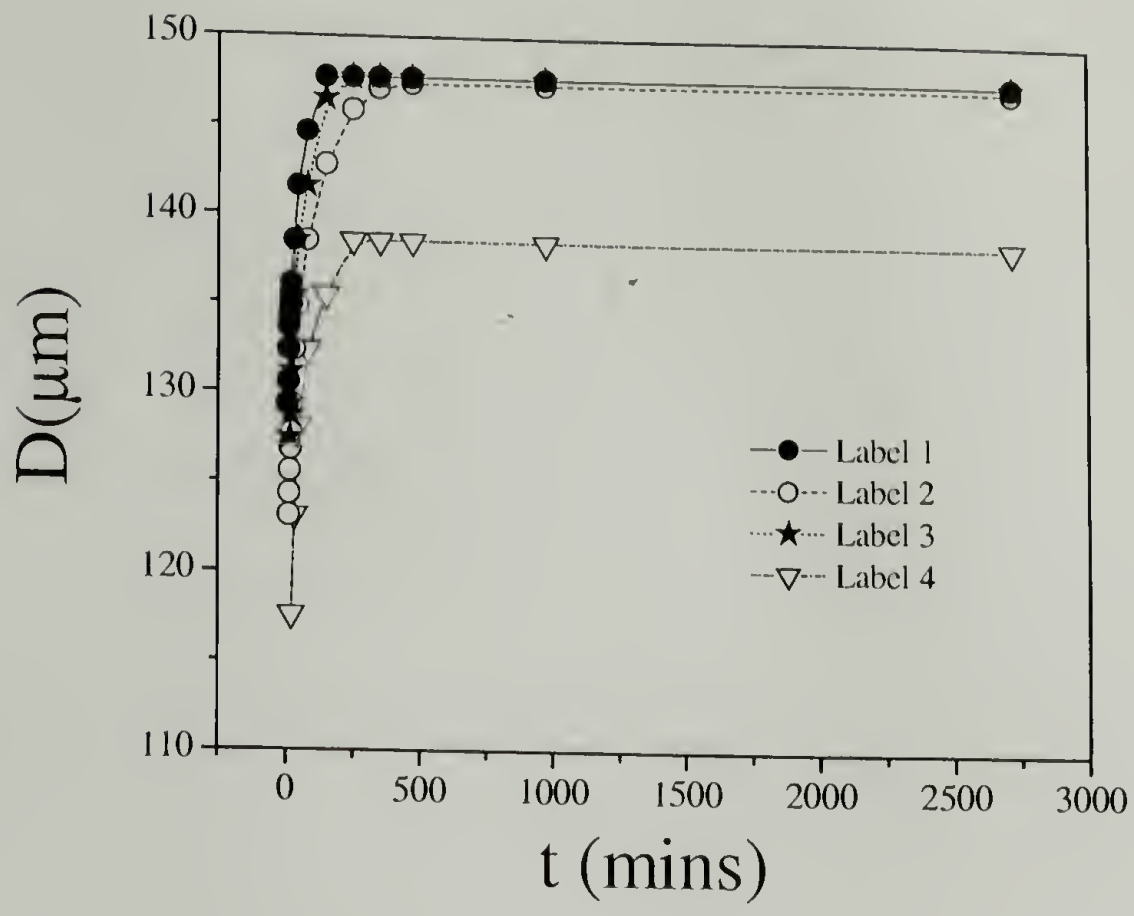

(c)

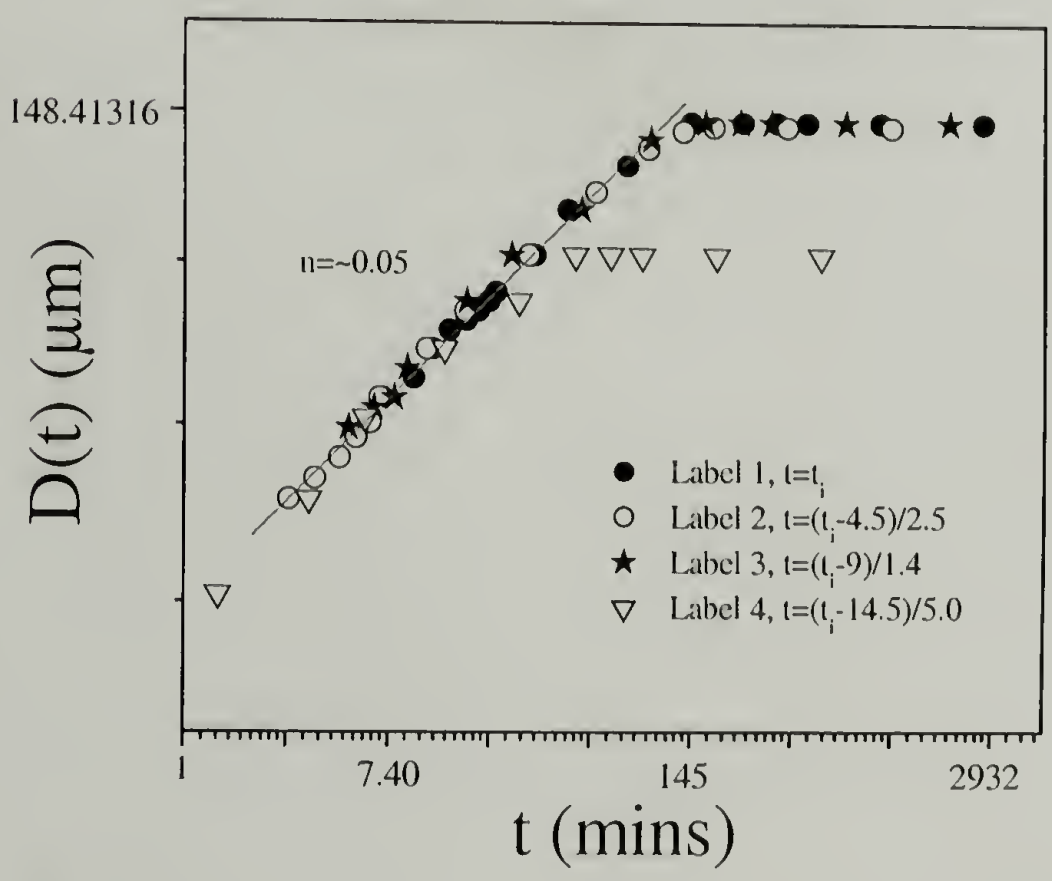

Continued on next page

Figure 4.2, continued

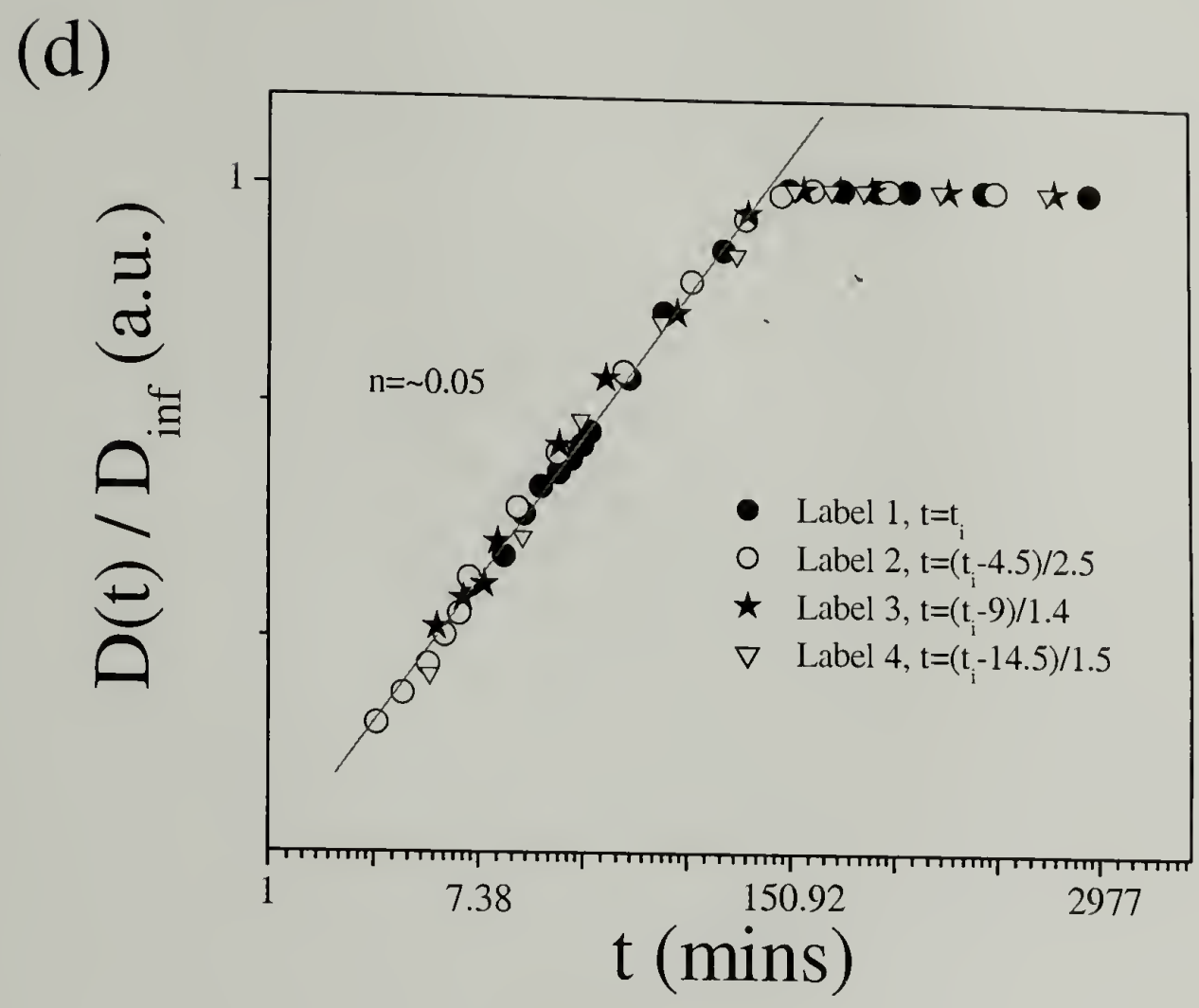

Figure 4.3. (a) The 3D AFM height image of the PSBr thin film exposed to 30 V for 3 days. The 2D FFT of AFM image is shown in the inset. (b) The corresponding section analysis of the AFM image. A draining-like feature in the vicinity of polymer pillars is marked as dotted ring.

(a)

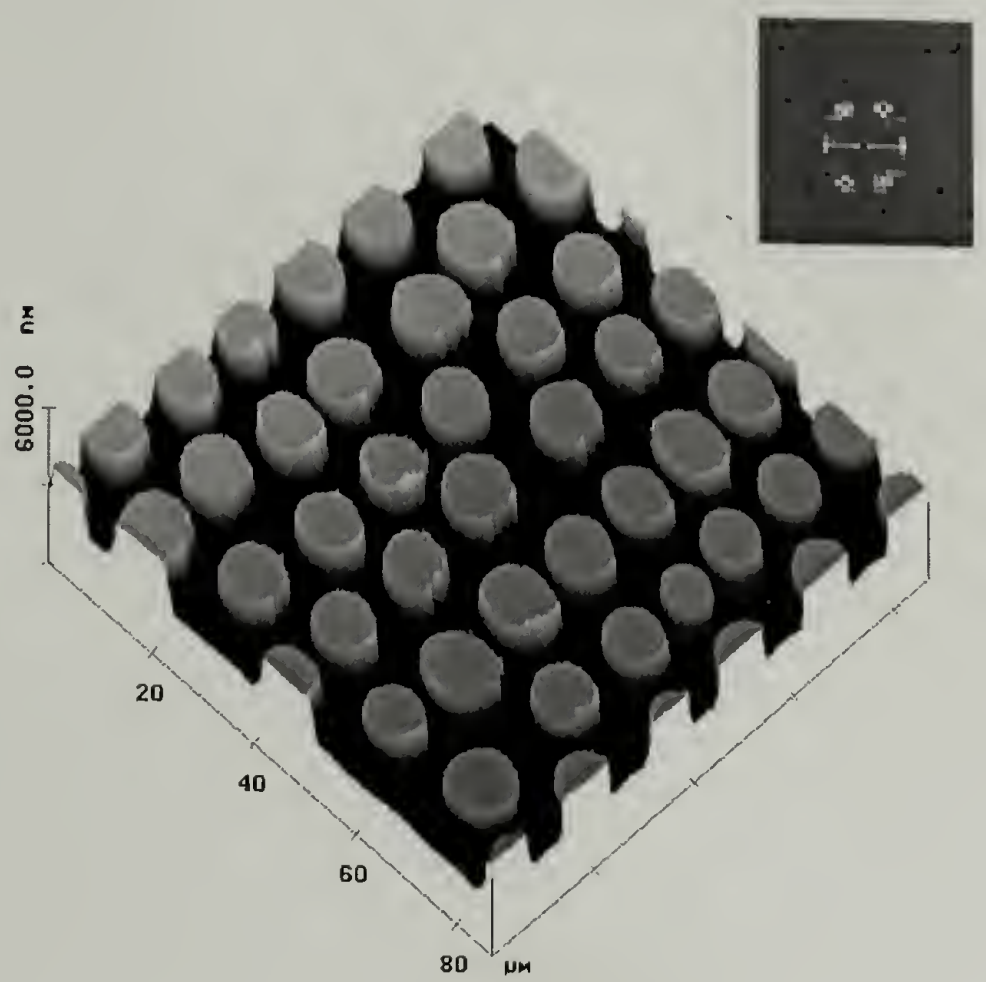

(b)

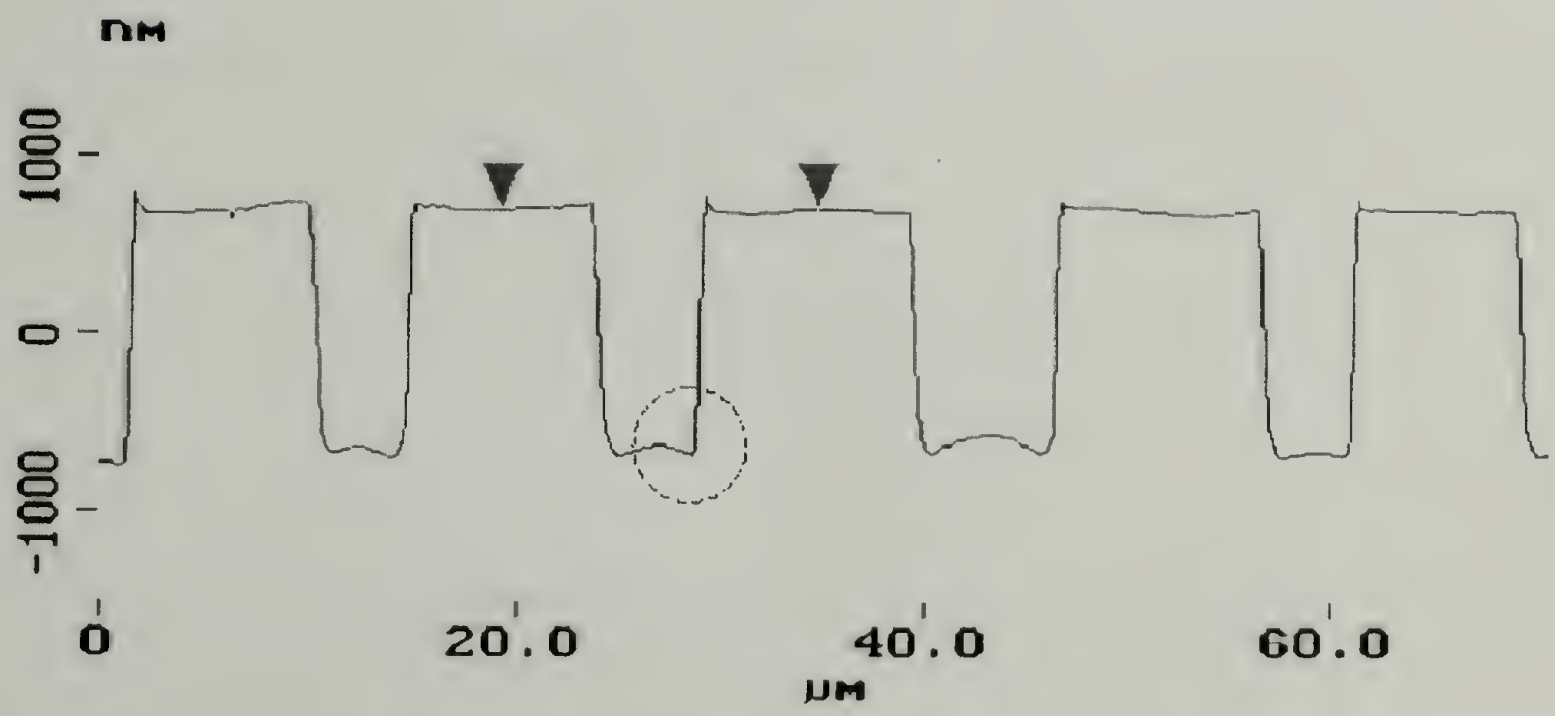

Figure 4.4. The schematic diagrams show the close packed hexagonal pillars from (a) top view, (b) side view.

(a)

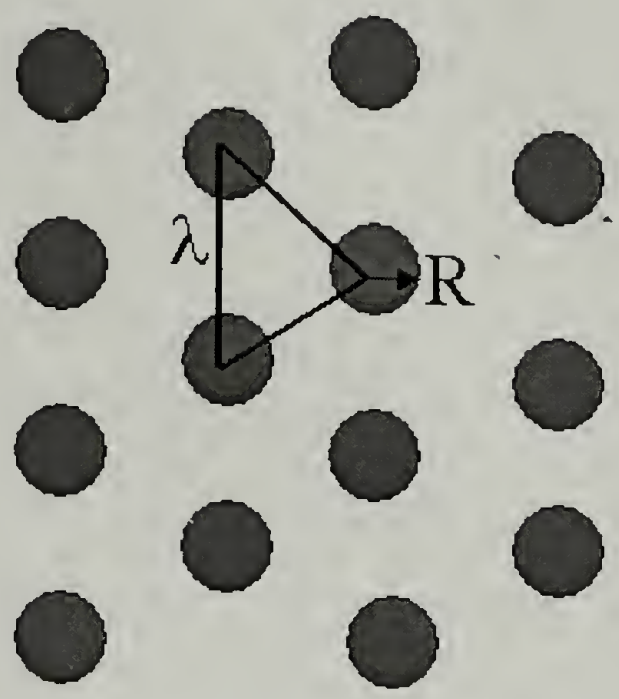

(b)

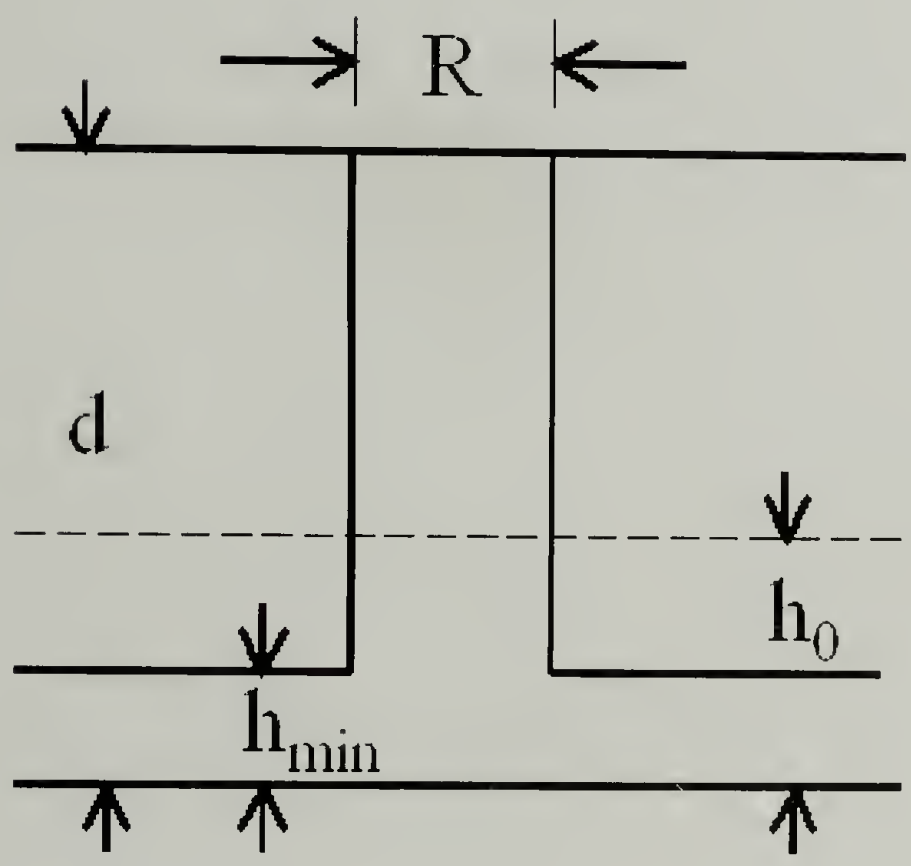

$$V = \frac{\sqrt{3}}{4}\lambda^2 \cdot h_0 \tag{3}$$

where λ is the characteristic distance between two pillars[18] and h_0 is the initial film thickness. After the formation of columns, there is film of polymer with a thickness, h_{min}, remaining on the substrate at the base of the columns. If the separation distance of the electrodes is d, and the columns have a radius R, then, by mass conservation,

$$V = \frac{1}{2}\pi R^2 (d - h_{\min}) + \frac{\sqrt{3}}{4}\lambda^2 \cdot h_{\min} \tag{4}$$

Solving for R,

$$R = \left[\frac{\sqrt{3}(h_0 - h_{\min})}{2\pi(d - h_{\min})}\right]^{\frac{1}{2}} \lambda \tag{5}$$

A reference distance λ_0, radius R_0, and electric field strength E_0 can be defined as

$$\lambda_0 = \frac{\varepsilon_0 U^2}{\gamma}(\varepsilon - 1)^2 \varepsilon \ , \ R_0 = \left[\frac{\sqrt{3}(h_0 - h_{\min})}{2\pi(d - h_{\min})}\right]^{\frac{1}{2}} \lambda_0 \ \text{ and } \ E_0 = \frac{U}{\lambda_0}$$

Using these, a reduced radius can be defined as

$$\frac{R}{R_0} = 2\pi\left(\frac{E_0}{E}\right)^{\frac{3}{2}} \tag{6}$$

Substituting the relevant parameters for a PSBr thin film with 30 V applied into equation (2) and (5) yields a λ=22.1 μm and R=6.93 μm, which agree well with λ=17.4 μm, and R=6 μm measured.

A master curve of R/R_0 as a function of E/E_0 is shown in Figure 4.5. For the experiments on PSBr, the geometry of the system (film thickness and electrodes separation distance), and field strengths have been varied. The solid line in the Figure 4.5 is the calculated reduced radius as a function of the reduced field strength. As can be seen, very good agreement with experimental observations is seen.

Figure 4.5. The master curve of the radius of polymer pillars R in varieties of thin film experiments as a function of the electric field strength in polymer thin films. The different symbols correspond to 2 data sets: ● PSBr/air single layer with h_{PSBr} = 740 nm, d =1.69-1.98 μm, U=24-60 V; ■ dPS/air single layer with h_{dPS} = 530 nm, d =1.06 and 1.85 μm, U=30 V. The straight line is calculated based on the equation (6) with a slope of 1.5.

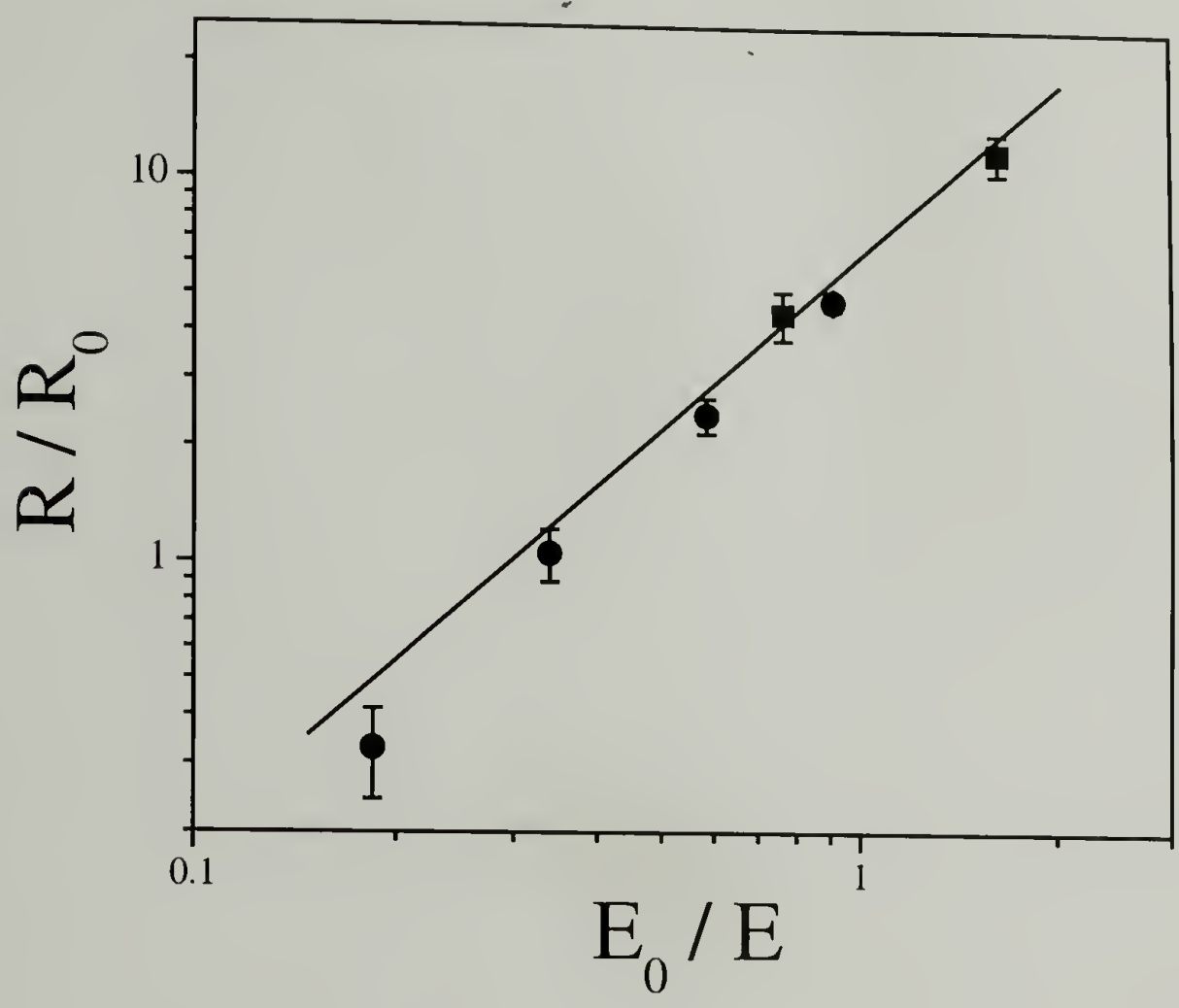

However, when the reservoir is exhausted and the thin film connecting the columns vanishes, then bare Si is exposed. Consequently, the columns are isolated and any growth or other coarsening mechanisms are arrested. Shown in Figure 4.6 where a dewetting front is moving across an OS film under an applied field of 30 V. The formation of the columns is evident. As the front progresses across the film, instabilities occur along the front producing the OS columns. Each of the columns is independent of the others and each column is now an isolated system. Consequently the number, size and shape remain invariant with time.

Figure 4.6. Optical micrographs from in-situ 196 nm OS thin film experiment show the time developments of OS pillars in 30 V. The image size is 950x730μm^2.

75mins

1250mins

2250mins

4250mins

Conclusions

The growth of columns formed from liquid thin films under an applied electric field was investigated. A simple model was presented to describe the size of the columns, where good agreement was found between experiments and calculations. The approach of the column diameter to its final equilibrium size is shown as the polymer reservoir becomes depleted. Column growth can be fully arrested if dewetting occurs or if the reservoir is fully depleted.

References

1. Swan, J. W. Stress and other effects produced in resin and in a viscid compound of resin and oil by electrification. *Proc. R. Soc. London* **62**, 38-46 (1897).

2. Glenn, W. E. Thermoplastic recording. *J. Appl. Phys.* **30**, 1870-1873 (1959).

3. Cressman, P. J. New type of thermoplastic deformation. *J. Appl. Phys.* **34**, 2327-2330 (1963).

4. Killat, U. Revised dynamical theory of thermoplastic deformation. *J. Appl. Phys.* **46**, 5169-5172 (1975).

5. Reynolds, J. M. Stability of an electrostatically supproted fluid column. *The Physics of Fluids* **8**, 161-170 (1965).

6. Melcher, J. R. & Smith, C. V. Electrohydrodynamic charge relaxation and interfacial perpendicular-field instability. *Phys. Fluids* **12**, 778-790 (1969).

7. Vizika, O. & Saville, D. A. The electrohydrodynamic deformation of drops suspend in liquid in steady and oscillatory electric-fields. *J. Fluid Mech.* **239**, 1-21
(1992).

8. Saville, D. A. Dielectric behavior of colloidal dispersions. *Colloid Surf.* **92**, 29-40 (1994).

9. Trau, M., Sankarn, S., Saville, D. A. & Aksay, I. A. Pattern formation in nonaqueous colloidal dispersions via electrohydrodynamic flow. *Langmuir* **11**, 4665-4672 (1995).

10. Trau, M., Sankarn, S., Saville, D. A. & Aksay, I. A. Electric-field-induced pattern formation in colloidal dispersions. *Nature* **374**, 437-439 (1995).

11. Saville, D. A. Electrohydrodynamics: the Taylor-Melcher leaky dielectric model. *Annu. Rev. Fluid Mech.* **29**, 27-64 (1997).

12. Anklam, M. R., Saville, D. A. & Prud'home, R. K. Electric-field-induced rupture of polymer-stabilized oil films. *Colloid Polym Sci* **277**, 957-964 (1999).

13. Saville, D. A. Electrohydrodynamic deformation of a particulate stream by a transverse electric field. *Physical Review Letters* **71**, 2907-2910 (1992).

14. Oddershede, L. & Nagel, S. R. Singularity during the onset of an electrohydrodynamic spout. *Physical Review Letters* **85**, 1234-1237 (2000).

15. Herminghaus, S. Dynamical Instability of Thin Liquid Films Between Conducting Media. *Phys. Rev. Lett.* **83**, 2359-2361 (1999).

16. Onuki, A. Interface instability induced by an electric field in fluids. *Physica A* **217**, 38-52 (1995).

17. Schaffer, E., Thurn-Albrecht, T., Russell, T. P. & Steiner, U. Electrically induced structure formation and pattern transfer. *Nature* **403**, 874-877 (2000).

18. Schafer, E., Thurn-Albrecht, T., Russell, T. P. & Steiner, U. Electrohydrodynamic instabilities in polymer films. *Europhysics Letters* **53**, 518-524 (2001).

19. Lin, Z. Q. et al. Electric field induced instabilities at liquid/liquid interfaces. *Journal of Chemical Physics* **114**, 2377-2381 (2001).

20. Lin, Z. Q., Kerle, T., Russell, T. P., Schafer, E. & Steiner, U. Structure formation at the interface of liquid/liquid bilayer in electric field. *Macromolecules* **35**, 3971-3976 (2002).

21. Lin, Z. Q., Kerle, T., Russell, T. P., Schafer, E. & Steiner, U. Electric field induced dewetting at the liquid-liquid interface. *Macromolecules* **35**, 6255 (2002).

22. Pease III, L. F. & Russel, W. B. Linear stability analysis of thin leaky dielectric films subjected to electric fields. *J. Non-Newtonian Fluid Mech.* **102**, 233-250 (2002).

23. Leach, A. K. & et al. (In preparation).

CHAPTER 5

TEMPORAL EVOLUTION OF SINGLE LAYER FILM UNDER CONFINEMENT IN ELECTRIC FIELD

Introduction

Harnessing instabilities in thin films is of considerable academically and technologically interest.[1-18] The generation of surface and interfacial structures and the influence of the periodic substrates have been investigated extensively.[8-19] Boltau et al studied the surface induced structure formation of a binary polymer films on patterned gold substrates.[11] Rockford et al recently reported a relationship between controlled nanoscale surface interactions and subsequent macromolecular ordering by applying striped surfaces of oxide and metal, where the stripe width is comparable to the size of a polymer molecule.[12] Sharma et al studied the dewetting behavior of thin liquid films on physically and chemically heterogeneous surfaces based on 3D nonlinear simulations by solving the equation of motion numerically.[8-10] A novel class of morphologies was found that were not predicted by the spinodal mechanism.

In addition to the structure formation driven by long range van der Waal forces mentioned above, electric fields have been shown to be an effective means to induce instabilities by the competition between the electrostatic force and interfacial tension at the liquid/air and liquid/liquid interfaces, producing ordered lateral structures.[20-25] Herminghaus predicted a dynamical instability of a thin dielectric film between conductive media, where the electric forces dominate the dispersive forces and amplify surface waves.[20] Schäffer et al. showed a well-defined characteristic

wavelength at the liquid film surface in studies of single layer films between parallel capacitor plates with an air gap in an external electric field.[21,22] By imposing a patterned master, submicrometer structures have been replicated with high fidelity.[21] The more general cases of the liquid/liquid bilayer and air/liquid/liquid trilayer experiments and model calculations showed a means by which structures can be produced over a wide range of length scales.[23-25] Similar observations were made by Chou and his coworker with no applied external electric field.[26-29] Analogous to the electric fields, thermal gradients across the surface of a thin film confined in between two parallel plates can generate thermomechanical instabilities and ultimately result in structure formation.[30] With patterned upper plate, replication can also be achieved.

Here, an alternative way to control the structure formation at the surface of a liquid thin film is presented by creating topographical patterns comprised of stripes with well defined widths. Growth of the instabilities under the area defined by these stripes on an upper electrode is accessible by optical microscopy. It is seen that the initial undulations are grown beneath the stripe pattern leading to the formation of columns. The finite size of the stripes is seen to markedly alter the characteristic wavelength of the fluctuations.

Experimental

Materials

Polyisoprene (PI) (MW= MW=4.0×10^4) was purchased from Aldrich Chemical Co. One side polished microscope slides used in this study, were purchased from Delta Technologies. A positive radiation sensitive resist, 7%

Poly(methyl methacrylate) Anisole solution (PMMA) (MW=9.5×10^4, Nano™ 950 PMMA A7) was purchased from Micro·Chem Inc.

Sample preparation

All Cr/Au stripe patterns (the upper electrodes) were prepared on the polished microscope slides by conventional electron-beam lithography (EBL) in the following way (Figure 5.1). A 650 nm thick 7% PMMA solution in anisole was spun onto a cleaned, polished microscope slide. The spin coated substrates were annealed at 180 °C for 30 minutes to remove the solvent completely. Since the glass substrates were insulating, a 160Å thick Au layer was thermally evaporated onto this resist layer to avoid charging during electron-beam exposure. A scanning electron microscope (SEM) was operated at a accelerating voltage of 20 kV to expose the resist and generate the desired electrode pattern at an area dose of 300 $\mu C/cm^2$. After the exposure, the Au layer was completely removed by dipping the sample in a gold etch solution for 1 minute[31] (The gold etch solution was made by dissolving 40 g KI and 10 g I_2 in 400 ml of water). The exposed samples were developed in a mixed solution of methyl isobutyl ketone (MIBK):isopropanol (IPA) (1:3) for 1 minute, which removed the PMMA in the exposed regions, creating a mask on the glass substrate. 10Å of Cr was thermally evaporated at a rate of 1.0 Å/s as an adhesion layer, following by a subsequent evaporation of 60Å thick Au at a rate of 2.0 Å/s. The remaining PMMA resist was then removed by leaving the sample in acetone for 2 hours, followed by a methanol rinse and nitrogen gas blow dry. After the fabrication, the Cr/Au stripes on the microscope substrate were examined with an optical

microscope prior to use. The Cr/Au stripe-like patterns were rectangle in shape with an essentially an infinitely long in length (4mm) and a finite in width.

The schematic diagram of the sample configuration used in this study is shown in Figure 5.2. 360 nm thick PI thin films were spin coated onto a freshly cleaned Si substrate. All film thicknesses were measured with a Rudolph Research AutoEL®-II ellipsometer using a helium-neon laser (λ=632.8 nm) at a 70° incidence angle. The samples were sandwiched in between an Si substrate (the lower electrode) and the patterned stripes on the microscope slide (the upper electrode). It should be noted that the total thickness of Cr/Au double layer is only ~ 7 nm so as to minimize the optical pathlength making it possible to monitor the structure formation in real time through the polished substrate. A small air gap is left on the top of PI thin film, which can be controlled by evaporating silicon oxide rails of a specified thickness onto the Si substrates. The experimental parameters of the samples used in the studies are given in Table 5.1.

All real time optical microscopy studies were performed at room temperature in reflection mode using an Olympus BX60 microscope.

Results and Discussion

The topographically patterned Cr/Au stripes on a substrate fabricated by EBL can be designed to be varied across the polished microscope slide producing a gradient (as shown in Figure 5.3) or they can be made periodic (as shown in Figure 5.10). The advantage of using the gradient pattern is that multiple experiments can be done simultaneously where the patterns are at equal potential in an applied electric

Figure 5.1. Schematic diagram of E-beam lithography process. The final thicknesses of Cr (acting as an adhesive layer) and Au are 1 nm and 6 nm, respectively. They are transparent and facilitate the observation of the structure formation in real time.

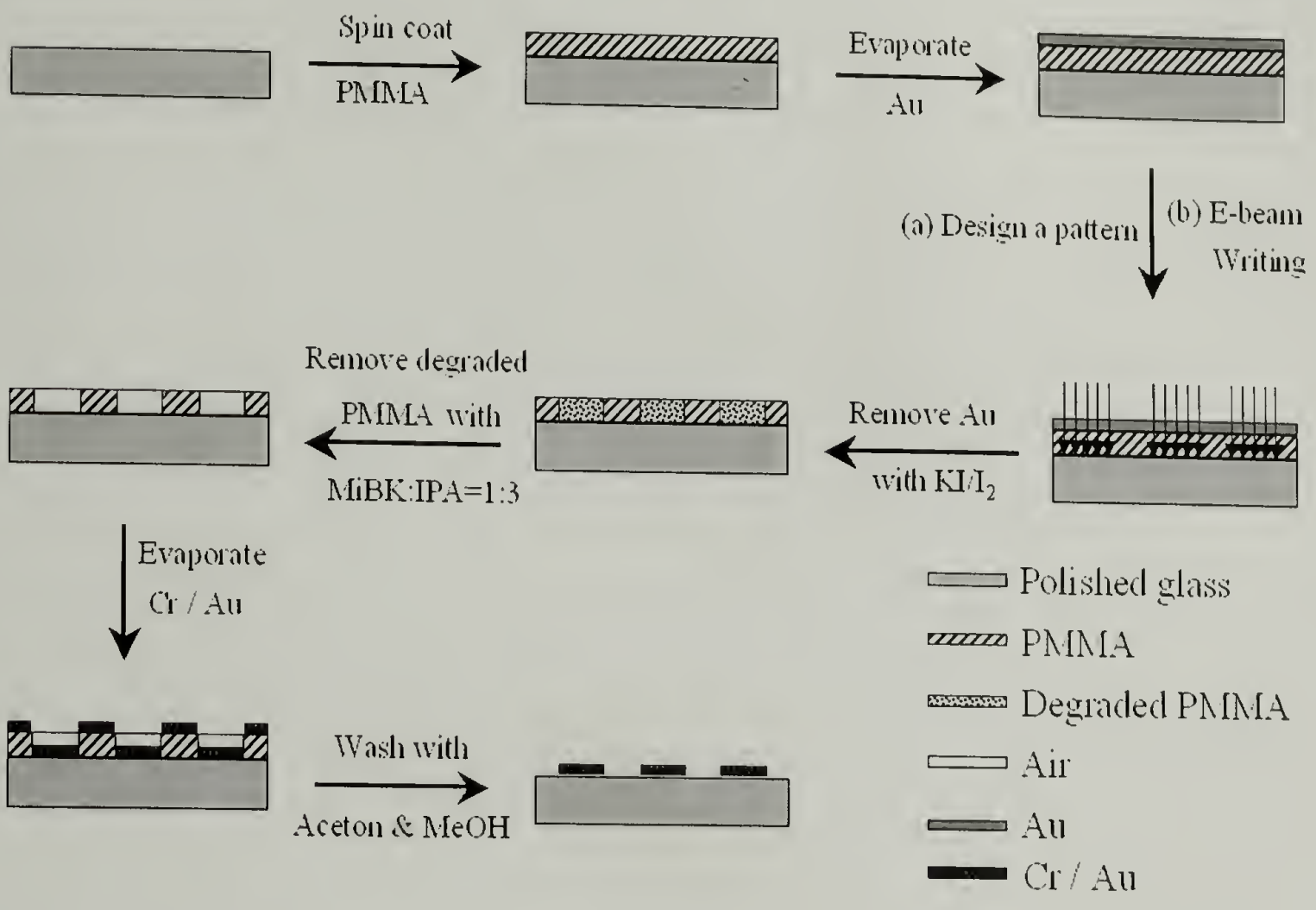

Figure 5.2. Schematic of sample configuration used in the studies from the side view under optical microscope. A single layer liquid film with a film thickness of h_0 is confined between Si wafer (lower electrode) and Cr/Au patterned stripes (upper electrode). A small amount of external electric field is applied across two electrodes. The electrode spacing, d, can be controlled by evaporating thin layer of SiOx as the insulate spacers at the edges of Si wafer. A direct observation of the spatial-temporal evolution of the thin film under Cr/Au stripes is accessible by optical microscope. The size of Cr/Au stripes can be tuned to be different as shown in the figure or be equal (5μm) with periodic spacing (100μm) in between as shown in Figure 5.10.

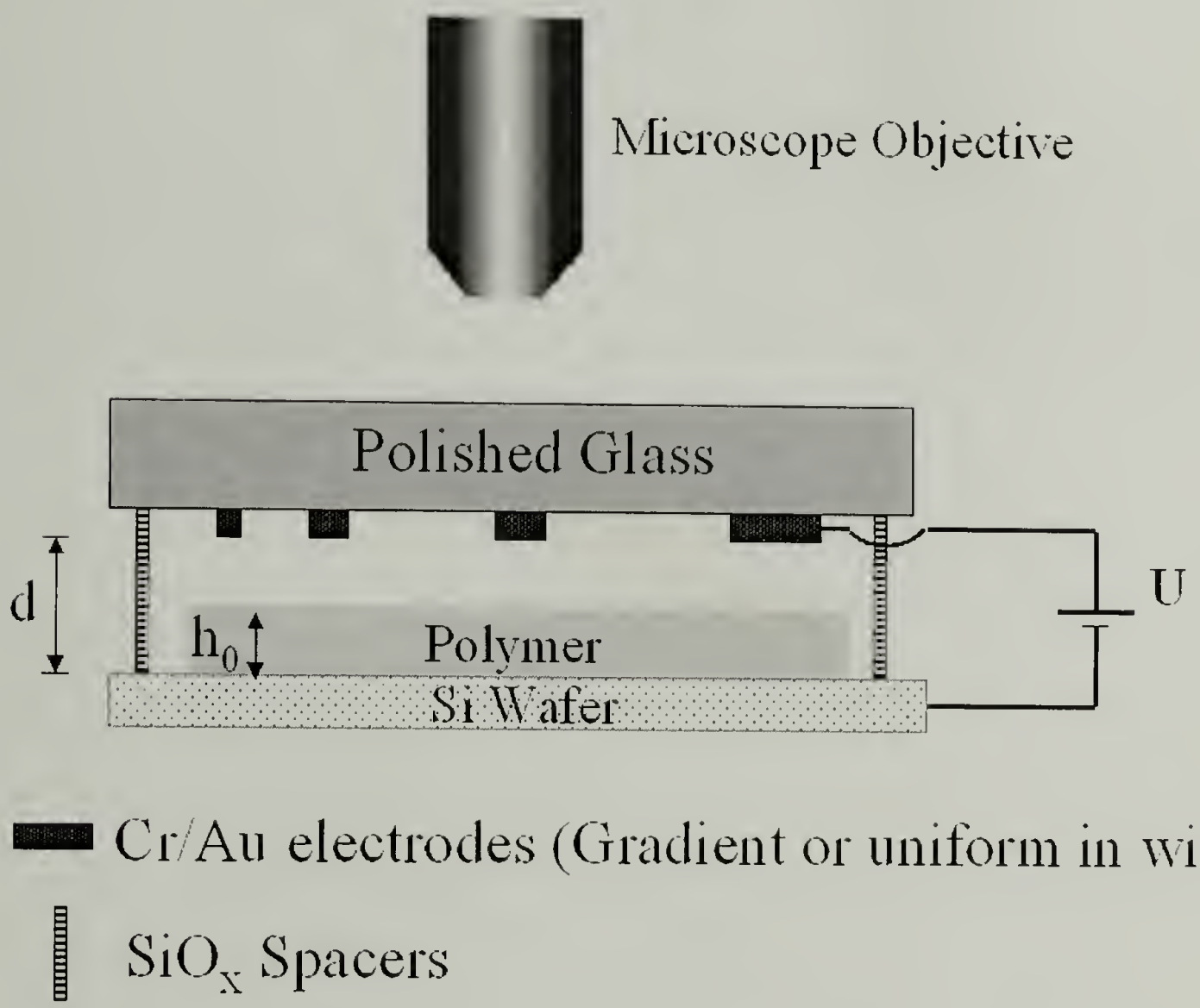

Table 5.1. Experiments list

Sample No.	Width of Cr/Au Stripes (μm)	Film Thickness (nm)	Average Electrode Spacing (μm)	Applied Voltage (V)
1	5, 10 and 50	360	2.0	40
2	5, 10, 50 and 156	360	1.4	40
3	10, 50 and 156	360	1.4	20
4	5	360	1.8	50

field. Since the glass transition temperature of PI is ~ -68°C, it was not necessary to heat the sample, thereby avoiding the generation of thermal gradients. The control experiments, where there was no external electric field applied, showed no development of fluctuations on the PI surface under 5 μm, 10 μm and 50 μm stripes at the room temperature over a time period of 2.25days as shown in Figure 5.3.

Three studies of PI thin films under gradient patterned electrodes Cr/Au were performed where the width of the electrodes were 5 μm, 10 μm, 50 μm and 156 μm, with a 100 μm lateral spacing between 5 μm and 10 μm stripes and 500 μm lateral spacing between 10 μm and 50 μm stripes, respectively. Figure 5.4 shows a series of optical micrographs of the temporal evolution of instabilities in a 360 nm thick PI film beneath a 50 μm wide Cr/Au stripe with 40 V applied at room temperature

(sample 1 in Table 5.1). The electrode spacing, d, is typically 2 μm. The height of the initially flat PI film is seen to fluctuate below the Cr/Au stripe as a direct consequence of the applied field. Since the electric field is stronger at the corner of the electrodes due to field boundary effects, the formation of first PI column at the edge of the electrode is seen at 243 mins. With time, periodic fluctuations grow along the length of the electrode as manifested in the results from 293 mins to 368 mins. With increasing time, more and more PI columns are formed with an average center-to-center distance between columns, $\lambda_{C\text{-}C}$, of 32 μm and column diameters of 13 μm. Similar (not shown) behaviors is seen with the 5 μm and 10 μm wide stripes, where $\lambda_{C\text{-}C}$ is ~31 μm with column diameters of 12 μm, which is much larger than 5μm and 10μm values of electrodes width.

Under the 50 μm stripe, rather than a single row of columns, two rows of columns are formed (sample 2 in Table 5.1) where the electrode spacing, d, was reduced to 1.4 μm while keeping the other parameters equal to those in the previous study (sample 1 in Table 5.1). Shown in Figure 5.5 are the optical micrographs of a 360 nm PI thin film under 5 μm, 10 μm, 50 μm and 156 μm Cr/Au electrodes as a function of time with 40 V applied at the room temperature. By comparing the time scale over which the polymer columns form to that in the previous study, it is clear that the structure formation is much faster with a reduced electrode spacing. Under the 5 μm wide electrode, $\lambda_{C\text{-}C}$ is ~24 μm with column diameters of 10 μm (Figure 5.5a). Similarly under the 10 μm electrode, $\lambda_{C\text{-}C}$ is ~23 μm with column diameters of 10.8 μm (Figure 5.5b). For the 50μm wide electrode, instead of a single row

Figure 5.3. Control experiment where there are no external electric field applied shows nothing happens at PI surface at room temperature. The size of the stripes from left to right are 50 μm, 10 μm and 5 μm, respectively.

Figure 5.4. Temporal evolution of 360 nm PI thin film under 50 μm Cr/Au stripe with a electrode spacing d of 2 μm in 40 V.

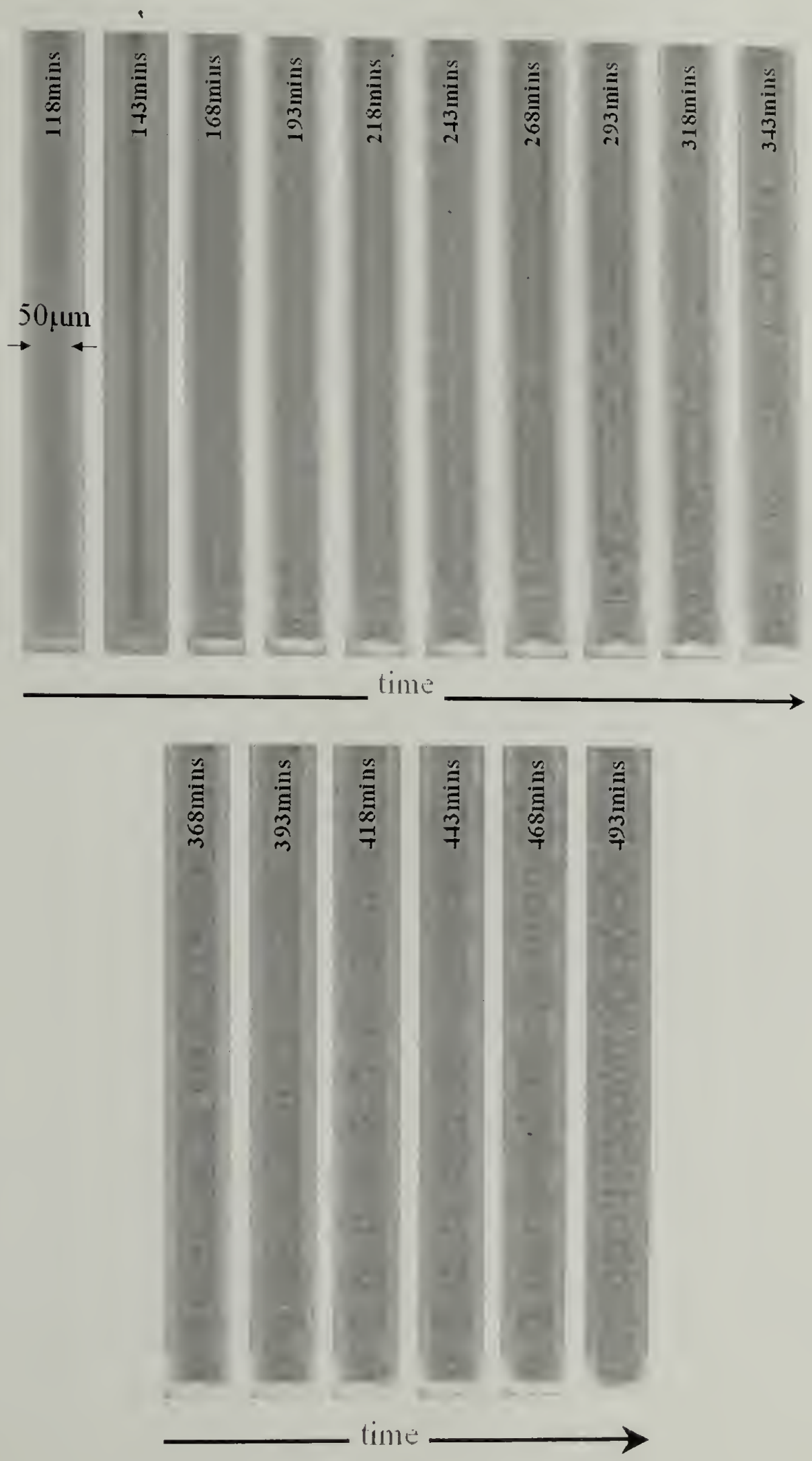

columns, two rows of columns with $\lambda_{C\text{-}C}$ of 24 μm form along the edge of the 50 μm wide electrode due to the increased field resulting from the decrease in the electrode spacing d from 2 μm (Figure 5.4) to 1.4 μm (Figure 5.5c). In addition, the increase in field strength causes the column formation to be more rapid. It takes ~11 mins to completely create the polymer columns, in comparison with ~493 mins in the first study. The time constant τ_{max} at which the instabilities occur is inversely proportional to approximate sixth power of the electric field, E_p, for polymer film confined in between two infinite large electrodes in an electric field[21-25],

$$\tau_{max} = \frac{3\eta\gamma[\varepsilon(d-h_0)+h_0]^6}{U^4\varepsilon^2(\varepsilon-1)^4\varepsilon_0^2h_0^3} = \frac{3\eta\gamma U^2}{h^3\varepsilon^2(\varepsilon-1)^4\varepsilon_0^2E_P^6} \quad (1)$$

where η, γ, h_0, d, U, ε and ε_0 are the viscosity, surface tension, the film thickness, the electrode spacing, the applied voltage, the dielectric constant of the liquid and the permittivity in vacuum, respectively. Consequently, the decrease in the time to form the columns may be expected from the size reduction. However, the influence of field boundary effects is evident and the simple scale for the infinite electrodes is not directly applicable. Structure formation begins at the edge of the 156 μm wide electrodes as shown in Figure 5.5d. The enhancement of instability at the film surface propagates from the side of the electrode. Along the electrode, $\lambda_{C\text{-}C}$ is ~24 μm with an average column diameter of 10.8 μm, identical to those for the 5, 10 and 50 μm wide electrodes. The autocorrelation functions of the structures formed under 5, 10, 50 and 156 μm wide electrodes are shown in Figure 5.6a. The cross sections of autocorrelation function patterns along the length and across the width of the electrodes are given in Figure 5.6b and 5.6c, respectively, from which both $\lambda_{C\text{-}C}$

along the length and across the width of the electrodes can be determined. The invariance of $\lambda_{C\text{-}C}$ of ~24 μm along the length of the electrode is clearly evident (Figure 5.6a). However, $\lambda_{C\text{-}C}$ across the width of the electrode is significantly impacted by the electrode width. 37 μm and 24 μm values are obtained under 50 μm and 156 μm wide electrodes, which are the reminiscence of distorted (under 50 μm) and normal (under 156 μm) hexagonal lattices, respectively, shown in Figure 5.6a.

It is obvious that the structure formation is much faster under 5μm and 10μm wide electrodes than those under 50 μm and 156 μm wide electrodes. This suggests that the stronger field boundary effects at the two edges of 5 μm and 10 μm stripes induce the stronger heterogeneity of the driving force, in comparison to that of the 50 μm and 156 μm cases. This is supported by the potential line calculations shown in Figure 5.7, where the larger field strength difference between the air layer (37 V drops over a distance of 1.04 μm) and the polymer thin film (3 V drops over a distance of 0.36 μm) under 5 μm wide electrode (Figure 5.7 a) is seen, in comparison with that under 50 μm wide electrode (35 V and 5 V drop over a distance of 1.04 μm and 0.36 μm in the air layer and the polymer thin film, respectively (Figure 5.7 b), which, in turn, produces a stronger driving force.

In the third study (sample 3 in Table 5.1), a thin PI film was placed under 20 V with an electrode spacing d of 1.4 μm. The temporal evolution of the electrohydrodynamic instabilities under 156 μm wide Cr/Au electrodes is shown in Figure 5.8b. The amplitudes of fluctuations on the surface of the film are markedly enhanced at the edges of the electrodes, leading to the formation of columns at the edge due to the heterogeneity of the electric field at the corners of the electrode.

Figure 5.5. Structure development of 360 nm PI thin film beneath different width Cr/Au stripes (a: 5 μm, b: 10 μm, c: 50 μm and d: 156 μm) with the electrode spacing d of 1.4 μm in 40 V.

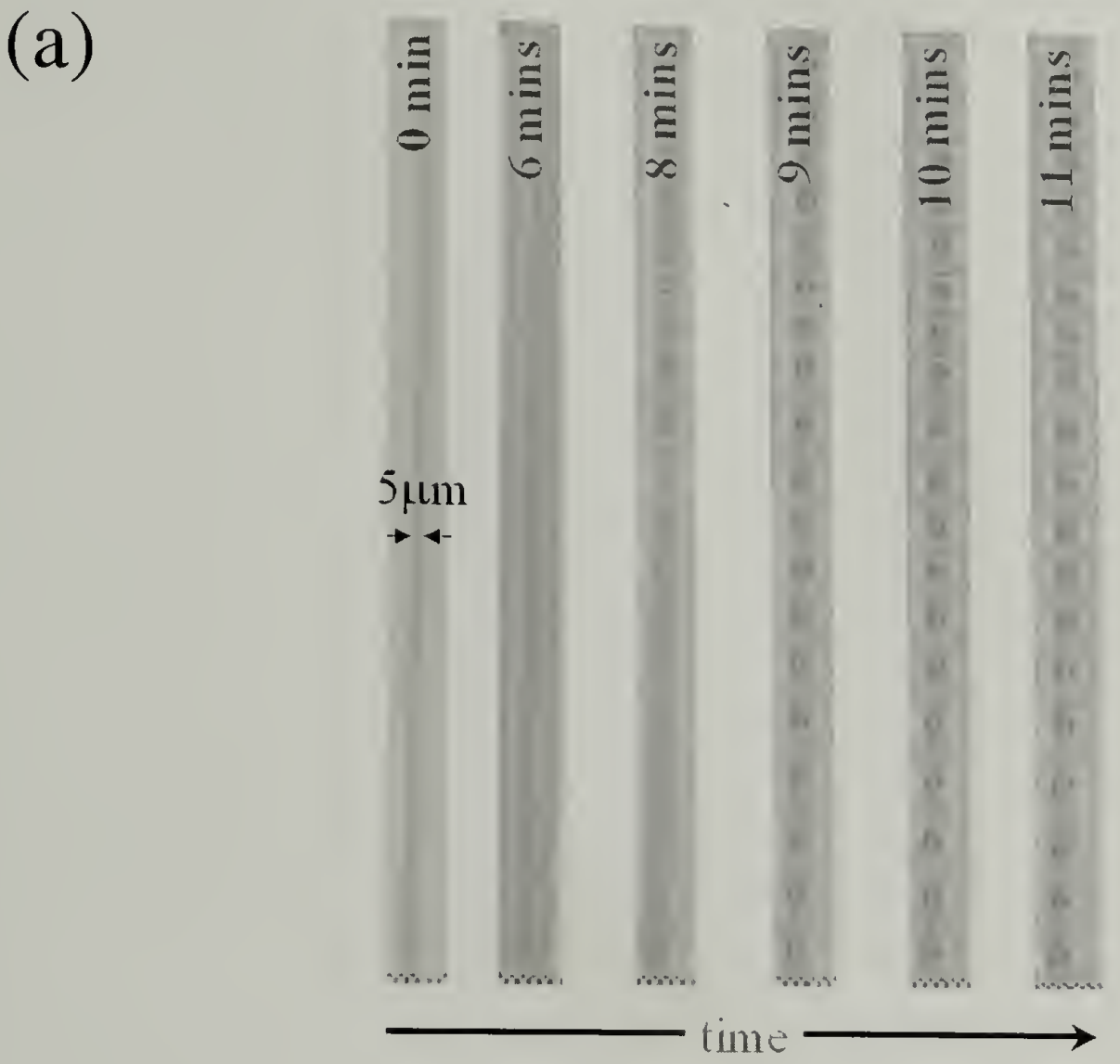

Continued on next page

Figure 5.5, continued

(b)

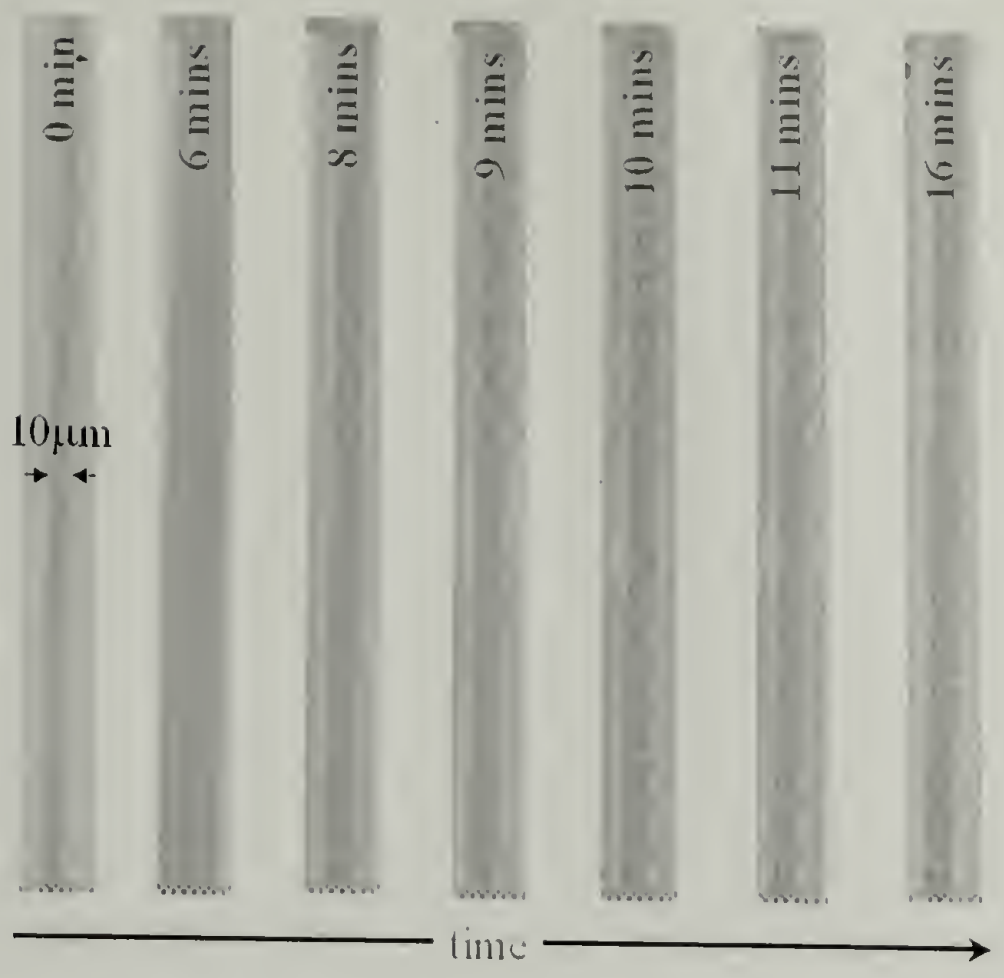

(c)

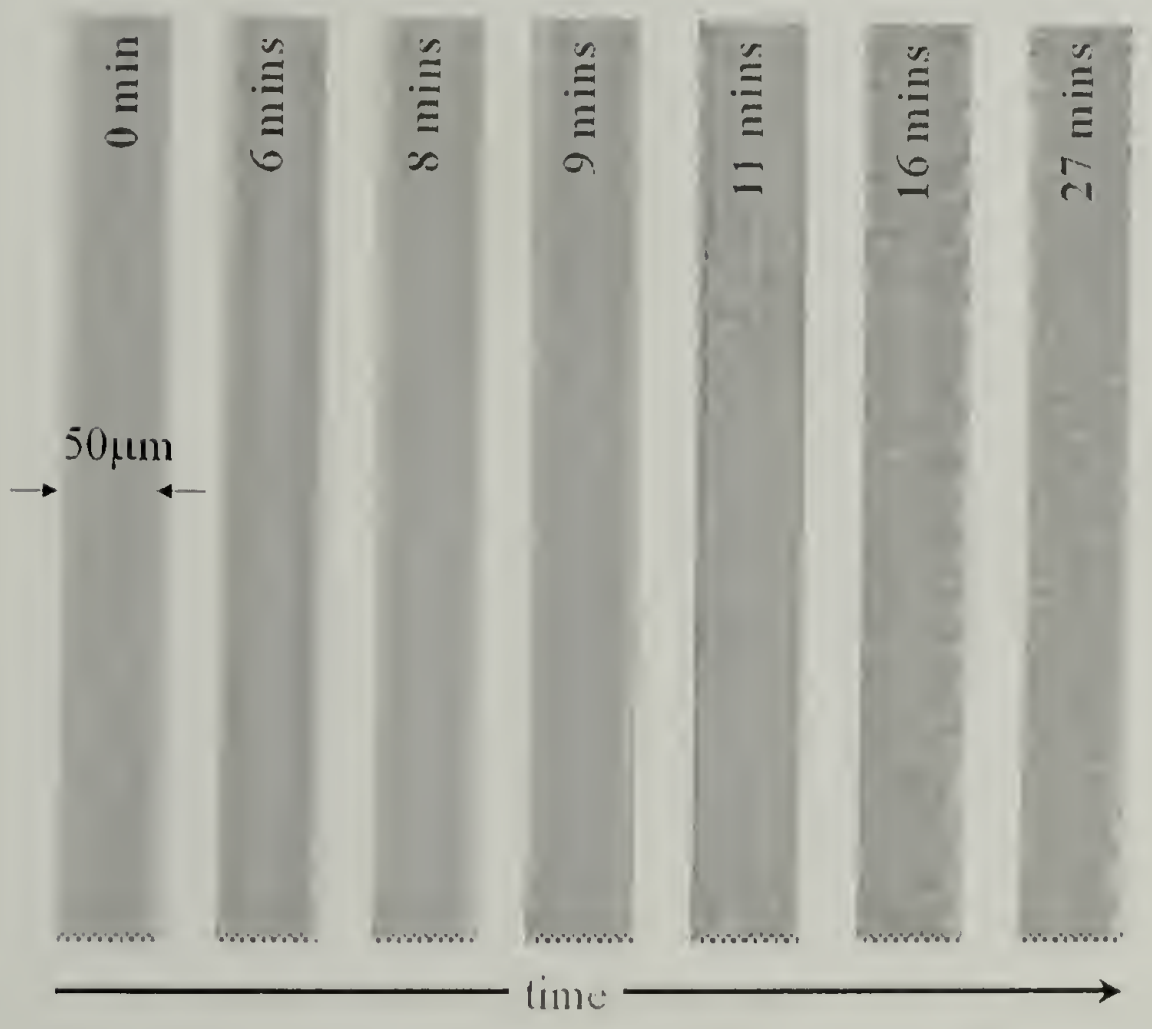

Continued on next page

(d)

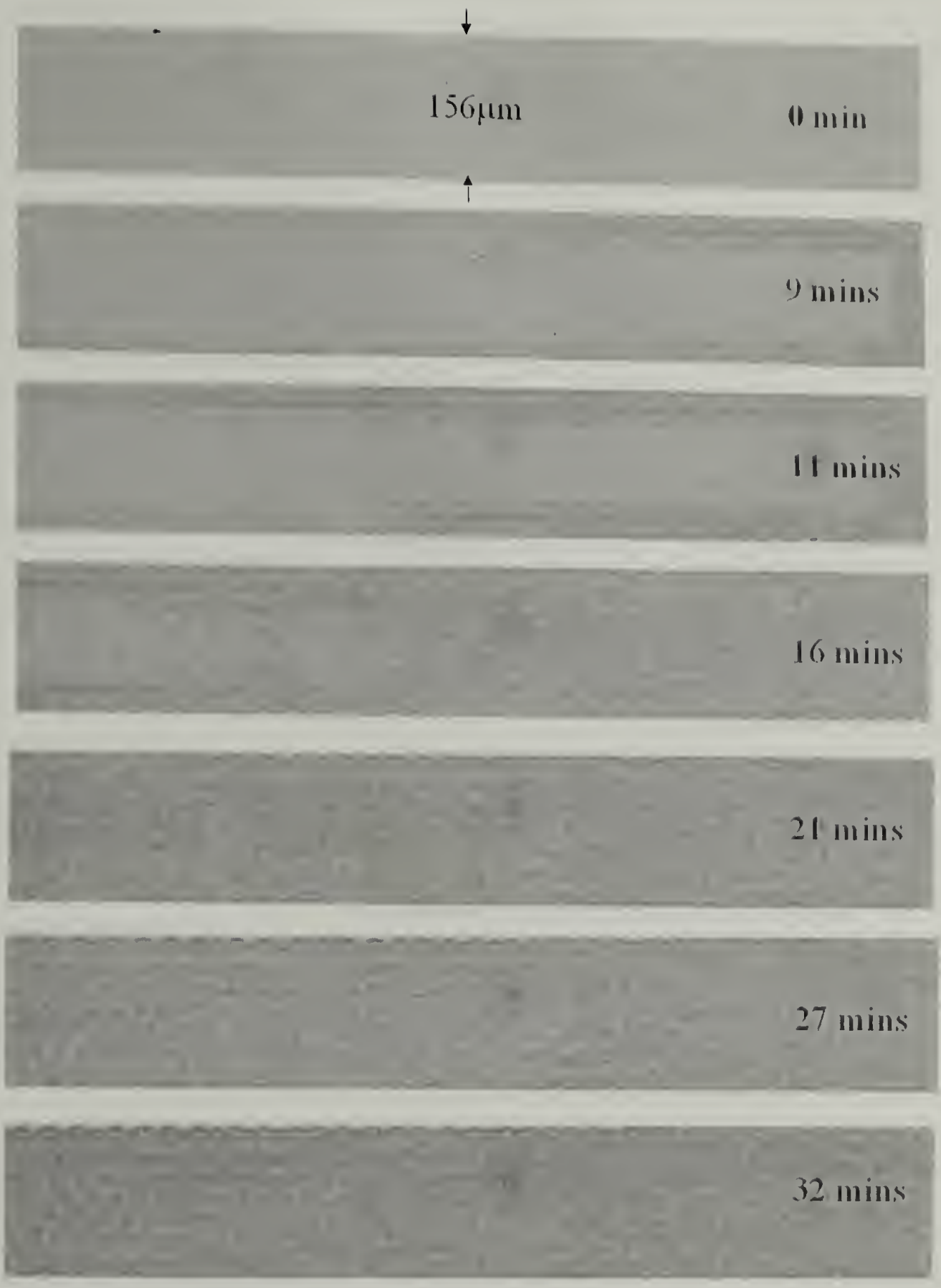

Figure 5.6. (a) Autocorrelation functions of optical images shown in Figure 5.5. (b) Section analysis of autocorrelation functions along the length of 5, 10, 50 and 156 μm wide electrodes. (c) Section analysis of autocorrelation functions across the width of 50 and 156 μm wide electrodes, respectively.

(a)

5μm 10μm 50μm 156μm

Continued on next page

Figure 5.6, continued

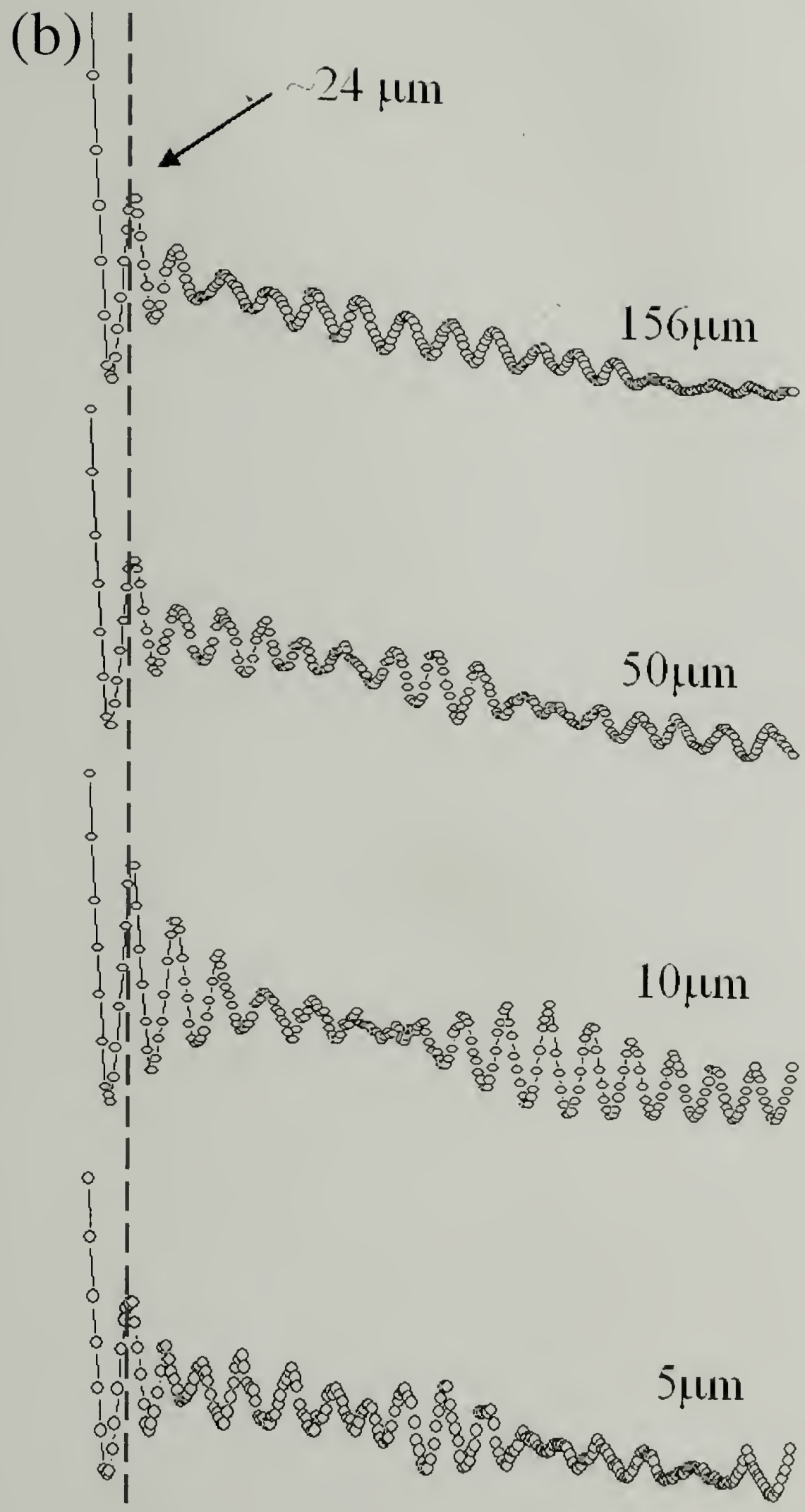

Continued on next page

(c)

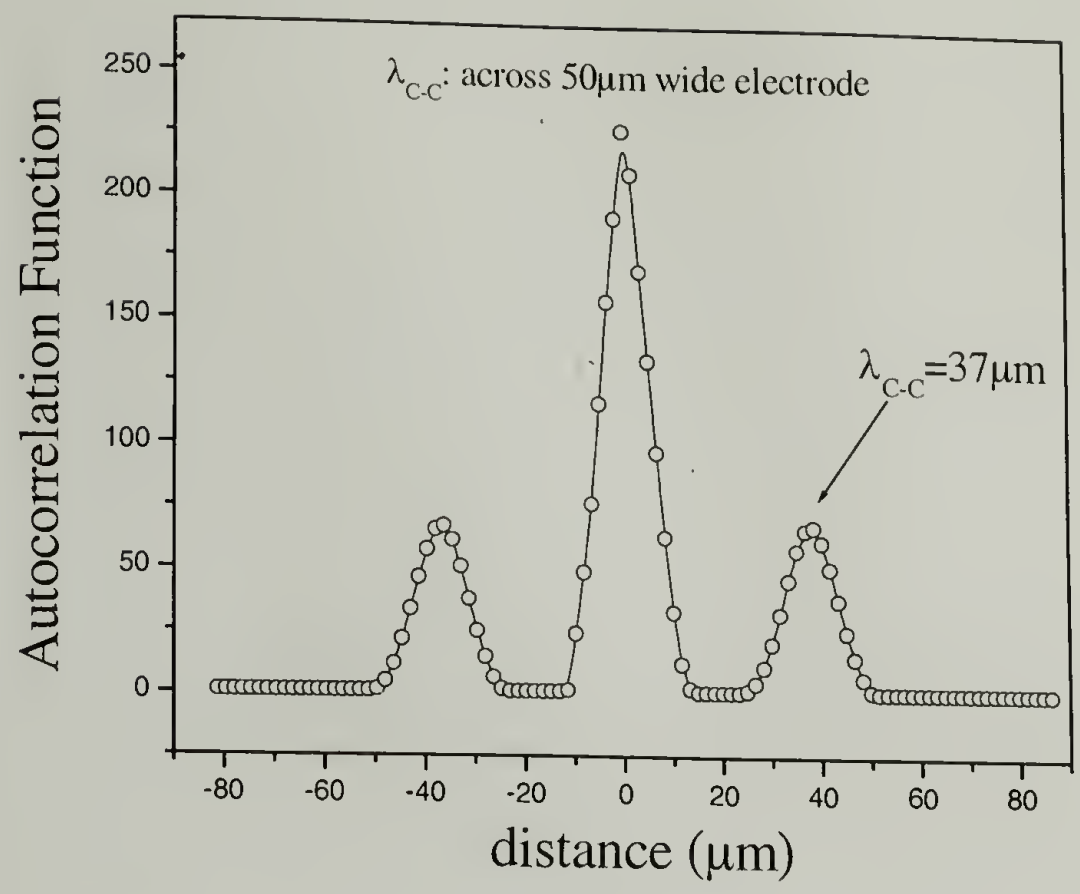
$\lambda_{C\text{-}C}$: across 50μm wide electrode
$\lambda_{C\text{-}C}$=37μm
Autocorrelation Function
distance (μm)
250
200
150
100
50
0
-80
-60
-40
-20
0
20
40
60
80

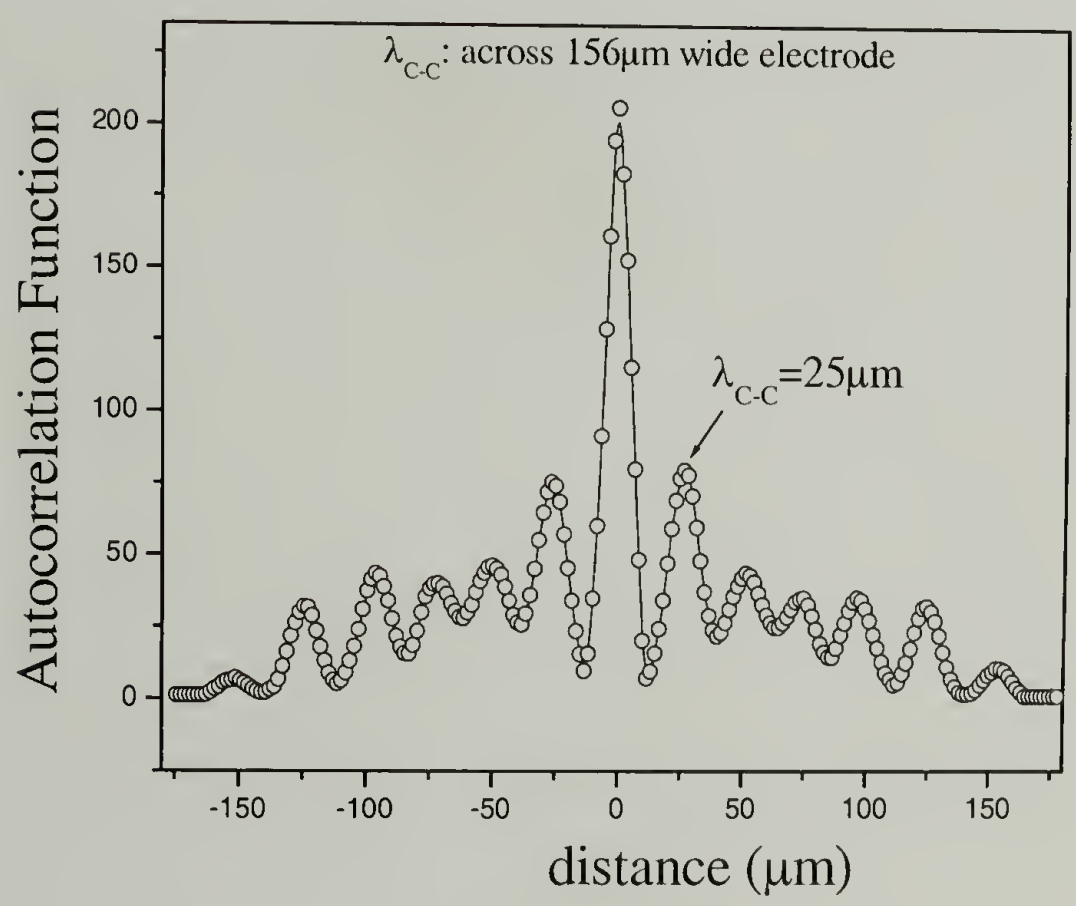
$\lambda_{C\text{-}C}$: across 156μm wide electrode
$\lambda_{C\text{-}C}$=25μm
Autocorrelation Function
distance (μm)
200
150
100
50
0
-150
-100
-50
0
50
100
150

They are amplified subsequently to form the hexagonal structures. No further changes are found later. With a reduced applied voltage, $\lambda_{C\text{-}C}$ increased to 43 μm, where five rows of PI columns were obtained. This contrasts seven rows of the columns found in the second study (Figure 5.5d) where 40 V was applied. However, two rows of columns with a $\lambda_{C\text{-}C}$ of 45 μm were obtained parallel to the edge of 50μm wide electrode (Figure 5.8a). With decreasing voltage, the applied field decreased, reducing the driving force to enhance fluctuations. In addition, the time required to produce the columnar structures increased. The autocorrelation function analysis of the corresponding optical micrographs show highly distorted hexagonal lattice under 50 μm wide electrode (not shown), in contrast to the regular hexagonal lattice 156 μm obtained under 156 μm wide electrode (not shown).

Figure 5.9 summarizes the center-to-center distance of the columns, $\lambda_{C\text{-}C}$, along the length of the electrodes and the number of rows of the PI columns formed normal to the width of the electrodes. With increasing width, the number of rows increased while the characteristic separation distance along the electrode remained constant.

The development of structure under periodic electrodes was also studied. Figure 5.10 shows a series of the optical micrographs illustrating the growth of PI columns under 5 μm periodic stripes separated by 100 μm with 50 V applied as a function of time at room temperature. The surface is featureless before 3 mins. After 4 mins, as judged by the changes in the interference colors, the film thickness changes both underneath and adjacent to the stripes. A row of the periodic variations in the thickness is seen along the stripes after 11mins. After 15 mins, well-defined

Figure 5.7. The model calculations of electric field and potential lines. 360 nm thin films (ε=2.37) are exposed to 40 V under 5 μm single stripe (a: potential line), 50 μm single stripe (b: potential line) and 5μm periodic stripes separated by 25 μm spacing (c and d: field line and potential line, respectively), respectively, with a electrode spacing d of 1.4μm.

(a)

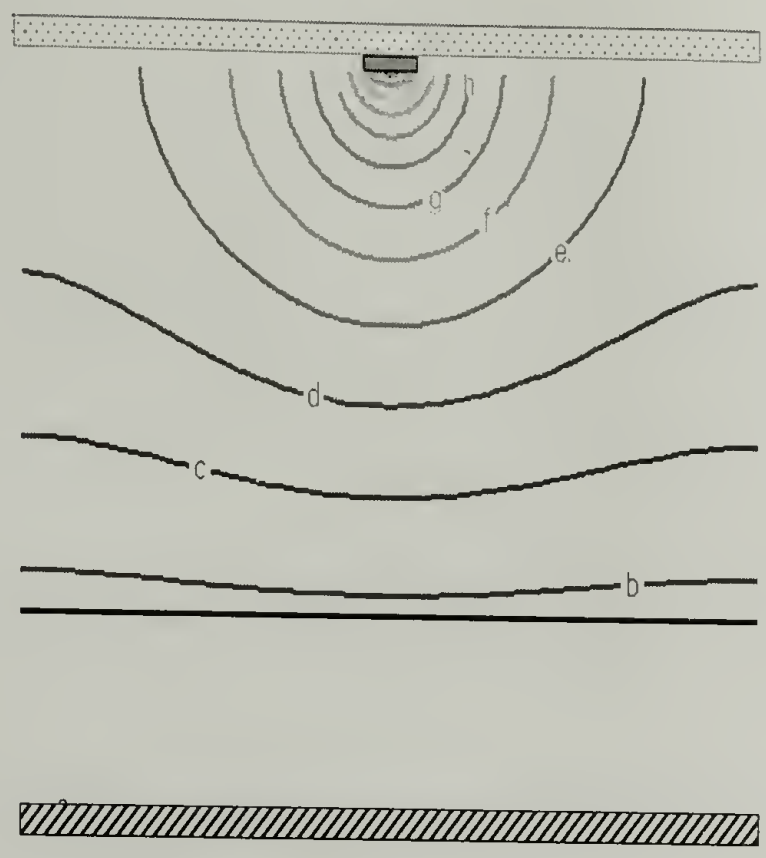

(b)

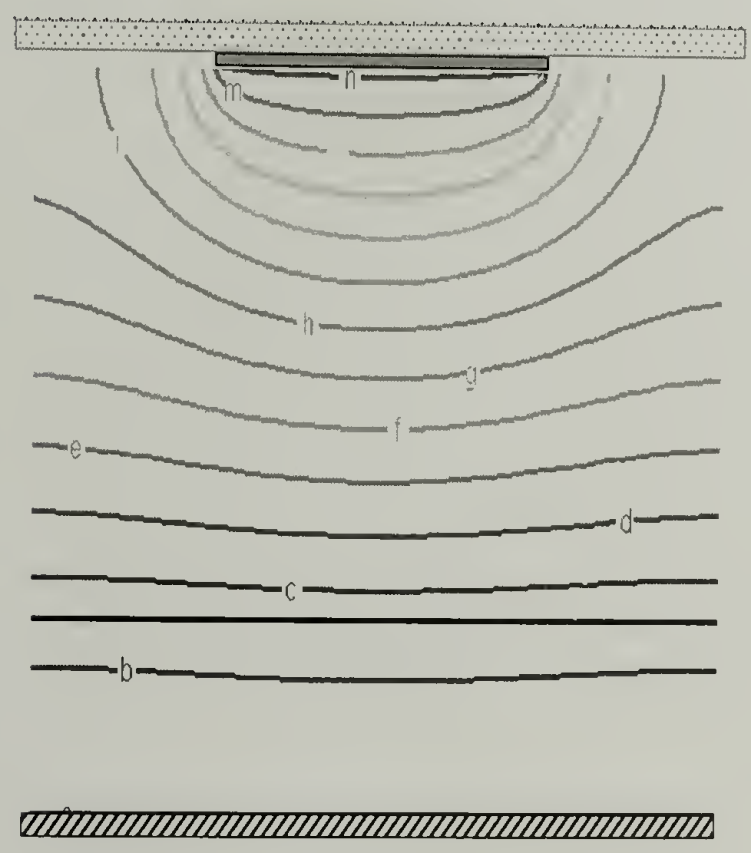

Continued on next page

(c)

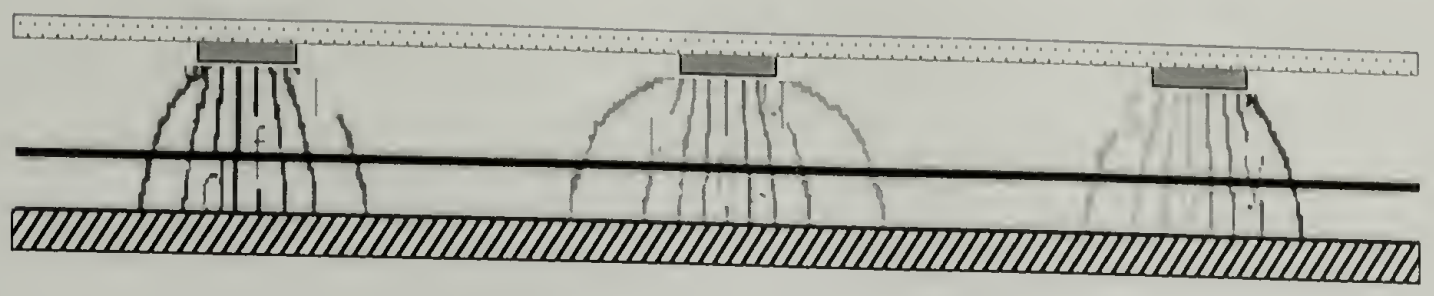

(d)

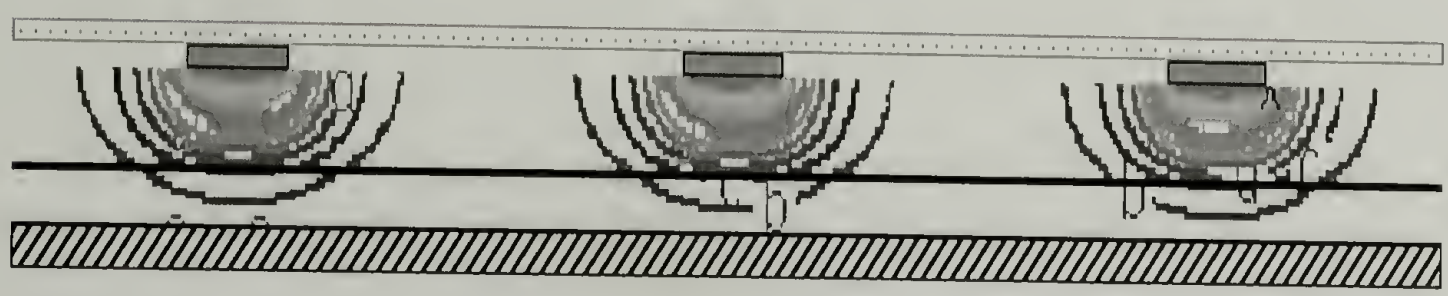

Figure 5.8. Structure development of 360 nm PI thin film beneath different width Cr/Au stripes (a: 50 μm and b: 156 μm) with an electrode spacing d of 1.4 μm in 20 V.

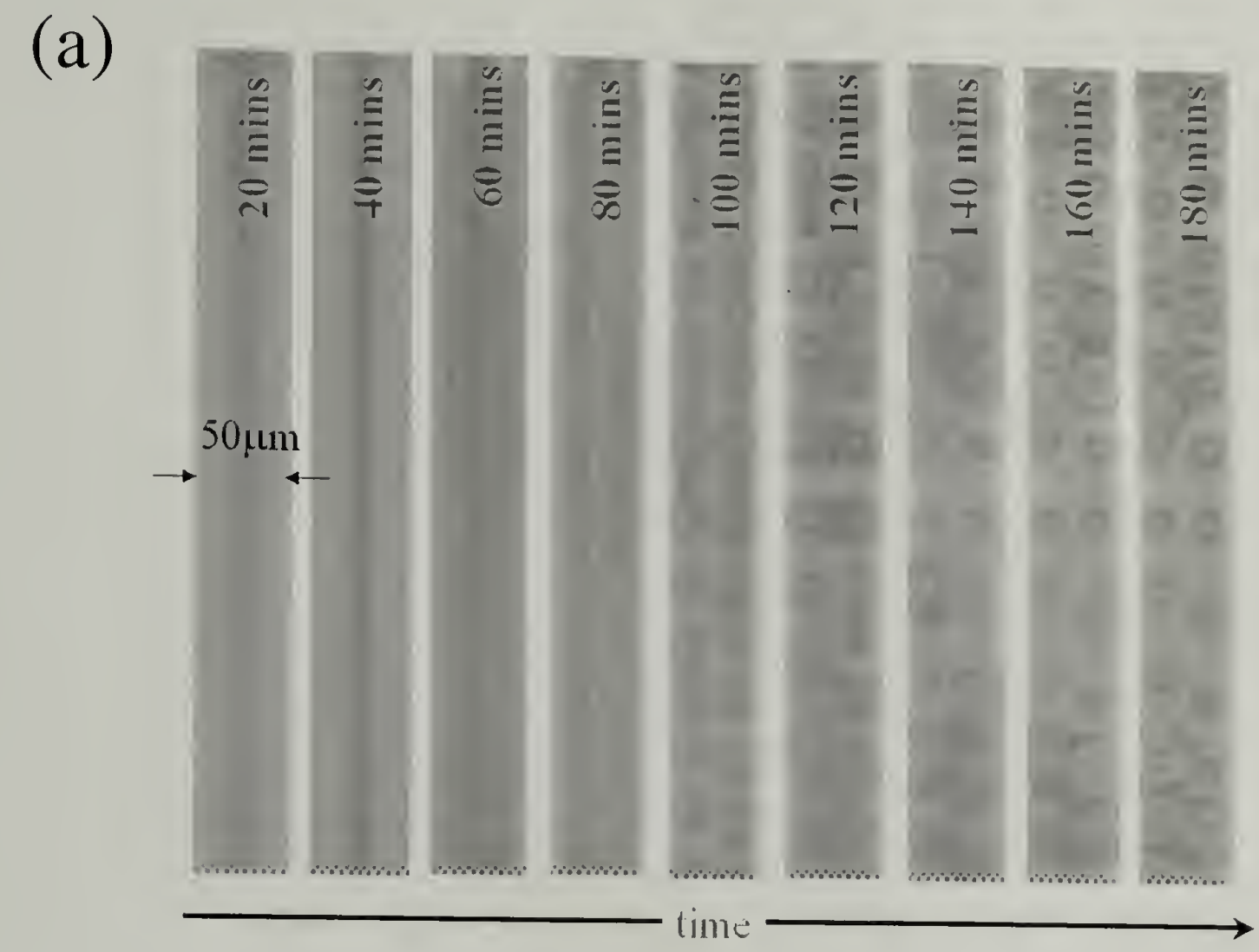

Continued on next page

Figure 5.8, continued

(b)

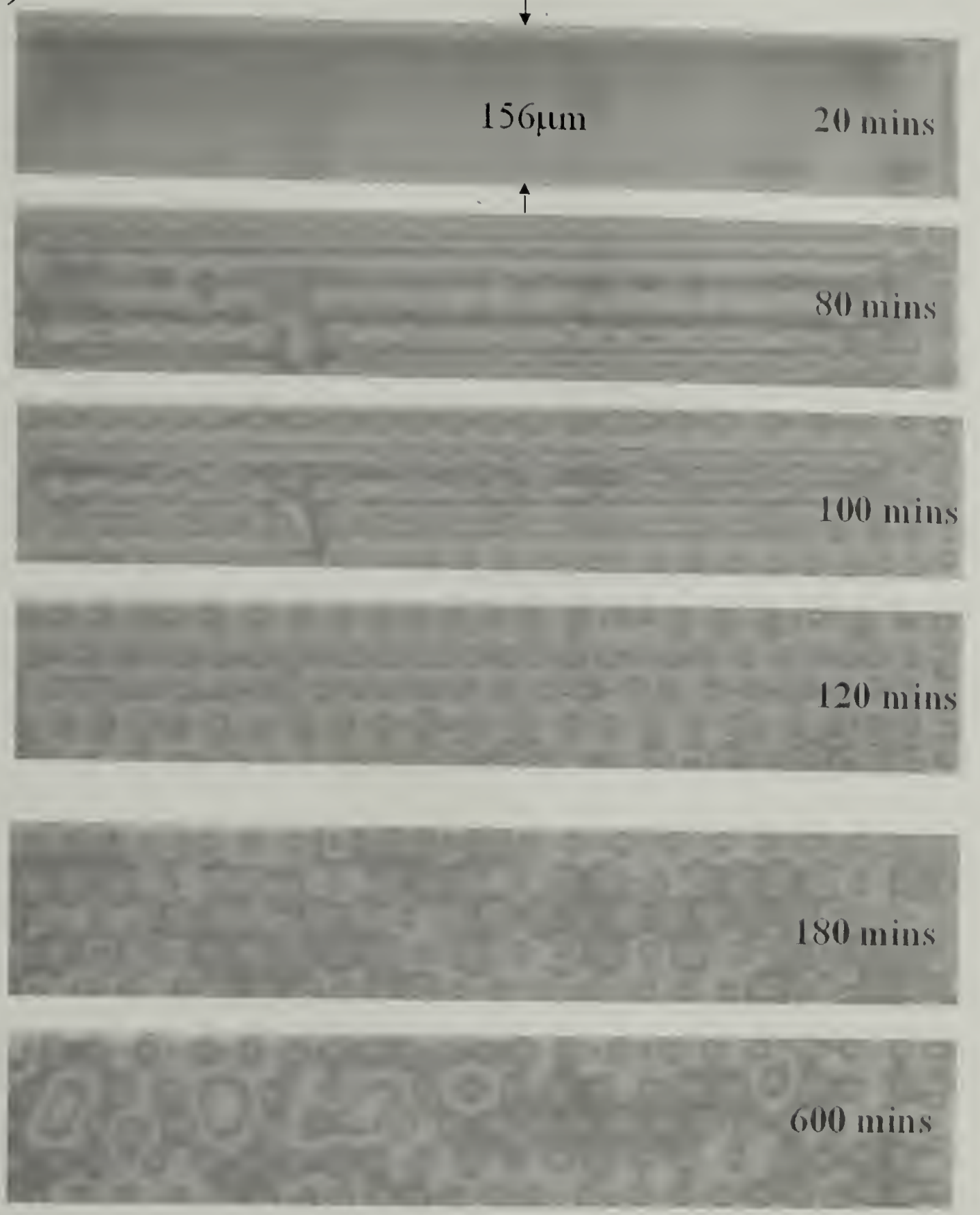

Figure 5.9. The center-to-center distance, $\lambda_{C\text{-}C}$, of polymer columns along the length of the electrodes in three systematic studies is shown in (a), where 360 nm PI thin film is exposed to ✳: 20 V, ★: 40 V and ○: 40 V with the electrode spacings of 1.4 μm, 2.0 μm and 1.4 μm, respectively. The number of rows of PI columns normal to the width of electrodes is shown in (b).

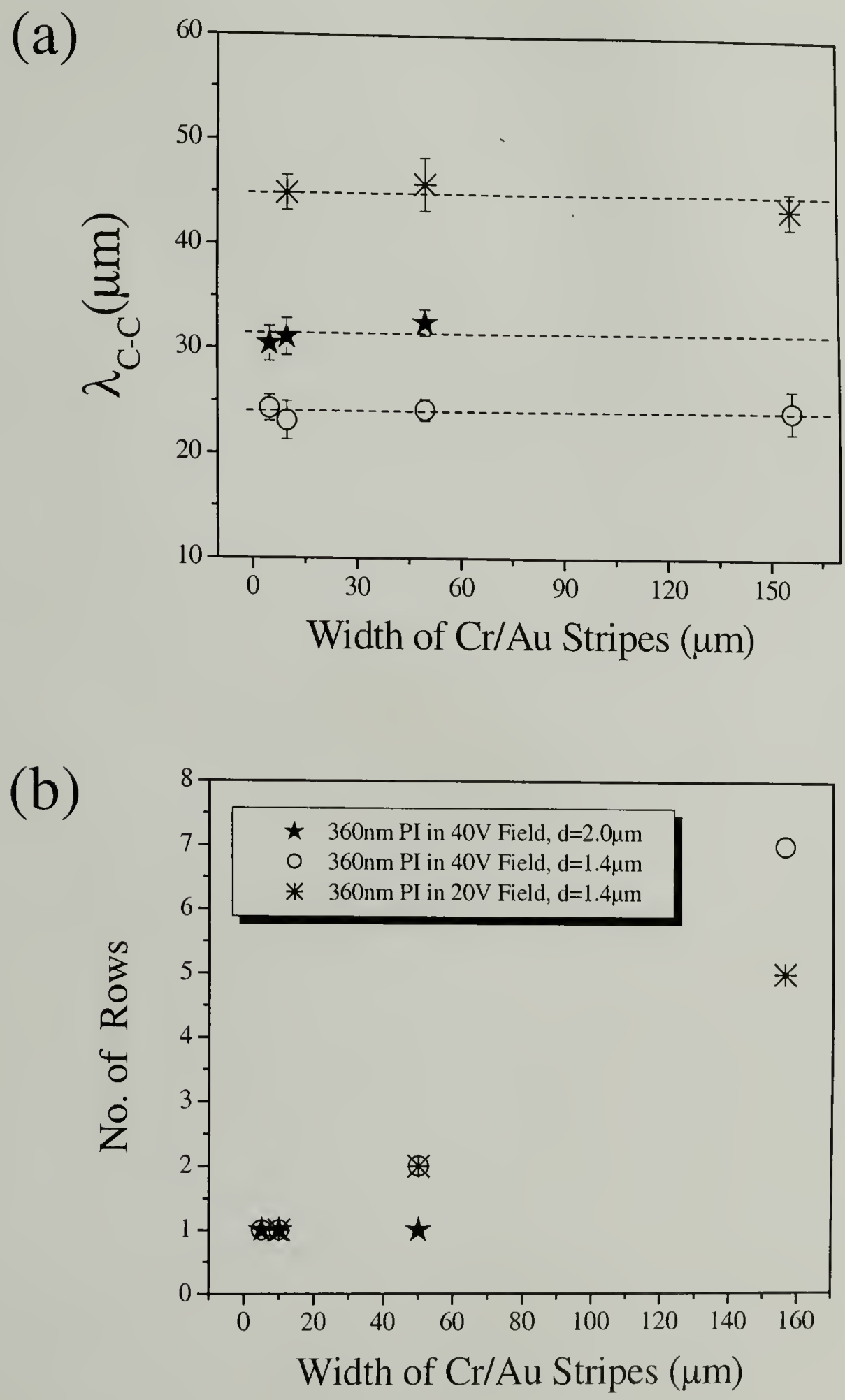

columns with $\lambda_{C\text{-}C}$ of 30 μm are evident. The uniform color of the film outside the electrode area shows that the film is undisturbed for times less than 16 mins. Thereafter the instabilities are evident along the sides of the stripes.

Ideally, instabilities are enhanced only underneath the patterned electrodes. The formation of structure outside of the electrode area results, more than likely, from the changes in the film topography due to flow of polymer into the structures forming under the electrodes, coupled with the extension of the electric field lines beyond the edges of the electrodes. This is shown in Figure 5.7 c and d, where weaker field is clearly evident.

While the replication of topographic features with patterned electrode using both electrostatic and thermal gradients has been investigated in great details[21,30], the structure formation shown here must precede replications. While a substantial coarsening of the structures was not evident in these studies, by increasing the film thickness at the fixed electrode spacing or using a smaller size of the patterned electrodes with the controlled wettability, replication can be realized. When the different shape mask patterns are applied, such as, circles and hexagons, interesting dynamic behavior might occur due to the field boundary effects.

Some Other Observations

As shown in the field line and potential lines calculations, field boundary effects at the sides of patterned stripes cause an inhomogeneity of the electrostatic force, which, in turn, induces the formation of structure outside of the electrode region. Another good example of this effect is shown in Figure 5.11, where UMASS

Figure 5.10. Structure formation of 360 nm PI thin film under 5 μm periodic Cr/Au stripes separated by 100 μm with an electrode spacing d of 1.8 μm in 50 V.

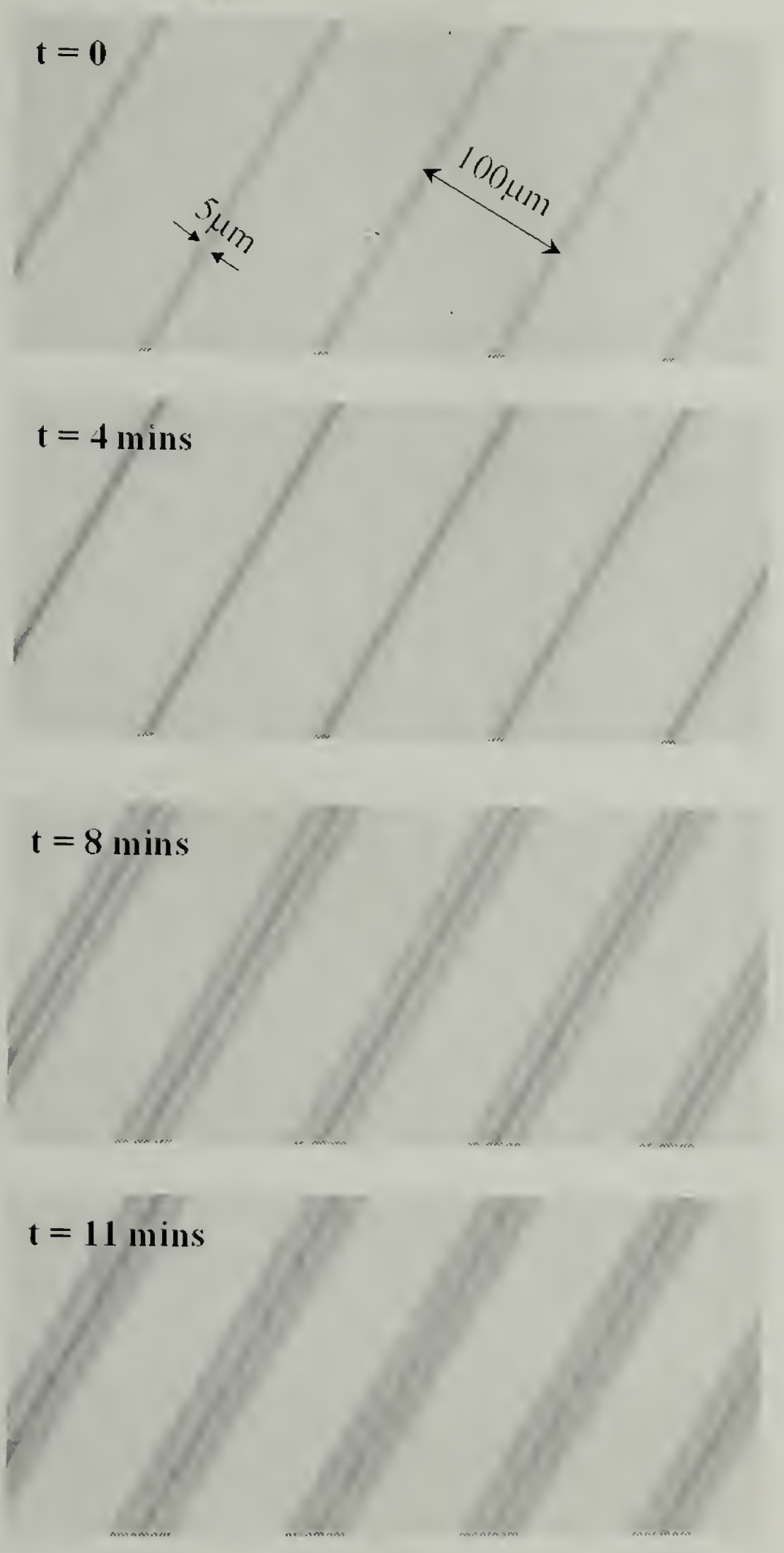

Continued on next page

Figure 5.10, continued

Continued on next page

Figure 5.10, continued

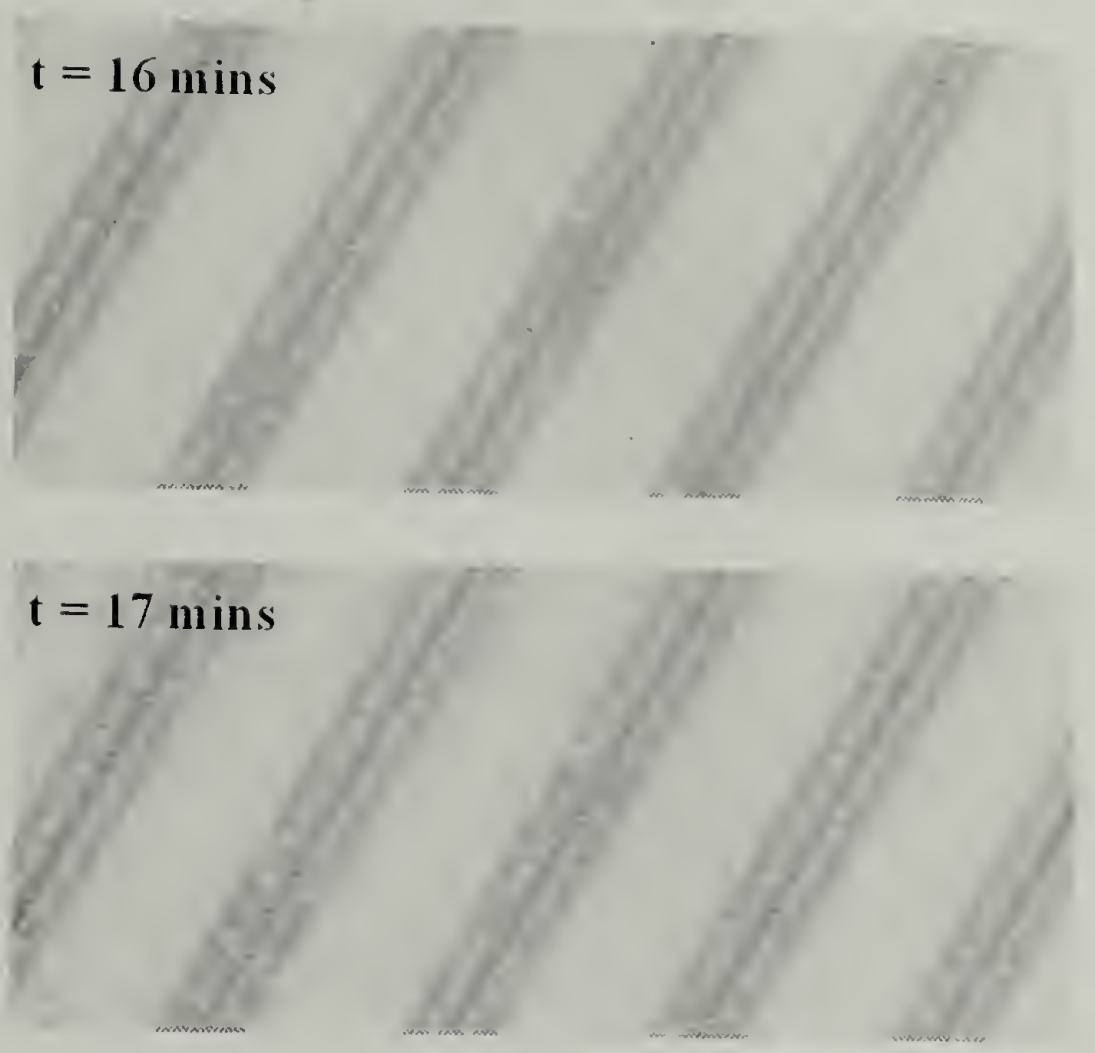

was used as a pattern in the upper electrode. The liquid polymer film under UMASS responds applied external electric field after 10 mins. However, in addition to the replication of the structures, instabilities in the film are seen outside of this area, giving rise to column formation.

If the applied external electric field is not strong enough, fluctuations still grow, although columns formation and replication do not occur. Shown in Figure 5.12 are the optical micrographs of PI thin film exposed in 50 V. Figure 5.13 shows the topologies of 96K PS thin film surface after exposed to electric field, where the cylindrical ridge is obvious.

Figure 5.11. PI thin film in electric field. The field boundaries effects on the structure formation imposed by the curved pattern (UMASS) are clearly evident.

Figure 5.12. 340 nm PI thin film is exposed to 50V under 5 μm stripes separated by 100 μm. The image sizes are 1062x797μm^2. (a) and (b) Before and after exposed to the electric field; (c) and (d) The formed structures before and after removal of the Cr/Au periodic stripes.

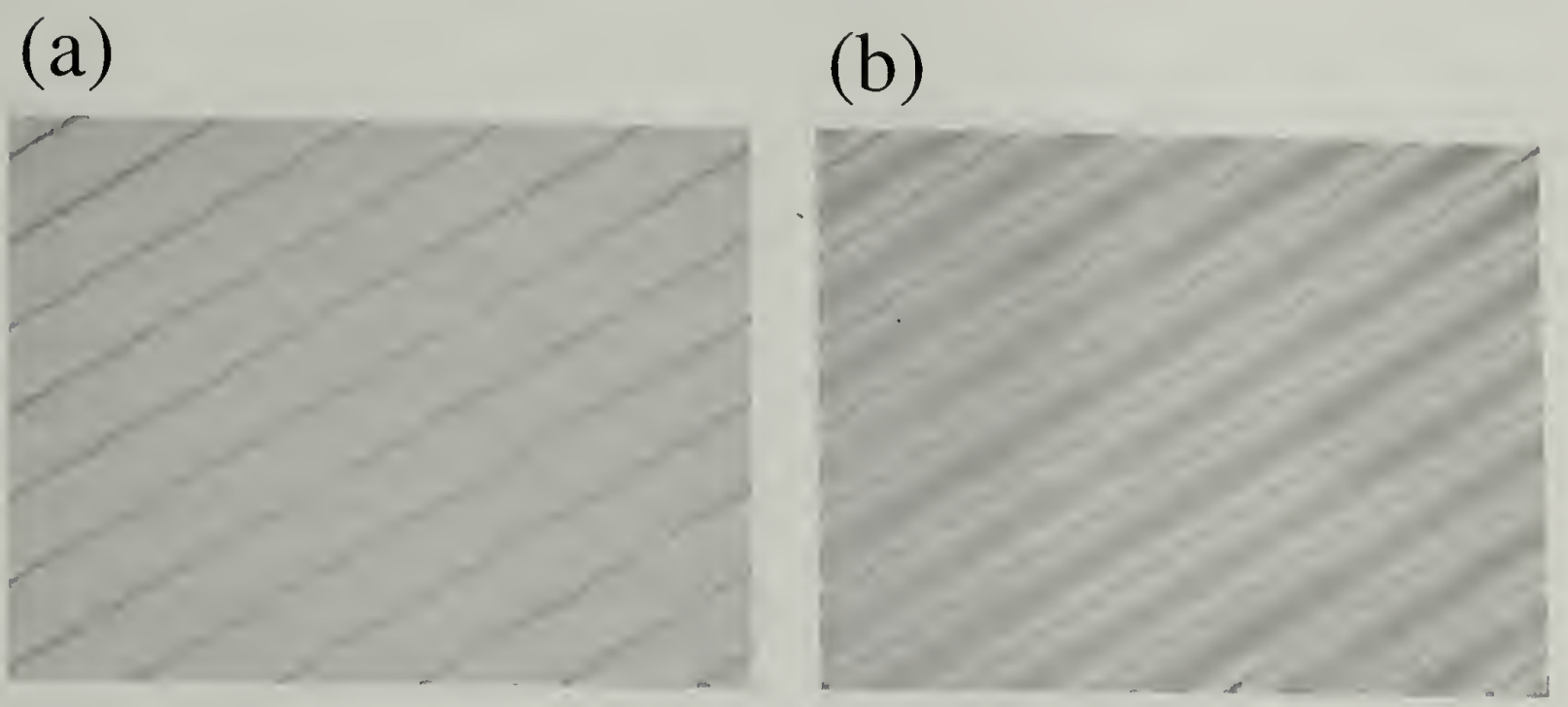

Figure 5.13. 96K PS thin film under 10 μm Cr/Au stripe in the electric field. (a) 2D AFM height image, (b) 3D AFM height image, (c) Section analysis of the AFM scan.

(a)

(b)

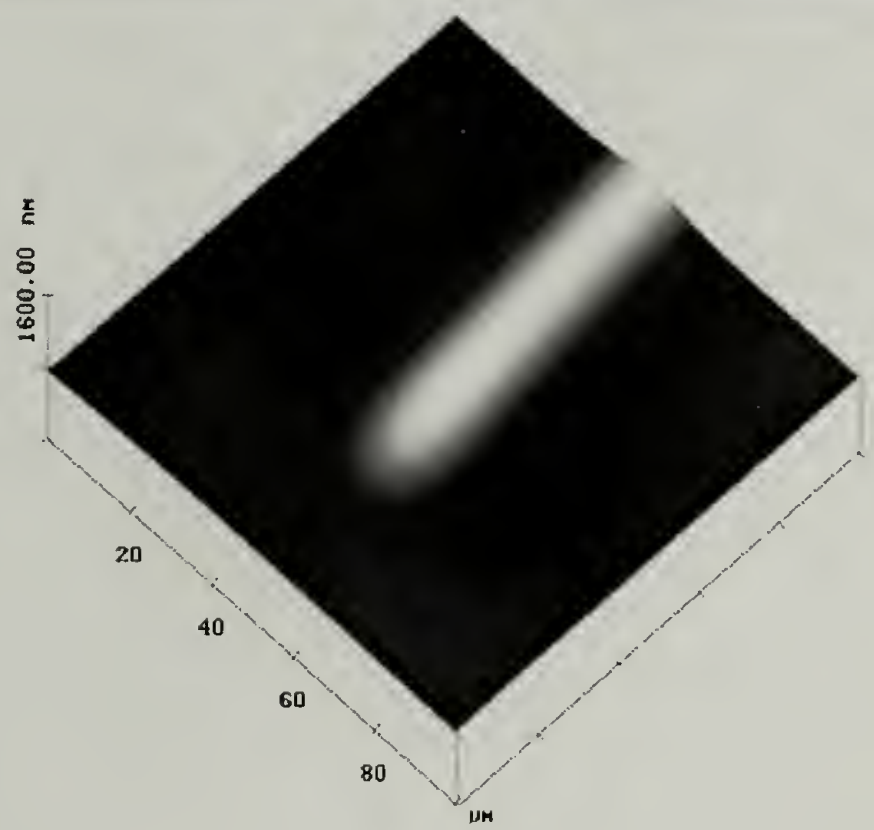

(c)

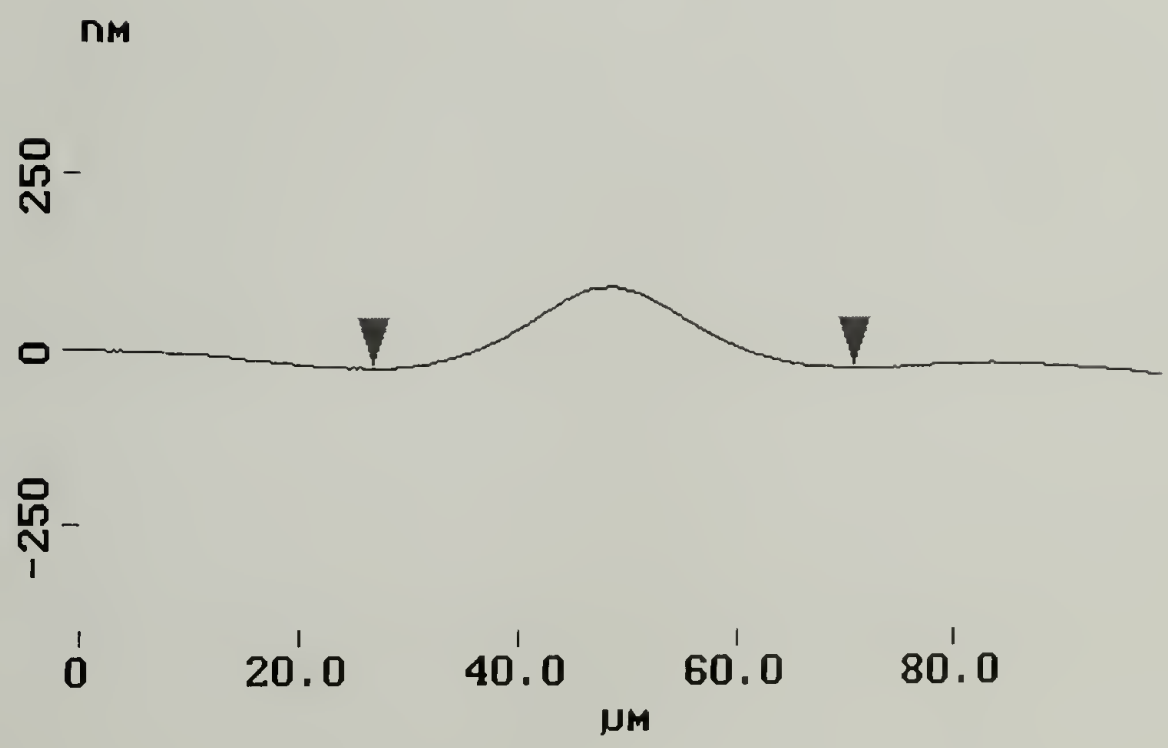

Conclusions

A laterally heterogeneous external electric field imposed by a patterned electrode is shown to be effective to destabilize the thin film surface and lead to replication. The evolution of electrohydrodynamic instabilities leads to the columnar structure formations directly under the imposed patterns and was studied as a function of the time. The center-to-center distance, λ_{c-c}, between the columnar structures along the length of the electrodes is found to be independent of electrodes width. However, the λ_{c-c} across the width of the electrodes is significantly impacted by the electrode width. Consequently, a finite size effect is seen. Studies as a function of the electrode width and characteristic wavelength of the instabilities should lead to a fundamental understanding and optimization of the pattern replication and transfer and impact the extension of the process to more complicated pattern design.

References

1. deGennes, P. G. Wetting: statics and dynamics. *Reviews of modern physics* **57**, 827-863 (1985).

2. Brochard-Wyart, F. & Daillant, J. Drying of solids wetted by thin liquid films. *Can. J. Phys.* **68**, 1084-1088 (1990).

3. Brochard-Wyart, F., Martin, P. & Redon, C. Liquid/liquid dewetting. *Langmuir* **9**, 3682-3690 (1993).

4. Brochard-Wyart, F., Debregeas, G. & deGennes, P. G. Spreading of viscous droplets on a non viscous liquid. *Colloid Polym Sci* **274**, 70-72 (1996).

5. Reiter, G. Dewetting of thin polystyrene films. *Phys. Rev. Lett.* **68**, 75-78 (1992).

6. Khanna, R. & Sharma, A. Pattern formation in spontaneous dewetting of thin apolar films. J Colloid and Interface *Science* **195**, 42-50 (1997).

7. Sharma, A. & Khanna, R. Pattern formation in unstable thin liquid films. *Physical Review Letters* **81**, 3463-3466 (1998).

8. Konnur, R., Kargupta, K. & Sharma, A. Instability and morphology of thin liquid films on chemically heterogeneous substrates. *Physical Review Letters* **84**, 931-934 (2000).

9. Kargupta, K., Konnur, R. & Sharma, A. Instability and pattern formation in thin liquid films on checmically heterogeneous substrates. *Langmuir* **16**, 10243-10253 (2000).

10. Kargupta, K. & Sharma, A. Dewetting of thin films on periodic physcially and chemically patterned surfaces. *Langmuir* **18**, 1893-1903 (2002).

11. Boltau, M., Walheim, S., Mlynek, J., Krausch, G. & Steiner, R. Surface induced structure formation of polymer blends on patterned substrates. *Nature* **391**, 877 (1998).

12. Rockford, L. et al. Polymers on nanoperiodic, heterogeneous surfaces. *Physical Review Letters* **82**, 2602-2605 (1999).

13. Suh, K. Y., Kim, Y. S. & Lee, H. H. Capillary force lithography. *Advanced Materials* **13**, 1386-1389 (2001).

14. Suh, K. Y. & Lee, H. H. Dynamic instability of strongly confined thin polymer films in spinodal dewetting. *Physical Review Letters* **87**, 135502-1-1355-2-4 (2001).

15. Suh, K. Y. & Lee, H. H. Free energy of distorted polymer films in highly confined three-dimensional systems. *Macromolecules* **34**, 6456 (2001).

16. Suh, K. Y., Park, J. & Lee, H. H. Controlled polymer dewetting by physical confinement. *J Chem Phys* **116**, 7714 (2002).

17. Suh, K. Y., Yoo, P. J. & Lee, H. H. Meniscus formation and breakdown of thin polymer films in microchannels. *Macromolecules* **35**, 4414 (2002).

18. Yoo, P. J., Suh, K. Y. & Lee, H. H. Short- and long-range interactions in thin films of polymer blends in microchannels. *Macromolecules* **35**, 3205 (2002).

19. Johnson, W. C. & Wise, S. M. Phase decompostion of a binary thin film on a patterned substrate. *J Chem Phys* **81**, 919 (2002).

20. Herminghaus, S. Dynamical Instability of Thin Liquid Films Between Conducting Media. *Phys. Rev. Lett.* **83**, 2359-2361 (1999).

21. Schaffer, E., Thurn-Albrecht, T., Russell, T. P. & Steiner, U. Electrically induced structure formation and pattern transfer. *Nature* **403**, 874-877 (2000).

22. Schafer, E., Thurn-Albrecht, T., Russell, T. P. & Steiner, U. Electrohydrodynamic instabilities in polymer films. *Europhysics Letters* **53**, 518-524 (2001).

23. Lin, Z. Q. et al. Electric field induced instabilities at liquid/liquid interfaces. *Journal of Chemical Physics* **114**, 2377-2381 (2001).

24. Lin, Z. Q., Kerle, T., Russell, T. P., Schafer, E. & Steiner, U. Structure formation at the interface of liquid/liquid bilayer in electric field. *Macromolecules* **35**, 3971-3976 (2002).

25. Lin, Z. Q., Kerle, T., Russell, T. P., Schafer, E. & Steiner, U. Electric field induced dewetting at the liquid-liquid interface. *Macromolecules* **35**, 6255 (2002).

26. Chou, S. Y. & Zhuang, L. Lithographically induced self-assembly of periodic polymer micropillar arrays. *J. Vac. Sci. Technol. B* **17**, 3197-3202 (1999).

27. Chou, S. Y., Zhuang, L. & Guo, L. Lithographically induced self-construction of polymer microstructures for resistless patterning. *Appl. Phys. Lett.* **75**, 1004-1006 (1999).

28. Deshpande, P., Sun, X. & Chou, S. Y. Observation of dynamic behavior of lithographically induced self-assembly of supramolecular periodic pillar arrays in a homopolymer film. *Appl. Phys. Lett.* **79**, 1688-190 (2001).

29. Deshpande, P. & Chou, S. Y. Lithographically induced self-assembly of microstructures with a liquid-filled gap between the mask and polymer surface. *J. Vac. Sci. Technol. B* **19**, 2741-2744 (2001).

30. Schäffer, E., Harkema, S. & Steiner, U. Thermomechanical film instabilities induced by a temperature gradient. Submitted.

31. Maissel, L. I. & Glang, R. *Handbook of Thin Film Technology* (McGraw-Hill, Inc., 1983).

BIBLIOGRAPHY

Amundson, K. et al. Effect of an electric-field on block copolymer microstructure. *Macromolecules* **24**, 6546-6548 (1992).

Amundson, K., Helfand, E., Quan, X., Hudson, S. D. & Smith, S. D. Alignment of lamellar block-copolymer microstructure in an electric-field. 2. mechanisms of alignment. *Macromolecules* **27**, 6559-6570 (1994).

Amundson, K., Helfand, E., Quan, X. & Smith, S. D. Alignment of lamellar block-copolymer microstructure in an electric-field. 1. alignment kinetics. *Macromolecules* **26**, 2698-2703 (1993).

Anastasiadis, S. H., Gancarz, I. & Koberstein, J. T. Compatabilizing effect of block copolymers added to the polymer/polymer interface. *Macromolecules* **22**, 1449-1453 (1989).

Anastasiadis, S. H., Russell, T. P., Satija, S. K. & Majkrzak, C. F. Neutron reflectivity studies of the surface-induced ordering of diblock copolymer films. *Physical Review Letters* **62**, 1852-1855 (1989).

Anklam, M. R., Saville, D. A. & Prud'homc, R. K. Electric-field-induced rupture of polymer-stabilized oil films. *Colloid Polym Sci* **277**, 957-964 (1999).

Ashok, B., Muthukumar, M. & Russell, T. P. Confined thin film diblock copolymer in the presence of an electric field. *Journal of Chemical Physics* **115**, 1559-1564 (2001).

Batchelor, G. K. *An introduction to fluid dynamics* (Cambridge University Press, Cambridge, 1967).

Bischof, J., Scherer, D., Herminghaus, S. & Leiderer, P. Dewetting modes of thin metallic films: Nucleation of holes and spinodal dewetting. *Physical Review Letters* **77**, 1536-1539 (1996).

Blake, T. D., Clarke, A. & Stattersfield, E. H. An investigation of electrostatic assist in dynamic wetting. *Langmuir* **16**, 2928-2935 (2000).

Bodycomb, Y., Funaki & Kimishima, K. Single-grain lamellar microdomain from a diblock copolymer. *Macromolecules* **32**, 2075 (1999).

Boker, A. et al. Large scale domain alignment of a block copolymer from solution using lectric fields. *Macromolecules* **35**, 1319-1325 (2002).

Boltau, M., Walheim, S., Mlynek, J., Krausch, G. & Steiner, R. Surface induced structure formation of polymer blends on patterned substrates. *Nature* **391**, 877 (1998).

Brochard-Wyart, F. & Daillant, J. Drying of solids wetted by thin liquid films. *Can. J. Phys.* **68**, 1084-1088 (1990).

Brochard-Wyart, F., Debregeas, G. & deGennes, P. G. Spreading of viscous droplets on a non viscous liquid. *Colloid Polym Sci* **274**, 70-72 (1996).

Brochard-Wyart, F., Martin, P. & Redon, C. Liquid/liquid dewetting. *Langmuir* **9**, 3682-3690 (1993).

Budkowski, A., Klein, J., Steiner, U. & Fetters, L. J. Diblock copolymers attached to homopolymer surfaces and interfaces. *Macromolecules* **26**, 2470-2478 (1993).

Buguin, A., Vovelle, L. & Brochard-Wyart, F. Shocks in Inertial Dewetting. *Phys. Rev. Lett.* **83**, 1183-1186 (1999).

Chou, S. Y. Patterned magnetic nanostructures and quantized magnetic disks. *Proceedings of the IEEE* **85**, 652-671 (1997).

Chou, S. Y. & Zhuang, L. Lithographically induced self-assembly of periodic polymer micropillar arrays. *J. Vac. Sci. Technol. B* **17**, 3197-3202 (1999).

Chou, S. Y., Zhuang, L. & Guo, L. Lithographically induced self-construction of polymer microstructures for resistless patterning. *Appl. Phys. Lett.* **75**, 1004-1006 (1999).

Cohen I., Li H., Hougland J.L., Mrksich M. & Nagel, S. R. Using selective withdrawal to coat microparticles. *Science* **292**, 265 (2001).

Cressman, P. J. New type of thermoplastic deformation. *J. Appl. Phys.* **34**, 2327-2330 (1963).

Cross, M. C. & Hohenberg, P. C. Pattern formation outside of equilibrium. *Rev. Mod. Phys.* **65**, 851-1112 (1993).

Daikhin, L. I., Kornyshev, A. A. & Urbakh, M. The effect of electric field on capillary waves at the interfaces of two immiscible electrolytes. *Chemical Physics Letters* **309**, 137-142 (1999).

Daikhin, L. I., Kornyshev, A. A. & Urbakh, M. Capillary waves at soft electrified interfaces. *Journal of Electroanalytical Chemistry* **483**, 68-80 (2000).

Dalnoki-Veress, K., Nickel, B. G. & Dutcher, J. R. Dispersion-Driven Morphology of Mechnically Confined Polymer Films. *Physical Review Letters* **82**, 1486-1489 (1999).

deGennes, P. G. Wetting: statics and dynamics. *Reviews of modern physics* **57**, 827-863 (1985).

Derjaguin, B. V., Churaev, N. V. & Muller, V. M. *Surface forces* (Consultants Bureau, New York, 1987).

Deshpande, P. & Chou, S. Y. Lithographically induced self-assembly of microstructures with a liquid-filled gap between the mask and polymer surface. *J. Vac. Sci. Technol. B* **19**, 2741-2744 (2001).

Deshpande, P., Sun, X. & Chou, S. Y. Observation of dynamic behavior of lithographically induced self-assembly of supramolecular periodic pillar arrays in a homopolymer film. *Appl. Phys. Lett.* **79**, 1688-190 (2001).

Fichet, G., Stutzmann, N., Muir, B. V. O. & S., H. W. T. Microembossing of elastomeric triblock copolymers. *Advanced Materials* **14**, 47-51 (2002).

Fox, T. G. & Flory, P. J. The glass temperature and related properties of polystyrene. Influence of molecular weight. *J. Polym Sci* **14**, 315-319 (1954).

Glenn, W. E. Thermoplastic recording. *J. Appl. Phys.* **30**, 1870-1873 (1959).

Helfand, E. & Tagami, Y. Theory of the interface between immiscible polymers. II. *J. Chem. Phys.* **56**, 3592-3601 (1972).

Helfand, E. & Wasserman, Z. R. Block copolymer theory. 4. narrow interface approximation. *Macromolecules* **9**, 879 (1976).

Herminghaus, S. Dynamical Instability of Thin Liquid Films Between Conducting Media. *Phys. Rev. Lett.* **83**, 2359-2361 (1999).

Higgins A.M. & R.A.L., J. *Nature* **404**, 476 (2000).

Israelachvili. *Intermolecular and surface forces* (Academic, London, 1992).

Jacobs, K., Herminghaus, S. & Mecke, K. Thin liquid polymer films rupture via defects. *Langmuir* **14**, 965-969 (1998).

Joanny, J. F. Wetting of a liquid substrate. *PhysicoChemical Hydrodunamics* **9**, 183-196 (1987).

Johnson, W. C. & Wise, S. M. Phase decompostion of a binary thin film on a patterned substrate. *J Chem Phys* **81**, 919 (2002).

Kargupta, K., Konnur, R. & Sharma, A. Instability and pattern formation in thin liquid films on checmically heterogeneous substrates. *Langmuir* **16**, 10243-10253 (2000).

Kargupta, K. & Sharma, A. Dewetting of thin films on periodic physcially and chemically patterned surfaces. *Langmuir* **18**, 1893-1903 (2002).

Kerle, T., Yerushalmi-Rozen, R., Klein, J. & Fetters, L. J. van der Waals stable thin liquid films: Correlated undulations and ultimate dewetting. *Europhys. Lett.* **44**, 484-490 (1998).

Khanna, R. & Sharma, A. Pattern formation in spontaneous dewetting of thin apolar films. *J Colloid and Interface Science* **195**, 42-50 (1997).

Killat, U. Revised dynamical theory of thermoplastic deformation. *J. Appl. Phys.* **46**, 5169-5172 (1975).

Kohler, J., Riess, G. & Banderet, A. *Eur. Polym. J.* **4**, 173 (1968).

Konnur, R., Kargupta, K. & Sharma, A. Instability and morphology of thin liquid films on chemically heterogeneous substrates. *Physical Review Letters* **84**, 931-934 (2000).

Kyrylyuk, A. V., Zvelindovsky, A. V., Sevink, G. J. A. & Fraaije, J. G. E. M. Lamellar alignment of diblock copolymers in an electric field. *Macromolecules* **35**, 1473-1476 (2002).

Lambooy, P., Phelan, K. C., Haugg, O. & Krausch, G. Dewetting at the liquid-liquid interface. *Physical Review Letters* **76**, 1110-1113 (1996).

Leach, A. K. & et al. (In preparation).

Lin, Z. Q. et al. Electric field induced instabilities at liquid/liquid interfaces. *Journal of Chemical Physics* **114**, 2377-2381 (2001).

Lin, Z. Q., Kerle, T., Russell, T. P., Schafer, E. & Steiner, U. Structure formation at the interface of liquid/liquid bilayer in electric field. *Macromolecules* **35**, 3971-3976 (2002).

Lin, Z. Q., Kerle, T., Russell, T. P., Schafer, E. & Steiner, U. Electric field induced dewetting at the liquid-liquid interface. *Macromolecules* **35**, 6255 (2002).

Macosko, C. W. *Rheology principles, measurements and applications* (Wiley, New York, 1994).

Maissel, L. I. & Glang, R. *Handbook of Thin Film Technology* (McGraw-Hill, Inc., 1983).

Mansky, P. et al. Large-area domain alignment in block copolymer thin films using electric fields. *Macromolecules* **31**, 4399-4401 (1998).

Mazur, K. More data about dielectric and electret properties of poly(methyl methacrylate). *J. Phys. D: Appl. Phys.* **30**, 1383-1398 (1997).

Melcher, J. R.

Melcher, J. R. Electrohydrodynamic and magnetohydrodynamic surface waves and instabilities. *Phys. Fluids* **4**, 1348-1354 (1961).

Melcher, J. R. & Schwarz, W. J. Interfacial relaxation overstability in a tangential electric field. *Phys. Fluid* **11**, 2604-2616 (1968).

Melcher, J. R. & Smith, C. V. Electrohydrodynamic charge relaxation and interfacial perpendicular-field instability. *Phys. Fluids* **12**, 778-790 (1969).

Mitlin, V. S. Dewetting of solid surface: analogy with spinodal decompostion. *J Colloid and Interface Science* **156**, 491 (1993).

Morkved, T. L. et al. Local control of microdomain orientation in diblock copolymer thin films with electric fields. *Science* **273**, 931-933 (1996).

Oddershede, L. & Nagel, S. R. Singularity during the onset of an electrohydrodynamic spout. *Physical Review Letters* **85**, 1234-1237 (2000).

Onuki, A. Interface instability induced by an electric field in fluids. *Physica A* **217**, 38-52 (1995).

Pease III, L. F. & Russel, W. B. Linear stability analysis of thin leaky dielectric films subjected to electric fields. *J. Non-Newtonian Fluid Mech.* **102**, 233-250 (2002).

Pelrine, R., Kornbluh, R., Pei, Q. & Joseph, J. High-Speed Electrically Actuated Elastomers with Strain Greater Than 100%. *Science* **287**, 836-839 (2000).

Qu, S. et al. Dewetting dynamics at a polymer-polymer interface. *1997* **30**, 3640-3645 (1997).

Reiter, G. Dewetting of thin polystyrene films. *Phys. Rev. Lett.* **68**, 75-78 (1992).

Reiter, G. & Khanna, R. Real-time determination of the slippage length in autophobic polymer dewetting. *Physical Review Letters* **85**, 2753-2756 (2000).

Reiter, G., Khanna, R. & Sharma, A. Enhanced Instability in thin liquid films by improved compatibility. *Physical Review Letters* **85**, 1432 (2000).

Reiter, G. et al. Destabilising effect of long-range forces in thin liquid films on wettable substrates. *Europhys. Lett.* **46**, 512-518 (1999).

Reynolds, J. M. Stability of an electrostatically supproted fluid column. *The Physics of Fluids* **8**, 161-170 (1965).

Rockford, L. et al. Polymers on nanoperiodic, heterogeneous surfaces. *Physical Review Letters* **82**, 2602-2605 (1999).

Rosa, C. D., Park, C. & Thomas, E. L. Microdomain patterns from directional eutectic solidification and epitaxy. *Nature* **405**, 433 (2000).

Ruckenstein, E. & Jain, R. K. Spontaneous rupture of thin liquid films. *Faraday Trans. 2* **70**, 132-146 (1974).

Saville, D. A. Electrohydrodynamic deformation of a particulate stream by a transverse electric field. *Physical Review Letters* **71**, 2907-2910 (1992).

Saville, D. A. Dielectric behavior of colloidal dispersions. *Colloid Surf.* **92**, 29-40 (1994).

Saville, D. A. Electrohydrodynamics: the Taylor-Melcher leaky dielectric model. *Annu. Rev. Fluid Mech.* **29**, 27-64 (1997).

Schafer, E., Thurn-Albrecht, T., Russell, T. P. & Steiner, U. Electrohydrodynamic instabilities in polymer films. *Europhysics Letters* **53**, 518-524 (2001).

Schäffer, E., Harkema, S. & Steiner, U. Thermomechanical film instabilities induced by a temperature gradient. submitted (2002).

Schaffer, E., Thurn-Albrecht, T., Russell, T. P. & Steiner, U. Electrically induced structure formation and pattern transfer. *Nature* **403**, 874-877 (2000).

Seemann, R., Herminghaus, S. & Jacobs, K. Shape of a liquid front upon dewetting. *Physical Review Letters* **87**, 196101-1-196101-4 (2001).

Sens, P. & Isambert, H. Undualtion instability of lipid membrane under an electric field. *Physical Review Letters* **88**, 128102-1-128102-4 (2002).

Sferrazza, M., Heppenstall-Bulter, M. & Cubitt, R. Interfacial Instability Driven by Dispersive Forces: The Early Stages of Spinodal Dewetting of a Thin Polymer Film on a Polymer Substrate. *Physical Review Letters* **81**, 5173 (1998).

Sharma, A. & Khanna, R. Pattern formation in unstable thin liquid films. *Physical Review Letters* **81**, 3463-3466 (1998).

Stange, T. G. & Evans, D. F. Nucleation and growth of defects leading to dewetting of thin polymer films. *Langmuir* **13**, 4459 (1997).

Strobl, B. *The physics of polymer* (Spinger-Verlag, Inc., 1997).

Suh, K. Y., Kim, Y. S. & Lee, H. H. Capillary force lithography. *Advanced Materials* **13**, 1386-1389 (2001).

Suh, K. Y. & Lee, H. H. Dynamic instability of strongly confined thin polymer films in spinodal dewetting. *Physical Review Letters* **87**, 135502-1-1355-2-4 (2001).

Suh, K. Y. & Lee, H. H. Free energy of distorted polymer films in highly confined three-dimensional systems. *Macromolecules* **34**, 6456 (2001).

Suh, K. Y., Park, J. & Lee, H. H. Controlled polymer dewetting by physical confinement. *J Chem Phys* **116**, 7714 (2002).

Suh, K. Y., Yoo, P. J. & Lee, H. H. Meniscus formation and breakdown of thin polymer films in microchannels. *Macromolecules* **35**, 4414 (2002).

Suo, Z. & Liang, J. Theory of lithographically-induced self-assembly. *Appl. Phys. Lett.* **78**, 3971-3973 (2001).

Swan, J. W. Stress and other effects produced in resin and in a viscid compound of resin and oil by electrification. *Proc. R. Soc. London* **62**, 38-46 (1897).

Tanner, L. H. The spreading of silicone oil drops on horizontal surfaces. *J. Phys. D: Appl. Phys.* **12**, 1473-1484 (1979).

Thurn-Albrecht, T., DeRouchey, J., Russell, T. P. & Jaeger, H. M. Overcoming interfacial interactions with electric fields. *Macromolecules* **33**, 3250-3253 (2000).

Thurn-Albrecht, T. et al. Ultrahigh-density nanowire arrays grown in self-assembled diblock copolymer templates. *Science* **290**, 2126-2129 (2000).

Thurn-Albrecht, T. et al. Nanoscopic templates from oriented block copolymer films (vol 12, pg 787, 2000). *Advanced Materials* **12**, 1138-1138 (2000).

Thurn-Albrecht, T. et al. Nanoscopic Templates from Oriented Block Copolymer Films. *Advanced Materials* **12**, 787-791 (2000).

Trau, M., Sankarn, S., Saville, D. A. & Aksay, I. A. Pattern formation in nonaqueous colloidal dispersions via electrohydrodynamic flow. *Langmuir* **11**, 4665-4672 (1995).

Trau, M., Sankarn, S., Saville, D. A. & Aksay, I. A. Electric-field-induced pattern formation in colloidal dispersions. *Nature* **374**, 437-439 (1995).

Tsori, Y. & Andelman, D. Thin film diblcok copolymers in electric field: transition from perpendicular to parallel lamellae. *Macromolecules* **35** (2002).

Vitt, E. & Shull, K. R. Equilibrium contact angle for polymer/polymer interfaces. *Macromolecules* **28**, 6349-6353 (1995).

Vizika, O. & Saville, D. A. The electrohydrodynamic deformation of drops suspend in liquid in steady and oscillatory electric-fields. *J. Fluid Mech.* **239**, 1-21 (1992).

Vrij, C. *Discuss Faraday Soc.* **42**, 23 (1967).

Wang, C., Krausch, G. & Geoghegan, M. Dewetting at a polymer-polymer interface: Film thickness dependence. *Langmuir* **17**, 6269-6274 (2001).

Weiss, P. To bead or not to bead. *Science News* **155**, 28-30 (1999).

Wu, S. *Polymer interface and adhesion* (Marcel Dekker, 1982).

Xie, R., Karim, A., Douglas, J. F., Han, C. C. & Weiss, R. A. Spinodal dewetting of thin polymer films. *Phys. Rev. Lett.* **81**, 1251-1254 (1998).

Yoo, P. J., Suh, K. Y. & Lee, H. H. Short- and long-range interactions in thin films of polymer blends in microchannels. *Macromolecules* **35**, 3205 (2002).

Yu, Z., Wu, W., Chen, L. & Chou, S. Y. Fabrication of large area 100nm pitch grating by spatial frequency doubling and nanoimprint lithography for subwavelength optical applications. *J. Vac. Sci. Technol. B* **19**, 2816-2819 (2001).